UNIVERSITY OF NOTTINGHAM



Refinement of the Grain Structure of Selective Laser Melted Ti-6Al-4V via Induction Heat Treatment

Zhiyi Zou

Doctoral Thesis

Submitted in Fulfilment of the Requirements for the Award of Doctor of Philosophy

July 2020

Acknowledgements

First and foremost, I would like to express my gratitude to my supervisors Marco Simonelli, Juliano Katrib, Georgios Dimitrakis and Richard Hague for their patient, support and guidance throughout this study.

Marco always has been the first person to help me in the past four years. As an excellent researcher and an outstanding individual, he has taught me many things. In multiple times, I even felt that my performance was not worth his efforts. It is a great honour to explore the beauty of AM and metallurgy under his guidance. For this, I would like to thank you for everything, Marco.

Juliano and George led me into the world of induction heating. Juliano demonstrated what is the true meaning of critical thinking, and taught me how to notice the errors and omissions hidden in the plain sight. His rigorous style undoubtedly helped me grow into a better researcher. Thanks, Juliano. George always responded quickly to my needs and his creativity expanded the possibilities of this project. His kindness and patient helped me unload the stress and frustration. Thanks, George.

Thank you to Richard for providing critical and fundamental supports to help this project run smoothly. I still remember his words on research ".. PhD is more than working from 9am to 5pm, but a lifestyle … ". It is a privilege to study in this world-class research group under his leadership.

I also would like to express sincere thanks to all the technicians and researchers, who provided their generous help in the past four years. Thanks to Mark Hardy, Mark East and Joe White from the CfAM for helping me 'tune' the SLM system and tolerating of my carelessness. Thanks to Buss Thomas, Mason Max, Jason Greaves and Graham Malkinson from the Wolfson building for helping me set up the induction heating system and perform all the tensile tests. Thanks to Neigel Neate and Martin Roe from the NMRC for the

help with the EBSD experiments. Last but not least, thanks to Ryan Maclachlan from the Loughborough University for his help with the EBSD investigations and the useful discussions.

A special thanks goes to my dearest friend Irene Xu. Though you and I are living in different continents, you provided endless mental supports to help me survive all those frustrating times, and reminded me what the purpose of life is. There are highs and lows in life. Life in top law school is hard, but I have no doubt that a determined person like you can get through the tough times and achieve something special. Come on girl, make a difference in this unsatisfactory world!

Finally, I am eternally grateful to my parents. Your continuous support is the reason why I can still pursue my dream at this age without fearing of failure. You understand my dream and encourage me to pursue it. I consider myself extremely lucky to have a family like this. This work is mainly dedicated to you.

Abstract

Selective laser melting (SLM) has been shown to be an attractive manufacturing route for the production of α/β titanium alloys, and in particular Ti-6Al-4V. Post-process heat treatments are widely used to tune the microstructure and improve the mechanical properties of the as-built parts. However, conventional heat treatments cannot transform the coarse elongated prior-β structure in a satisfying way, which limits the use of Ti-6Al-4V produced by SLM. The principal aim of the present study is to investigate how the initial microstructure formed in SLM can be exploited to achieve β-grain refinement via induction heat treatment. The microstructure and tensile properties following such heat treatments are discussed. As well as the microstructure evolution and recrystallisation phenomena responsible for the refinement.

The effect of induction heat treatment on the tensile properties and microstructure of the SLM specimens were initially investigated. It was found that, after heat treated to a temperature around β transus via induction heating (short time β annealing), a typical microstructure consisted of equiaxed or quasi-equiaxed prior-β grains can be observed. In comparison to the microstructure obtained after conventional heat treatment, a refinement of the morphology of the prior-β grains can be observed. It was also found that the width of the α lamellae is smaller than what was observed in specimens subjected to conventional heat treatment. It was found that this microstructure can provide tensile properties equivalent to or better than what was obtained after conventional heat treatment, and also might provide a potential to achieve isotropic behaviour and improve fatigue resistance.

The microstructure evolution leads to the observed β grain refinement was then investigated. It was found that a mixed morphology of prior-β grains appears when the temperature approaches β transus. Such mixed

morphology consists of both newly formed equiaxed prior-β grains and original columnar prior-β grains. It was found that the equiaxed prior-β grains grow from the recrystallised high angle boundary (HAB) β, which are nucleated during the induction heat treatment. It was found that, since the HAB has higher mobility, the equiaxed HAB β grain grows faster compared to the original β grains. Therefore, the original columnar morphology is gradually replaced, and the microstructure evolves toward the observed refined morphology.

The nature of the observed recrystallisation phenomena was then investigated. It was found that the recrystallised β is related to individual adjacent α/α' laths via Burger Orientation Relationship (BOR), and can be nucleated either in the interior of the individual α phase, at the α/β boundary or at the prior-β grain boundary. Therefore, the recrystallisation process is identified as epitaxial recrystallisation. It can be assumed that the driving force for the observed epitaxial recrystallisation origins from the stored energy of deformation that is typically expressed by the high densities of lattice defects found after SLM in the core and at the boundary of the martensitic as-built microstructure. The induction heat treatment would exacerbate such epitaxial recrystallisation and result in significant refinement of the structure.

This study achieves for the first time the refinement of the β grain structure of additively manufactured Ti alloys via simple heat treatment. Further, this study investigates for the first time the microstructure evolution during the β annealing of Ti-6Al-4V produced by SLM, especially in its early stage. Lastly, this study demonstrates for the first time how epitaxial recrystallisation nucleate and progress in additively manufactured Ti alloys.

List of publications

Zhiyi Zou, Marco Simonelli, Juliano Katrib, Georgios Dimitrakis, Richard Hague, "Refinement of the grain structure of additive manufactured titanium alloys via epitaxial recrystallization enabled by rapid heat treatment", *Scripta Materialia* 180 (2020): 66-70.

Contents

Acknowledgements I

Abstract III

List of publications V

CHAPTER 1 1

1 Introduction 1

CHAPTER 2 4

2 Literature review 4

2.1 Metallurgy of titanium and titanium alloys 4

2.1.1 Introduction 4

2.1.2 Metallurgy of pure titanium 4

2.1.3 Titanium alloys classification 7

2.1.4 Physical metallurgy of Ti-4Al-4V 9

2.2 Metal powder bed fusion additive manufacturing 16

2.2.1 Introduction 16

2.2.2 Principles of laser-based metal powder bed fusion additive manufacturing 16

2.2.3 Selective laser melting of metal powders 18

2.3 Selective Laser Melting of Ti-6Al-4V and Post-process Heat Treatment 23

2.3.1 Introduction 23

2.3.2 Selective laser melting of Ti-6Al-4V 24

2.3.3 Strategies and final tensile properties of post-process heat treatment 28

2.3.4 Microstructure and texture transformation in post-process heat treatment 38

2.4 Induction Heating Technique.....47
2.4.1 Introduction.....47
2.4.2 Principles of induction heating.....48
2.4.3 Typical equipment for induction heating system.....52
2.5 Summary and gap in knowledge.....57
2.6 Aim and objectives of this study.....58
CHAPTER 3.....60
3. Material and Methods.....60
3.1 Material used in this study.....60
3.2 Post-process heat treatments for the received Ti-6Al-4V.....63
3.2.1 Conventional heat treatment: heating system and experimental procedure.....64
3.2.2 Induction heat treatments: heating system and experiment procedure.....65
3.2.3 Design of the temperature gradient heat treatment.....76
3.3 Tensile testing of the SLM Ti-6Al-4V under the different investigated conditions.....78
3.4 Characterisation of the specimen microstructure and crystallographic texture.....79
3.4.1 Sample Preparation for Microstructural Characterisation.....80
3.4.2 Techniques for microstructure analysis.....81
3.4.3 Techniques for crystallographic texture analysis.....82
CHAPTER 4.....89
4. Tensile properties of SLM Ti-6Al-4V under the different investigated conditions.....89
4.1 Tensile properties of SLM Ti-6Al-4V in the as-built condition.....89

4.2 Tensile properties of SLM Ti-6Al-4V after conventional heat treatments 91

4.3 Tensile properties of SLM Ti-6Al-4V after induction heat treatment....92

4.3.1 Induction heat treatment above 980°C.....92

4.3.2 Induction heat treatment above 1005°C.....95

4.3.3 Induction heat treatment above 1030°C.....98

4.3.4 Induction heat treatment above 1030°C without subsequent ageing.....102

4.4 Comparison and discussion of the induction heating processes and the corresponding tensile properties of SLM Ti-6Al-4V.....105

4.4.1 Consistency of the induction heating processes 105

4.4.2 Tensile properties of SLM Ti-6Al-4V that were subjected to different heat treatments.....106

4.5 Summary 110

CHAPTER 5.....112

5. Influence of heat treatments on the microstructure of SLM Ti-6Al-4V 112

5.1 Microstructural constituents of SLM Ti-6Al-4V subjected to heat treatments 113

5.2 Typical microstructure of SLM Ti-6Al-4V that were subjected to different heat treatment 117

5.2.1 Typical microstructure of SLM Ti-6Al-4V in as-built condition 117

5.2.2 Typical microstructure of SLM Ti-6Al-4V that were treated with conventional heating 119

5.2.3 Typical microstructure of SLM Ti-6Al-4V that were treated with induction heating.....123

5.3 Crystallographic textures and phase orientation maps of SLM Ti-6Al-4V that were subjected to different heat treatment.....128

5.3.1 Crystallographic textures and phase orientation of SLM Ti-6Al-4V in as-built condition 128

5.3.2 Crystallographic textures and phase orientation of SLM Ti-6Al-4V that were treated with conventional heating 130

5.3.3 Crystallographic textures and phase orientation of SLM Ti-6Al-4V that were treated with induction heating 131

5.4 Summary 136

CHAPTER 6 138

6. Early stages of microstructural evolution during beta annealing of SLM Ti-6Al-4V 138

6.1 The evolution of microstructural morphology during the early stages of β annealing 139

6.2 The evolution of crystallographic texture during the early stages of β annealing 146

6.3 Summary 154

CHAPTER 7 155

7. Epitaxial recrystallisation of β grain in SLM Ti-6Al-4V during rapid heat treatment 155

7.1 Development of α and β phase in SLM Ti-6Al-4V during heating 156

7.1.1 Microstructural evolution from room temperature to 800°C 156

7.1.2 Recrystallisation of β grain observed in the microstructure at 850°C 160

7.1.3 Microstructural evolution above 850°C 167

7.2 Development of the recrystallised β in SLM Ti-6Al-4V during heat treatment 170

7.3 Summary 177

CHAPTER 8 179

8. Conclusions and future work 179

8.1 Conclusions 179

8.2 Future work.....182

Appendix A 184

Appendix B 193

References 195

CHAPTER 1

1 Introduction

Thanks to a combination of high specific strength, corrosion resistance and biocompatibility, titanium alloys - especially Ti-6Al-4V - have a wide range of applications in the aerospace, medical, automotive and chemical industries (Polmear et al., 2017). Moreover, additive manufacturing (AM) of Ti-6Al-4V can provide unprecedented design freedom with a promising buy-to-fly ratio and has attracted significant attention over the past decades (Dutta and Froes, 2016).

It has been extensively shown that Selective Laser Melting (SLM), one of the most promising AM techniques, can produce near net-shape fully dense Ti-6Al-4V, which, after heat treatment, can achieve a mechanical property comparable to its wrought counterparts (Beese and Carroll, 2016, Qian et al., 2016). However, the as-built SLM Ti-6Al-4V possess limited properties such as high residual stress, low ductility (elongation <10%) and mechanical anisotropy (Leuders et al., 2013, Losertová and Kubeš, 2017). Early attempts have been made to improve the properties of as-built materials via various in-situ heat treatments but, at present, there is no convincing solution that has been universally accepted by the community (Ali et al., 2017, Li et al., 2016, Liu et al., 2015). Thus, additional heat treatments after the SLM process, also known as post-process heat treatments, are widely used to achieve a better balance of mechanical properties (Chandramohan et al., 2018, Zhang et al., 2018).

For the design of heat treatments for Ti-6Al-4V, β transus temperature is a crucial parameter as, above this temperature, the alloy enters into a single β phase region (Lütjering and Williams, 2007). Therefore, conventional heat treatments of Ti-6Al-4V are typically divided into two groups, sub-transus (below β-transus) and super-transus (over β-transus), depending on whether

the soaking temperature is lower or higher than the β-transus temperature, respectively (Zhang et al., 2018).

Research on the sub-transus heat treatment of SLM Ti-6Al-4V has established a well-recognised theory to explain the texture formation during this process (Ding et al., 2017a, Zhang et al., 2018). Current understanding based on what has been established suggests that sub-transus heat treatment can achieve a compromise between ductility and strength (ASTM, 2014a, ASTM, 2014b, SAE, 2016), however, sub-transus heat treatment cannot change the original elongated columnar prior-β grain, which might result in mechanical anisotropy and limited fatigue resistance (ter Haar et al., 2016, AmirMahyar et al., 2017, Losertová and Kubeš, 2017).

Super-transus heat treatment (also known as β annealing) of SLM Ti-6Al-4V has been shown to have the potential to develop an equiaxed β grain structure (Nandwana et al., 2019), however, conventional heat treatment requires sufficient dwell time (exposure duration usually lasting several hours) to achieve uniform heating, which leads to an uncontrolled coarsening of the grain structure and a related loss in ductility and strength (Vilaro et al., 2011, Vrancken et al., 2012). Additionally, there are currently only a limited amount of studies on the mechanisms that describe the formation of equiaxed grain structures during super-transus heat treatment. The lack of understanding in this area further hinders the application and development of such heat treatments.

In this study, a rapid volumetric heating method – induction heating – will be applied to β anneal SLM Ti-6AL-4V, with the objective of achieving uniform heating (temperature spread within 5%) above the β transus temperature while limiting dwell times (range of a few seconds). By restricting the growth of the β grain during β annealing, the aim of this work is to develop a microstructure consisting of refined equiaxed or quasi-equiaxed prior-β grains, with mechanical properties comparable or even superior to conventional heat treated SLM Ti-6Al-4V. Such refinement of the prior-β

grains after heat treatment will be the first time reported for additively manufactured Ti alloys.

Additionally, this study aims to increase the understanding of the metallurgy of SLM Ti-6AL-4V in two further aspects: firstly, the microstructure evolution that happens during the proposed heat treatment will be characterised and studied; secondly, the mechanisms that describe the formation of equiaxed grain structures during super-transus heat treatment will be analysed and discussed. To date, explicit knowledge and detailed information needed to understand these aspects have never been revealed before.

A review of metallurgy of Ti-6Al-4V is reported in chapter 2, as well as selective laser melting of Ti-6Al-4V and its related post-process heat treatment, followed by an introduction of induction heating. The materials used and the experimental procedures of this research are presented in Chapter 3. Chapter 4 reports the temperature recorded in the heat treatments and the tensile properties of the specimens investigated in this project. The microstructure obtained after different heat treatments are analysed in Chapter 5. The microstructure evolution during the proposed super-transus heat treatments is further characterised and studied in Chapter 6. Chapter 7 tracks real-time microstructure transformation through high-temperature EBSD and proposes a potential mechanism to explain the observed texture evolution during super-transus heat treatment. Finally, conclusions and suggestions for future work are reported in Chapter 8.

CHAPTER 2

2 Literature review

2.1 Metallurgy of titanium and titanium alloys

2.1.1 Introduction

One of the main objectives of this study is to understand the microstructure evolution of selective laser melted Ti-4Al-4V during early stage beta annealing. In order to study the connections between the microstructure of the alloy before and after heat treatment and to contextualise the results presented in this research, a review of the physical metallurgy of titanium and titanium alloys will be presented in this chapter.

This chapter starts with the metallurgy of pure titanium in section 2.1.2, especially the relationship between its different crystal structures. A classification of titanium alloys will be described in section 2.1.3, which provides information about where Ti-6Al-4V stands in the Ti alloy family. The rules of solidification and solid phase transformations of Ti-6Al-4V are reviewed in section 2.1.4.

2.1.2 Metallurgy of pure titanium

Most metals are crystalline material, which means their atoms are arranged in an orderly form when the material is in solid state. The smallest group of atoms that constitute this repeating arrangement is called the unit cell, the forms and the dimensions of the unit cells fully reflect the symmetry of the crystal structure of the given material. (Froes, 2015)

Titanium, with a melting point of 1668°C, is an allotropic element that has two different crystallographic forms in solid state, which are hexagonal close-packed (hcp) structure and body-centred cubic (bcc) structure, as displayed separately in Figure 2.1 (Froes, 2015). The hcp structure exists at room

temperature, referred to as α phase as Figure 2.1(a) shows (Froes, 2015). When pure Ti is heated up to 883°C, the original hcp structure will transform to the bcc structure, known as the β phase as Figure 2.1(b) shows (Froes, 2015). For titanium and its alloys, the lowest equilibrium temperature that maintains the entire material in the β phase is usually referred to as the β transition temperature, or β transus (Lütjering and Williams, 2007).

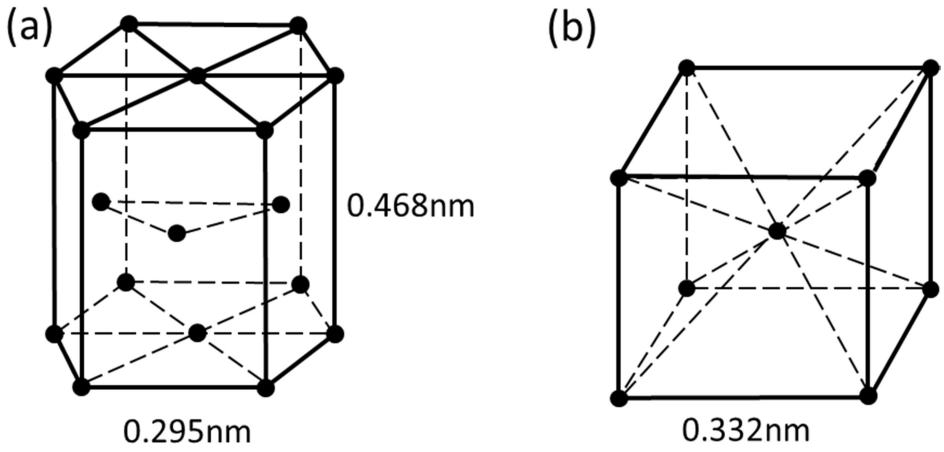


Figure 2.1. Crystal structure of pure Titanium, (a) Unit cell of α phase, (b) Unit cell of β phase

In most cases, the transformation between hcp α and bcc β follows a well-established Burger Orientation Relationship (BOR) (Burgers, 1934), which is expressed in Equation 2-1:

$$\{1\ 1\ 0\}\beta // \{0\ 0\ 0\ 1\}\alpha$$

$$< 1\ 1\ 1 > \beta // < 2\ \bar{1}\ \bar{1}\ 0 > \alpha \qquad \textit{Equation 2-1}$$

This relationship indicates that after phase transformation, one of the {110} family of planes in the β phase remains parallel to one of the {0001} planes of the α phase. Additionally, one of the bcc <111> directions remain parallel to the one of the hcp <2 $\bar{1}$ $\bar{1}$ 0> directions.

Since there are 6 non-parallel equivalent {110} planes and 4 no-parallel equivalent <111> directions in the bcc structure, a maximum of 24 rotations can be used to characterise different inherited α orientations for a given

parent β orientation. According to the commutation properties of the rotation observed in the mathematical work (Humbert et al., 1995), these 24 rotations can be splits into two identical subsets of 12 rotations. Thus, only 12 possible new α orientations exist for a given β phase (also known as 12 α variants). Vice versa, hcp α have 2 equivalents {0001} plane and 6 equivalents <2 $\bar{1}$ $\bar{1}$ 0> direction, which leads to 6 potential corresponding β orientations (6 β variants) for a given α orientation, as demonstrated in Figure 2.2 (Humbert et al., 1995, Glavicic et al., 2003).

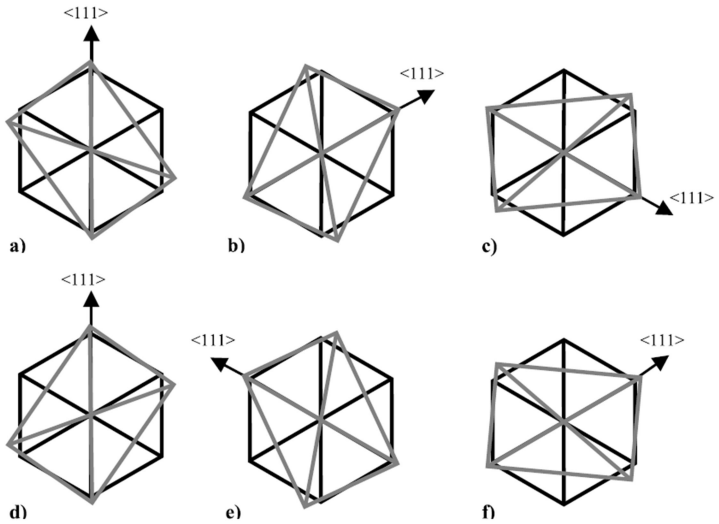


Figure 2.2. Graphical representation of 6 potential corresponding β orientations for a given α phase (Glavicic et al., 2003)

Based on the BOR, α variants arise from a given β orientation are linked with each other by six axis-angle rotation pairs as reported in Table 2.1 (Wang et al., 2003). Vice versa, β variants that share the same corresponding α are also linked with each other by specific axis-angle rotation pairs, as reported in Table 2.2 (Cayron, 2008),

Table 2.1. List of six axis-angel rotation pairs that link the α variants arising from the β to α transformation (Wang et al., 2003)

Type	Axis-Angel Pair
A	0°
B	[1 1 $\bar{2}$ 0] / 60°
C	[-1.377, -1, 2.377, 0.359] / 60.83°
D	[$\bar{1}$0 5 5 3] / 63.26°
E	[1, -2.38, 1.38, 0] / 90°

F	[0 0 0 1] / 10.53°

Table 2.2. List of six axis-angel rotation pair operators that link the β variants arising from the α to β transformation (Cayron, 2008)

Type	Axis-Angel Pair
A	0°
B	[0 $\bar{1}$ $\bar{1}$] / 60°
C	[0 1 1] / 60°
D	[0 1 1] / 49.47°
E	[0 1 1] / 10.52°
F	[1 1 1] / 60°

Effectively, for titanium and its alloys, the BOR links the α phase and the β phase. It limits the possible orientations that can occur during phase transformation. The BOR has an important implication that makes it possible to predict the texture and phase orientation of titanium and its alloys in different conditions (Pilchak et al., 2017). Additionally, this can also be used to examine the relationships between individual α or/and β phases (Balachandran et al., 2017).

2.1.3 Titanium alloys classification

Adding one or more alloying elements to pure Ti can significantly alter the β transus temperature and the phase composition at room temperature (Donachie, 2000). Elements that dissolve preferentially in the α phase further stabilise the α phase at elevated temperature, thereby raising the β transus. Among the alloying elements, aluminium, oxygen and nitrogen are found to stabilise the α phase. On the other hand, elements that have a tendency to stabilise the β phase at a lower temperature are classified as β stabilisers, which can be divided into two groups based on their working mechanisms. One group, referred to as β- isomorphous, includes the elements that are miscible in the β phase, like vanadium, molybdenum and columbium. The other group have a tendency to form a eutectoid system with titanium, such as iron, nickel, copper and silicon (Polmear et al., 2017).

Based on the typical phase composition at room temperature, titanium alloys can be categorised into three groups:

- α alloys, which generally do not contain beta phase at room temperature;
- α-β alloys, which contains both α and β phase at room temperature and all composition will completely transform to β at elevated temperature;
- β alloys, which tends to retain the β phase at a lower temperature.

Figure 2.3 shows the classification of several commonly seen Ti alloys and the effects of α/β stabilisers on the phase composition at room temperature.

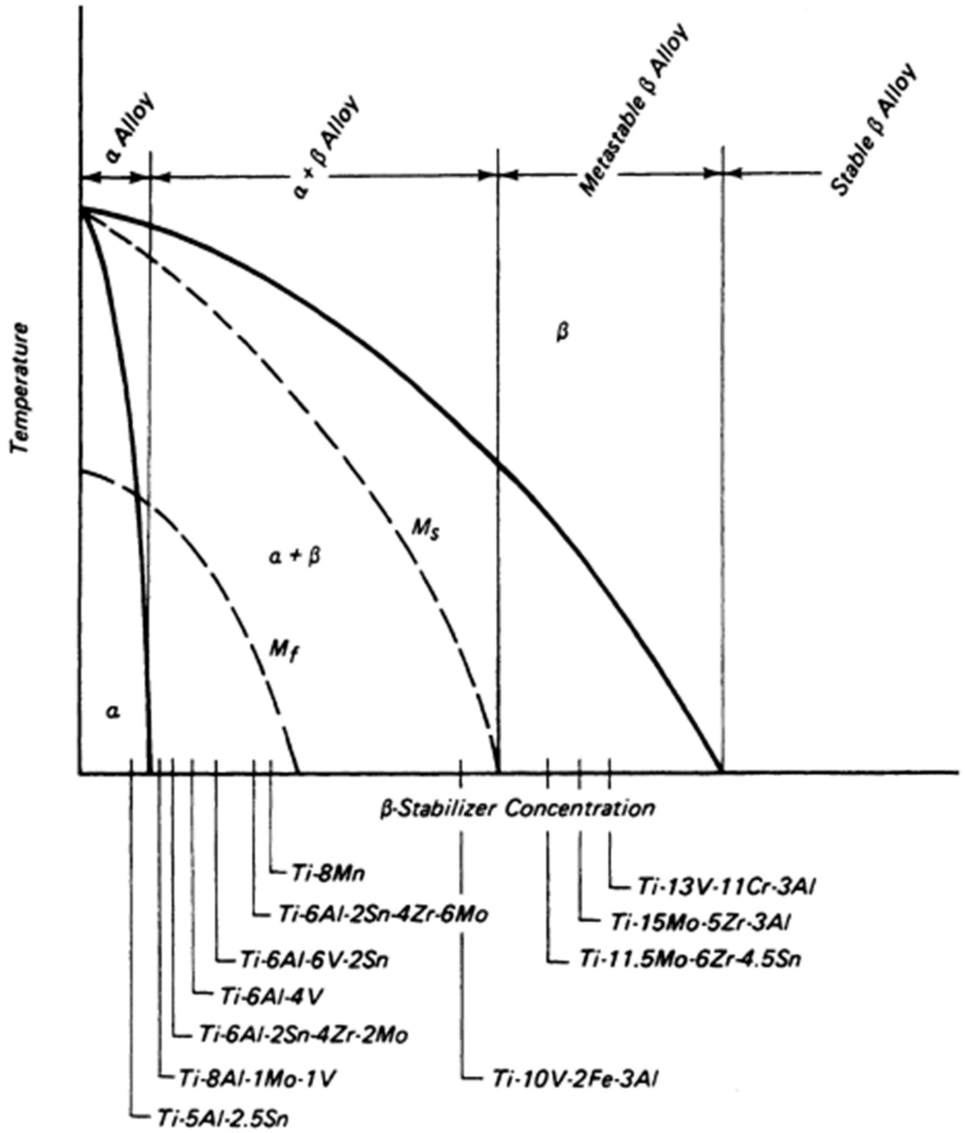


Figure 2.3. Ti alloys classification and effect of alloying elements on phase composition (Donachie, 2000)

2.1.4 Physical metallurgy of Ti-4Al-4V

Ti-6Al-4V, the most commonly used titanium alloy, is an α-β alloy with a nominal composition of 6 wt% aluminium and 4wt % vanadium. According to ASTM B348-13, the acceptable chemical composition of Ti-6Al-4V bars and billets are demonstrated in Table 2.3 (ASTM, 2013). ASTM F2924-14 states that the selective laser melted Ti-6Al-4V products should follow the same chemical requirements as commercial bars and billets (ASTM, 2014b).

Table 2.3 Chemical requirements of Ti-6Al-4V bars and billets according to ASTM B348-13 (ASTM, 2013)

Composition, Weight Percentage							
Aluminium	Vanadium	Carbon max	Oxygen max	Nitrogen max	Hydrogen max	Iron max	Titanium
5.5-6.75	3.5-4.5	0.08	0.20	0.05	0.015	0.40	Balance

Ti-6Al-4V shares a similar allotropic transformation to pure titanium, the nominal β transus temperature under equilibrium heating is 995°C. However, the real β transus may vary for specific Ti-6Al-4V materials, depending on impurities and the content of alloy element, which can cause a deviation of ± 28°C (Lütjering and Williams, 2007, Welsch et al., 1993, SAE, 2014). For a given Ti-6Al-4V material, the β transus is also subject to the chosen heating rate. Research suggests that the β transus of Ti-6Al-4V shifts towards higher temperature when the alloys are treated at a higher heating rate (Boivineau et al., 2006). This phenomenon could be attributed to non-equilibrium conditions under high heating rates (Boivineau et al., 2006, Kaschnitz et al., 2002). Idhil Ismail *et al*. (2016) provide a series of experimental results for mass fraction of β phase versus temperature under different heating rates, as shown in Figure 2.4, which suggests the β transus increase from 1015°C under equilibrium heating (0.25°C/s) to 1075°C under a heating rate of 200°C/s. It also reveals that, under a heating rate of 10°C/s, there is only a marginal increase in the temperature of the onset α→β transformation relative to equilibrium heating, while a significant increase on the onset temperature starts to appear at a higher heating rate like 50°C/s.

In general, the microstructure of Ti-6Al-4V varies from case to case subject to different conditions, but they all can be described by a combination of the composition and arrangement of different phases.

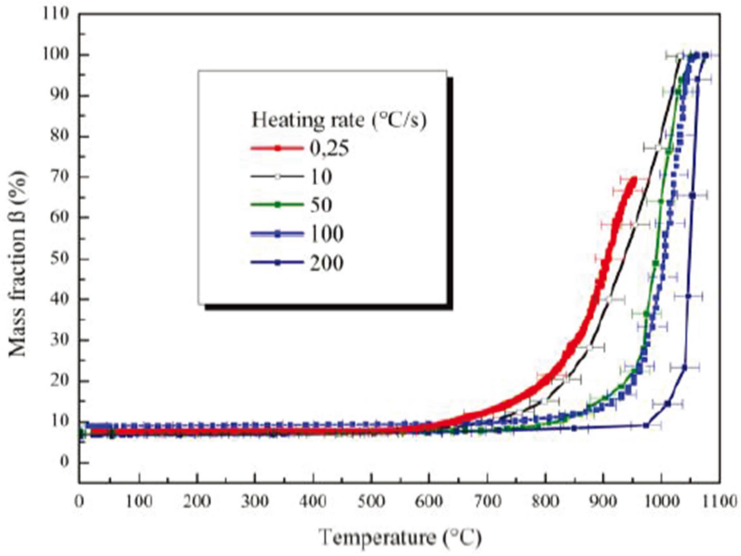


Figure 2.4. Evolution of mass fraction (β phase) versus temperature at different heating rates, ranging from 0.25°C/s to 200°C/s (Idhil Ismail et al., 2016)

2.1.4.1 Phase transformation in Ti-6Al-4V

α and β phase are the only two equilibrium phases present in Ti-6Al-4V. Nevertheless, rapid cooling of Ti-6Al-4V can introduce several metastable phases. *Figure 2.5* demonstrates the phase compositions that Ti-6Al-4V can acquire when cooling from the β phase at different rates (Ahmed and Rack, 1998). When cooling at a very high rate, the β phase will transform into martensitic phases. The most common titanium martensite is the hcp α'-type with a lenticular or acicular morphology, which can be obtained at a cooling rate between 410°C/s and 525°C/s (or above). In addition to martensitic transformation, another composition-invariant transformation, β to α_m massive happens at lower quenching rates from 20°C/s to 410°C/s, which results in a patch-like α_m phase. The equilibrium transformation, β to α, only occurs at slow cooling, when the cooling rate is lower than 20°C/s. (Ahmed and Rack, 1998)

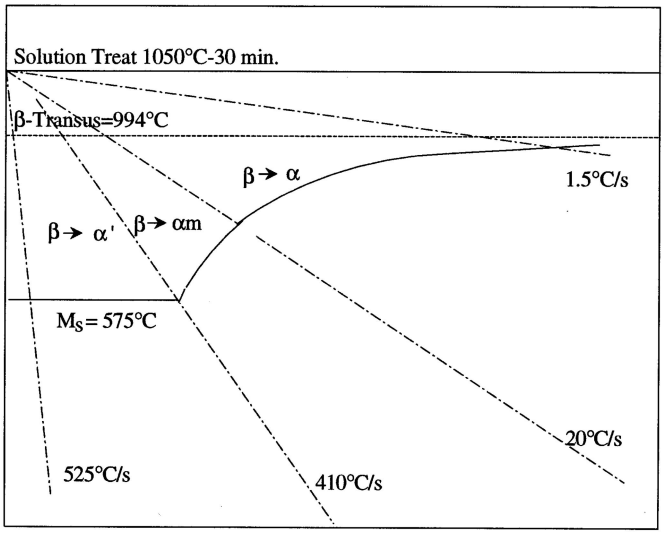


Figure 2.5. Schematic continuous cooling diagram for Ti-6Al-4V, β-solution treated at 1050°C (Ahmed and Rack, 1998)

2.1.4.2 **Texture formation in Ti-6Al-4V**

While phase transformation is mostly correlated to the cooling rate, the texture (appearance of phase arrangement) formation is a more complicated situation, which is affected both by the work process and heat process.

The most commonly seen commercial Ti-6Al-4V raw material is semi-finished casting products like ingots, billets, plates or sheets. Their original texture is a solidification microstructure that normally contains equiaxed β grain or columnar β grain developed from chill zones adjacent by either water cooled or air cooled structures (Lütjering and Williams, 2007). In traditional manufacturing of Ti-6Al-4V components, a fabrication process normally includes deformation and heat treatments (known as thermal-mechanical process) (Salem et al., 2008, Fan et al., 2018). A typical processing route is shown in Figure 2.6 (Lütjering and Williams, 2007).

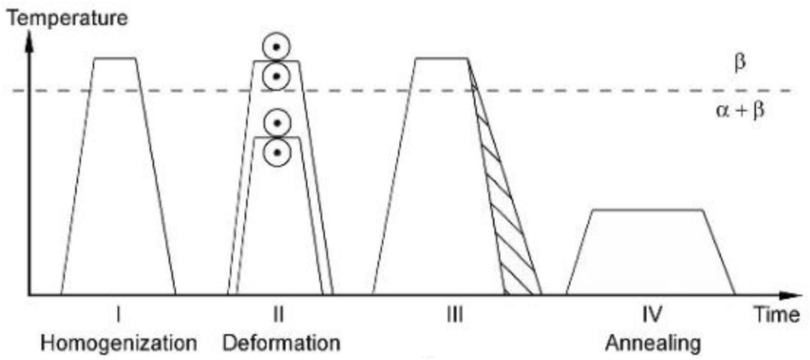


Figure 2.6. The typical processing route for traditional manufacturing of Ti-6Al-4V(Lütjering and Williams, 2007)

Ti-6Al-4V is generally considered difficult to machine due to the high strength (yield strength normally around 800Mpa), therefore forging is the principal shaping process used for making Ti-6Al-4V components, others like extrusion or rolling are also often applied (Lütjering and Williams, 2007).

During the shaping process, deformation texture will form in the products. (Salem et al., 2008, Fan et al., 2018). Research shows if the deformation is conducted at a low temperature in the α+β region, it will directly induce a preferred texture in the α phase; while when the deformation process temperature is close to or higher than the β transus, the preferred texture will be imparted in the β phase (Lütjering and Williams, 2007). In the case of unidirectional rolling, a so-called basal/transverse (B/T) texture would develop at 800°C. While at higher temperatures (950°C), a so-called transverse (T) texture would form instead, as demonstrated in Figure 2.7 (Lütjering and Williams, 2007).

After the deformation process, a heat treatment process is often applied to tune the final microstructure of Ti-6Al-4V (Donachie, 2000). The typical final microstructure of traditional Ti-6Al-4V normally contains equiaxed and/or lamellar α phase plus residual β phase, as presented in Figure 2.8 (Donachie, 2000).

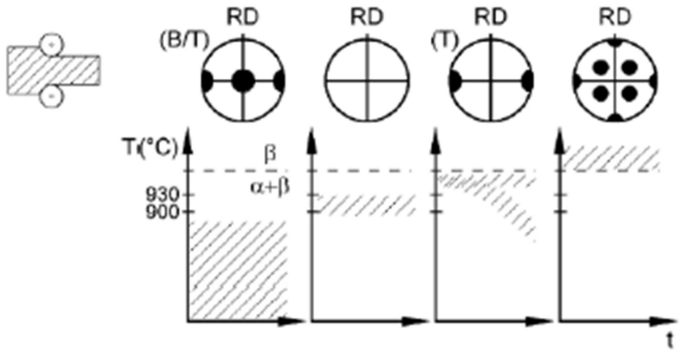


Figure 2.7 Deformation textures in α+β Ti alloys represented through {0001} pole figures (Lütjering and Williams, 2007)

When the maximum heating temperature is below the β transus, some α phase will not experience α to β transformation. Such remained original α phase is referred to as primary α, as the equiaxed α phase that black arrows indicate in Figure 2.8 (a) - (d). The martensites or α phase transformed from β phase during the cooling is called transformed β (or secondary α for newly generated α), as the lamellar α phase red arrows indicate in Figure 2.8 (c) (d). Although primary α and secondary α are both hcp structure α phase, they can be easily recognised by different morphology due to their different formation routes. In addition, secondary α has significantly higher vanadium content in comparison to primary α since it transforms from the β phase which is naturally vanadium-rich (Salem et al., 2008).

β grain, which is formed in the high temperature single β region, is normally referred to as prior-β grain, since it exists prior to β to α transformation (Donachie, 2000, Polmear et al., 2017). The prior-β grain usually contains multiple α and β phase across the micromorphology, and sometimes its grain boundaries can be plotted by the existence of grain boundary α, as black arrows indicated in Figure 2.9.

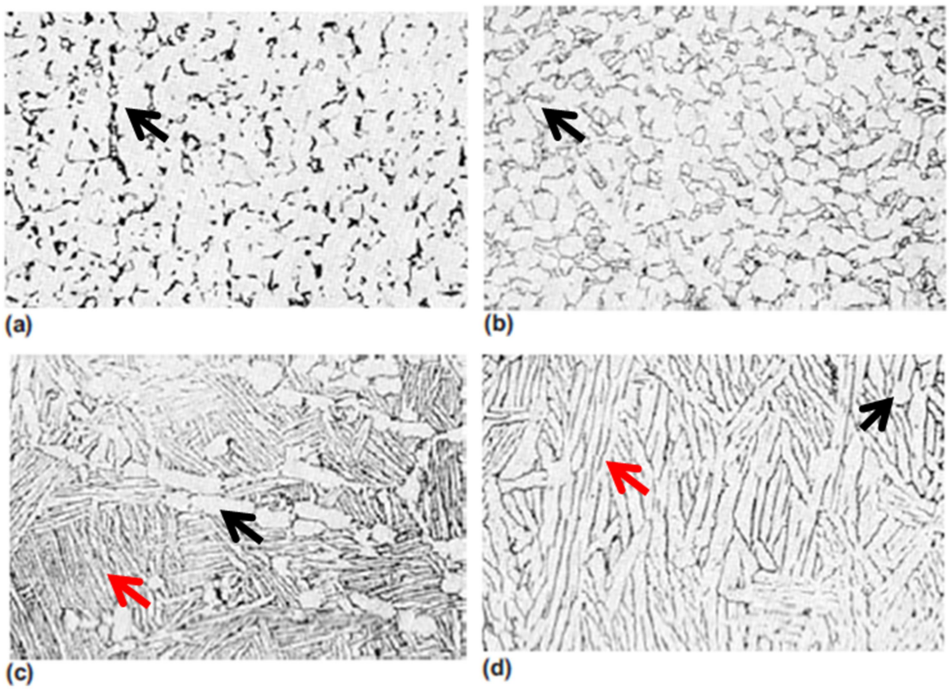


Figure 2.8. Optical microscopy images showing typical microstructure of Ti-6Al-4V obtained via different heat process. (a)(b) Equiaxed primary α and intergranular β. (c)(d) Equiaxed primary α in a lamellar secondary α (transformed β) matrix, with residual β between the α phase. (Donachie, 2000)

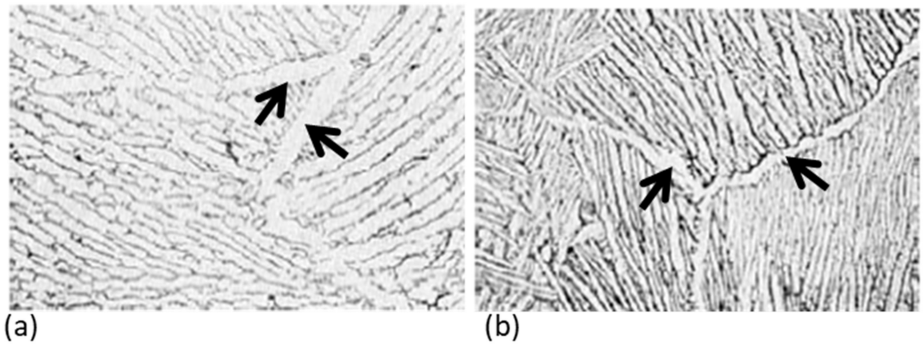


Figure 2.9. Optical microscopy images showing plate-like lamellar secondary α (transformed β) with continues grain boundary α. (Donachie, 2000)

The texture formed in the heat process relates to the grain growth and phase transformation. The growth of primary α and prior-β grain is a diffusion controlled growth, which is influenced by peak temperature and soaking time (Meng et al., 2017b, Semiatin et al., 2003). On the other hand, the texture of secondary α is controlled by supersaturation, diffusivity, and the cooling rate. Among these three factors, supersaturation affects the nucleation of α nuclei, while diffusivity controls the epitaxial growth of the nuclei, and the cooling

rate rules the variants selection (Meng et al., 2017a, Semiatin et al., 2003). It is found that the growth of primary α competes with the precipitation of secondary α, as it will consume the supersaturation in the matrix (Meng et al., 2017a).

Although there are 12 possible orientations when secondary α transform from β, the variant selection across the material is not a random distribution.

When the high temperature β transform to secondary α during cooling, there are 12 possibilities for the orientation of the secondary α according to BOR. However, the variant selection among these 12 possibilities is not a random process. There is a correlation observed between the cooling rate and preferred variant selection (Shi et al., 2016). It is suggested that the local stress can be developed during cooling since the thermal expansion of the phase is different. Consequently, some variants are chosen preferentially in order to minimise the elastic strain energy and the local strain (Qiu et al., 2016, Shi et al., 2014, Shi and Wang, 2013). It is also reported that, since the variants' selection at the grain boundary can be affected by the adjacent prior-β grain as well as the lattice defects (dislocations, twins etc.) at the grain boundary, different variants selection rules may be applied at the prior-β grain boundary, compared to what is inside the prior-β grain, which leads to the appearance of grain boundary α (Shi et al., 2014).

Since limited β is retained at room temperature, the study of the original texture in Ti-6Al-4V is complicated. Several studies suggest a method to deduce the texture of original β phase from measured α phase texture (Glavicic et al., 2003, Glavicic et al., 2004, Pilchak et al., 2017). In their practice, the β phase texture is generated by back calculation (named hereafter as reconstruction), where the texture of the β phase is deduced from the orientations measured in the α variants at room temperature.

2.2 Metal powder bed fusion additive manufacturing

2.2.1 Introduction

Metal powder bed fusion (M-PBF) is one of the major metal additive manufacturing (AM) technologies which can directly produce near net-shape metal products, reduce raw material consumption and provide design freedom (Ian Gibson, 2015, Uriondo et al., 2015, Murr et al., 2012). Such technology has attracted significant attention in the past two decades, leading to enormous development and understanding about the technique and the physical mechanism related to these technologies (De Formanoir et al., 2016, DebRoy et al., 2018, Dutta and Froes, 2016).

The principles of general M-PBF AM will be introduced in section 2.2.2, particularly the laser-based system. As the specific M-PBF technique used in this study, selective laser melting (SLM) will then be explored in section 2.2.3.

2.2.2 Principles of laser-based metal powder bed fusion additive manufacturing

The basic concept of M-PBF AM is to fabricate a product by sintering or melting metal powder from powder bed additively, normally achieved through layer by layer. All M-PBF techniques share some similar characteristics, which include one or more energy sources to fuse powder particles, a method to limit the powder fusion within a prescribed region at each layer, and a powder spreading system to add and smooth powder layers (Ian Gibson, 2015).

In order to selectively promote the temperature within a prescribed area, high energy beams are frequently chosen as heat sources. Currently, laser and electron beams are the favourable options to be applied in commercial equipment (De Formanoir et al., 2016, DebRoy et al., 2018). However, other

choices, like pulsed plasma arc, also have the potential to be equipped in the future (Lin et al., 2016). A schematic of the operating principle shared by all M-PBF techniques is presented in Figure 2.10. During the manufacturing process, the high energy beams scan the designated region on the top layer of the powder bed to fuse the powder in the area. After that, a new layer of powder will be spread onto the surface of the powder bed, and then the fusing process continues. The whole process takes place in an enclosed chamber filled with protective gas (normally nitrogen or argon) to minimise oxidation of the powdered material (Ian Gibson, 2015).

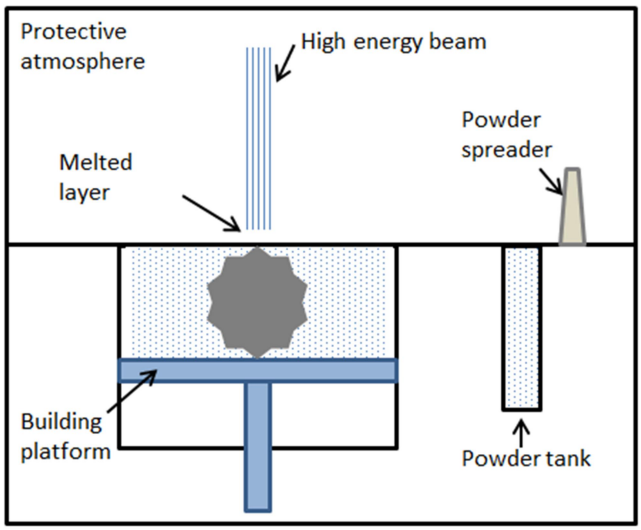


Figure 2.10 Schematic of metal powder bed fusion additive manufacturing operating principle

The M-PBF technique that uses a laser as the energy source to fuse loose powders is known as laser powder-bed fusion, or more generally as selective laser melting (SLM). Compared to other commonly used high energy beams, laser is a more concentrated energy beam. It usually has a focus spot with a diameter of less than 100µm (Vayre et al., 2012). Therefore, with a higher processing accuracy, SLM normally has a lower building speed. Table 2.4 reports some typical building parameters of SLM. The typical building parameters of the electron beam based system (known as EBM) are also listed as a comparison (Vayre et al., 2012). By using multiple lasers, which

achieves multiple scanning spots at the same time, SLM building speed can be significantly increased (Wen et al., 2014).

Table 2.4 Building parameters of SLM and EBM respectively (Vayre et al., 2012)

Technology	SLM	EBM
Manufacturer	3D system	Arcam
Building speed (in cm^3/h)	5-20	55-80
Layer thickness (µm)	20–100	50-200
Dimensional quality (mm)	0.2	0.4

2.2.3 Selective laser melting of metal powders

As one of the most successful commercialised metal AM techniques, selective laser melting attracted significant attention in the past decade, both in industry and academia. There are many companies that provide commercial SLM system in the market: EOS, Renishaw, Concept Laser, SLM Solutions etc.

Fibre laser is the key element of an SLM system. Solid-state Nd:YAG lasers are the type of laser currently used in most of the commercial systems, and can be worked either in continues-wave (CW) mode or pulsed mode. Research suggests that the Nd:YAG lasers with a wavelength of 1.06µm have a better absorbability for metal powders, compared with other types of lasers, like CO_2 lasers which normally have a wavelength of 10.6µm (Kruth et al., 2003). Meanwhile, the pulsed mode has certain potential benefits over CW mode. For example, it has a tendency to form a flat molten region when melting metal powders, instead of disconnected balls (Ian Gibson, 2015).

Precise process parameter control is fundamental for successful fabrication. For a modern SLM system, controllable process parameters can be classified into four groups (Sutton et al., 2017, Fox et al., 2016, Parry et al., 2016, Ian Gibson, 2015):

- Laser-related parameters, which include laser power, spot size etc.

- Scan-related parameters, which include scan speed, scan spacing/hatch distance and scan pattern;
- Powder-related parameters, which include particle size, shape and surface roughness, powder bed density, layer thickness etc.
- Temperature-related parameters, which include powder bed temperature, baseplate pre-heating temperature etc.

These parameters are strongly independent but also mutually interact with each other. These parameters can significantly change the width, depth, shape and continuity of the melt pool, which is the fundamental element for quality control (Yadroitsev et al., 2010, Criales et al., 2017). By in-situ monitoring the absorptivity of metallic powder against 1070nm laser through direct calorimetric measurements, Trapp et al. (2017) also describes the influence of process parameters on the absorptivity.

During the SLM process, appropriate input energy density is crucial for melt pool control and the stability of printing, as lack of laser energy input leads to lack of fusion, while superabundant energy may cause disturbance or vaporisation in the melt pool leading to the appearance of keyhole and balling (Shipley et al., 2018, Leuders et al., 2013). A set of basic process parameters, which include Laser power (P), scan speed (v_L), hatching distance (d) (distance between two successive scan tracks) and layer penetration depth (h), can be used to determine the input laser volumetric energy density (u), as indicated in Equation 2-2.

$$\text{Volumetric energy density} \quad \mathrm{u} = \frac{P}{V_L * d * \mathrm{h}} \qquad \text{Equation 2-2}$$

The acceptable combination of these four parameters, which will lead to a preferred volumetric energy density, is known as the process window (Kruth et al., 2004). Figure 2.11 presents an example of the process window developed for SLM of iron-based powder at different laser working mode (Kruth et al., 2004). It demonstrates the appearance of balling or disconnection of the scan track under unsuited parameter combinations.

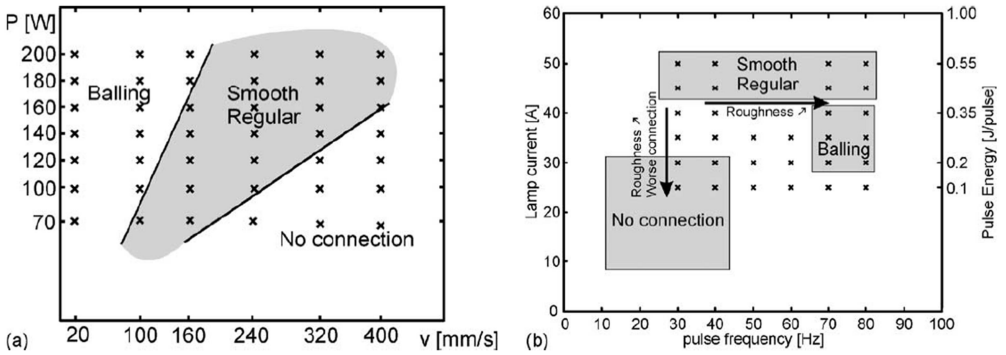


Figure 2.11. Example of process window developed for SLM of iron-based powder: (a) continues-wave (CW) operation, (b) pulsed operation (Kruth et al., 2004)

In addition to energy density, scan pattern and scan strategy (the arrangements of scan tracks and directions) can have a profound influence on the thermal stress (also known as residual stress), since different scan path will introduce different local thermal environments (Parry et al., 2016, Robinson et al., 2018). A large number of scan strategies have been developed by researchers to examine such impact, some of which are shown in Figure 2.12, in which the X-Y surface represent the laser scan surface of the top powder bed layer (Zaeh and Branner, 2010, Haiko Pohl, 2001, Roberts, 2012). A common understanding has been accepted by the community that dividing the entire scan area into small sections (for example, 5mm*5mm squares (Carter et al., 2014)) then scanning them separately can help to achieve lower residual stress (Robinson et al., 2018, Ali et al., 2018).

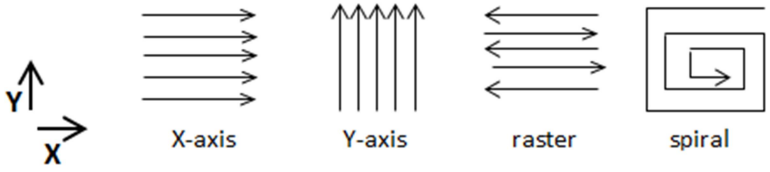


Figure 2.12. Examples of different scanning strategies (Zaeh and Branner, 2010, Haiko Pohl, 2001, Roberts, 2012)

Powder characteristics can also have an impact on the fabrication and the density of the SLM products. Research suggests that both the particle size, shape and surface roughness can affect the flowability and the spreading of

the powder and, therefore has crucial influences on the packing density of the powder bed (Sutton et al., 2017). Nowadays, powder bed densities typically range between 50% and 60 % for most commercially available powders (Ian Gibson, 2015). Other than that, the microstructure of the powder particles also has an impact on the part properties. Starr et al. (2012) describe the final microstructures of 17-4 stainless steel samples produced by different powders. Argon-atomised martensite powder produced fully martensite products, while the parts produced by nitrogen-atomised austenitic powder have retained the austenitic phase. It suggests there is a possibility that the as-built microstructures of the selective laser melted Ti-6Al-4V can also be affected by the microstructure of the raw powder.

In order to predict and control the printing process and product quality, the physical mechanism involved in the process need to be studied (Das, 2003). Using real-time monitoring and finite element method (FEM) simulation, understanding of the fluid flow in the melt pool have been established in the recent years (Khairallah et al., 2016, Bidare et al., 2018). Khairallah et al. (2016) and King et al. (2015) suggest laser-induced recoil pressure and Marangoni convection leads to a strong dynamical melt flow inside the melt pools, which generates most of the defects observed in SLM process. Recent research suggests that defects can also be introduced by the vapour driven micro-particles carried out from the melt pool under the influence of ambient gas flow (Ly et al., 2017). The development of understanding the related physics can help to improve the current SLM system as well as to minimise the workload of optimisation of process parameters.

The melt pool in SLM process has limited size (laser spot size normally has a diameter around 10 -20μm) and travels at a very high speed (varies from case to case, from 200mm/s to 1000mm/s), where the material melts and then solidifies in milliseconds, which leads to a high cooling rate and local stresses. Criales et al. (2017) measured a heating rate between 600 °C/ms and 1000 °C/ms, and cooling rates of 150 °C/ms during the SLM process. A cooling

rate close to 450°C/ms is also reported by Lane and Moylan (2016). Residual stresses are often considered to be the most critical factor that leads to the premature failure of the printing as well as the unacceptable performance of the as-built green part.

In order to reduce the residual stresses in the printed parts, various in-situ heat treatments are applied or proposed for the SLM system (Shim et al., 2017, Vrancken et al., 2016, Schwarze and Schoeneborn, 2015, Porch and Mcfarland, 2016). The mechanism is either pre-heating the baseplate (Meiners et al., 2004, Vora et al., 2015, Li et al., 2016), heating top surface of the powder bed (Philippi and Mattes, 2009, Jan et al., 2013) or spatial heating of the entire (or large portion of) the powder bed (Flesch and Mottin, 2013, Graichen, 2013).

Controlling the temperature-related parameters during the SLM process is crucial to minimise the residual stresses in the printed parts. However, current in-situ heat treatment attempts all have their limitations. They either cannot achieve uniform heating within the printed part regardless of the geometry, or risk of sintering powder particles at the unwanted area because of holding the powder at elevated temperature (above 800°C) throughout the entire printing process. Thus, currently, there is lack of a convincing in-situ heating solution for SLM process, which makes post-process heat treatments usually inevitable for metal SLM (Etter et al., 2015a, Facchini and Magalini, 2012). It is now well proven that through appropriate post-process treatment, SLM products can achieve mechanical properties equivalent or better than its cast or wrought counterparts (De Formanoir et al., 2016, Hossain et al., 2016, Vrancken et al., 2012, Beese and Carroll, 2016).

Similar to many traditional manufacturing processes like casting or forging, post-process heat treatments usually are applied on as-built parts (as known as green parts) after the SLM process. It can help to relieve the residual stresses or tuning the microstructure, so the desired mechanical properties

can be achieved (LeBrun et al., 2015, Etter et al., 2015b, Etter et al., 2015a, Totten, 2006).

Due to the significant similarities between these processes, most of the post-heat treatment routes are applied directly from experience and knowledge established on the traditional metal process. However, such designed routes do not always lead to the best properties due to the unique microstructure that SLM as-built products often owns (Baker et al., 2017). In order to make the best use of post-process heat treatment, further studies on the heat treatment process and its mechanism are required (Qian et al., 2016). Baker et al. (2017) even suggest that new nomenclatures are preferred for AM Ti alloys. They point out that the traditional designations do not clearly describe the distinct microstructural features that AM products have, which can be misleading in some situations. New nomenclatures can help to distinguish the AM features from traditional heat treatments and microstructures.

2.3 Selective Laser Melting of Ti-6Al-4V and Post-process Heat Treatment

2.3.1 Introduction

Selective laser melting (SLM) of Ti-6Al-4V has attracted significant attention over the past decade, since its near net-shape manufacturing ability can significantly decrease buy-to-fly ratio (the ratio between the weight of raw material and the end-use component), and therefore reduce manufacturing costs (Dutta and Froes, 2016, Yap et al., 2015). Extensive studies have been done on related topics, especially regarding the fabrication and post-process heat treatments (Simonelli, 2014, Fan and Feng, 2018, Thijs et al., 2010, Shipley et al., 2018).

The progress made on SLM Ti-6Al-4V fabrication is reviewed in section 2.3.2. Section 2.3.3 then summarises the post-process heat treatments applied to Ti-6Al-4V produced by SLM and the related mechanical properties. Finally,

section 2.3.4 describes the microstructure and texture transformations during such heat treatments.

2.3.2 Selective laser melting of Ti-6Al-4V

It is widely proven that by applying an optimised process window, near fully dense (>99%) Ti-6Al-4V components can be fabricated by SLM (Dutta and Froes, 2017, Yang et al., 2016, Nazarova et al., 2015). An example of a good process window for SLM of Ti-6Al-4V is shown in Figure 2.13. It is developed by Gong et al. (2013) for Raymor Ti-6Al-4V powder.

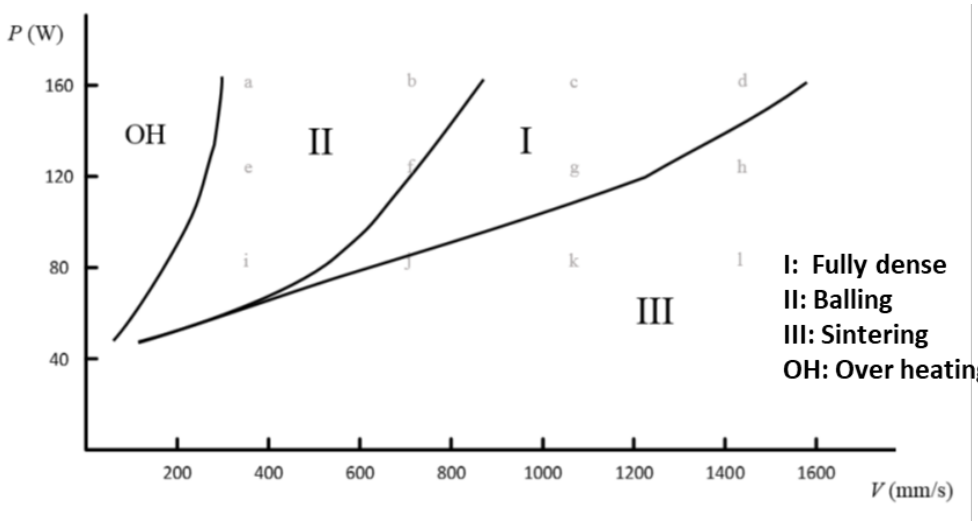


Figure 2.13. Process window developed for SLM Raymor Ti-6Al-4V powder by Gong et al. (2013)

Due to the layer-to-layer characteristic of selective laser melting (SLM) process, SLM Ti-6Al-4V has its unique microstructure, which is completely different from the wrought or hot-rolled product (Thijs et al., 2010).

During the solidification of the melt pool, since the underneath pervious solidified layer has a much higher thermal conductivity than surrounding powders, most of the heat will dissipate through the solidified layer, which means it dissipates parallel to the building direction (Rombouts et al., 2006). This unidirectional heat dissipation leads to the growth of columnar prior-β grain followed with the building direction, as shown in Figure 2.14 (a) (Shunmugavel et al., 2017). The width of the columnar grain is positively

correlated with the hatch distance in laser scan, and varies from approx. 10µm to 200 µm (Thijs et al., 2010). Meanwhile, the melt pool is driven by the laser moving at a speed of hundreds to thousands millimetre per second, which brings in an extremely fast cooling from melt to α domain around 10^4 °C/s (Xu et al., 2015, Yang et al., 2016). The cooling rate is so extreme that upon cooling, martensite α' phases form within prior-β grain in the morphology of acicular shape, as shown in Figure 2.14 (b) (Thijs et al., 2010). The variants selection during the β → α' transformation is also ruled by the extreme cooling rate. Therefore normally only 5 to 7 α' variants can be observed within each prior-β grain and also could not observe any grain boundary α/α' at the prior-β grain boundary (Yang et al., 2016).

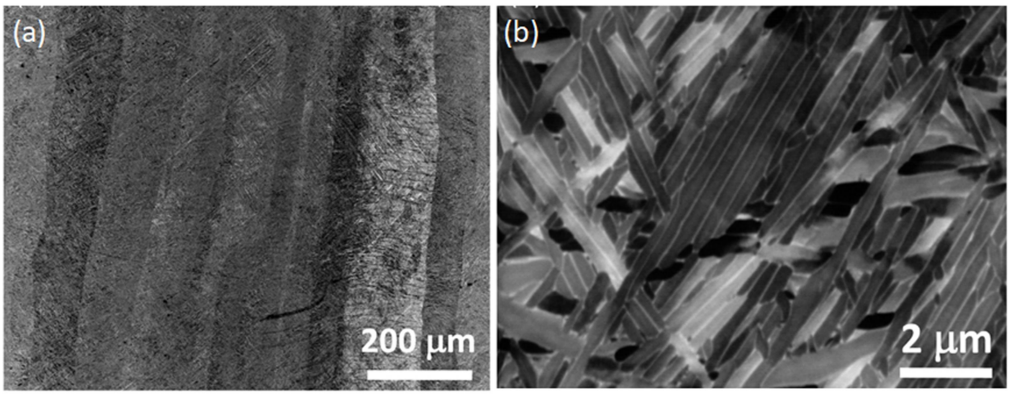


Figure 2.14 SEM backscatter electron micrographs showing typical microstructures of SLM-fabricated Ti-6Al-4V, (a) columnar prior-β grain, (b) α' martensite formed inside the prior-β grains (Xu et al., 2015).

Some of the reported tensile properties (building direction 90° to the baseplate, test direction parallel to the elongated direction of the columnar prior-β grain) with such as-built microstructure are summarised in Table 2.5. It is obvious the as-built parts can normally achieve yield strength and ultimate tensile strength surpasses 1000MPa with elongation around 7%. Compared to the minimum requirements for Ti-6Al-4V products in ASTM B348, which is 828 MPa in yield strength, 895 MPa in ultimate tensile strength and 10% in elongation, it is clear that the low ductility hinders the use of as-built products (ASTM, 2013). The low ductility is caused by the nature of martensite α'. This metastable phase contains a high density of

dislocations and twins (Zhang et al., 2018), which leads to a brittle appearance with high strength and low ductility (Yang et al., 2016, Shunmugavel et al., 2017). Besides the low ductility, it is also known that the columnar shape is an anisotropy structure since the different amount of grain boundaries (weak structure) need to be crossed under different loading direction (W. Kurz, 1991). Therefore, the mechanical properties of as-built Ti-6Al-4V vary with test direction, with the best loading direction parallel to the elongated direction of the columnar prior-β grain. Such anisotropic behaviour is commonly reported in researches (Chen et al., 2017, Simonelli et al., 2014, Wu et al., 2016a).

Table 2.5 Reported tensile properties of as-built SLM Ti-6Al-4V with fully α' martensite within the columnar prior-β grain (building direction 90° to the baseplate, test direction parallel to the elongated direction of the columnar prior-β grain)

Source	Young's modulus E (GPa)	Yield Strength σ_y (Mpa)	Ultimate Tensile Strength UTS (MPa)	Elongation ε (%)
Luca et al. (2010)	110 ± 5	990 ± 5	1095 ± 10	8.1 ±0.3
Vilaro et al. (2011)	105 ± 5	1137 ± 20	1206 ± 8	7.6 ± 2
Vrancken et al. (2012)	109.2 ± 3.1	1110 ± 9	1267 ± 5	7.28 ± 1.1
Simonelli et al. (2014)	113 ± 5	1075 ± 25	1199 ± 49	7.6 ± 0.5
Mertens et al. (2014)	112	1166 ± 6	1324 ± 6	2 ± 0.7
Moletsane et al. (2016)	112 ± 2	1098 ± 2	1265 ± 5	9.4 ± 0.5
Shunmugavel et al. (2017)	/	964 ± 2	1041 ± 25	7 ± 3
Xu et al. (2017b)	105.8 ± 20.1	1056 ±20.1	1196 ± 18.8	7.0 ± 1.8
Guzanová et al. (2017)	110 ± 15	1140 ± 50	1290 ± 50	7

The brittle α' phase is formed under various thermal cycles. In the SLM process, the melted layer soon will be covered by a new layer of power, and then the laser works to melt the new layer. Thus the microstructure formed during the laser fusion will be influenced by subsequent repeating heat transferred from the above layer (Yang et al., 2016). Figure 2.15 demonstrates the thermal cycles a given layer would experience during the SLM process. The peak temperature drops for each successive cycle since the given layer moves away from the working surface (Yang et al., 2016). In Figure 2.15, T_L represents for the liquid line, T_S represents for the solid line, T_β represents for the β transus temperature, and M_S represents for the temperature that martensite α' starts to decompose. The final remaining microstructural constituents form at different cycles. Therefore the observed α' in the as-built microstructure (Figure 2.14) is a combination of primary, secondary and tertiary α'.

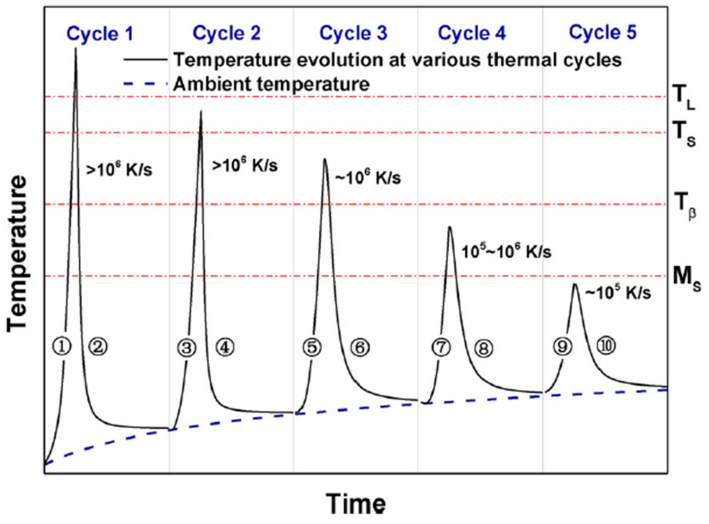


Figure 2.15 Schematic diagram illustrating the thermal cycles experienced by Ti-6Al-4V during SLM. The temperature of a given layer is reported as a function of the five successive layer depositions (Yang et al., 2016).

Recent studies suggest such subsequent heat can be used to decompose martensite α', so an α+β microstructure can be created in as-built status. Xu et al. (2015) were the first to achieve such in-situ decomposition. They advise that a lower energy density (33.74J/mm^3) tends to increase martensite retention, while a higher energy density (50.62J/mm^3) can enable

decomposition under suitable parameters setting. They achieved an ultrafine lamellar α+β structure with a high yield strength (1106 ± 6 MPa) and improved ductility (11.4 ± 0.4%) (Xu et al., 2015). The following work by Barriobero-Vila et al. (2017) presents a similar finding. By using a narrow hatch distance (40μm), which leads to a high energy density (243J/mm^3), they obtained fine lamellar α + β microstructure with intermetallic α_2 – Ti_3Al along the building direction (Barriobero-Vila et al., 2017). The formation of α2 particles is believed to be the results of Al segregation during rapid cooling and strongly affected by the intense intrinsic heat treatment, which is intentionally imposed by the applied parameters setting (Barriobero-Vila et al., 2017).

2.3.3 Strategies and final tensile properties of post-process heat treatment

Due to the low ductility, anisotropy and high residual stresses presented in the as-built SLM products, post-process treatment is often required in order to achieve the desired mechanical properties. However, since SLM is a near net-shape process, the thermal-mechanical treatment that is normally applied for traditional Ti-6Al-4V components cannot be used, as it will reshape the geometry of as-built components. Therefore, post-process heat treatments are normally applied (Vrancken et al., 2012, Zhang et al., 2018). Most of the reported post-process heat treatments are conducted by the conventional furnace, while others via a technology called hot isostatic pressing (HIP) (Qiu et al., 2013). Different from the simply heating, the HIP process requires applying a uniformed high pressure during the soaking. However, this technique will not be discussed in this section.

Since the β transus temperature is crucial for microstructure transformation, the conventional heat treatment can be divided into two groups, sub-transus (below β-transus) and super-transus (over β-transus) (AmirMahyar et al., 2017, Zhang et al., 2018).

Significant work has been done to study the post-process heat treatment of SLM Ti-6Al-4V. Table 2.6 summarises some of the reported treatments and their tensile properties. Based on the information provided in the literature, variations between heat-treated result and as-built ones is calculated and also listed in Table 2.6, so the comparison between different heat treatments can be clearly explicated.

Some of the representative treatments and corresponding tensile properties are plotted in Figure 2.16. In Figure 2.16, specified colour scheme are applied to represent the soaking temperature used during the different heat treatments: black stands for as-built condition, grey stands for soaking temperature lower than 600°C, magenta stands for soaking temperature between 600°C-750°C, blue represents soaking temperature between 750°C-900°C, green represents soaking temperature between 900°C-990°C, orange represents soaking temperature between 990°C-1015°C, and red represents soaking temperature above 1015°C.

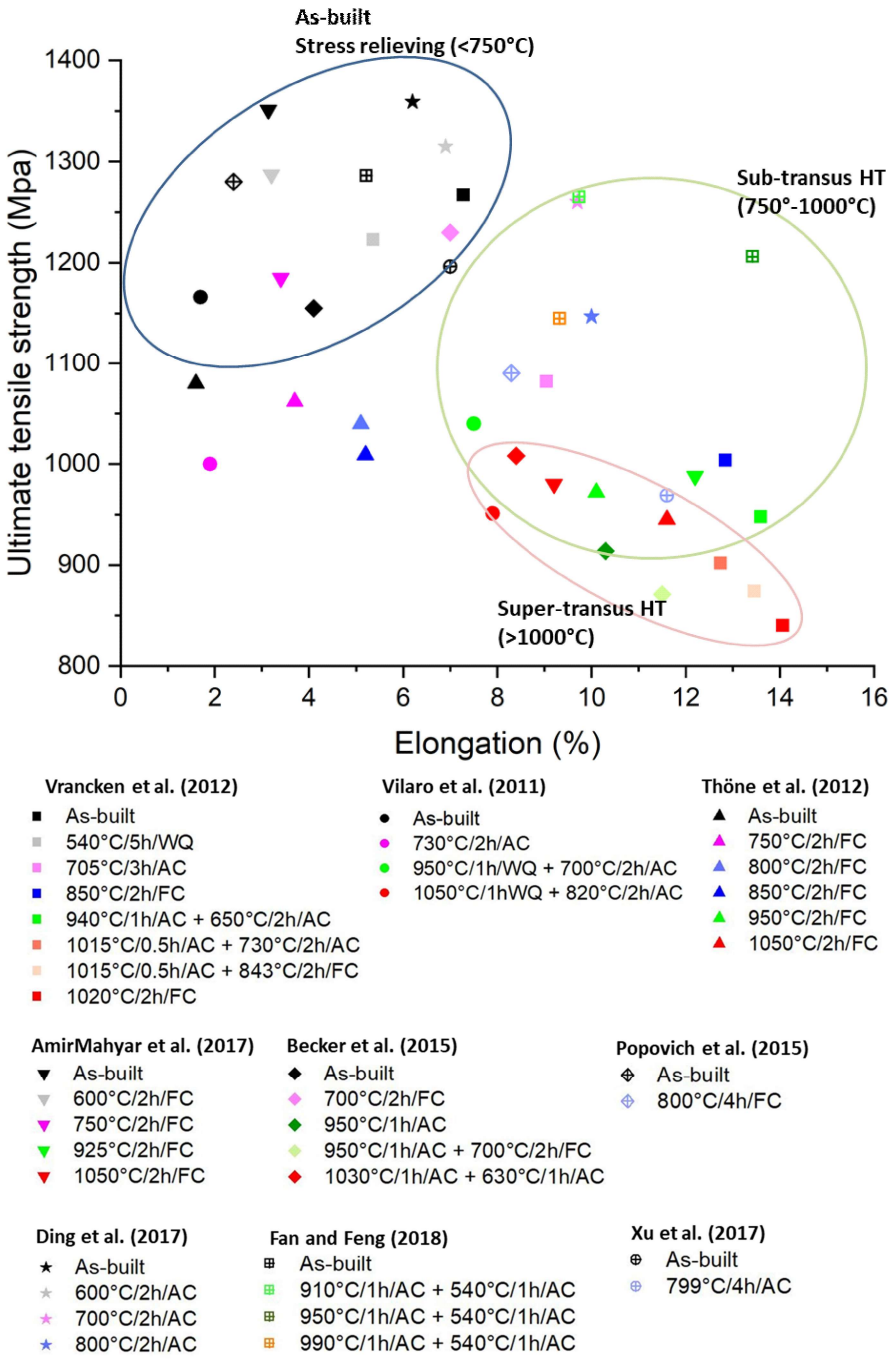


Figure 2.16. Reported heat treatments and tensile properties of heat treated SLM Ti-6Al-4V (WQ means water quench, FC means furnace cooling, AC means air cooling and HT means heat treatment).

According to these studies, some common understanding can be established regarding the heat treatment and related tensile properties.

For sub-transus heat treatment, a higher soaking temperature leads to lower strength and better ductility (Vilaro et al., 2011, Thöne et al., 2012, Vrancken

et al., 2012, Becker et al., 2015, AmirMahyar et al., 2017). A treatment temperature lower than 750°C usually cannot provide significant influence in tensile properties, since martensite α' normally fully decomposes at a temperature higher than 800°C (Yang et al., 2016). Therefore, such heat treatments are often applied to relieve the residual stresses, also known as stress relieving process.

During sub-transus heat treatments, besides the different soaking temperatures, cooling methods also have an impact on the tensile properties. Air cooling (AC) and furnace cooling (FC) can provide better ductility compare to water quench (WQ), because the high cooling rate in WQ can easily bring in newly formed martensite α' in the annealed microstructure (Vrancken et al., 2012). The influence of dwell time on properties is limited since the growth of either α or β phase is hindered by one another (Ter Haar and Becker, 2018, Vrancken et al., 2012).

Those tendencies do not persist when the soaking temperature exceeds β transus (super-transus heat treatment). In single phase filed, a higher soaking temperature or a longer dwell time will always lead to a worse strength and/or ductility, due to the growth of prior-β grain (Vilaro et al., 2011, Vrancken et al., 2012).

Compared to sub-transus heat treatment, super-transus treatment sometimes can provide a slightly better ductility (Vilaro et al., 2011, Thöne et al., 2012), but it always comes with an unacceptable sacrifice in strength (Vrancken et al., 2012, Leuders et al., 2013, Leuders et al., 2014, Chandramohan et al., 2018).

As a result of these studies and established understandings, several standards were recently published to guide the post-process heat treatment for additively manufactured Ti-6Al-4V, which are summarised in Table 2.7. In order to achieve the best ductility with acceptable strength, a soaking temperature above 900°C and below β transus with air cooling or furnace

cooling is suggested in each standard (ASTM, 2014a, ASTM, 2014b, SAE, 2016).

Table 2.6 Reported heat treatments and tensile properties of heat treated SLM Ti-6Al-4V.

Temperature (°C)	Dwell time (h)	Cooling	Young's modulus, E (Gpa)	Ultimate tensile strength, UTS (MPa)	Variation in comparison to as-built, ΔUTS (%)	Yield strength, σy (MPa)	Variation in comparison to as-built, $\Delta\sigma_y$ (%)	Elongation, ε (%)	Variation in comparison to as-built, Δε (%)	Source
540	5	WQ	112.6 ± 30.2	1223 ± 52	-3.47	1118 ± 39	+0.72	5.36 ± 2.02	/	Vrancken et al. (2012)
705	3	AC	114.6 ± 2.2	1082 ± 34	-14.60	1026 ± 35	-7.57	9.04 ± 2.03	+24.18	
850	2	FC	114.7 ± 3.6	1004 ± 6	-20.76	955 ± 6	-13.96	12.84 ± 1.36	+76.37	
850	5	FC	112.0 ± 3.4	965 ± 20	-23.84	909 ± 24	-18.11	premature failure	/	
940 followed by 650	1 2	AC AC	115.5 ± 2.4	948 ± 27	-25.18	899 ± 27	-19.01	13.59 ± 0.32	+86.68	
1015 Followed by 730	0.5 2	AC AC	112.8 ± 2.9	902 ± 19	-28.81	822 ± 25	-25.95	12.74 ± 0.56	+75	
1015 followed by 843	0.5 2	AC FC	114.9 ± 1.5	874 ± 23	-31.02	801 ± 20	-27.84	13.45 ± 1.18	+84.75	
1020	2	FC	114.7 ± 0.9	840 ± 27	-33.70	760 ± 19	-31.53	14.06 ± 2.53	+93.13	

730	2	AC	110 ± 29	1000 ± 53	-14.24	900 ± 101	-6.44	1.9 ± 0.8	+11.76	Vilaro et al. (2011)
950 followed by 700	1 2	WQ AC	98 ± 3	1040 ± 4	-10.81	925 ±14	-3.85	7.5 ± 2	+341.18	
1050 followed by 820	1 2	WQ AC	95 ± 4	951 ± 55	-18.44	836 ± 64	-13.10	7.9 ± 2	+364.71	
750	2	FC		1062	-1.67			3.7	+131.25	Thöne et al. (2012)
800	2	FC		1040	-3.70			5.1	+218.75	
850	2	FC		1009	-6.57			5.2	+225	
950	2	FC		972	-10			10.1	+531.25	
1050	2	FC		945	-12.5			11.6	+625	
600	2	FC		1287	-4.74			3.2	+1.91	AmirMahyar et al. (2017)
750	2	FC		1185	-12.29			3.4	+8.28	
925	2	FC		988	-26.87			12.2	+288.84	
1050	2	FC		980	-27.46			9.2	+192.99	
Stress relief				1230	+6.49			7.0	+70.73	Becker et al. (2015)
950	1	FC		914	-20.87			10.3	+151.22	

950 followed by 700	1 2	AC FC		871	-24.59			11.5	+180.49	
1030 followed by 630	1 2	AC AC		1008	-12.73			8.4	+104.88	
600	2	AC		1315	3.23			6.9	+12	Ding et al. (2017b)
700	2	AC		1260	7.28			9.7	+57	
800	2	AC		1147	15.6			10	+61	
800	2	FC		1040	-3.70	962	-4.56	5	+212.5	Leuders et al. (2013)
1050	2	FC		945	-12.5	798	-20.83	11.6	+625	
800	2	FC		1228.1 ± 32.4	-6.60			8 ± 1.5	+100	Leuders et al. (2014)
1050	2	FC		986.4 ± 45.2	-24.98			13.8 ± 1.3	+245	
910 Followed by 540	1 4	AC AC		1265	-1.63	1195	-3.16	9.74	+86.59	Fan and Feng (2018)
950	1	AC		1206	-6.22	1122	-9.08	13.42	+157.09	

Followed by 540	4	AC								
990 Followed by 540	1 4	AC AC		1145	-10.96	1056	-11.63	9.32	+78.54	
640	4	FC		1225 ± 4	-7.27	1104 ± 8	-5.32	7.4 ± 1.6	+270	Mertens et al. (2014)
710	2	FC		1165 ± 5.4	+6.30	1086 ± 1.5	+6.78	15 ± 0.5	+25	Greitemeier et al. (2017)
730	2	FC	113 ± 9	1057 ± 8	-7.52	958 ± 6	-2.04	12.4 ± 0.7	+5.08	Simonelli et al. (2014)
799	4	AC	94.9 ± 15.6	969 ± 14.4	-18.98	902 ± 16.2	-14.58	11.6 ± 2.4	+65.71	Xu et al. (2017b)
800	4			1090	-14.84	1000	-16.67	8.3	+245.83	Popovich et al. (2015)

Table 2.7 Suggested conventional heat treatments for additive manufactured Ti-6Al-4V in published standards (ASTM, 2014a, ASTM, 2014b, SAE, 2016)

Standard	Heating and atmosphere	Temperature °C	Dwell time	Cooling and atmosphere
1. ASTM F2924 − 14. (ASTM, 2014b) 2. ASTM F3001 − 14.(ASTM, 2014a)	N/A	Stress relieving 593°C	2h±0.25	N/A
	N/A	Annealing 704°C	2h±0.25	Air or furnace cool
	N/A	Solution heat treatment and aging 954°C Or 941°C (ELI) Followed by 704°C Or 482°C	(1) 15min, <2.5mm thickness; (2)add 1min for each additional 2.5mm, 2.5mm to 25mm thickness; (3) add 20min for each additional 12.7mm over 25mm, >25mm thickness 4h Or 8h	Inert gas back-fill cool or air cool N/A
3. AMS 4999A. (SAE, 2016)	Vacuum or argon and/or helium	Solution heat treatment and aging 899°C to 927°C Followed by 538°C	2h to 4h 4h ± 0.25	Argon and/or helium gas cool to below 427°C Insert, vacuum or air atmosphere Air or furnace cool

2.3.4 Microstructure and texture transformation in post-process heat treatment

Different tensile properties under different heat treatments are driven by the microstructure and texture formed during the heating process. Thus, understanding the transformation of microstructure and texture during post-process is crucial for heat treatment designs.

2.3.4.1 Sub-transus heat treatment

A significant number of researches have been carried out on conventional sub-transus heat treatment of SLM Ti-6Al-4V in recent years (Vrancken et al., 2012, Wu et al., 2016c, AmirMahyar et al., 2017, Zhang et al., 2018, ter Haar et al., 2016, Ding et al., 2017a). A shared understanding of microstructure evolution in the α+β field during heat treatment has been established.

At a relative low temperature (about 200°C to 400°C), recovery of the microstructure starts by annihilation or rearrangement of the defects (dislocation, twins etc.) in the crystal structure, which leads to a reduction of the stored energy and partial relief of the residual stress (Totten, 2006, Lütjering and Williams, 2007).

The martensite α' starts to decompose at a temperature ranging from 400 to 800°C, depending on the level of impurities within the material (Gil Mur et al., 1996, Wu et al., 2016b, Qazi et al., 2003). Zhang et al. (2018) stated that the martensite decomposition starts with α phase nucleation at the boundary of acicular α' phase, pushing vanadium element to the boundary of the newly formed α phase, then β phase will form at the vanadium-rich area. In that way, the recovered α phase would share a similar parallel arrangement to the original acicular α', with β phase remaining trapped between those α laths. Energy-dispersive X-ray spectroscopy (EDS) line scan of an α and β mix area were used to verify the element partitioning, and Figure 2.17 demonstrates the significant vanadium enrichment in the β phase. Such element partitioning during the α' decomposition is also observed by Vilaro et al.

(2011) using SEM under the backscattered mode. The two phases exhibit a slight chemical contrast. Scanning transmission electron microscopy (STEM) images from Wu et al. (2016b) revealed that chemical contrast can be observed at the place where the constitution can still be indexed as α' phase by electron diffraction pattern, which suggests the element partitioning may even happen before α' decomposition. A recent study suggests that during the decomposition of α', the β phase can also nucleate at the lattice defects that within α/α' (Haubrich et al., 2019).

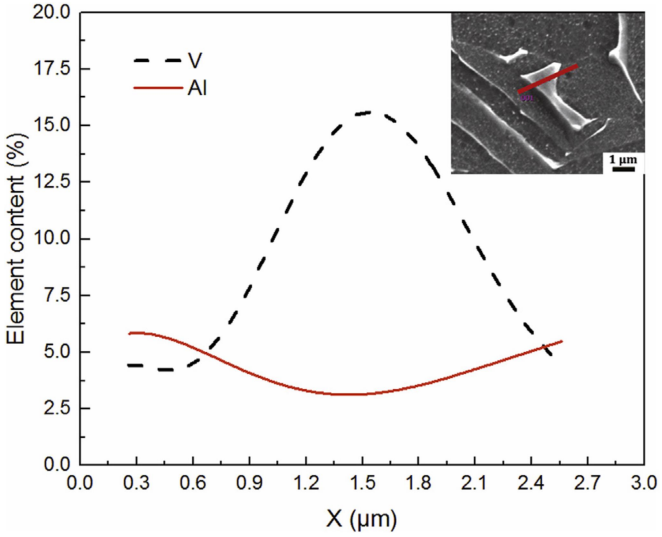


Figure 2.17. Element partitioning in the heat-treated SLM Ti-6Al-4V at 850°C/2 h/Furnace cool. The red line shows the EDS line scan position (Zhang et al., 2018)

The martensite α' is believed to be fully decomposed around 900 °C (Zeng and Bieler, 2005). No original acicular α' can be observed in samples that are heat-treated beyond this temperature. Microstructure with a lamellar mixture of α and β is present inside the columnar prior-β grain (Figure 2.18). Without the hindrance of retained α', both α and β phase show noticeable growth (Zhang et al., 2018). However, such growth is still limited even after holding at high temperature for a long time, because of the competitive growth of both α and β matrix (Vrancken et al., 2012). Figure 2.19 shows samples heat treated at 940°C for 2h and 20h respectively, notice the limited growth in α grain size, although the morphology of few α phases begins to

form into an equiaxed structure as indicated by the arrows in Figure 2.19(b) (Vrancken et al., 2012).

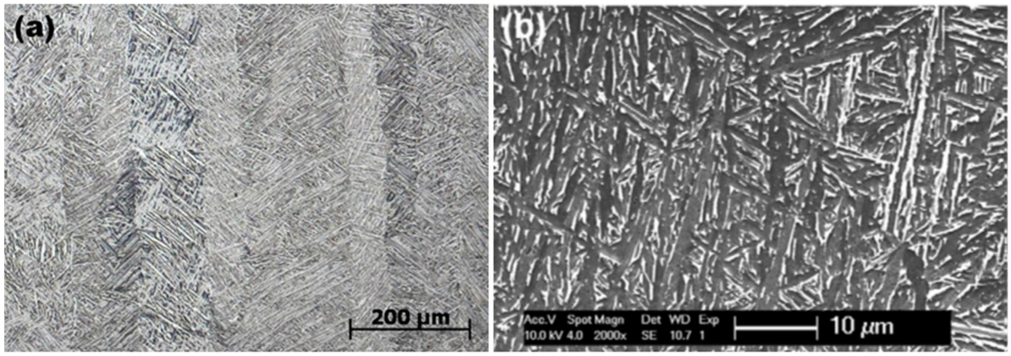


Figure 2.18. Microstructure of SLM Ti-6Al-4V (a) after 1h at 940°C followed by 2h at 650°C. After heat treatment, a lamellar mixture of α and β is present inside the columnar prior-β grain, by optical microscopy image. (b) after 2h at 843°C, Widmanstätten pattern of lamellar α and β is presented, by backscatter electron image. (Vrancken et al., 2012)

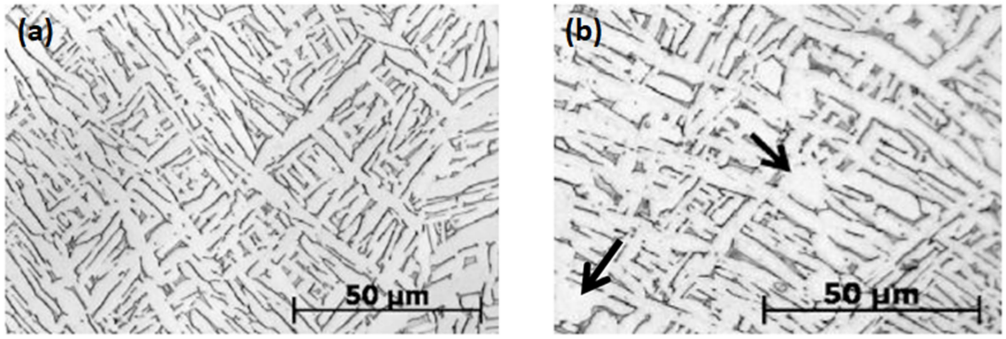


Figure 2.19. Optical microscopy images showing microstructure after sub-transus heat treatment for (a) 2 h and (b) 20 h with the arrows showing some α has started to globularise (Vrancken et al., 2012).

Some universal findings can be summarised from different studies related to sub-transus heat-treatment (Zhang et al., 2018, Wu et al., 2016b, Vrancken et al., 2012, Vilaro et al., 2011, Baker et al., 2017, AmirMahyar et al., 2017, Xu et al., 2017b, Chandramohan et al., 2018):

1. Sample processed at high temperature, close to the β transus-temperature, have larger β-fraction, as well as larger α lamella width, due to the α to β transformation and grain growth at high temperature.

2. The columnar prior-β grain structure remains unchanged during sub-transus heat treatment, with no visible difference in columnar width compared to the untreated state (Figure 2.18 (a)).
3. The soaking temperature is a key parameter to control the evolution of the microstructure of Ti-6Al-4V. While soaking duration, heating rates and cooling rates (as long as it maintains the equilibrium transformation) have less significant influences in controlling the microstructure evolution. Both α and β phase will tend to coarsen but will hinder each other, resulting in limited grain growth. However, such hinder effect rapidly diminishes as the temperature is close to β transus, since the α- fraction decreases rapidly at this temperature range.

2.3.4.2 Super-transus heat treatment

Different from sub-transus heat treatment, the researches related to super-transus heat treatment are not only limited but also showing conflicting understandings.

As temperature rises above the β transus, all α phase transforms into the β phase. Single phase appears inside the heated sample. Under these circumstances, both temperature, holding time and cooling rate have a significant influence on the microstructure.

As the pioneers in Ti-6Al-4V super-transus treatment study, Vrancken et al. (2012) heated SLM Ti-6Al-4V at 1050°C for 2h. Extensive growth of columnar grain has been observed, showing a significant increase in width, while the length of the columnar grain does not show noticeable growth (Figure 2.20). They believed grain grows rapidly and unhindered in single-phase region that several original prior-β grains merge to one large grain. Since the width of the newly formed grain gets a significant increase, the length to width ratio drops, the grain presents a semi-equiaxed structure, as shown in Figure 2.20 (b).

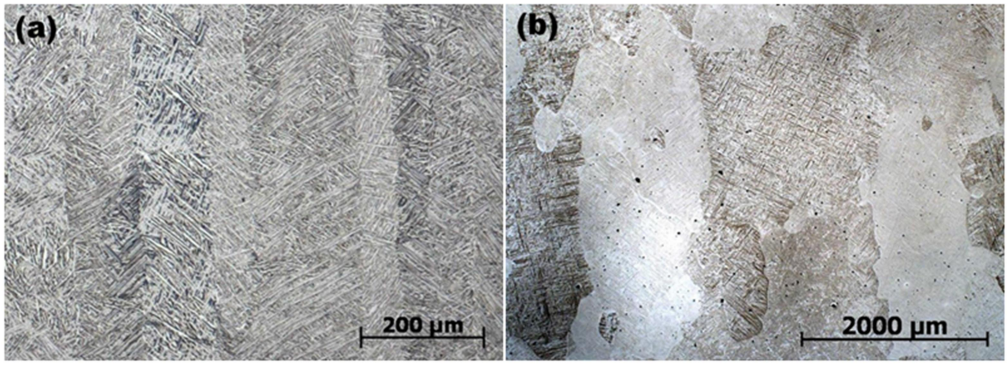


Figure 2.20. Optical microscopy images showing the side view of SLM Ti-6Al-4V (a) after 1h at 940°C followed by 2h at 650°C, furnace cooling (b) after 2h at 1015°C, water quench, indicating the extensive growth of the columnar grains(Vrancken et al., 2012)

Other researches studied the evolution of the microstructure of SLM Ti-6Al-4V at a lower temperature (1000°C/2h) (Zhang et al., 2018) or a shorter time (1050°C/1h) (Vilaro et al., 2011). The results reveal that the β grains do not always keep the original length during the heat treatment. In both researches, the length of the newly formed β grain has noticeably shortened in comparison to the original prior-β grain. On the other hand, the studies report a significant grain width growth after heat treatment (several times the original) (Figure 2.21). The columnar features disappear and are replaced with large equiaxed β grains. This transformation suggests that the original columnar prior-β grain might therefore split during the treatment.

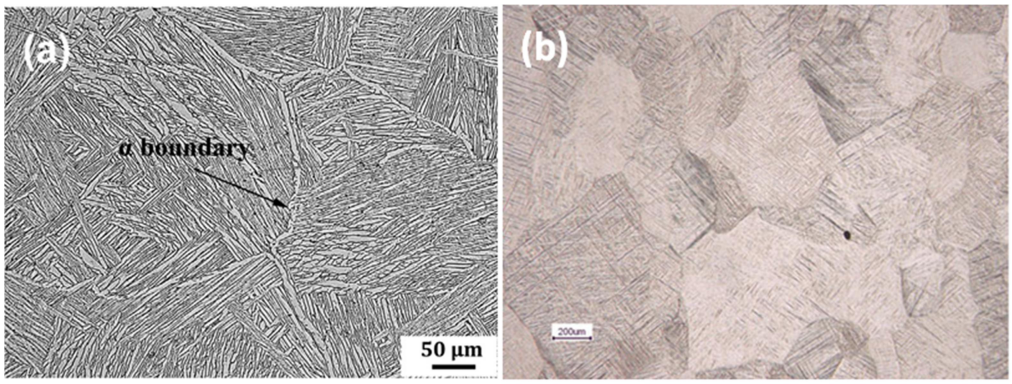


Figure 2.21. Optical microscopy images showing the side view of SLM Ti-6Al-4V (a) after 2h at 1000°C followed with furnace cooling (Zhang et al., 2018) (b) after 1h at 1050°C followed with water quench (Vilaro et al., 2011)

Different mechanisms have been proposed to explain such split of the columnar morphology. Vilaro et al. (2011) considered it as a shearing mechanism in conjunction with crystallographic deformation (bcc β to hcp α'). Based on this assumption, they believed that such observed split of prior-β grains could only be achieved under a high cooling rate, such as watering quenching (Vilaro et al., 2011). Since the phase transformation happens more rapidly under high cooling rate, watering quenching would lead to a more intense shearing. However, other research presents evidence that challenges this assumption, as Zhang et al. (2018) achieved similarly spilt of the columnar grains under a much lower cooling rate (furnace cooling).

Zhang et al. (2018) suggested that such deformation may be driven by the reduction of interfacial energy, but they did not give further explanation about their assumption. However, it can be assumed that when entering into the single phase region, the interfacial energy at the original prior-β grain boundary will drop. Therefore the original columnar morphology cannot be maintained and will transform into an equiaxed morphology, since the latter one requires less interfacial energy to retain stable.

Recent research on super-transus HIP treated additively manufactured Ti-6Al-4V revealed similar morphological changes in the prior-β grain (Nandwana et al., 2019). By reconstructing the orientation of prior-β grain in as-built and super-transus status, Nandwana et al. (2019) pointed out the significant change in the prior-β grain orientation between the two conditions, as shown in Figure 2.22. This observation indicates that the microstructure evolution during the super-transus heat treatment is controlled by the recrystallisation and growth of new β grains, rather than the general growth of the existing columnar β grains. Three possible nucleation mechanisms for the recrystallisation are also proposed in the research. One possible mechanism is that the β phase generated from α' decomposition acts as recrystallised nuclei. Since the Burgers orientation relationship provides multiple possibilities, the decomposed β may not have the same orientation with the

original parent β. These differently oriented β grains, growing competitively with the parent β phase, would lead to the change in the overall texture. The other two possible mechanisms are the nucleation induced by dislocations or residual stresses.

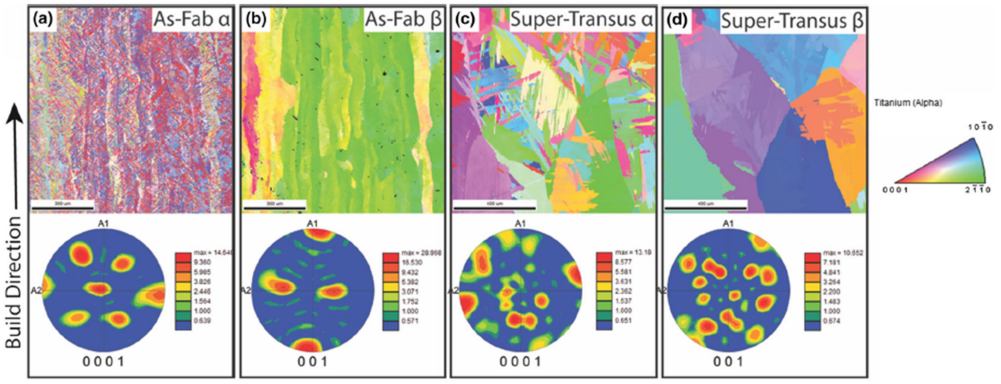


Figure 2.22. Pseudo colour IPF maps and relevant pole figures for the α and β phases in the as-fabricated and super-transus HIPed conditions on planes parallel to the build direction (Nandwana et al., 2019).

The lack of understanding of the microstructure evolution during super-transus heat treatment is due to an apparent reason. The contradiction between sufficient uniform heating and fast grain growth makes it difficult for conventional heating to achieve a relatively small grain size in the single phase field.

It is known that the properties of titanium alloys strongly depends on the grain size of the high temperature phase. Smaller grain size can lead to a better property, as evidenced by the experimental results provided by Ivasishin and Teliovich (1999). Such finding corresponds with the classic Hall-Petch Relationship, that for a polycrystalline material, there is a quantitative relationship between the increase in the yield stress and the decreases in its grain size (Callister and Rethwisch, 2007). During the elastic deformation stage, the grain boundaries hinder the further propagation of the dislocation, since it requires more energy for a dislocation to change direction and move into a different orientated neighbouring grain. Furthermore, the grain boundary is also much more disordered/mismatched compare to the interior

of the grain, which prevents the movement of the dislocations along a continuous slip plane (Callister and Rethwisch, 2007). For a material with smaller grain size, more prolonged grain boundary means more obstruction on the dislocation movement. Therefore the onset of the plasticity will be postponed, leading to increased yield strength (Callister and Rethwisch, 2007). Further than that, in the fatigue test, the resistance of the crack nucleation is positive relative to the yield strength of the tested material (Jeong et al., 2017), hence a smaller grain size can also results in a higher fatigue resistance.

Meanwhile, coarse prior-β grain often leads to unacceptable mechanical properties as noted in the experimental data presented in section 2.3.3. Such predictable unfavourable results have made researchers reluctant to conduct super-transus treatments in their studies.

When studying the mechanism leads to the microstructure evolution of SLM Ti-6Al-4V during the super-transus heat treatment, researches on the β annealing of traditional manufactured Ti-6Al-4V can be used as a guide. However, caution should always be exercised when trying to apply the established understandings directly to additive manufactured alloys, since there is a clear difference in the staring microstructure between as-built SLM Ti-6Al-4V and traditional counterparts.

Pilchak et al. (2017) recently conducted an enlightening research on the evolution of the microstructure of Ti-6Al-4V in the earlier stages of β annealing. Their study on the hot-rolled Ti-6Al-4V showed that the microstructure evolution at this stage is not controlled by the general grain growth, but rather by nucleation-and-growth events. In their study, samples were soaked at 1012°C for a series of limited times, ranging from 0 to 12.5 minutes, which provided snapshots of the continuous microstructure evolution. By reconstructing β grains, they pointed out that small amounts of atypical β grains, which has a high-disoriented angle (misorientation at the grain boundary higher than 10°) compared to the rest of β grains (as shown in

Figure 2.23), worked as nuclei at the beginning of microstructure evolution. The β grains grow from these nuclei will consume the nearby original β grains via the migration of high angle boundaries.

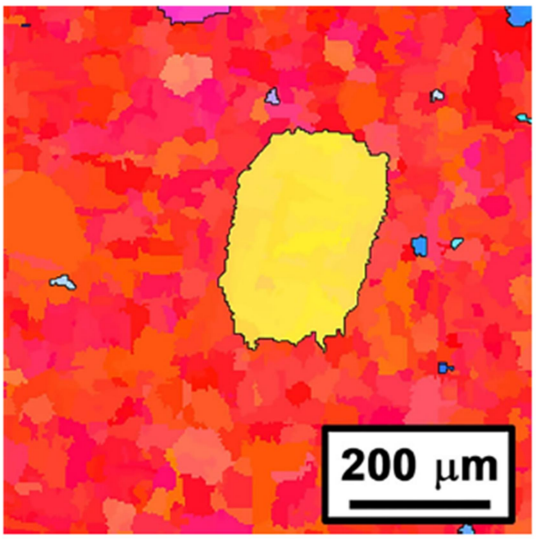


Figure 2.23. Reconstructed normal direction (<001> direction) inverse pole figure map of β grain in a Ti-6Al-4V sample annealed above the beta transus for 31.5 s (Pilchak et al., 2017).

Even though currently there is lack of understanding about the mechanisms, which lead to the observed columnar to equiaxed transformation of the prior-β grain after β annealing of SLM Ti-6Al-4V, it is still safe to assume that by limiting the grain growth involved in the single β region, there is potential possibility to obtain refined equiaxed prior-β grain. A refined equiaxed morphology of the prior-β grains cannot only improve the mechanical properties of the material but also help to reduce anisotropic behaviour.

The idea of limiting grain growth in the single β region would be achievable, if the exposure time of the material in that temperature region can be controlled to a minimum. However, due to the slow heating rate inherited from the heating mechanism, the conventional furnace is difficult to be exploited to achieve limited soaking time.

Conduction heating and induction heating are the two commonly applied approaches for volumetric rapid heating of solid metal. For conduction

heating, the heating component is series connected to the electrode, heat is then generated due to the loss of power caused by electric resistance (Liang et al., 2015). However, such a heating method is usually restricted by the geometry of heating targets and surfers from the problem of non-uniform temperature distribution (Karbasian and Tekkaya, 2010). For induction heating, which is widely used in metal processing, there is no direct contact between the heat source and heated component. As a high efficiency and non-contact heating method, it can deliver high energy into the material in a short time (Rudolf et al., 2000). All of these make the induction heating an ideal choice for this study.

It is also reported that, other than limiting the grain growth, there are other mechanisms that can lead to further refinement of the high temperature grain structure under the rapid heating (Ivasishin and Teliovich, 1999). Induction heating has been applied on austenitic steel to achieve grain refinement (Scott and Spruiell, 1974). Researchers believed that the stress relaxed from the rapid fcc structure to bcc structure transformation of the austenitic steel would contribute to the formation of random orientations, thus refine the austenite grains (Ivasishin and Teliovich, 1999). Studies on the induction heating of traditional Ti-6Al-4V suggests that the hcp to bcc transformation of Ti-6Al-4V could not introduce enough relaxed stress that leads to the same formation of random orientation (Ivasishin and Teliovich, 1999). However, it is still interesting to study how the SLM Ti-6Al-4V microstructure reacts under rapid heat treatment, since there is lack of previous studies on the related subject.

2.4 Induction Heating Technique

2.4.1 Introduction

In order to study early stage beta annealing of SLM Ti-6Al-4V, a rapid volumetric heating method is needed. Induction heating is chosen in this study. Induction heating takes place within an electromagnetic field. Energy

is transferred to the part via electromagnetic waves, which can avoid direct contact of the heat source and heated part. The targets of induction heating are mainly metal. The frequency of the electromagnetic waves involved in induction heating usually ranges from a few Hz to several MHz, which belongs to the range of radio frequency (Ulaby, 2014). According to frequency and wavelength, the entire electromagnetic waves family can be presented in the form of a continuum, known as the electromagnetic spectrum (Ulaby, 2014), as shown in Figure 2.24. In the vacuum, the relationship between frequency f and wavelength λ, can be described by Equation 2-3, in which C stands for the speed of light in the vacuum (Ida, 2015). The wavelength represents for the propagate ability of the electromagnetic waves. Therefore, for achieving a longer propagate distance, a low-frequency electromagnetic wave is preferred (Ida, 2015).

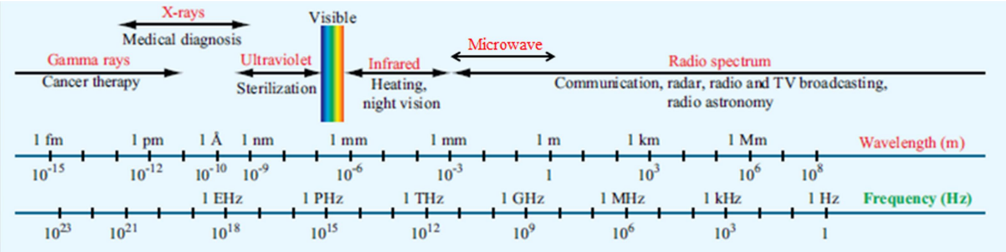


Figure 2.24. The electromagnetic spectrum (Ulaby, 2014)

$$\lambda = \frac{C}{f} \qquad \text{Equation 2-3}$$

In this chapter, the principles of induction heating are explained in section 2.4.2, followed by the introduction of typical equipment required for an induction heating system in section 2.4.3.

2.4.2 Principles of induction heating

Induction heating is commonly used to heat the whole or a part of solid metals in industry. It has various applications include melting, mass heating or heat treatment (tempering, annealing etc.) During the induction heating process, for most metal material, the heat first appears within the limited depth of the material. It is the joule heating caused by the eddy current. The

remaining part of the material will then be conductively heated via the heat from joule heating (Totten, 2006).

2.4.2.1 Heating induced by eddy current and magnetic hysteresis

During the induction heating, alternating current flows through the induction heating applicator and generates an oscillating electromagnetic field in the near space, which induces an alternating current in the metal part located within the electromagnetic field. The induced alternating current, generally known as eddy currents, would flow in the metal part and result in joule heating (Zinn and Semiatin, 1988).

Eddy current heating is the dominant heating mechanism for non-magnetic materials and the main heating mechanism for magnetic materials. For magnetic material, especially for ferromagnetic material, a small amount of heat comes from the friction of oscillating magnetic dipoles caused by magnetic hysteresis (Haimbaugh, 2001). The magnetic dipoles will change their direction following the change of magnetic field direction, with some hysteresis, as shown in Figure 2.25. This kind of vibration will also create some heat. However, its contribution is much less than eddy current heating, therefore is typically ignored in theoretical analyses.

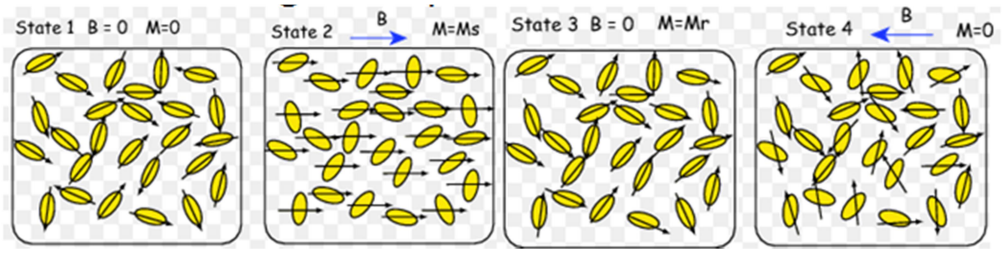


Figure 2.25. Magnetic dipoles change their direction following with magnetic field change

Therefore, for induction heating, calculating the distribution of eddy currents is crucial for predicting the temperature distribution within the heated part. A significant amount of theoretical analyses aimed to calculate eddy current distribution in typical conditions has been conducted in the past (Dodd and

Deeds, 1968). Based on these results, combined with computer-aided numerical tools, the simulation of a much more complex situation can be carried out (Kurose et al., 2009, Zanming et al., 2001).

2.4.2.2 The penetration depth of the electromagnetic wave and the skin effect

Electromagnetic fields have limited penetration depth for metal materials. Electromagnetic wave decays exponentially after penetrating metals due to the presence of free electrons (Chen et al., 2006). Since the magnitudes of the eddy currents are decreasing rapidly from the surface, the induced current only flows within a limited depth, generally known as skin effect (Mucha et al., 1987). Approximately 86% of joule heating occurs at a limited depth from the surface of the material. This limited depth is defined as penetration depth, also known as reference depth in some literature. Penetration depth can be calculated through Equation 2-4, in which d stands for penetration depth (cm), ρ stands for the electrical resistivity of the work-piece (Ω·cm), μ stands for the relative magnetic permeability of the work-piece and f stands for the frequency of the current in the induction heating applicator (Hz).

$$\mathrm{d} = 5000\sqrt{\rho/\mu f} \qquad \text{Equation 2-4}$$

The value of penetration depth relates to AC current frequency and workpiece material properties (Acero et al., 2006, Davies, 2007). According to the literature (Zinn and Semiatin, 1988), the penetration depth of some materials are shown in Figure 2.26. The penetration depth of some commonly used SLM material can also be calculated based on Equation 2-4, shown in Table 2.8. (the data of Al and Ti are taken from Rudnev et al. (2002), the data of 316L and Ti6Al4V are calculated by the author).

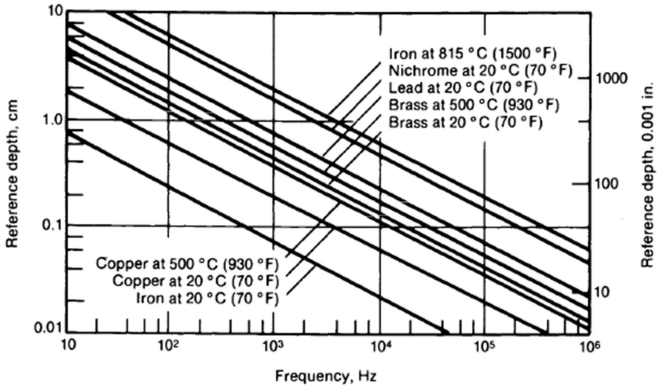


Figure 2.26. The penetration depth of some materials as a function of resonant frequency (Zinn and Semiatin, 1988)

With temperature increase, due to the increase of the metal resistance, the penetration depth will also increase. However, Table 2.8 shows that such increase is limited for most materials. During the heating process, when penetration depth is smaller than the centre to the surface distance of the heated part, the heat will be conductively transferred from surface to interior. With sufficient time, uniform heating can be obtained (Haimbaugh, 2001, Davies, 2007).

Table 2.8 Penetration depth (mm) of some materials as a function of resonant frequency (Rudnev et al., 2002)

Metal	Temperature (℃)	ρ (μΩ·m)	Frequency (KHz)						
			0.06	0.50	1	4	10	70	200
Al	20	0.027	10.7	3.70	2.61	1.30	0.83	0.31	0.18
	250	0.053	15.0	5.18	3.66	1.83	1.16	0.44	0.26
	500	0.087	19.2	6.64	4.69	2.35	1.48	0.56	0.33
316L	20	0.690	53.9	18.7	13.2	6.61	4.18	1.58	0.93
	800	1.150	69.6	24.1	17.1	8.53	5.39	2.04	1.21
	1200	1.240	72.3	25.1	17.7	8.86	5.60	2.12	1.25
Ti	20	0.500	45.9	15.9	11.3	5.62	3.56	1.34	0.80
	600	1.400	76.8	26.6	18.8	9.41	5.95	2.25	1.33
	1200	1.800	87.1	30.2	21.3	10.7	6.75	2.55	1.51
Ti-	20	1.780	96.5	33.4	23.6	11.8	7.48	2.83	1.67

6Al-4V	700	1.900	99.7	34.6	24.4	12.2	7.73	2.92	1.73

2.4.3 Typical equipment for induction heating system

A basic induction heating system usually includes a power supply, an induction coil, a heat station for matching and tuning as well as a cooling system.

2.4.3.1 Power supply

The power supply for induction heating is essentially a frequency and phase changer. It converts the input current, which usually is the three-phase current from the utility power line (frequency of 50Hz or 60Hz), into the required alternating current (AC). The most commonly used conversion process for induction heaters based on a single coil is shown in Figure 2.27.

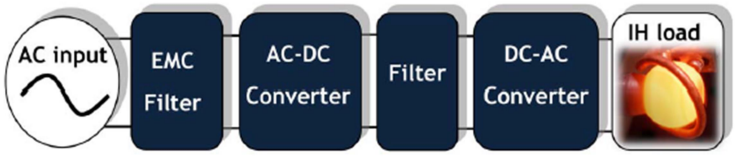


Figure 2.27.Typical power conversion flow in an IH system (Luc et al., 2014)

First, an electromagnetic compatibility (EMC) filter is used to fix the electromagnetic properties of input power, which can ensure that the power delivered to the converter complies with the standards (Heldwein et al., 2004). After that, a converter converts alternating current (AC) into direct current (DC). This process is called the rectifier stage. It can be either a non-controlled process or a controlled one. A diode rectifier is often used in non-controlled stage. A controllable rectifier stage is usually achieved either by using a controllable rectifier (Imaz et al., 2012) or by using a diode rectifier plus a dc–dc converter (Luc et al., 2014). In some cases, a power factor corrector block is equipped in the system. It connects to the AC-DC converter to increase voltage and adjust current waveform. After that, the dc–ac power

converter converts the direct current (dc) into medium or high frequency alternating currents to supply the induction heating applicator. The operating frequency of typical induction heating powder supply is usually between 20 kHz and 1 MHz, depending on the applications (Luc et al., 2014).

Power supplies are generally classified by the different elements applied in the DC-AC convention process (as known as inversion process) (Luc et al., 2014). Different types of power supplies fit different output power and frequency demands, as Figure 2.28 shows (Konas, 1970, Frank and Der, 1982, Haimbaugh, 2001). Power supplies equipped with inverters are referred to as solid-state sources, while those equipped with oscillators are referred to as radio frequency sources. In addition to that, inverters can be classified as containing thyristors or transistors. Silicon controlled rectifiers (SCRs) are thyristors, while isolated gate bipolar transistors (IGBTs) and metal-silicon-dioxide field-effect transistors (MOS FETs) are transistors.

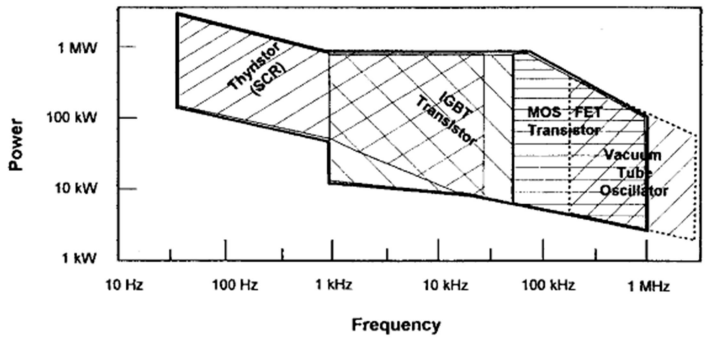


Figure 2.28. Power type used for induction heating (Zinn and Semiatin, 1988)

The most important factors for power supply are frequency (f), voltage (v), current (I) and output power (P). For a certain power unit, the first three factors determine the last one, output power. In practice, usually, only one of the first three factors is adjusted to control the output power, and the remaining two factors will be self-matched or self-tuned. Most of the inverters used in the power supplies are voltage-fed or current-fed. Various methods can be applied to control the output power, as shown in Figure 2.29 (Rudnev et al., 2002, Haimbaugh, 2001).

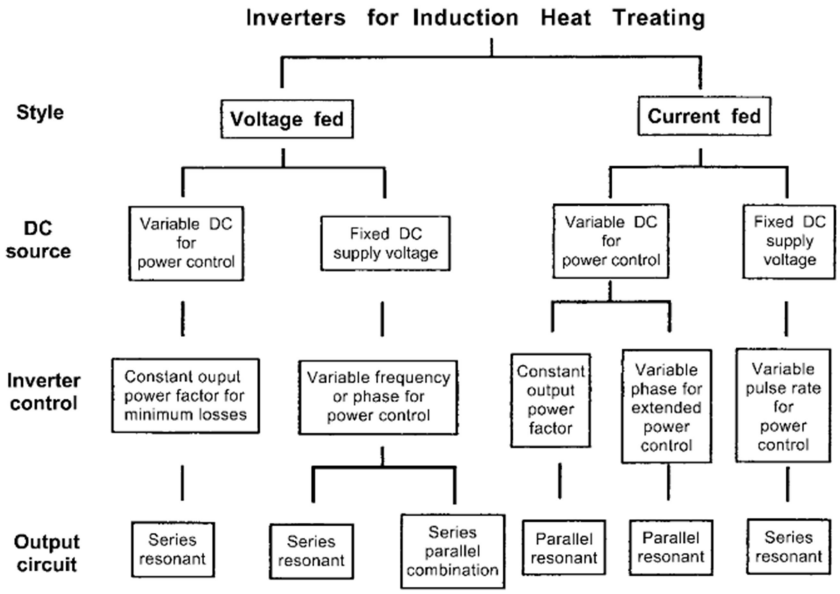


Figure 2.29. Control methods of power supply (Haimbaugh, 2001)

2.3.4.2 Heat station

Before connecting to the induction heating applicator, the power source needs to connect to a heating station, which can help to tune the frequency and match the voltage or the impedance of the heating load (Zinn and Semiatin, 1988).

The major part (in some cases, the only part) of heat station is a resonant tank (Luc et al., 2014). The induction heating load (heating applicator with its heating target) can be modelled as an equivalent resistor R_{eq} and equivalent inductor L_{eq}, as shown in Figure 2.30(a). Based on different models, the resistor and inductor can be connected in series or parallel. These two elements are coupled with external capacitors and/or inductors, which form a complete resonant tank. The most used configurations of the resonant tank are series resonant (Figure 2.30(b)), parallel resonant circuits (Figure 2.30(c)), or the hybrid LLC series parallel resonant circuit (Figure 2.30(d)). The series resonant RLC circuit (Luc et al., 2010) is commonly used in voltage-fed inverters (Figure 2.29). The series capacitor can help to achieve zero voltage across the device during the switching process, known as zero voltage switching (ZVS), means nearly zero switching losses. In contrast, the parallel-

resonant RLC circuit (Steigerwald, 1988) used in current-fed inverters, help to achieve zero current through the device during switching, known as zero current switching (ZCS). The hybrid series-parallel LLC circuit (Chudjuarjeen et al., 2011) is a typical parallel resonance series with an inductor, which can achieve short-circuit protection. Therefore, it is especially suitable for high power industrial applications. (In this research, voltage-fed power supply and series resonant RLC circuit were applied).

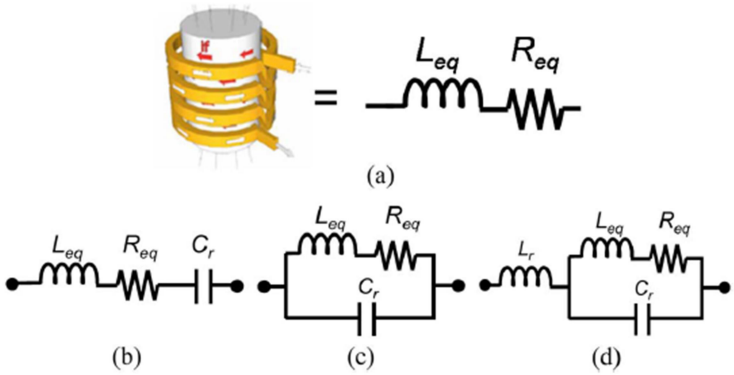


Figure 2.30 (a) equivalent model of an IH load; Fig.4 (b)(c)(d) basic resonant configurations: (b) series, (c) parallel, and (d) hybrid series-parallel LLC.

Besides the resonant tank, heat station may also include a transformer to help to match the voltage.

Through matching or tuning, the system can deliver the designed maximum output power from the power supply to the IH load. In order to minimise system losses, the heat station is often located near the power supply. In many cases, even in the same enclosure (as in this research) (Haimbaugh, 2001, Zinn and Semiatin, 1988).

2.4.3.3 Induction coil

Induction coils are the most commonly seen induction heating applicator. They are the element where the alternating current induces a concentrated electromagnetic field used for heating. In order to maximise the energy conversion efficiency, most induction coils are made of copper, since its low electrical resistance could help to minimise the energy loss. Thus the vast

majority of electric energy could convert into potential energy in the electromagnetic fields (Zinn and Semiatin, 1988).

The design of the induction coil is based on a large number of empirical formulas, which deduce from theoretical analyses of several simple coil geometries (Baker, 1957, Zinn and Semiatin, 1988). There are three basic coil geometries, which are commonly used, as solenoid coil, pancake coil and internal coil, as shown in Figure 2.31. For the solenoid coil, the space within the coil has the most considerable flux, which can be used to heat the workpiece. For the pancake coils, flux from only one surface intersects the workpiece. For the internal coils, only the flux on the outside of the coil is utilised. Generally speaking, the solenoid coil has the highest efficiency and internal coil has the least efficiency. Though there are an immeasurable amount of coil geometries, most of them can be considered as a deformation or combination of these basic geometries (Haimbaugh, 2001, Zinn and Semiatin, 1988).

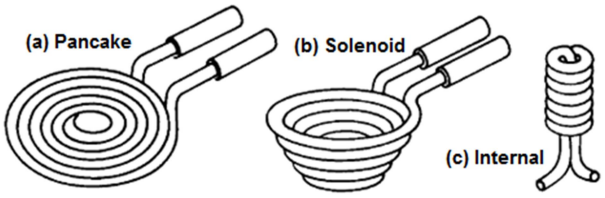


Figure 2.31. Basic induction coil geometries (Zinn and Semiatin, 1988)

Besides empirical formulas and accumulated experience, designers nowadays also use computational techniques (like Finite Element Method, Finite Difference Method etc.) as well as computer-aided numerical tools to simulate and optimise the coil design (Boadi et al., 2005, Rudnev et al., 2002). The most crucial part of coil design simulation and optimisation are the electrical equivalent parameters extraction (equivalent resistor R_{eq} and equivalent inductor L_{eq} as mentioned in 2.1.2) (Acero et al., 2006), the efficiency optimisation (Wojda and Kazimierczuk, 2013), and the heat distribution optimisation (Candeo et al., 2011).

2.4.3.4 Cooling system

During the induction heating process, the alternating current flows through the copper induction coil, which will heat the coil considerably. Therefore, a cooling system is required to prevent the coil from overheating. In practice, water cooling is the most commonly used cooling method. Water flows through the coil and carries excessive heat away, then exchange heat with air at the cooling tower to form a loop. In some special circumstances, other coolants, ones with greater heat capacity or higher vaporisation temperature, will be applied (Haimbaugh, 2001).

2.5 Summary and gap in knowledge

The production of Ti-6Al-4V products via selective laser melting has attracted significant attention during the past decade, due to its ability to provide high design freedom as well as a high buy-to-fly ratio. It is proven that as a reliable technique, it can produce near net-shape and near fully dense parts with mechanical properties after heat treatment close to wrought parts. However, unfavourable properties like high residual stress, low ductility and anisotropic mechanical properties obstruct the use of as-built products. (Dutta and Froes, 2016, Shunmugavel et al., 2017, Shipley et al., 2018)

Recent efforts on the fabrication of Ti-6Al-4V by SLM have focused on applying in-situ heat treatment, either through a refinement of process parameters or by the use of additional heating sources. While localised heat cycle can be used to induce the in-situ decomposition of martensite α', which leads to better ductility, applying additional heating sources have demonstrated the possibility to reduce thermal gradients during manufacturing, so that components with lower residual stress can be fabricated. (Xu et al., 2015, Xu et al., 2017a, Deckers et al., 2014)

Nevertheless, currently, the attempts of in-situ improvement could not completely tackle the unfavourable properties introduced by the printing mechanisms (Deckers et al., 2014). Thus, the post-process heat treatment is

crucial for SLM Ti-6Al-4V, as it will help to improve the properties of the printed products. Researches on conventional sub-transus heat treatments have established a well-recognised theory to explain the microstructure and the texture formation during the process. It suggests that, after sub-transus heat treatment, a balanced tensile property with improved ductility and acceptable strength can be achieved (Chandramohan et al., 2018, Fan and Feng, 2018, Ter Haar and Becker, 2018, Liu and Shin, 2019). However, the morphology of columnar prior-β grain remains in the microstructure after the sub-tansus heat treatments, which suggests the products will still present a mechanical property with anisotropic behaviour (Zhang et al., 2018).

Super-transus heat treatments have the potential to form equiaxed β grain in the microstructure. However, conventional heat treatment requires long dwell times to achieve uniform heating, which leads to undesirable coarsening of the grain structure (Vilaro et al., 2011, Vrancken et al., 2012). Furthermore, limited studies on the texture formation during the super-transus heat treatment restrict the development of such treatment route.

2.6 Aim and objectives of this study

This study aims to control the size of the prior- β grains obtained in sub-transus heat treatment of SLM Ti-6Al-4V and improve the understanding of the texture formation during the heat treatment process.

Initially, this study aims to refine the size of prior-β grain in super-transus heat treatment via limited dwell time and rapid heating rate, and study its influence on tensile properties and microstructure of Ti-6Al-4V produced by SLM. It is believed that the limited dwell time and rapid heating rates might lead to a refinement of the overall grain size and, more particularly, a refined equiaxed prior-β grain structure which might result in better tensile properties.

In addition, this study aims to increase the knowledge regarding the texture formation in super-transus heat treatments, especially the early stages of β

annealing. The understanding of the microstructural evolution of SLM Ti-6Al-4V in early stages of β annealing might provide useful information, which can help the design of new heat treatment routes for the realisation of superior properties.

If all the aim and objectives of this study are achieved, a refinement of the prior-β grains after heat treatment will be reported for additively manufactured Ti alloy for the first time. In addition, the explicit knowledge and detailed information related to early-stage β grain formation and growth in the additively manufactured Ti alloy will be revealed for the first time.

CHAPTER 3

3. Material and Methods

This chapter describes the experimental methodologies used in the present study, including materials, experimental setup and methods, as well as characterisation technologies. The sections are summarised as follow: Section 3.1 describes the materials used in the study, focusing on the chemical and thermal characteristics of the received SLM Ti-6Al-4V. Section 3.2 gives a description of the various heat treatments used in this research to post-process the as-built materials. Two different types of heating methods are applied in this study, conventional heating and induction heating. All the conventional heat treatments are conducted using a commercial conventional furnace, while all induction heating is conducted via a bespoke induction heating system. The details of the bespoke set up for this system will be given, and the reliability of the system will also be evaluated and reported. Section 3.3 introduces the tensile test studies, which are conducted to examine the tensile properties of the SLM Ti-6Al-4V after different treatments. Section 3.4 describes the techniques used to characterise the microstructure and crystallographic texture of the samples. The methodology used for the reconstruction of the parent β phase is also reported in this section. Details on the code used to perform the reconstruction of the parent β phase are provided in Appendix A.

3.1 Material used in this study

The material used in this study were Ti–6Al–4V (grade 23) cylinders of 9mm diameter and 60 mm length produced by selective laser melting (SLM) at 90° build angle to the build platform. Hereafter, the material will be referred to as SLM Ti-6Al-4V. The produced cylinders were manufactured on an EOSINT M290 system and provided by 3T Additive Manufacturing Ltd. Dimensional errors of the received cylinders are less than 0.2mm.

Primary chemical compositions of the received material were examined at 3 random locations on the XZ cross-section of a randomly selected cylinder. At each location, an area of approx. 1.5mm * 1mm was scanned by energy-dispersive (EDS) detector equipped in a Hitachi TM 3030 scanning electron microscope (SEM). The detected compositions that have a weight percentage (wt%) more than 0.5% are reported in *Table 3.1*. EDS results suggest a homogeneous distribution of the chemical compositions in the received material. The ratio of Aluminium to Vanadium in the received material is slightly in favour of Aluminium compared to the nominal value (6 Aluminium vs 4 Vanadium). Since Aluminium acts as an α stabiliser (Lütjering and Williams, 2007), it can be assumed that the β transus temperature of the received material might be marginally higher than the theoretical value of 995°C.

Table 3.1. Primary chemical compositions of the received Ti-6Al-4V

wt%	Location 1	Location 2	Location 3	Average
Titanium	90.76	90.87	91.03	90.89
Aluminum	5.81	5.75	5.61	5.72
Vanadium	3.43	3.38	3.36	3.39

The β transus temperature of the received material was ascertained by a thermal analysis technique known as Simultaneous Differential Analysis (SDT). SDT analyses the sample simultaneously via two different thermal analysis techniques, thermogravimetric analysis (TGA) and differential scanning calorimetry (DSC). TGA tracked the changes in weight of the sample over time or temperature, while DSC tracked the changes in heat flow (Xu *et al*., 2005) during heating. A TA Instruments TGA-SDTQ600 analyser was used to conduct the analysis. Four samples weighted between 10mg to 15mg were prepared from the received cylinder. Each of them was heated at a constant rate of 10.00°C/min from room temperature (25°C) to 1200°C in an argon atmosphere. Measured results are shown in Figure 3.1.

It can be noticed that, throughout the measurement, disregarding the initial stage, two spikes of the heat flow appear in Figure 3.1. The first spike is induced by the initial decomposition of martensitic α'. It happens at a temperature between 500°C to 600°C. The second spike, as circled by the black dash line, is induced by the completion of the α to β transformation. The onset temperature and the end temperature of the second spike in different measurements are summarised in *Table 3.2*. Among these two temperatures, the onset temperature of the spike indicates that some part of the test sample begins to be α phase free at the said temperature, while the end temperature means that the entire test sample is α phase free at the said temperature. Since the β transus temperature is the temperature where the entire material enters into the single β phase region, it can be presented by the measured end temperature, which has an average value of 1013.35°C. This value has excellent consistency across different measurements. The standard deviation of the average value is 4.59°C.

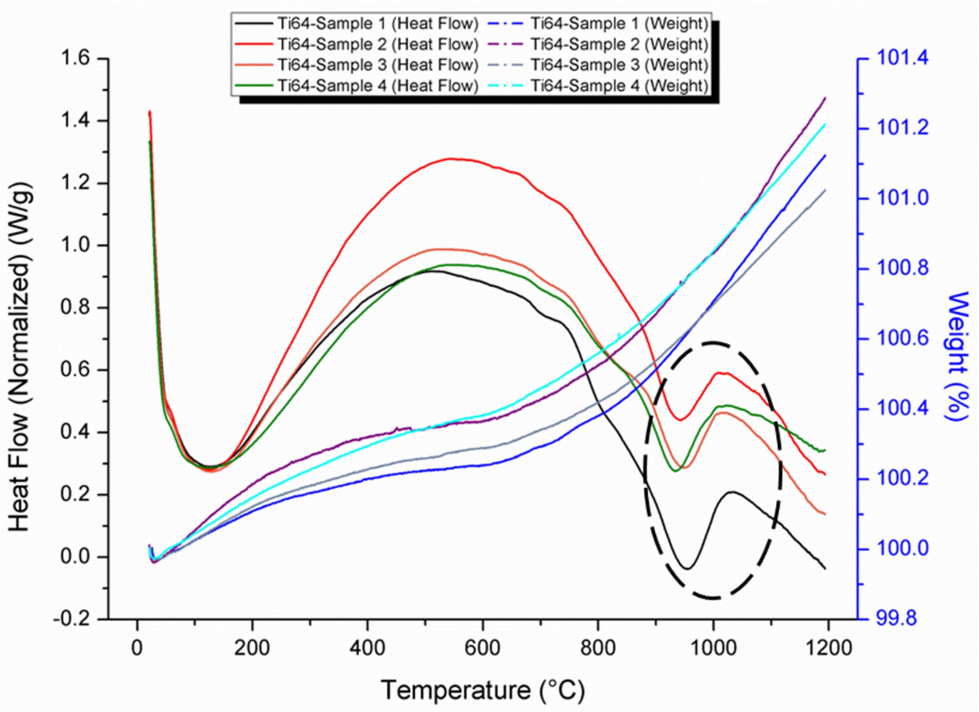


Figure 3.1. Simultaneous Differential Analysis (SDT) results of the received Ti-6Al-4V

Table 3.2. Onset temperature and end temperature of the second spike in different measurements

	Onset Temperature	End Temperature (β-transus)
Sample 1	954.99°C	1019.72°C
Sample 2	934.47°C	1009.92°C
Sample 3	944.14°C	1013.67°C
Sample 4	930.27°C	1010.09°C
Average	940.97°C	1013.35°C ± 4.59°C

3.2 Post-process heat treatments for the received Ti-6Al-4V

In this study, 5 different heat treatment routes were applied to post-process the received Ti-6Al-4V. One of the heat treatment routes consisted entirely of conventional heating processes, hereafter referred to as “conventional heat treatment”, while the remaining 4 heat treatment routes consisted partially or completely of induction heating process, hereafter referred to as “induction heat treatments”.

For each heat treatment, a group of 5 received SLM Ti-6Al-4V cylinders were heat treated at the same condition and procedures. The tensile properties and microstructures of these heat treated samples are presented and analysed in Chapter 4 and Chapter 5, respectively. The process route for each heat treatment will be schematised by a time vs temperature chart in the corresponding section.

Details of the conducted conventional heat treatment will be introduced in section 3.2.1, while details of the conducted induction heat treatments will be described in section 3.2.2.

Other than these heat treatments, a designed gradient heating process of the received material was also conducted in this research, to study the

microstructure evolution in the specific temperature range. The related results are discussed in Chapter 6. Details of the applied gradient heating will be presented in section 3.2.3.

3.2.1 Conventional heat treatment: heating system and experimental procedure

An ML M5 bench top furnace was used to conduct all the conventional heating processes involved in this study. This was a commercial muffle furnace that could be heated up to 1200°C. It has a maximum output power of 3kW. The furnace was controlled via a Eurotherm 3216 multiple program controller. For all the conducted conventional heating process, a constant heating rate of 10°C/min was applied. After the soaking, the specimens were air-cooled. The average cooling rate of air cooling was measured at about 7°C/min. The process route for the applied conventional heat treatment is shown in Figure 3.2. It is arranged according to the published standards. The samples will first be annealed at 925°C for 2 hours then subsequently aged at 700°C for 4 hours (ASTM, 2014a, ASTM, 2014b, SAE, 2016).

In order to eliminate the risk of oxidation during the conventional heating process, all the specimens were vacuum-sealed (O_2 level < 10 ppm) in silica ampoules before any conventional heating process.

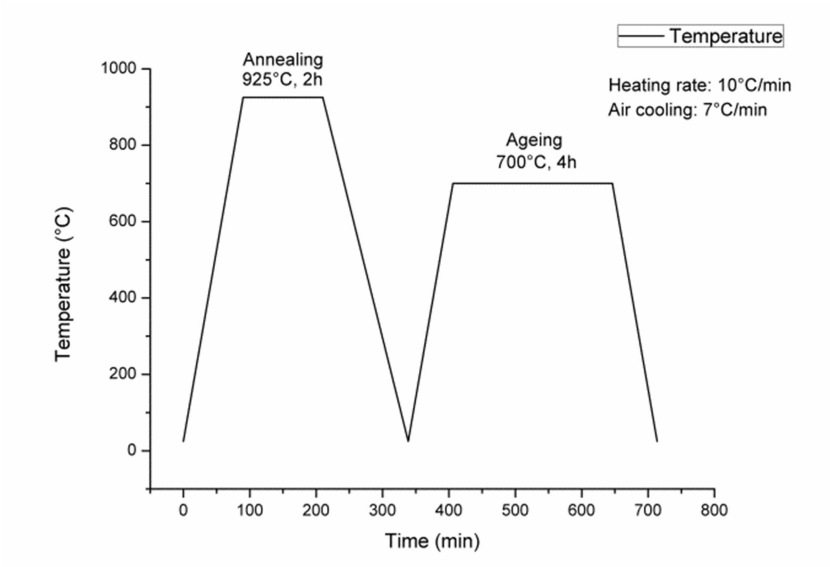


Figure 3.2. The process route for the applied conventional heat treatment.

3.2.2 Induction heat treatments: heating system and experiment procedure

3.2.2.1 Process route for the applied induction heat treatments

Among the 4 groups of induction heat treatments, 3 of them contained two heating stages. The first stage was an initial rapid induction heating process (at a higher temperature), and the second stage was a subsequent conventional ageing process (at a lower temperature). The schematic of this type of process route is shown in Figure 3.3. Since the induction heating process had limited dwell time at the target heating temperature, it will introduce a spike shape in the schematic. Therefore, the target heating temperature will appear as the peak temperature in the temperature profile. The subsequent conventional ageing process in the applied induction heat treatments follows the same procedure as what has been described in the conventional heat treatment. Depending on the target heating temperature (peak temperature) of the induction heating process, these 3 induction heat treatments are hereafter referred to as:

- Induction heat treatment above 980°C: target heating temperature was set at 980 °C

- Induction heat treatment above 1005°C: target heating temperature was set at 1005 °C
- Induction heat treatment above 1030°C: target heating temperature was set at 1030 °C

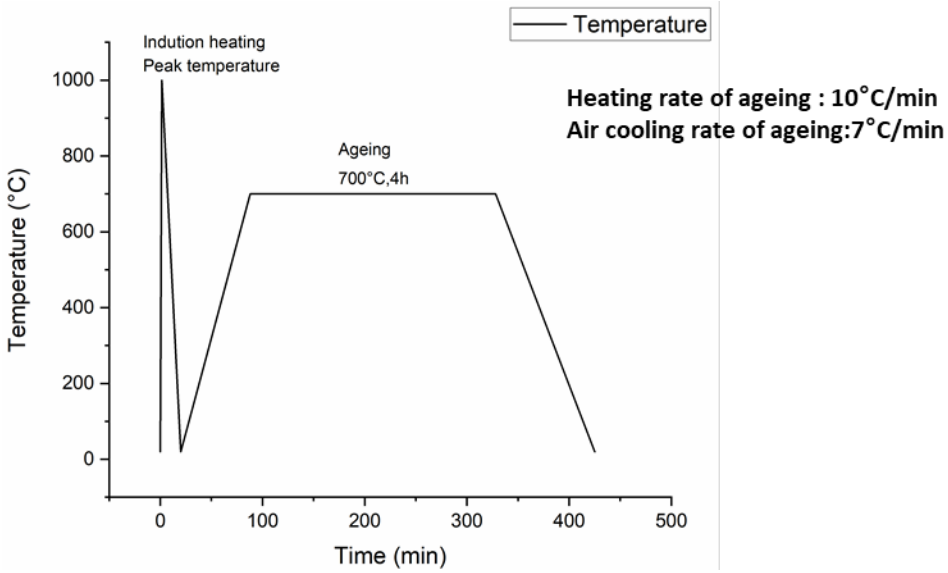


Figure 3.3. Schematic showing the process route of the applied induction heat treatments, which contained an initial rapid induction heating process (at a higher temperature) and a subsequent conventional ageing process (at a lower temperature).

In addition to these 3 induction heat treatments, another group of induction heat treatment was also conducted in this study. It only contained the initial rapid induction heating process, and did not include any of the subsequent ageing processes. The schematic of this type of process route is shown in Figure 3.4. The target heating temperature for this group of heat treatment was set at 1030°C. This induction heat treatment hereafter is referred to as:

- Induction heat treatment above 1030°C without subsequent ageing

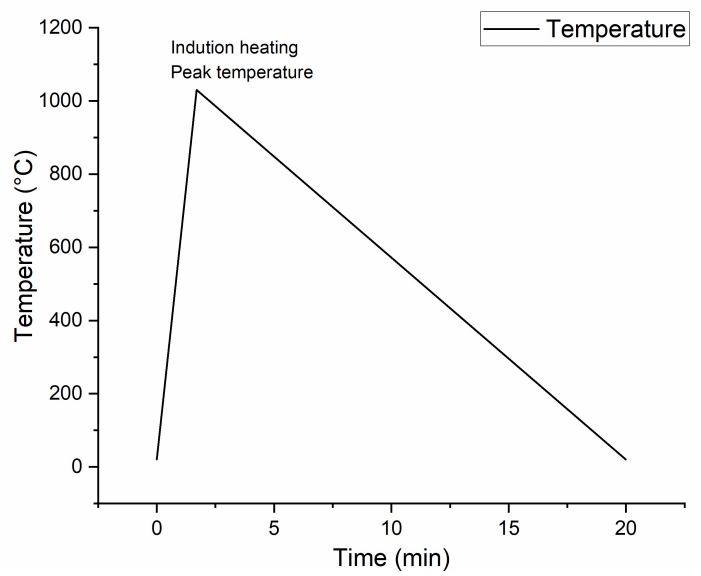


Figure 3.4. Schematic showing the process route of the applied induction heat treatments, which only contained a rapid induction heating process.

3.2.2.2 Induction heating system assembled for this research

A bespoke induction heating system was used to conduct all the induction heating investigations carried out in this study. The apparatus used is shown in Figure 3.5. This system consisted of 4 functional units including a heating unit, a specimen fixture, an O_2 control/monitor unit and a temperature record/monitor unit.

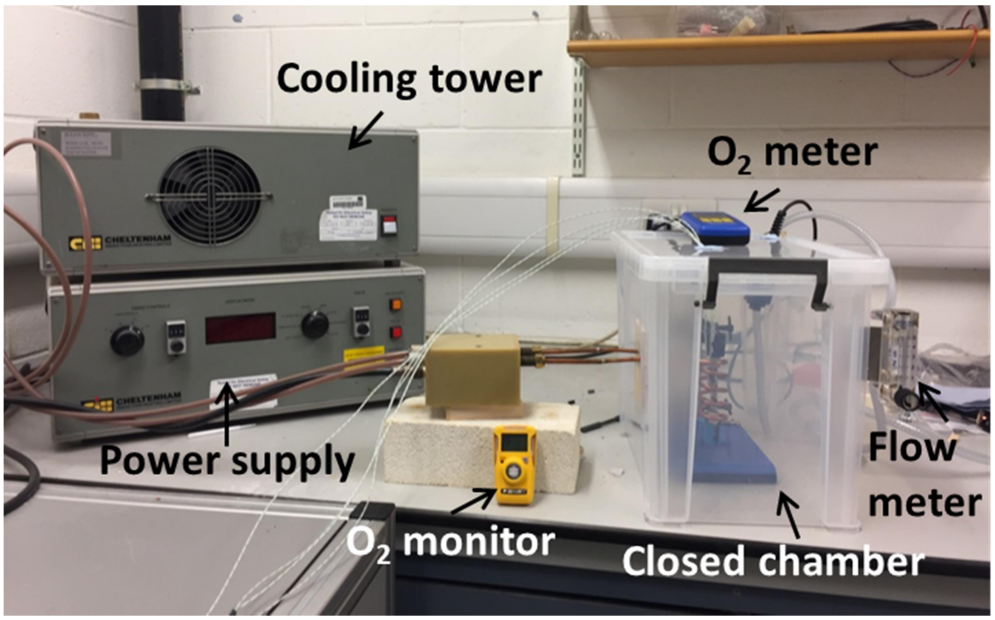


Figure 3.5. The system used for the induction heat treatments of the received Ti-6Al-4V

The heating unit includes a Cheltenham TR1 induction heater and a customised solenoid coil. The induction heater came with a voltage-fed power supply, which had a maximum power level of 1kW, and a fan assisted cooling tower, which kept water circulating to cool the induction coil. The customised coil was a 5 turn solenoid coil with 30mm outer diameter and 90 mm height, as shown in Figure 3.6 (a). The coil was made in house using a 5mm diameter copper pipe (thickness of the pipe was 1mm). This heating unit can work stably at a resonating frequency of about 200 kHz.

A specimen fixture unit was designed to position the specimen in the centre of the coil during the heating process, as shown in Figure 3.6(a). A schematic of the fixture is presented in Figure 3.7. A retort stand and 2 retort clamps are used to fix the position of the specimens, while 2 heat insulators made by alumina were used to prevent heat dissipation through the solid support. The drawing of the alumina heat insulator is presented in Figure 3.8. This support features a 3mm deep shallow hole with a diameter of 9.2mm to accommodate the Ti-6Al-4V cylinders produced by SLM.

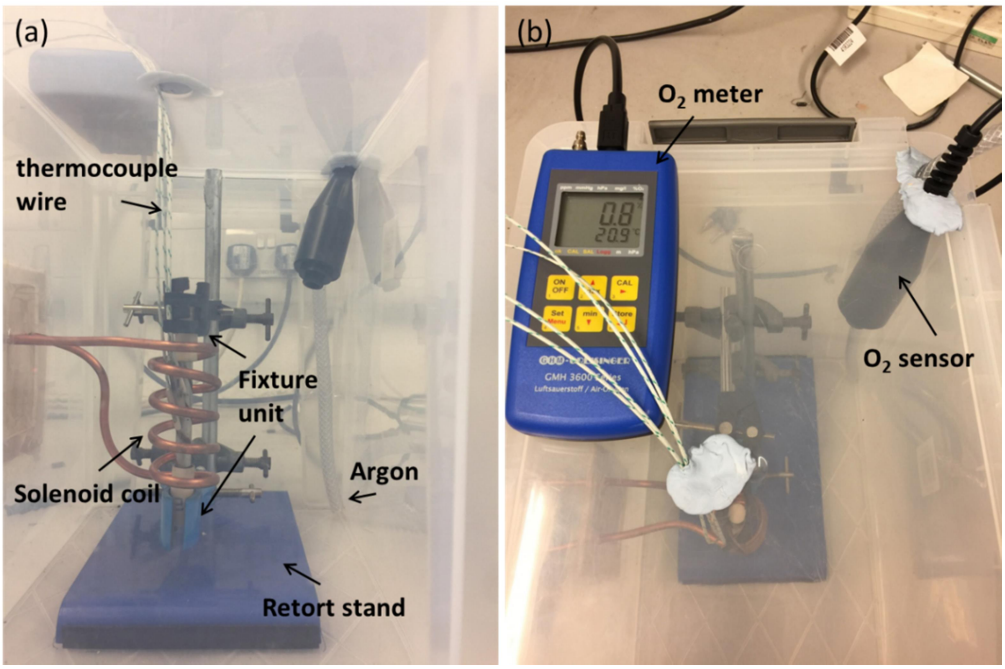


Figure 3.6. Detail set up within the closed chamber: (a) side view; (b) top view.

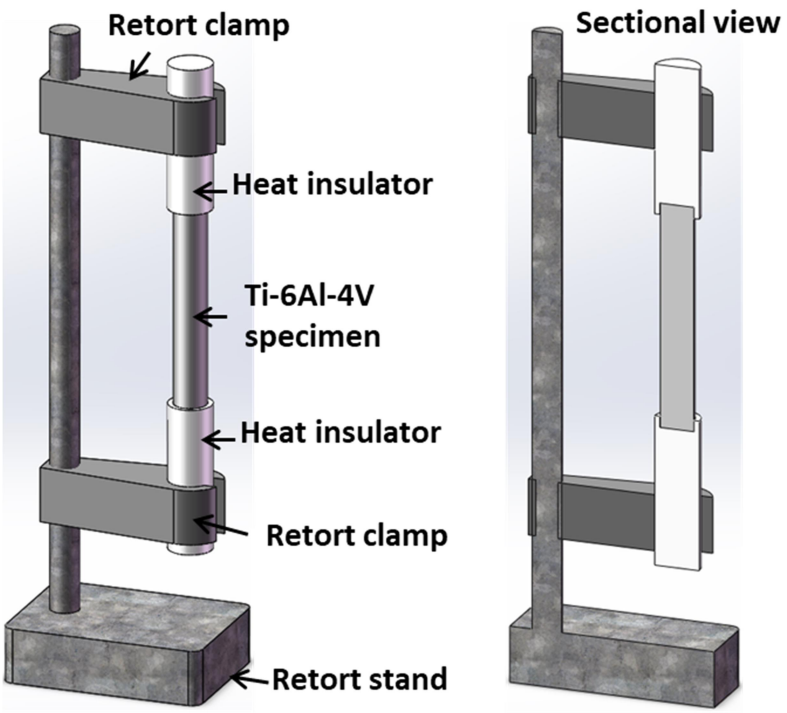


Figure 3.7. Schematic of the design of the specimen fixture.

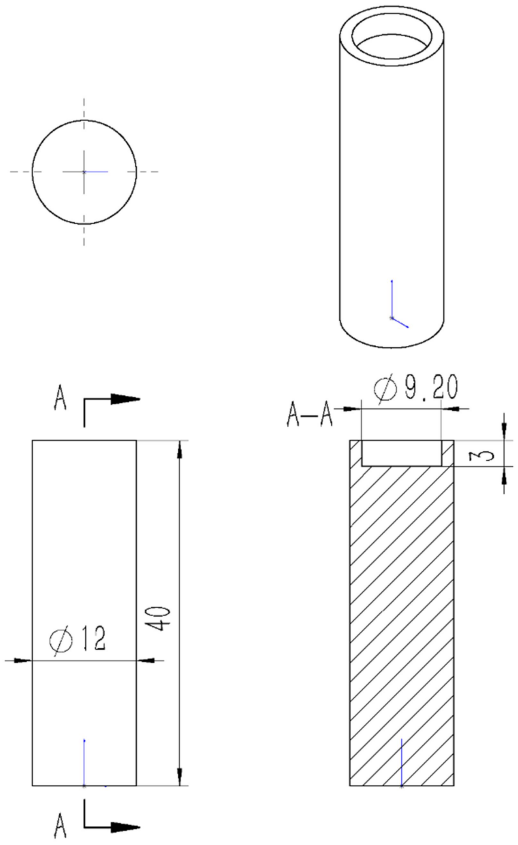


Figure 3.8. Drawing of the used alumina heat insulator (unit: mm)

A closed chamber was set up to create a protective argon atmosphere, as shown in Figure 3.5 and Figure 3.6. This helped to minimise the oxidation of the specimen during induction heating. The feeding speed of the argon flow was controlled by a variable area flowmeter, which could adjust the feeding speed between 0.4L/min to 5L/min, as shown in Figure 3.5. During the heating process, the O_2 level inside the chamber was monitored by a Greisinger GMH 3600 O_2 meter, as shown in Figure 3.5 and Figure 3.6. The O_2 sensor was placed at a location that is closer to the top of the chamber than the upper surface of the coil, as shown in Figure 3.6 (b). Since the argon (1.7838 kg/m^3, at 0°C and 1 bar) is heavier than the air (1.2754 kg/m^3, at 0°C and 1 bar), the lower part of the chamber should have a higher argon concentration. Such placement of the O_2 sensor could ensure that the actual O_2 level around the specimen is lower than the value monitored by the senor.

To ensure the operator working in an environment that has sufficient O_2, the O_2 level in the laboratory room was monitored by a BW Clip O_2 detector, as shown in Figure 3.5.

Prior to switching on the induction heater, argon gas was fed into the chamber at a constant rate of 3L/min. After the O_2 concentration in the chamber reached to a level lower than 1%, the feeding rate of the argon gas was increased to a constant rate of 5L/min. Therefore, the O_2 level in the chamber could be maintained. After that, the induction heater was switched on to perform the induction heating process. Every induction heating processes and subsequent cooling processes conducted in this research were performed in an atmosphere with O_2 concentration below 1%.

Type K thermocouples shielded with a twin-bore alumina tube were used to measure the temperature during the induction heating, as shown in Figure 3.9. Two wires of the thermocouple were separated with each other in the tube. The twin-bore alumina tube can help to reduce the disturbance on the temperature measurement, which is caused by the alternating electromagnetic field (induced by the coil). The ends of the two wires of the

thermocouple were welded to the surface of the Ti-6Al-4V cylinder. For each thermocouple, the two welding points of the wires were separate but close to each other. Therefore, the thermocouple could not be heated directly via the induction heating, since no closed-loop for eddy current to be formed within the thermocouples.

The other end of the thermocouples were connected to a 4 channel NI-9211 temperature input module. Through this module, the noise in the measurement was reduced, and the temperature data was displayed and recorded via LabVIEW software at a refresh rate of 2Hz.

The received cylinders were heated up during the heat treatment and then machined to tensile specimens. The tensile properties of the gauge area were then tested and recorded. Details about the tensile specimens will be explained in section 3.3. The gauge area was machined from a 20.4mm length area located in the middle portion of the Ti-6Al-4V cylinder. To ensure the middle portion of the Ti-6Al-4V cylinder was uniformly heated during the induction heat process, the temperature in that area was monitored. For each cylinder, a total of 4 thermocouples were welded at different heights of the middle region, each of them had a spacing of 7mm, as shown in Figure 3.9.

During the induction heating, an output power of 980W was used to heat specimens to different target temperatures. Once the target temperature was reached, the power supply was turned off, and the specimens were gas-cooled in the argon environment. An example of the heating and cooling profile recorded in the induction heating process is shown in Figure 3.10, which shows the Ti-6Al-4V cylinder experienced a rapid heating process and limited soaking time was applied at the target heating temperature. The recorded heating and cooling profiles for each induction heating process are reported in detail in Chapter 4.

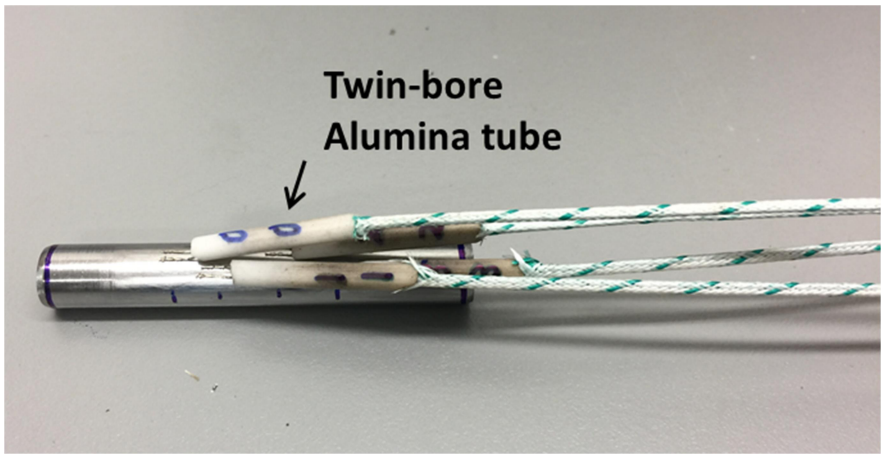


Figure 3.9. Thermocouples shielded with twin-bore Alumina tubes were welded at different locations symmetrically distributed around the middle portion of the specimens.

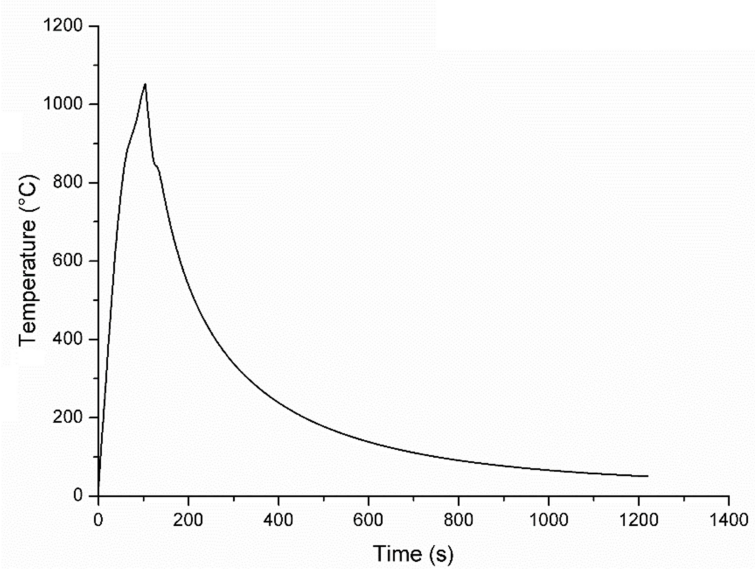


Figure 3.10. Example of the heating and cooling profile recorded in the induction heating process, which shows the Ti-6Al-4V cylinder experienced a rapid heating process and limited soaking time was applied at the target heating temperature.

3.2.2.2 Reliability of the point thermal analysis

In this study, a reproducible and uniform heating process was required to be delivered to the middle portion of the Ti-6Al-4V cylinders by the induction heating system. Point thermal analyses (thermocouples) were applied to monitor the uniformity of the heating. The successful operation of this

temperature monitoring system was built on the assumption that, during induction heating, the temperature will be evenly distributed in the cross-sectional area of the cylinder. In this way, the temperature measured at the edge of the specimen could, at least in first approximation, represent the temperature of the entire cross-section. Therefore, instead of monitoring the temperature distribution of the entire area in the induction heat treatment, the temperature at a few different heights were measured.

In order to support this assumption and prove the reliability of the point thermal analysis, the uniformity of the temperature distribution at the cross-section area will be examined in this section.

During induction heating, relatively uninform heating can be achieved, as long as the Joule heating that occurred within the penetration depth can be effectively transferred to the rest of the material. Therefore, a proper match is required between the penetration depth and the diameter of the heating target. As introduced in section 2.4.2, the penetration depth is closely linked to the frequency of the induction heating system and the physical properties of the target material. SLM Ti-6Al-4V specimens with cross-section size of 10mm * 10mm were used to examine the uniformity of the temperature distribution in the cross-sectional area. Since the cross-section size of these specific specimens is larger than that of the received cylinders, the uniformity of the temperature distribution in these specific specimens could allow for estimating the uncertainties related to the temperature distribution in the cylinders.

The top surface of these specific specimens was polished prior to induction heating for temperature monitoring. A FLIR T400 infrared camera was used to record the temperature of the polished surface during the heating process. This infrared camera could capture a thermographic image every 10s. The thermography image was then processed by the analysis software FLIR Tools+ to read the temperature data embedded in the image pixel by pixel

(36 pixel * 36 pixel). The average emissivity of the polished Ti-6Al-4V surface was calibrated prior to the heating, to a value of 0.32.

A total of 3 specimens were heated by the assembled induction heating unit to estimate the uniformity of the temperature distribution in the specimens. For each specimen, thermography images were captured every 10s after the start of the heating process. The induction heating process typically lasted for 80 seconds. Therefore a total of 8 thermography images were generally obtained from each process. The temperature distribution at every 10s was read from the thermography image and demonstrated in a 3D map, as shown in Figure 3.11. Each 3D plot presented in the figure represents a profile of the temperature distribution obtained at different times. From bottom to top, they were obtained from 10s to 80s of the heating process, respectively. For each plotted point in the 3D temperature map, the specific location on the samples can be read on the X and Y axis.

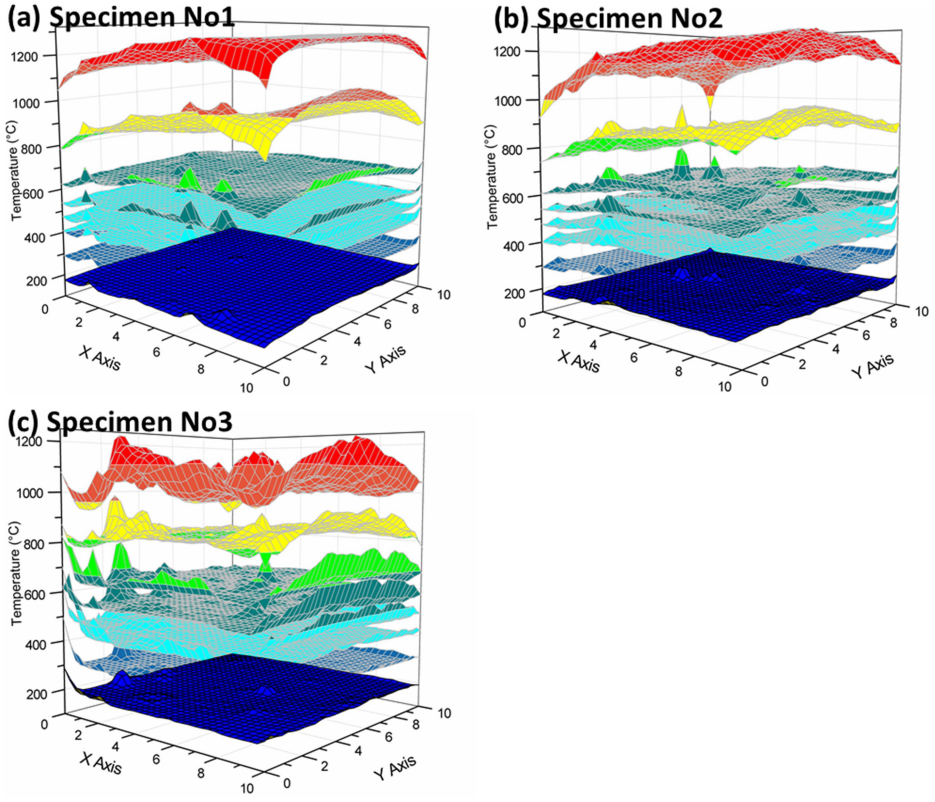


Figure 3.11. Temperature distribution measured on the top surface of the Ti-6Al-4V samples produced by SLM during induction heating: (a-c) show the measured temperature distribution of Specimen No1 to No3, respectively.

It can be observed from Figure 3.11 that temperature distribution at the top surface the Ti-6Al-4V samples maintained an excellent uniformity at relatively lower heating temperatures. At a higher temperature, abnormal disturbance can be observed on the temperature distribution, appearing as peaks and troughs in the temperature map. These anomalous measurements were assumed to be caused by porosities and scratches on the sample surface. The porosities were inherited from the SLM process, while the scratches were introduced during the polishing process. Because of the absence of the Ti-6Al-4V material in the porosities and scratches, the real emissivity in these locations at relatively high temperature is significantly different from the average value used in the measurements, which leads to an inaccurate measurement at certain spots, as shown in Figure 3.11 (c) specimen No. 3. Therefore, in order to examine the uniformity of the temperature distribution, as well as to compare the temperature data obtained in different heating processes, the average temperature and the standard deviation at every 10s is calculated and presented in Figure 3.12. The calculated average temperature at every 10s present a good consistency across different heating processes, which proves the reproducibility of the induction heating process. The standard deviation is always maintained at a reasonable level, a value which is smaller than 5% of the average temperature, which suggests a uniform distribution of the temperature in the cross-sectional area. Therefore, the temperature measured at the edge of the specimen can represent the temperature of the entire cross-section, and thermocouples measuring surface temperatures could provide reliable measurements of the temperature during induction heating. A further discussion on the reliability of the induction heating process will be included in Chapter 4, where the temperature measured during various induction heat treatments will be presented and analysed.

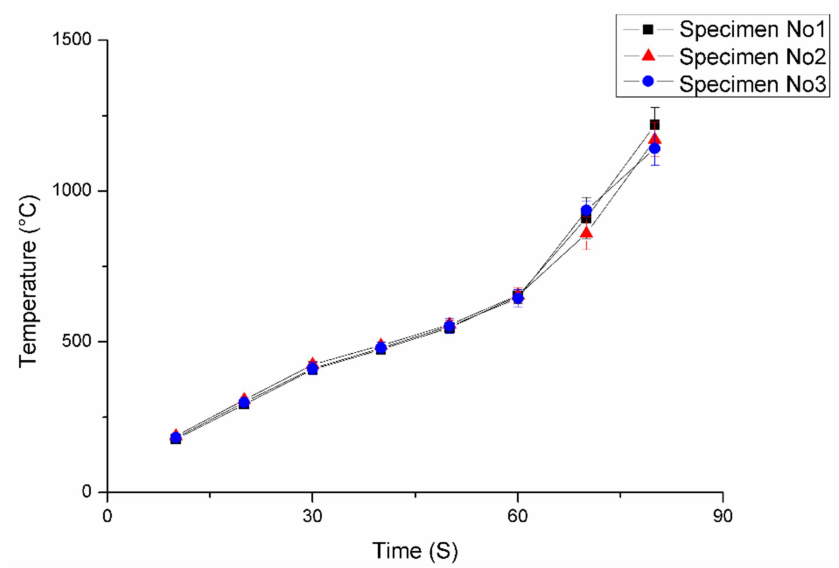


Figure 3.12. The average and corresponding standard deviation of the temperature on the top surface of the Ti-6Al-4V samples produced by SLM. The measurements were performed every 10s from the start of the induction heating process.

3.2.3 Design of the temperature gradient heat treatment

Studying the microstructure evolution of SLM Ti-6Al-4V during early stage β annealing is an essential part of this research. In the previously published researches on the microstructure evolution during heat treatment, traditional experimental methodologies are commonly applied (Vrancken et al., 2012, Huang et al., 2015, Wu et al., 2016c, Fan and Feng, 2018). According to these methodologies, the same batch of materials will be heated separately to different temperatures. Therefore, a series of microstructure will be obtained after the heating process. Each of the microstructures will represent a specified stage in the microstructure evolution. Based on the analysis of the observed microstructure, the reasonable hypothesis, which can link all the characterised stage, will be proposed to explain the potential evolution process. However, since the observation is a discontinuous process, gaps exist between the characterised stages.

To overcome this gap, a different experimental methodology was designed where the target material is heated with a specified thermal gradient.

Hereafter, this experimental methodology will be referred to as “gradient heating”. During a single heating process, due to the gradient heating, different positions of the material will be heated to a different temperature. Since the temperature distribution within the material is continuous, a continuously evolved microstructure, therefore, can be obtained in the material.

The gradient heating process was implemented via an experimental kit modified from the induction heating system described in section 3.2.2. To achieve the desired gradient heating, the bottom heat insulator of the original fixture was replaced with a new one, which had a 10mm deep hole, as shown in Figure 3.13. The heat insulator was made by alumina, which can significantly reduce the penetration of the electromagnetic field. Therefore, the material inserted into the insulator was unlikely to be heated by the alternating electromagnetic field during the induction heating. Therefore, a ‘cold end’ was created in the bottom part of the Ti-6Al-4V cylinder, as indicated in Figure 3.13 (a). However, the heat generated in other parts of the material during the induction heating was conductively transferred into this ‘cold end’. Due to this conductive heating, a thermal gradient was created within the material. The material located near the bottom part experienced a lower temperature, compared to the upper part of the material.

The heating procedure of the gradient heating was similar to that which was described in section 3.2.2 for the induction heat treatment. The gradient heating was also conducted in an argon environment with the power supply working at 204KHz and 980W. The power supply was turned off once the target temperature is reached, and the specimens were gas cooled in an argon environment.

By using this modified fixture, when the material was heated to a temperature of about 1000°C, a temperature gradient of 20°C could be created within the middle portion of the Ti-6Al-4V cylinder. Therefore, a

continuously evolved microstructure could be obtained within the area. The obtained microstructure will be presented and analysed in Chapter 6.

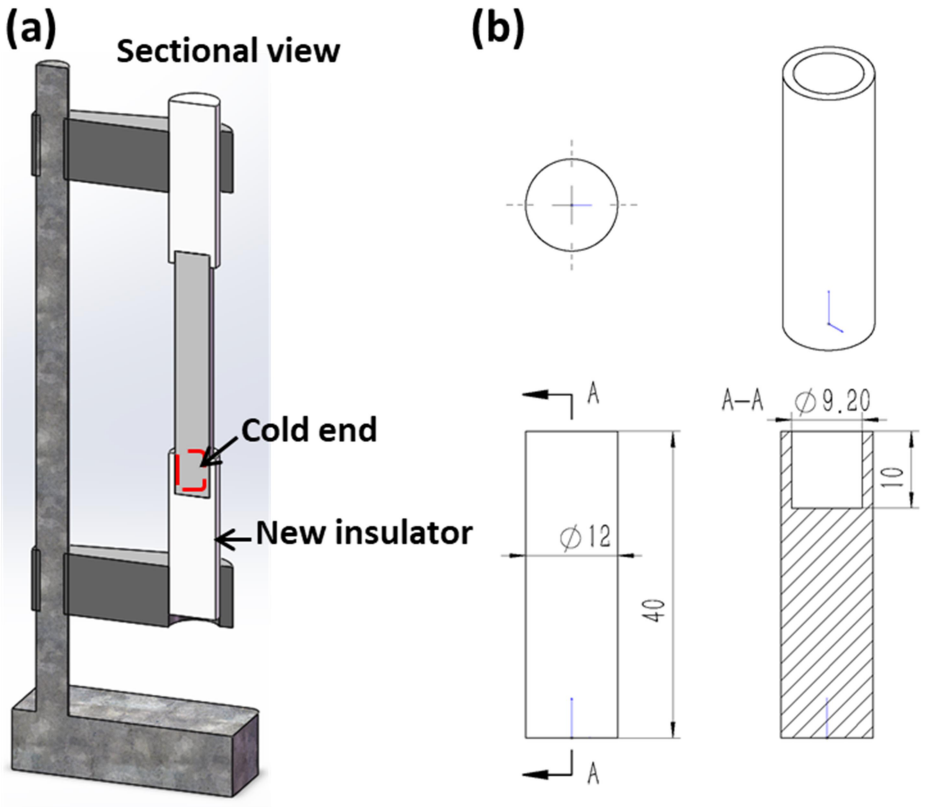


Figure 3.13. The modified fixture used to implement the designed gradient heating: (a) Schematic of the design, sectional view; (b) drawing of the new insulator used to create 'cold end'(unit: mm)

3.3 Tensile testing of the SLM Ti-6Al-4V under the different investigated conditions

A series of tensile tests were carried out to examine the tensile properties of SLM Ti-6Al-4V after different heat treatments. Heat treated SLM Ti-6Al-4V cylinders were machined into tensile specimens with gauge dimension of Φ4mm * 20.4mm (proportional to ASTM E8/E8M-16a) (ASTM, 2016). The drawing of the tensile specimen is shown in Figure 3.14.

By removing a sufficient amount of material from the heated cylinder, the potential oxidation layer, which may be produced during the heat treatment, was completely removed. AMS2801B suggests a metal removal of 0.39mm

for Ti-6Al-4V after heating at 1038°C for 1 hour in an air environment (SAE, 2014). Therefore, the metal removal (1.3mm) conducted in this research should be more than sufficient.

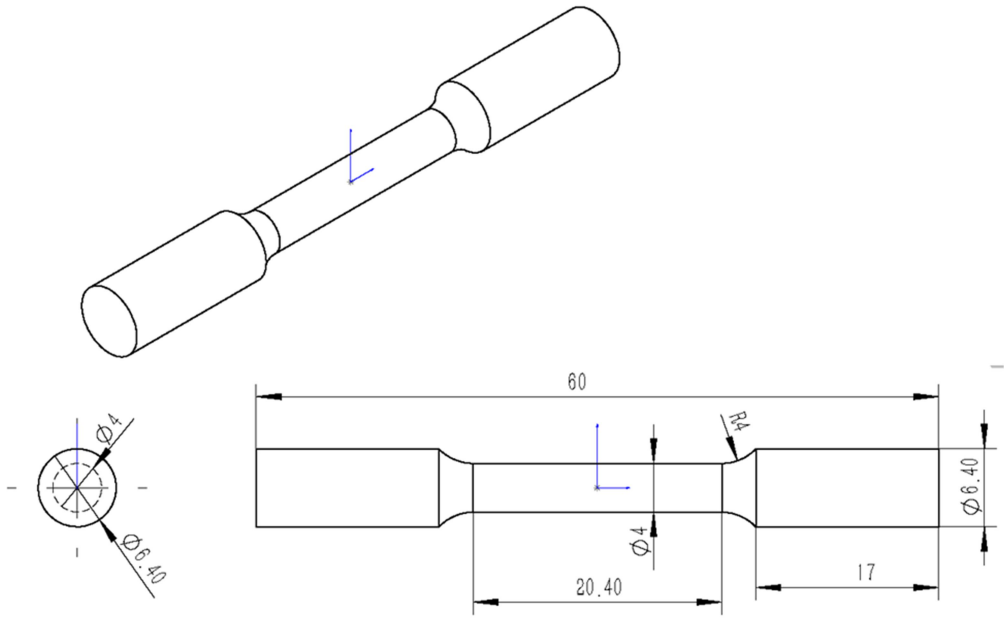


Figure 3.14. Drawing of the tensile test specimens used in this research

All the tensile tests were conducted at room temperature (20°C) on an Instron 5969 at a strain rate of 0.14 mm/min. The strain rate was chosen according to ASTM B348-13 (ASTM, 2013). A video extensometer was used to track the initial elongation of the gauge area. After the elongation exceeds the threshold value, which is 2.5% for as-built specimens and 9% for the heat treated specimens, the rest of the elongation was tracked by the testing apparatus up to the fracture of the specimen. The obtained tensile properties of SLM Ti-6Al-4V under different condition are presented and compared in Chapter 4.

3.4 Characterisation of the specimen microstructure and crystallographic texture

Various characterisation techniques were used in this study to understand the microstructure of SLM Ti-6Al-4V under the different investigated conditions. Section 3.4.1 introduces the procedure for sample preparation,

and section 3.4.2 reports the techniques used for microstructure analysis. Finally, the techniques used to characterise the crystallographic texture are presented in section 3.4.3.

3.4.1 Sample Preparation for Microstructural Characterisation

A mirror-like surface is normally required for microstructure and crystallographic texture analysis. The specimens were first cross-sectioned using a silica carbide cutting blade and then mounted in conductive Bakelite. Grinding and polishing of the specimens were conducted following the protocol suggested by Struers for Ti alloys. Details on the grinding and polishing steps are listed in *Table 3.3*.

Table 3.3.Grinding and polishing procedure used in this research

Process	Wheel/Cloth	Lubricant	Force	Speed	Time
Plane grinding	Grit 400	Water	25N	300rpm	Until Plane
Fine grinding	MD-Largo	9 µm diamond paste	25N	150rpm	5 min
Polishing	MD-Chem	OP-S + 10% H_2O_2	20N	150rpm	As needed

The final step was a chemical-mechanical polishing with a mixture of 0.03µm colloidal silica suspension (OP-S) and hydrogen peroxide (H_2O_2, 30% diluted) on an MD-chem cloth (Struers). The addition of hydrogen peroxide allows continuous removal of the reaction product between titanium and the silica suspension, leaving the surface free of colloidal silica adhesive and mechanical deformation. After the chemical-mechanical polishing, the specimens were immersed in distilled water and ultrasonically cleaned for 15 mins. The specimens were then cleaned individually under tap water and finally dried with methylated spirits and a strong stream of hot air.

Where needed, the specimens were etched using an etchant solution named Kroll's reagent. This etchant is a water-based solution containing HF and HNO_3, which is widely used for commercial Ti alloys (Donachie, 2000). The Kroll's reagent used in this research consists of:

- 4ml HF (48% concentration)
- 10ml HNO_3 (68% concentration)
- 86ml H_2O (distilled)

3.4.2 Techniques for microstructure analysis

Observations of the microstructure of SLM Ti-6Al-4V under different conditions were carried out using a Nikon Optiphot 100 optical microscope at various magnification from x5 to x50. A detailed study of the microstructural was performed using the following electron microscopes at various magnification from x1000 to x5000:

- JEOL 6060LV SEM
- JEOL 7100F FEG-SEM

The microstructure, grain morphology and size was determined using secondary and backscatter electron imaging.

The microstructural constituents of the material under different conditions were carried out using X-ray Diffraction (XRD) via Bruker D8 ADVANCE with the DAVINCI XRD system. As a powerful non-destructive characterisation technique, XRD can provide various information about the tested crystalline materials, like structures, phases and preferred crystal orientations (Kohli, 2012). The diffraction of the X-ray is caused by the elastic scattering of the X-ray photons in a crystal lattice, as shown in Figure 3.15 (Chatterjee, 2001). Such diffraction can be used to determine the lattice spacing via Bragg's Law, as shown in Equation 3.1 (Chatterjee, 2001).

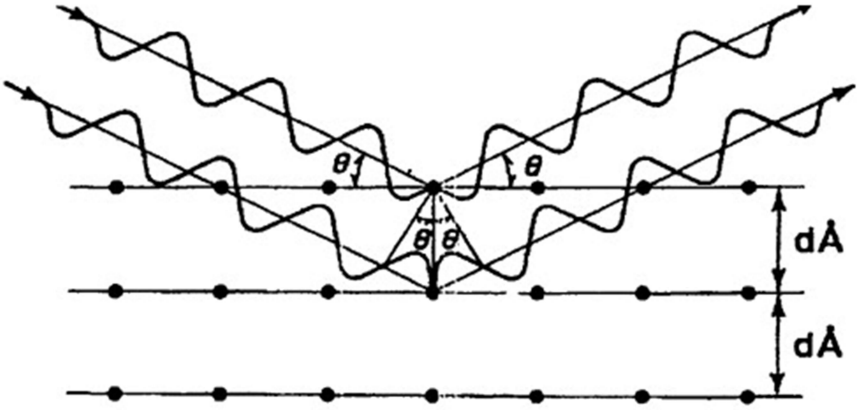


Figure 3.15. Schematic showing the diffraction of X-ray in a crystal lattice(Chatterjee, 2001)

$$n\lambda = 2d\ \sin\theta \qquad \text{Equation 3-1}$$

Where n is an integer called the order of reflection, λ is the wavelength of x-rays, d is the spacing between the crystal planes of the given specimen and θ is the angle between the incident beam and the normal to the reflecting lattice plane, as indicated in Figure 3.15. By measuring the angle θ, the interplanar spacing d of every single crystallographic phase can be determined (Misture and Snyder, 2001).

During the XRD scan, the full diffraction patterns of the tested specimen were recorded. These data were then compared with the standard line patterns available for various compounds in the Powder Diffraction File (PDF) database.

3.4.3 Techniques for crystallographic texture analysis

3.4.3.1 Electron backscatter diffraction (EBSD) technique

Electron backscatter diffraction (EBSD) is an additional module to an SEM that has the ability of mapping the crystallographic orientation across a designated area in a polycrystalline polished sample (Rollett and Barmak, 2014).

Since it can give microstructural and crystallographic texture information at the same time, it is useful to the study of the microstructure of complex alloys like Ti-6Al-4V.

EBSD is based on the interaction of a high-energy beam with the crystal plane. When an electron beam is focused on a tilted specimen of 70°, the interaction leads to a scattering of the electrons in all possible directions. As the scattered electrons interact with crystallographic planes within the crystal lattice, those satisfying Bragg's law are coherently diffracted out of the sample along the crystal planes, as shown in Figure 3.16. When the scattered electrons collide with a phosphor screen placed close to the specimen (detector in Figure 3.16), a form of band patterns can be captured, as shown in Figure 3.17. Such a pattern is also known as an EBSD pattern. Each band in the pattern, known as Kikuchi band, has a luminance that depends on the intensity of the diffraction (Adams et al., 2013).

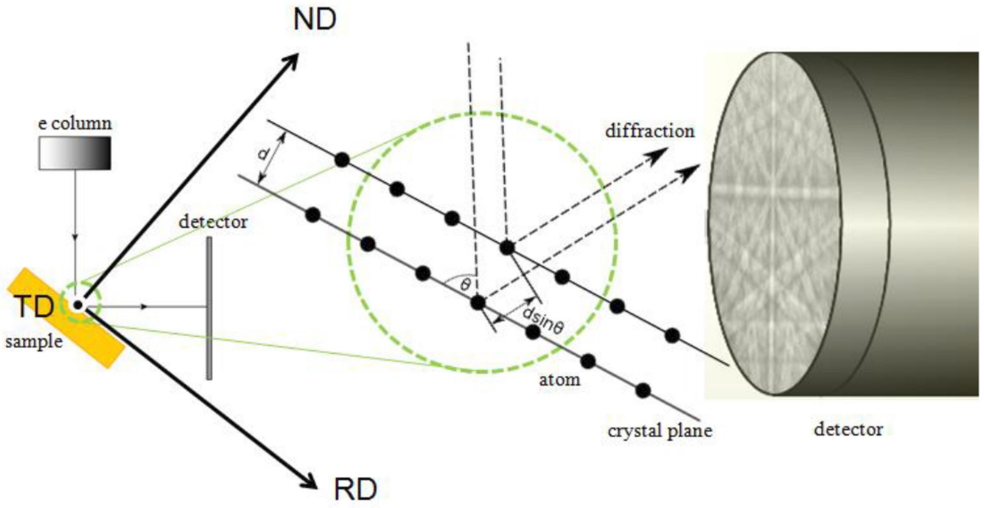


Figure 3.16. Schematic of the generation of the EBSD signal (EDAX,2014)

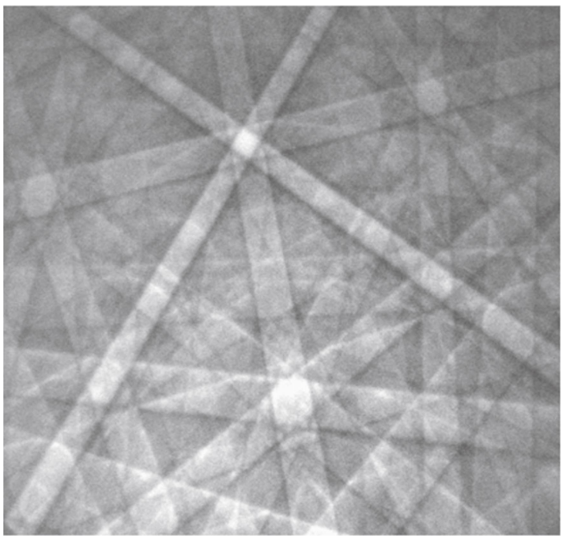


Figure 3.17. Example of EBSD pattern, obtained from single-crystal silicon (Adams et al., 2013)

Two types of information can be deduced from the EBSD pattern. Intersections of the Kikuchi bands can be used to determine the crystal structure of the grain that has been scanned. The width of the Kikuchi bands can be used to deduce the interplanar spacing of the grain structure. Therefore, the EBSD pattern can provide all the angular information needed to calculate the orientation of the investigated grain. It should be noted that the calculated orientation is related to a fixed coordinate reference system. Usually, a sample coordinate system (ND, RD, TD) as indicated in Figure 3.16 is used. Effective interpretation of the EBSD pattern hence allows the identification of the phase in the material and the orientation of individual grains with respect to such coordinate system.

In this study, the EBSD results are represented in two ways. The crystallographic texture across an area are presented in inverse pole figure (IPF) orientation maps, and the orientation of individual grains will be presented in discrete pole figures (PF).

The IPF orientation maps are established based on the idea that each crystal orientation relative to the user-defined reference frame is represented by a specific colour. Each measured crystal orientation is reduced to a point on a reference inverse pole figure (known as the unit triangle). A unique colour is

then assigned to each point in the unit triangle. Therefore, different colours are linked to different orientations. By matching the colour of the grain in orientation map with the colour in the unit triangle, the orientation of the grain therefore can be determined. An example is shown in Figure 3.18.

In this study, all the calculated orientations are fixed to the sample reference frame (ND, RD, TD), and all the IPF unit triangle are plotted along RD (known as Z-IPF), as the RD of the sample reference frame is parallel to the building direction of the SLM Ti-6Al-4V (Z direction of the original sample frame). The location of the examined section (frontal plane) related to the original sample frame is shown in Figure 3.19 (a), while the correlation relationship between the sample reference frame (ND, RD, TD) of the EBSD measurement and the original sample frame is shown in Figure 3.19 (b).

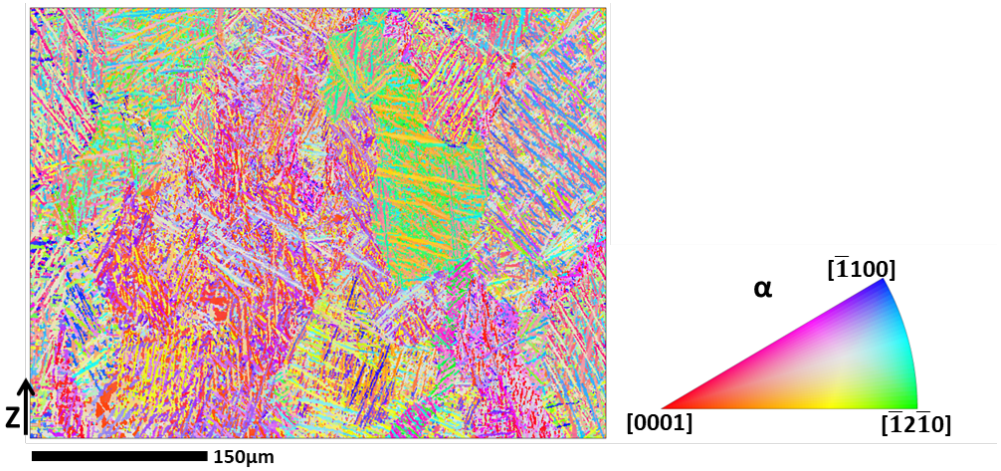


Figure 3.18. Example of Z-IPF map of SLM Ti-6Al-4V and corresponding colour scheme unit triangle. In this map, α grains with [0001] plane normal parallel to RD/building direction are shown in red.

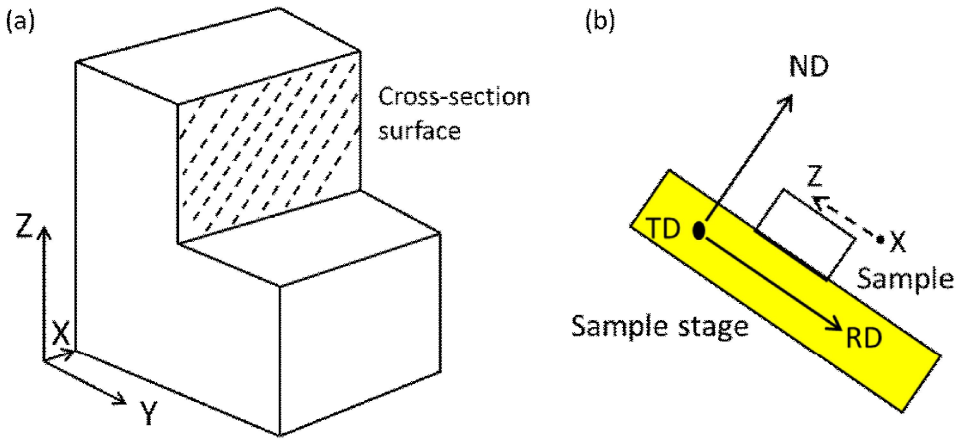


Figure 3.19. (a) Schematic showing the location of the examined section related to the original sample frame. (b) Schematic showing the correlation relationship between the sample reference frame of the EBSD measurement (ND, RD, TD) and the original sample frame.

The discrete pole figure can be used to interoperate the orientation of individual grains. In the discrete pole figure, the orientations are represented in stereograms. The plots of the stereogram are formed by projecting each plane of the investigated crystal cell onto a unit sphere, as shown in Figure 3.20. Due to the specific orientation of the crystal cell in the unit sphere, the projected points have their unique positions on the southern hemisphere of the unit sphere. Therefore, by reading the intersections with the equatorial plane, a specific orientation of the investigated crystal cell can be determined.

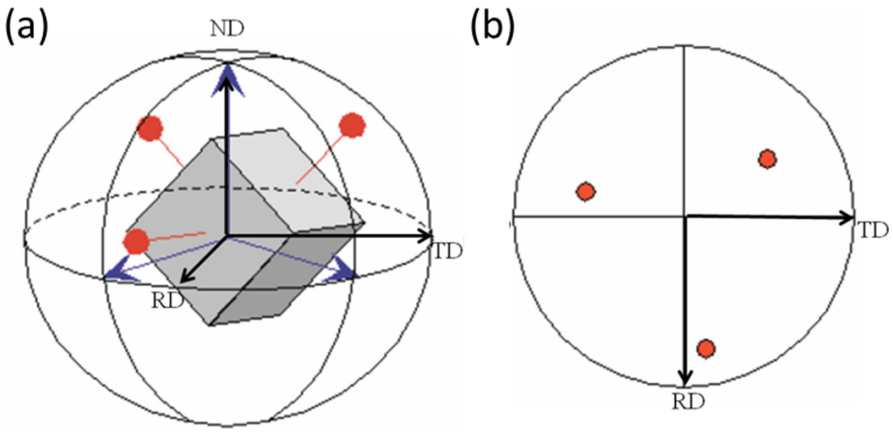


Figure 3.20. (a) projection of the planes of the crystal cell, (b) corresponding discrete pole figure (EDAX, 2014)

3.4.3.2 SEM systems involved in this research to obtain the EBSD data

Two different SEMs were used in this research to obtain the EBSD data at room temperature:

- JEOL 7100F FEG-SEM
- Helios G4 PFIB UXe DualBeam Microscopes

Prior to the EBSD scan, the investigated specimens were titled to 70° to maximise the intensity of backscattered electrons. Step sizes varying from 0.3µm to 1.5 µm were used in this research based on the size of the investigated area.

In order to track the microstructure evolution, in-situ high-temperature EBSD scans were conducted in this research using JEOL 7100F FEG-SEM. Polished thin plates were prepared to with dimensions approx. 3mm * 3mm * 1mm. The specimens were then mounted on a Gatan Murano in-situ heating stages using high-temperature carbon paste. This heating stage allowed for controlled and progressive heating of the specimens (up to 980 °C) with the simultaneous SEM imaging and EBSD capabilities. In this study, a heating rate of 0.5°C/s was used during the in-situ high-temperature EBSD, and nanoindentation marks were plotted on the sample surface to help to locate the interested area. The SEM was vacuumed during the study to avoid any oxidation. The results obtained from high-temperature EBSD will be reported and discussed in Chapter 7.

The collected data from EBSD scan was analysed using HKL-Channel 5™, OIM and the MATLAB toolbox MTex.

3.4.3.3 Reconstruction of the prior-β phase

Most of the crystallographic texture was obtained at room temperature with the limited amount of β phase retained in the structure. In order to study the texture of prior-β grain, where needed, the high-temperature β-phase was reconstructed from the room temperature α-phase via the Burger Orientation Relationship (BOR).

In this research, an in-house Matlab script was developed and used to perform the automatic reconstruction of the β phase. The detail of the script is introduced in Appendix A, and the validation of the script is presented in Appendix B.

In practice, the reconstruction was carried out computing the common β grain for every 4 neighbouring α grains in the EBSD dataset. This method was based on the theory described in the relevant literature (Humbert et al., 1995, Humbert et al., 1994). The orientation of each α grain presented in the measured dataset was initially imported into Matlab using a set of Euler angles ϕ1, Φ, ϕ2. Due to the crystal symmetry, rotational symmetry elements were applied to the original orientation, so that the independent orientations could be distinguished. In the script, the rotational symmetry elements of the α and β phases (12 and 24, respectively) were described using the equations established in previous related research (Humbert et al., 1995). The BOR was described by a Bunge's rotation matrix D (135°, 90°, 325°). By applying the rotation matrix on the independent orientations, for each input α orientation, every possible BOR related β orientation could be calculated. If 4 neighbouring α grains have a common β orientation solution (misorientation smaller than 10°), then such orientation would be recognised as the orientation of parent β.

CHAPTER 4

4. Tensile properties of SLM Ti-6Al-4V under the different investigated conditions

In this chapter, the tensile properties of SLM Ti-6Al-4V under different conditions are studied. The tensile properties of as-built samples are first tested, which establishes a baseline on the starting material: the related results are presented in section 4.1. Conventional furnace heat treatments were then conducted following published standards: the results are reported in section 4.2. The tensile properties of induction heat treated samples are then reported in section 4.3, as well as the heating and cooling profile recorded during these heat treatments. The heating and cooling rate of the different induction heating processes are compared in section 4.5, followed by a full comparison of tensile properties between different conditions. Any deviation to the conventional baseline in tensile properties can be considered purely related to the induction heat treatment, as the starting material was the same.

4.1 Tensile properties of SLM Ti-6Al-4V in the as-built condition

For three tested as-built condition samples, the tensile stress-strain curves are shown in Figure 4.1 and the obtained results are summarised in Table 4.1. All three samples started to yield at elongation of about 1.1%, and failed at elongation around 5% after achieving a certain level of necking in the gauge length of the specimens. According to ASTM B348, the minimum requirements for Ti-6Al-4V products should be 828 MPa in yield strength, 895

MPa in tensile strength and 10% in elongation (ASTM, 2013). The as-built samples present an insufficient ductility with surplus strength, which corresponds with other researches demonstrated in the literature (Zhang et al., 2018, Vilaro et al., 2011, Guzanová et al., 2017, Ding et al., 2017b). The relatively low ductility is clear evidence, which emphasises the necessity of post heat-treatment.

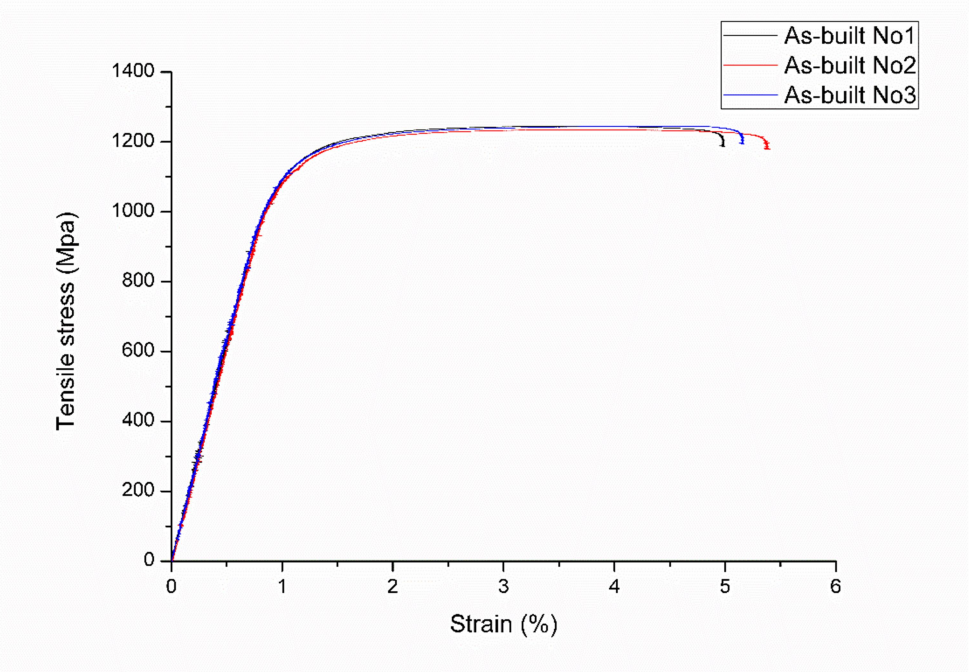


Figure 4.1 Stress-strain curve of tested as-built SLM Ti-6Al-4V samples

Table 4.1 Summary of the tensile test results of tested as-built SLM Ti-6Al-4V samples

Specimen	Young's modulus E (GPa)	UTS (MPa)	Yield stress σy (MPa)	Elongation ε (%)
No1	123.78	1244.78	1129.54	4.99
No2	123.55	1234.88	1114.95	5.41
No3	125.82	1245.02	1124.27	5.17
Average	124.38	1241.56	1122.92	5.19
Standard deviation	1.02	4.72	6.03	0.17

4.2 Tensile properties of SLM Ti-6Al-4V after conventional heat treatments

The procedure of conventional furnace heat treatment is established by following published standards, i.e. annealing at 925°C for 2 hours then ageing at 700°C for 4 hours.

For all five furnace heat treated samples, the tensile stress-strain curves are shown in Figure 4.2, and the obtained results are summarised in Table 4.2. The test results suggest that after the established conventional furnace heat treatment, the tensile properties of SLM Ti-6Al-4V achieve the requirement of ASTM B348 (ASTM, 2013).

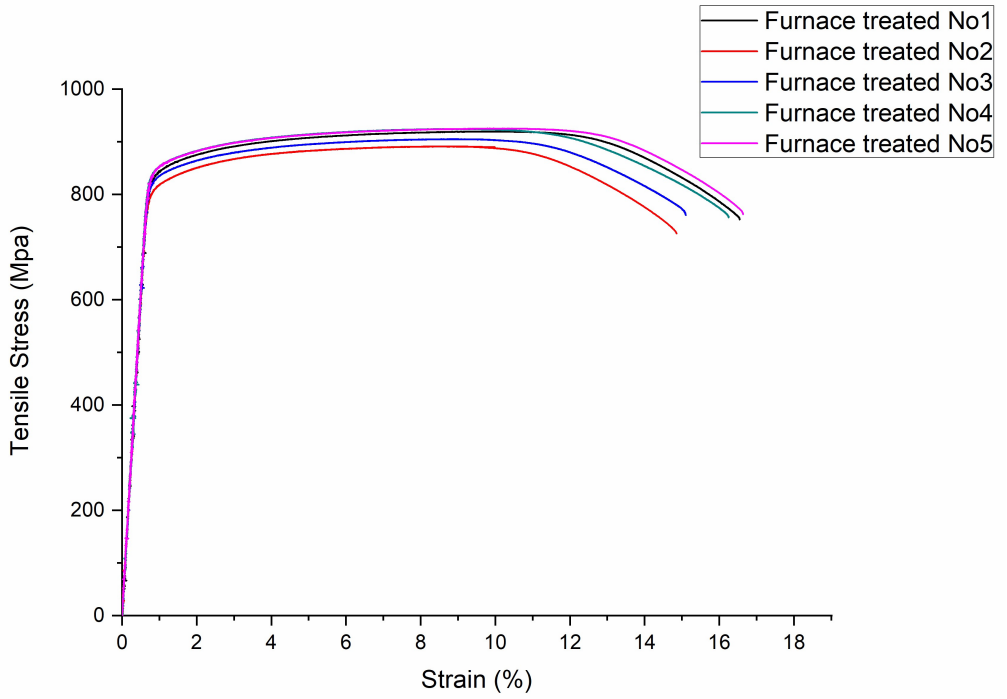


Figure 4.2 Stress-strain curve of tested furnace heat treated SLM Ti-6Al-4V samples

Table 4.2 Summary of the tensile test results of tested furnace heat treated SLM Ti-6Al-4V samples

Specimen	Young's modulus E (GPa)	UTS (MPa)	Yield stress σy (MPa)	Elongation ε (%)
No1	119.07	919.62	837.72	16.55
No2	120.4	891.36	810.11	14.87
No3	121.71	905.2	827.42	15.1
No4	123.31	924.45	846.07	16.26
No5	122.05	925.3	844.8	16.67
Average	121.31	913.19	833.22	15.89
Standard deviation	1.45	13.08	13.32	0.75

4.3 Tensile properties of SLM Ti-6Al-4V after induction heat treatment

Four different induction heat treatments were applied in this study. In this section, the heating and cooling profiles recorded during the specified induction heating processes are reported, as well as the tensile properties achieved after the corresponding heat treatments.

4.3.1 Induction heat treatment above 980°C

This section reports details on the heating and cooling profiles during the specified induction heat treatment and the tensile properties of the specimens that were subjected to this heat treatment.

4.3.1.1 Heating and cooling profile recorded during the specified induction heating process

The heating and cooling profile experienced by the specimens during the specified induction heating are presented in Figure 4.3. Figure 4.3 (a) to (e) shows the recorded temperature-time curves at different locations along the

gauge length of specimen No1 to 5, respectively. The average temperature profile of different specimens are shown in Figure 4.3 (f). The curves overlap with each other in all six figures suggesting a good consistency across the induction heating experiments.

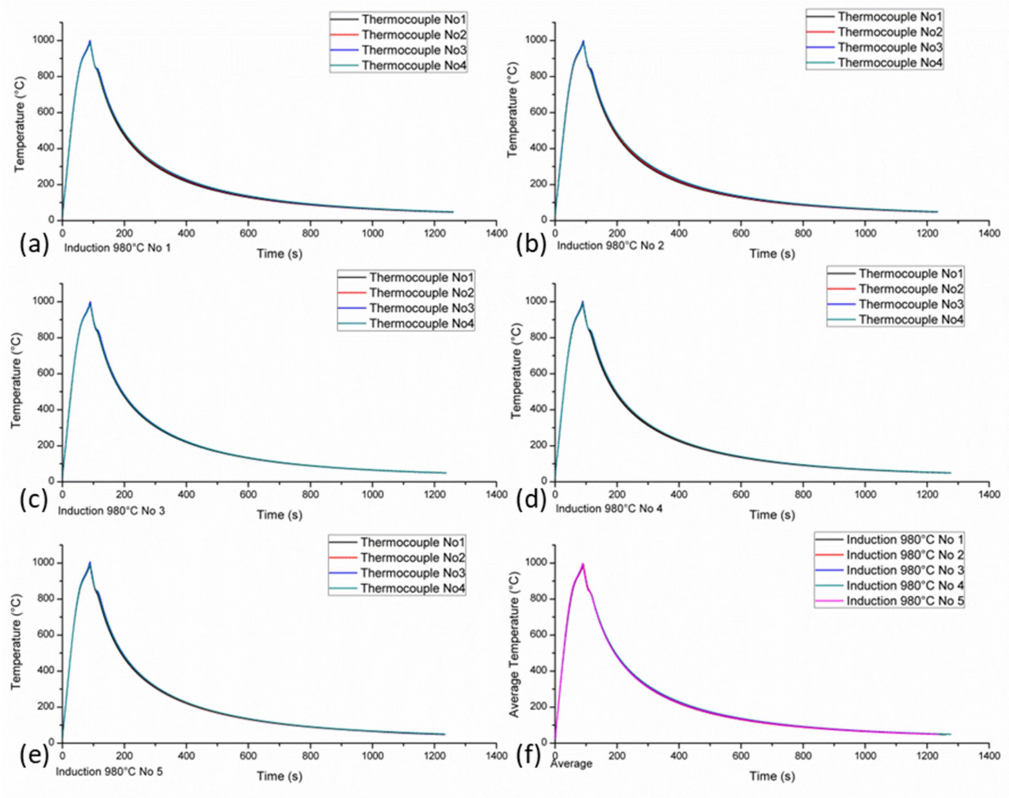


Figure 4.3 Heating and cooling profiles of induction heat treatment above 980°C: (a) to (e), recorded temperature-time curve of specimen No 1 to 5, respectively; (f) averaged temperature profile of different specimens.

For the specified induction heat treatment, the peak temperature achieved, heating rate and cooling rate are the three key indicators. Detailed values of such indicators in each heating process are summarised in Table 4.3. The recorded peak temperature ranges from 986°C to 1007°C, the temperature difference of which is 21°C. This temperature difference is within the acceptable range for the heat treatment of Ti-6Al-4V parts (36°C), as suggested in AMS2801B (SAE, 2014). For treated samples, the average heating rate is 10.29 ± 0.14 °C/s with an average cooling rate of 3.99 ± 0.06°C/s. The standard deviation of heating rate and cooling rate are both

smaller than 1.5% from the mean value, which indicates the conducted heat treatment is a consistent process.

Table 4.3 Summary of recorded peak temperature, heating rate and cooling rate regard to induction heat treatment above 980°C

	Peak Temperature (°C)					Heating rate (°C/s)	Cooling rate (°C/s)
Specimen	Thermocouple No1	Thermocouple No2	Thermocouple No3	Thermocouple No4	Average		(from peak to 400°C)
No1	991.13	997.94	1000.87	990.29	995.06	10.38	3.97
No2	989.59	992.49	998.85	986.77	991.93	10.04	4.06
No3	991.46	999.47	997.31	985.33	993.39	10.24	4.02
No4	989.98	1001.89	1002.53	995.54	997.49	10.35	3.89
No5	989.95	1002.42	1006.87	995.82	998.77	10.42	4.02

4.3.1.2 Tensile properties of SLM Ti-6Al-4V that were subjected to the specified heat treatment

The tensile stress-strain curves are shown in Figure 4.4, and the obtained results are summarised in Table 4.4. The test results suggest with a maximum treatment temperature extremely close to β transus, under limited soaking time and after ageing treatment, the tensile properties of treated SLM Ti-6Al-4V can also meet the requirement of ASTM B348 (ASTM, 2013).

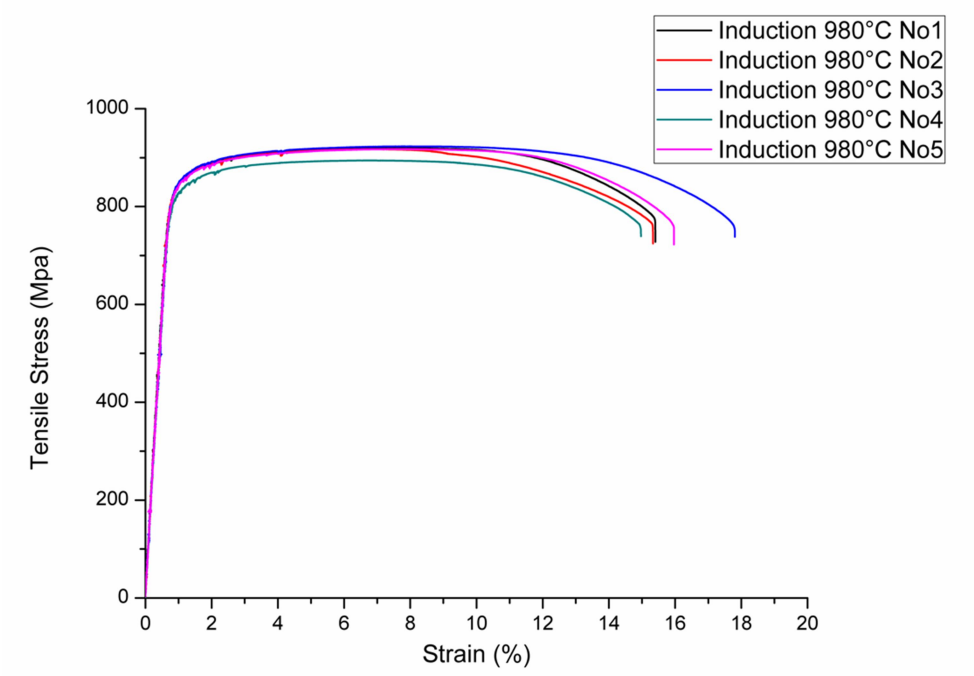


Figure 4.4 Stress-strain curve of SLM Ti-6Al-4V samples induction heat treated above 980°C followed by 700°C ageing for 4 hours.

Table 4.4 Summary of the tensile test results of SLM Ti-6Al-4V samples induction heat treated above 980°C followed by 700°C ageing for 4 hours

Specimen	Young's modulus E (GPa)	UTS (MPa)	Yield stress σy (MPa)	Elongation ε (%)
No1	119.41	919.63	834.95	15.42
No2	117.47	917.30	833.81	15.10
No3	114.33	923.27	841.32	17.82
No4	117.91	894.41	812.12	14.98
No5	117.99	917.59	831.84	15.98
Average	117.02	940.19	830.81	15.86
Standard deviation	1.62	10.24	9.87	1.04

4.3.2 Induction heat treatment above 1005°C

This section reports details on the heating and cooling profiles during the specified induction heat treatment and the tensile properties of the specimens that were subjected to this heat treatment.

4.3.2.1 Heating and cooling profile recorded during the specified induction heating process

Heating and cooling profile recorded during the specified induction heating are presented in Figure 4.5. Figure 4.5 (a) to (e) are the recorded temperature-time curves at different locations along the gauge length of specimen No1 to 5, respectively. The averaged temperature profile of different specimens are shown in Figure 4.5 (f).

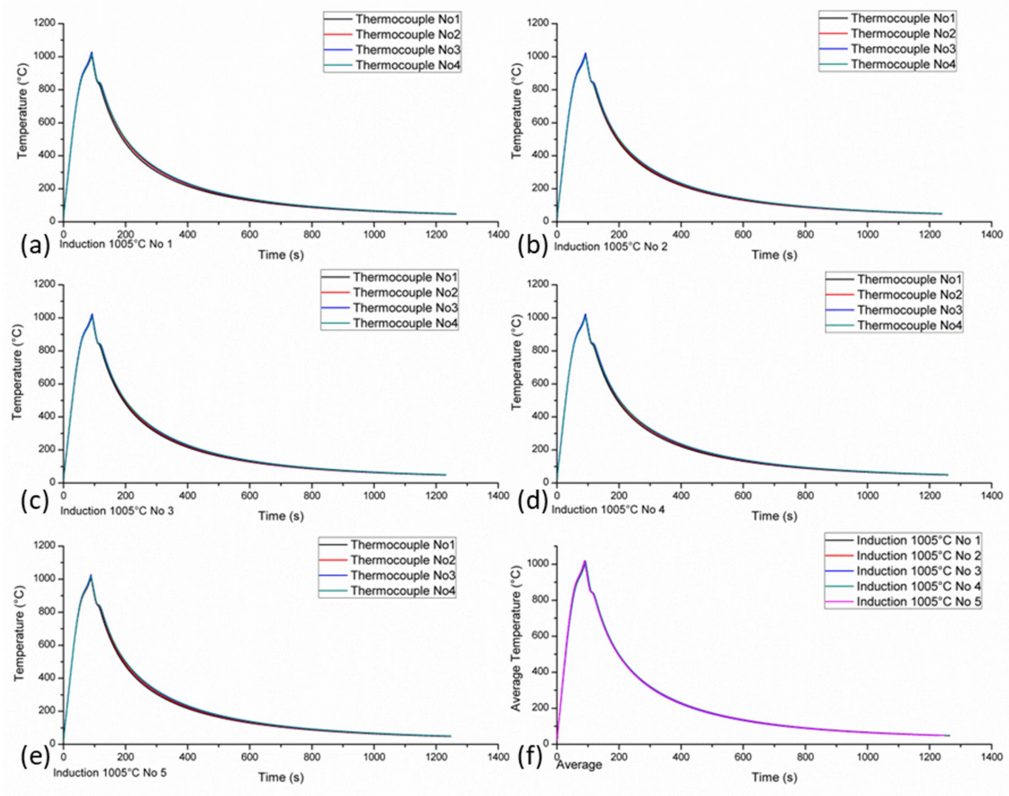


Figure 4.5 Heating and cooling profiles of induction heat treatment above 1005°C: (a) to (e), recorded temperature-time curve of specimen No 1 to 5, respectively; (f) averaged temperature profile of different specimens.

Table 4.5 Summary of recorded peak temperature, heating rate and cooling rate regard to induction heat treatment above 1005°C

	Peak Temperature (°C)					Heating rate (°C/s)	Cooling rate (°C/s)
Specimen	Thermocouple No1	Thermocouple No2	Thermocouple No3	Thermocouple No4	Average		(from peak to 400°C)
No1	1009.35	1024.97	1027.90	1015.76	1019.50	10.30	4.06
No2	1010.00	1012.58	1023.32	1007.34	1013.31	10.34	4.03
No3	1008.50	1016.58	1024.06	1009.73	1014.72	10.41	4.10
No4	1007.96	1018.21	1023.78	1009.18	1014.78	10.35	3.99
No5	1011.33	1017.90	1026.94	1019.86	1019.01	10.73	4.18

The peak temperature recorded, heating rate and the cooling rate for this group of treatment are summarised in Table 4.5. The recorded peak temperature ranges from 1007°C to 1028°C, the temperature difference of which is 21°C, within the acceptable range (36°C). For the treated samples, the average heating rate is 10.43 ± 0.16 °C/s with an average cooling rate of 4.07 ± 0.06°C/s. This group of heat treatment also presents good consistency.

4.3.2.2 Tensile properties of SLM Ti-6Al-4V that were subjected to the specified heat treatment

The tensile stress-strain curves are shown in Figure 4.6 and the obtained results are summarised in Table 4.6. The test results suggest for SLM Ti-6Al-4V, which were short time annealed at β transus temperature and then ageing treated, their tensile properties can also meet the requirement of ASTM B348 (ASTM, 2013).

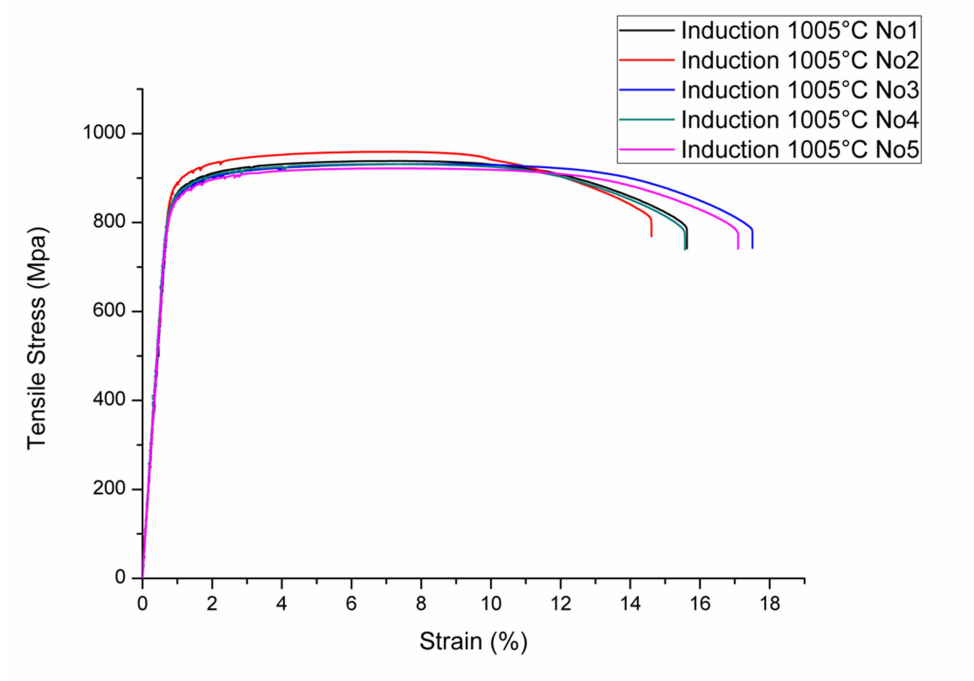


Figure 4.6 Stress-strain curve of SLM Ti-6Al-4V samples induction heat treated above 1005°C followed by 700°C ageing for 4 hours.

Table 4.6 Summary of the tensile test results of SLM Ti-6Al-4V samples induction heat treated above 1005°C followed by 700°C ageing for 4 hours

Specimen	Young's modulus E (GPa)	UTS (MPa)	Yield stress σy (MPa)	Elongation ε (%)
No1	116.73	938.68	860.95	15.54
No2	117.49	959.20	882.96	14.52
No3	116.21	931.67	849.74	17.42
No4	121.67	931.65	853.93	15.48
No5	118.74	922.13	843.12	17.01
Average	118.17	936.67	858.14	15.97
Standard deviation	1.95	12.44	13.70	1.07

4.3.3 Induction heat treatment above 1030°C

This section reports details on the heating and cooling profiles during the specified induction heat treatment and the tensile properties of the specimens that were subjected to this heat treatment.

4.3.3.1 Heating and cooling profile recorded during the specified induction heating process

Heating and cooling profiles recorded during induction heating are presented in Figure 4.7. Figure 4.7 (a) to (e) are the recorded temperature-time curves at different locations along the gauge length of specimen No1 to 5, respectively. Averaged temperature profiles of the different specimens are shown in Figure 4.7 (f). Peak temperature recorded, heating rate and cooling rate for this group of treatment are summarised in Table 4.7. The recorded peak temperature range from 1032°C to 1062°C, the temperature difference of which is 30°C, within the acceptable range suggested in section 3.2 (36°C). For treated samples, the average heating rate is 10.00 ± 0.21 °C/s with an average cooling rate of 4.22 ± 0.05 °C/s. This group of heat treatment also present good consistency.

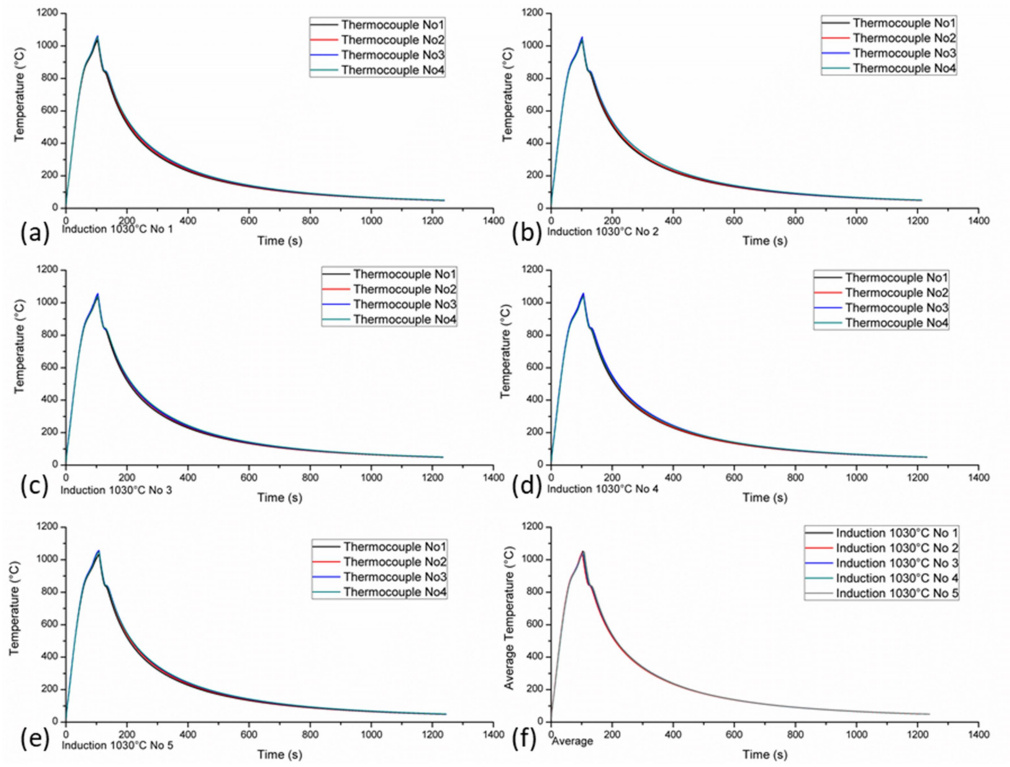


Figure 4.7 Heating and cooling profile of induction heat treatment above 1030°C: (a) to (e), recorded temperature-time curve of specimen No 1 to 5, respectively; (f) averaged temperature profile of different specimens.

Table 4.7 Summary of recorded peak temperature, heating rate and cooling rate regard to induction heat treatment above 1030°C

	Peak Temperature (°C)					Heating rate (°C/s)	Cooling rate (°C/s)
Specimen	Thermocouple No1	Thermocouple No2	Thermocouple No3	Thermocouple No4	Average		(from peak to 400°C)
No1	1037.53	1055.42	1061.49	1055.88	1052.58	10.12	4.18
No2	1032.05	1052.39	1055.61	1041.79	1045.46	10.30	4.19
No3	1033.42	1050.03	1056.63	1042.67	1045.69	10.01	4.18
No4	1041.08	1048.70	1058.56	1039.27	1046.90	9.92	4.23
No5	1032.81	1053.82	1057.29	1050.04	1048.49	9.66	4.31

4.3.3.2 Tensile properties of SLM Ti-6Al-4V that were subjected to the specified heat treatment

The tensile stress-strain curves are shown in Figure 4.8 and the obtained results are summarised in Table 4.8. The test results suggest that for SLM Ti-6Al-4V, which were short time annealed above β transus temperature and then ageing treated, their tensile properties can also meet the requirement of ASTM B348 (ASTM, 2013).

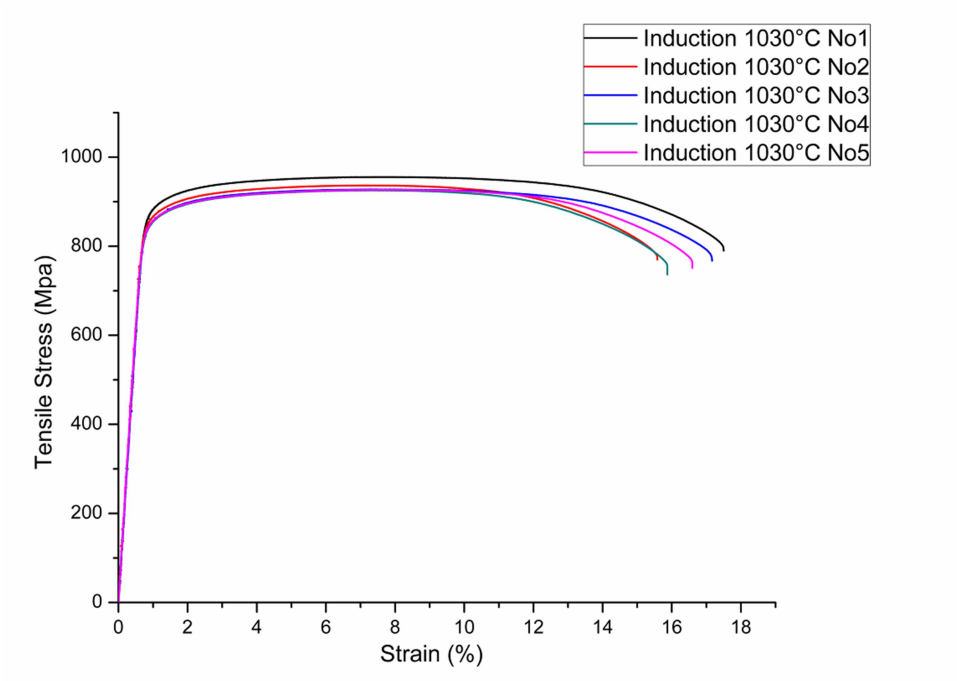


Figure 4.8 Stress-strain curve of SLM Ti-6Al-4V samples induction heat treated above 1030°C followed by 700°C ageing for 4 hours.

Table 4.8 Summary of the tensile test results of SLM Ti-6Al-4V samples induction heat treated above 1030°C followed by 700°C ageing for 4 hours

Specimen	Young's modulus E (GPa)	UTS (MPa)	Yield stress σy (MPa)	Elongation ε (%)
No1	121.34	955.73	873.47	17.53
No2	122.03	936.67	856.89	15.61
No3	120.42	927.65	847.22	17.19
No4	120.07	925.55	845.21	15.90
No5	122.05	926.68	846.03	16.62
Average	121.18	934.45	853.76	16.57
Standard deviation	0.81	11.34	10.71	0.73

4.3.4 Induction heat treatment above 1030°C without subsequent ageing

This section reports details on the heating and cooling profiles during the specified induction heat treatment and the tensile properties of the specimens that were subjected to this heat treatment.

4.3.4.1 Heating and cooling profile recorded during the specified induction heating process

Heating and cooling profile recorded during the specified induction heating are presented in Figure 4.9. Figure 4.9 (a) to (e) are the recorded temperature-time curves at different locations along the gauge length of specimen No1 to 5 respectively. Averaged temperature profiles of different specimens are shown in Figure 4.9 (f).

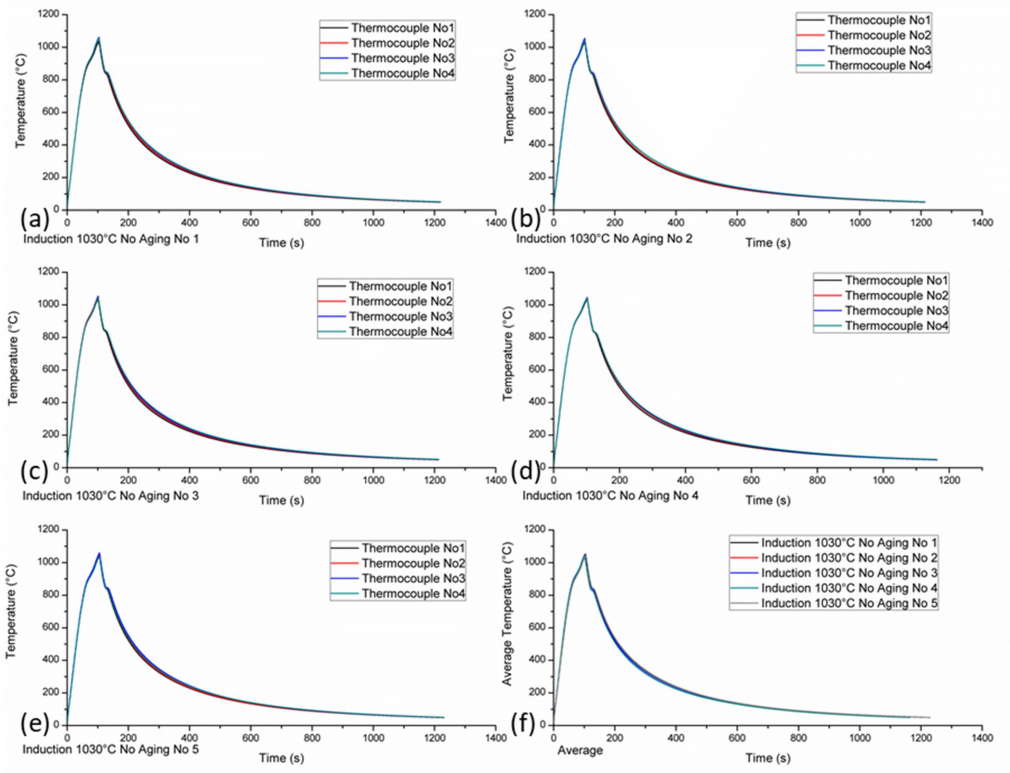


Figure 4.9 Temperature profiles of induction heat treatment above 1030°C without subsequent ageing: (a) to (e), recorded temperature-time curve of specimen No 1 to 5, respectively; (f) averaged temperature profile of different specimens.

The peak temperature recorded, heating rate and cooling rate for this group of treatment are summarised in Table 4.9. The recorded peak temperature ranges from 1031°C to 1062°C, the temperature difference of which is 31°C, which is within the acceptable range suggested in section 3.2 (36°C). For treated samples, the average heating rate is 10.20 ± 0.16 °C/s with an average cooling rate of 4.25 ± 0.08 °C/s. The last group of heat treatment still presents a good consistency.

Table 4.9 Summary of recorded peak temperature, heating rate and cooling rate regard to induction heat treatment above 1030°C without subsequent ageing

	Peak Temperature (°C)					Heating rate (°C/s)	Cooling rate (°C/s)
Specimen	Thermocouple No1	Thermocouple No2	Thermocouple No3	Thermocouple No4	Average		(from peak to 400°C)
No1	1036.95	1056.50	1061.47	1058.77	1053.42	10.18	4.19
No2	1031.19	1051.05	1054.66	1042.85	1044.94	10.29	4.19
No3	1037.72	1053.11	1050.66	1043.81	1046.32	10.40	4.22
No4	1036.67	1046.06	1044.69	1041.78	1042.30	10.22	4.41
No5	1041.76	1049.72	1060.34	1037.73	1047.39	9.93	4.22

4.3.4.2 Tensile properties of SLM Ti-6Al-4V that were subjected to the specified heat treatment

The tensile stress-strain curves are shown in Figure 4.10 and the obtained results are summarised in Table 4.10. The test results suggest with limited soaking time beyond the β transus, the tensile properties of treated SLM Ti-6Al-4V can meet the requirement of ASTM B348 even without proper ageing (ASTM, 2013).

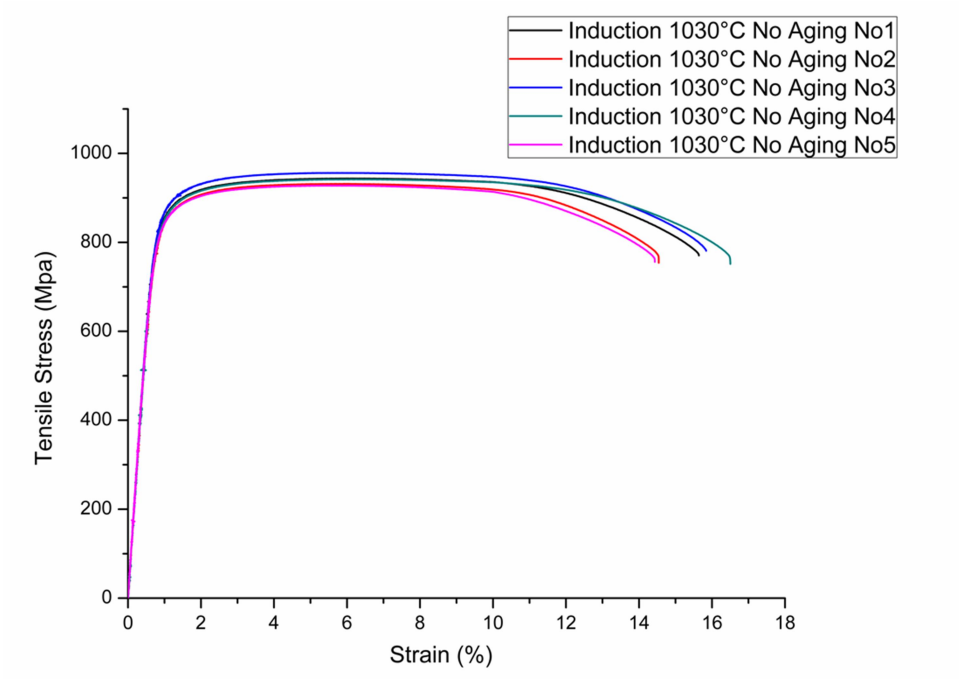


Figure 4.10 Stress-strain curve of SLM Ti-6Al-4V samples induction heat treated above 1030°C, without subsequent ageing

Table 4.10 Summary of the tensile test results of SLM Ti-6Al-4V samples induction heat treated above 1030°C, without subsequent ageing

Specimen	Young's modulus E (GPa)	UTS (MPa)	Yield stress σy (MPa)	Elongation ε (%)
No1	118.83	943.67	834.66	15.67
No2	116.54	931.64	823.41	14.57
No3	120.26	956.24	847.17	15.87
No4	117.83	941.78	831.15	16.53
No5	118.49	927.64	821.78	14.46
Average	118.39	940.19	831.63	15.42
Standard deviation	1.22	10.03	9.12	0.79

4.4 Comparison and discussion of the induction heating processes and the corresponding tensile properties of SLM Ti-6Al-4V

4.4.1 Consistency of the induction heating processes

In the presented study, four groups of specimens have been induction heat treated via the bespoke induction heating system. Consistency between each heating process is the key to achieving the intended experimental purpose. The results reported in section 4.3 evidence such consistency within each tested group. In addition, the average heating rate (room temperature to peak temperature) and average cooling rate (peak temperature to 400°C) of each group are compared in Table 4.11.

Two groups of samples were induction heat treated above 1030°, the group that was experienced a subsequently ageing treatment (reported in section 4.3.3) will be referred to as group one, the other group that has not experienced any ageing treatment (reported in section 4.3.4) will be referred to as group two.

Table 4.11 Summary of the average heating rate (room temperature to peak temperature) and average cooling rate (peak temperature to 400°C) of each induction heat treated group

Test group	Heating rate (°C/s)	Cooling rate (°C/s)
Induction heating above 980°	10.29 ± 0.14	3.99 ± 0.06
Induction heating above 1005°	10.43 ± 0.16	4.07 ± 0.06
Induction heating above 1030° (group one)	10.00 ± 0.21	4.22 ± 0.05
Induction heating above 1030° (group two)	10.20 ± 0.16	4.25 ± 0.08

Table 4.11 shows each test group sharing a steady heating rate around 10.2°C/s and a similar cooling rate. The cooling rate of high target

temperature group is insignificantly higher than the low target temperature group (i.e. 4.25°C/s vs 3.99°C/s), since heat exchange with ambient atmosphere for the former group is slightly more intense than the last one at the beginning of cooling due to a higher starting temperature, and the cooling rates reported in this research only counts the front part of the cooling. Ahmed and Rack (1998) suggest that non-equilibrium transformation of high temperature β only happens at a cooling rate higher than 20°C/s, which means insignificant difference around 4°C/s in the cooling rate will have limited influence on the final microstructure and tensile properties.

Thus, the recorded temperature indicates that the used induction furnace is a reliable apparatus to fulfil the task. Any difference in the final microstructure and tensile properties for different induction treated groups will directly be linked to the set target temperatures.

4.4.2 Tensile properties of SLM Ti-6Al-4V that were subjected to different heat treatments

All the tested stress-strain curves are summarised in Figure 4.11. A summary of average tensile properties of each condition tested in this research is present in Table 4.12, as well as the duration of each treatment. In addition, a full comparison displayed in the histogram is shown in Figure 4.12.

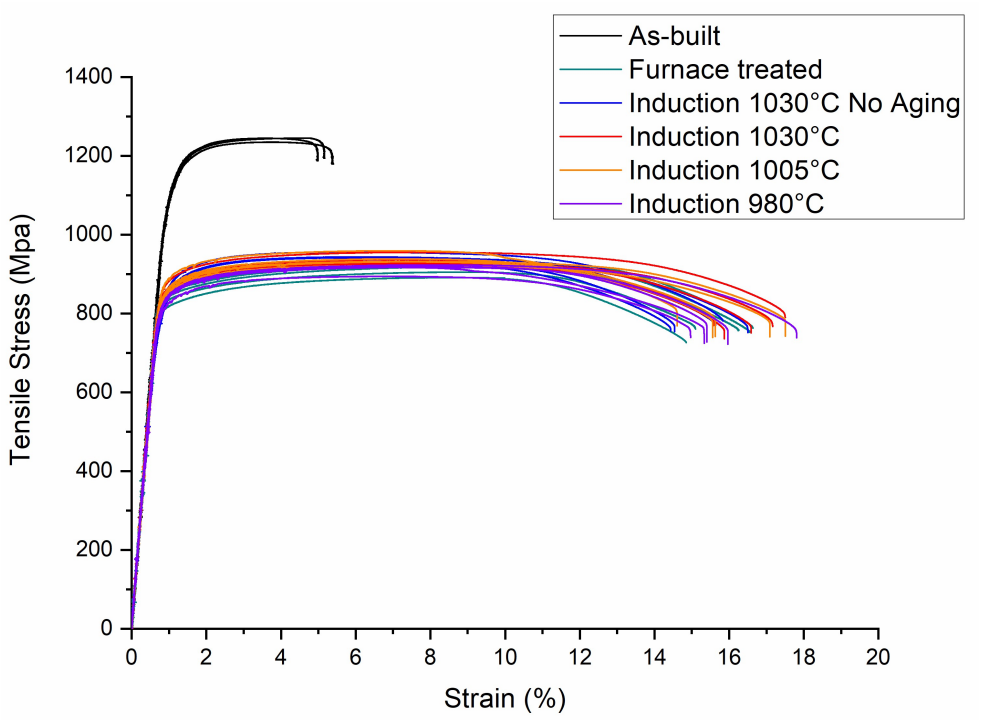


Figure 4.11 Summary of the stress-strain curves of SLM Ti-6Al-4V samples under different heat treatments

Table 4.12 Summary of average tensile properties and duration of treatment for each tested condition

	Young's modulus E (GPa)	UTS (MPa)	Yield stress σy (MPa)	Elongation ε (%)	Treatment duration (h)
As-built	124.38 ± 1.02	1241.56 ± 4.72	1122.92 ± 6.03	5.19 ± 0.17	/
Furnace treated	121.31 ± 1.45	913.19 ± 13.08	833.22 ± 13.32	15.89 ± 0.75	12
Induction 980°C	117.02 ± 1.62	914.44 ± 10.24	830.81 ± 9.87	15.86 ± 1.04	7.33
Induction 1005°C	118.17 ± 1.95	936.67 ± 12.44	858.14 ± 13.70	15.97 ± 1.07	7.33
Induction 1030°C	121.18 ± 0.81	934.45 ± 11.34	853.76 ± 10.71	16.57 ± 0.73	7.33
Induction 1030°C No aging	118.39 ± 1.22	940.19 ± 10.03	831.63 ± 9.12	15.42 ± 0.79	0.33

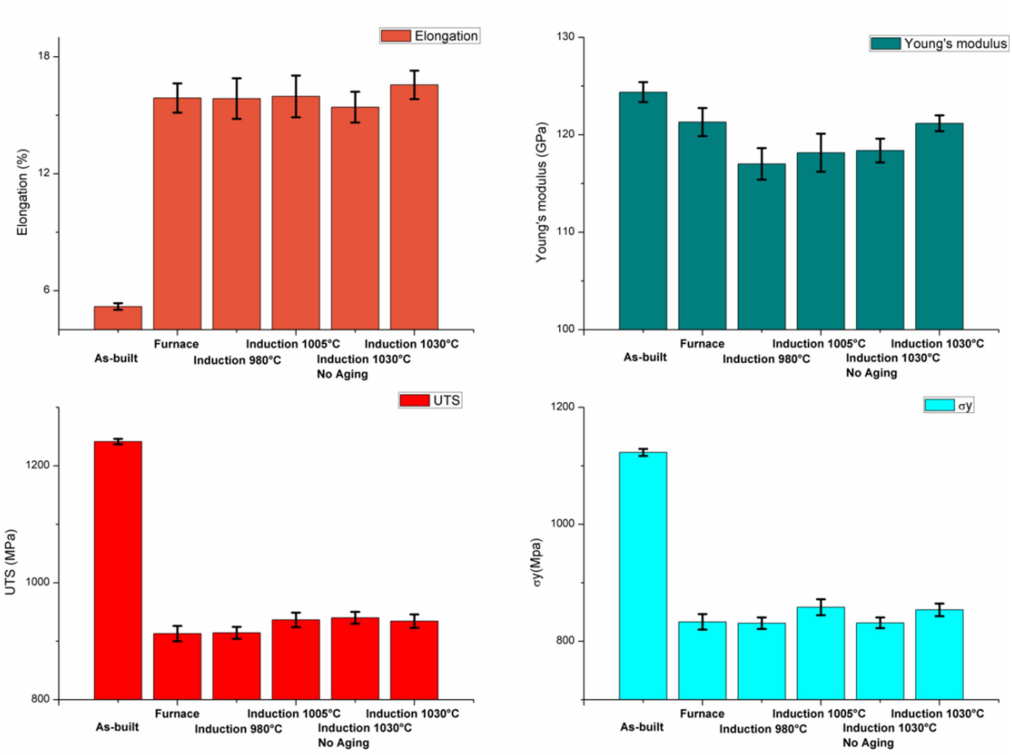


Figure 4.12 Comparison of average tensile properties for each of the conditions tested.

The test results further strengthened the universal understanding that for SLM Ti-6Al-4V, post-heat treatments provide a trade-off between the strength and ductility. By sacrificing certain strengths, the original low ductility existed in the as-built condition can be improved (Qian et al., 2016, AmirMahyar et al., 2017, Fan and Feng, 2018).

SLM Ti-6Al-4V specimens after all five post-heat treatments can achieve tensile properties that meet the requirement of ASTM B348 (ASTM, 2013). None of the tensile properties obtained after induction heat treatment is worse than that which was obtained after conventional furnace treatment. Due to the advantage of volumetric heating, both of the four induction groups enjoy much shorter process duration compared to furnace group. In extreme cases, without the subsequent ageing, it only takes 20 minutes to complete the specified induction heat treatment, while conventional treatment needs 12 hours to complete the whole process.

For samples that were first treated with induction heating to a temperature of about 980 and then experienced ageing treatment, their yield stress, UTS, and elongation are similar to the properties of the conventional heat treated ones. Differences in all three values between the two groups are smaller than 0.5%, which can be considered as negligible.

For samples that were first treated with induction heating to a temperature near or above the β transus (1005°C and 1030°C respectively) and then experienced ageing treatment, they possess an elongation similar to the conventional heat treated ones, but with higher yield stress and UTS. The difference between the elongation of the induction heat treated ones and the elongation of the conventional heat treated ones is within the range of calculated standard deviations. However, the differences in yield stress and UTS are beyond this range.

Compared to the conventional heat treated one, the improvements after induction heat treatment are not significant, which is 2% in UTS and 3% in yield stress. However, it clearly demonstrated that SLM Ti-6Al-4V after short time beta annealing could achieve strength at least equivalent to conventional sub-transus heat treatment, while conventional beta annealing normally leads to an unacceptable reduction in strength (Vilaro et al., 2011, Vrancken et al., 2012, Popovich et al., 2015).

For samples that were both treated with induction heating to a temperature about 1030°C, those experienced subsequent ageing appear to have a higher yield strength compared to the other one, which indicates the influence of age hardening. Ageing is a process that allows the alloying element to diffuse through the microstructure to achieve a more stable distribution. It can also promote the formation of intermetallic precipitation (Totten, 2006). Possible mechanisms for age hardening of Ti-6Al-4V are related to the α phase coarsening and the precipitation of nanometre-sized α_2 (Ti_3Al) particles inside the α phase (Lee et al., 2004, Carreon et al., 2017).

4.5 Summary

In this chapter, the tensile properties of SLM Ti-6Al-4V post-processed by different heat treatments were examined. The as-built samples possess a strong strength with low ductility, which cannot meet the requirements requested by related standards. This corresponds to the similar findings reported in the literature (Vilaro et al., 2011, Vrancken et al., 2012, Liu and Shin, 2019). For these reasons, post-process heat treatments are necessary for SLM Ti-6Al-4V components intended for industrial application.

It is shown that the induction heating apparatus used in this research can provide stable and consistent heating at an average heating rate about 10°C/s for target heating temperature around 1000°C. Benefit from the fast heating and the excluding of soaking at the target temperature, induction heat treated samples experienced a reduced process duration comparing to conventional heat treated samples.

It has been found all heat treated samples obtain tensile properties, which meet the requirement of related standards (ASTM, 2013, ASTM, 2014b). Samples treated with induction heating to a temperature below the β transus possess the similar tensile properties as samples treated with conventional heating, while the samples experienced short time beta annealing present an improved strength with a similar elongation compared to the conventional heat treated ones. The results suggest, on the tested size of SLM Ti-6Al-4V samples (60mm length and 9mm diameter), short time beta annealing can provide equivalent or improved tensile properties compared to conventional heat treated samples with reduced process duration.

The effect of age hardening is also shown in this research. The literature suggest the mechanisms are results of α phase coarsening and precipitation of intermetallic nanometre-sized α_2 (Ti_3Al) (Lee et al., 2004, Carreon et al., 2017).

The short time beta annealed samples provide completely different tensile properties compared to conventional beta annealed properties presented in the literature (Vilaro et al., 2011, Vrancken et al., 2012), which indicates a different morphology in the obtained microstructure. This will be discussed in Chapter 5.

CHAPTER 5

5. Influence of heat treatments on the microstructure of SLM Ti-6Al-4V

The mechanical properties of the material are closely related to its microstructure. According to section 2.3.3, SLM Ti-6Al-4V samples that are heat treated conventionally above β transus will obtain a significantly reduced strength compared to those treated below β transus. The samples treated with induction heating in chapter 4 present a different situation to its conventional heat treated counterparts (same target temperature above β transus), which suggests the existence of some microstructural differences. The microstructure of all heat treated SLM Ti-6Al-4V reported in chapter 4 will be characterised and analysed in this chapter, as well as their initial microstructure (untreated as-built). Interpretation of how microstructure influences the corresponding mechanical properties will also be discussed.

Microstructural constituents, identified by X-Ray Diffraction (XRD), subjected to different heat treatments, are compared in section 5.1, following by the discussion of their evolution. Typical microstructure observed under optical microscope and Scanning Electron Microscope (SEM) are analysed in section 5.2, focused on distinct characteristics under different heat treatments and their effects on mechanical properties. Phase orientation maps measured by Electron Backscatter Diffraction (EBSD) are presented in section 5.3, as well as corresponding reconstructed high-temperature β orientation maps. The mechanisms that may lead to the microstructure evolution during short time β annealing are also discussed in this section.

5.1 Microstructural constituents of SLM Ti-6Al-4V subjected to heat treatments

The XRD analysis of as-built material indicates the presence of the hcp phase only, as shown in Figure 5.1. For Ti-6Al-4V, the hcp pattern can be a result of either α-phase or martensitic α', as they all share a same crystalline structure and have similar lattice parameters (Luca et al., 2010, da Silva et al., 1999). Considering the cooling rate of solidification inside the melt pool during SLM processing – which is up up to 10^4°C/s (Criales et al., 2017, Everton et al., 2016) – the hcp microstructure here is interpreted as α'. Therefore, the metastable martensite is the only phase present at room temperature for as-built SLM Ti-6Al-4V, which is also the starting microstructure for all heat treatments.

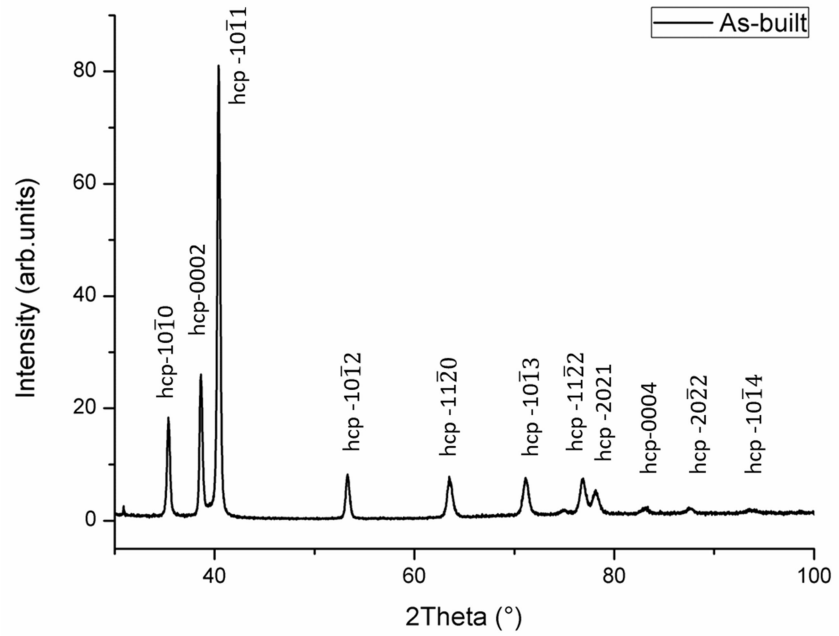


Figure 5.1 Typical XRD spectrum obtained from Ti-6Al-4V specimens in the as-built condition.

The XRD patterns of SLM Ti-6Al-4V subjected to different heat treatments are compared in Figure 5.2. A considerable resemblance is recognised in this figure as all XRD patterns share very similar waveform. Signal peaks are

detected at identical 2θ angles (2Theta) for different samples. Each signal peak represents a reflection of a particular crystalline structure with creation orientation, as demonstrated in Figure 5.3, using XRD pattern of samples induction heat treated above 1005°C as an example. Apparently, all XRD patterns in Figure 5.2 reveal a combination of hcp phase and bcc phase.

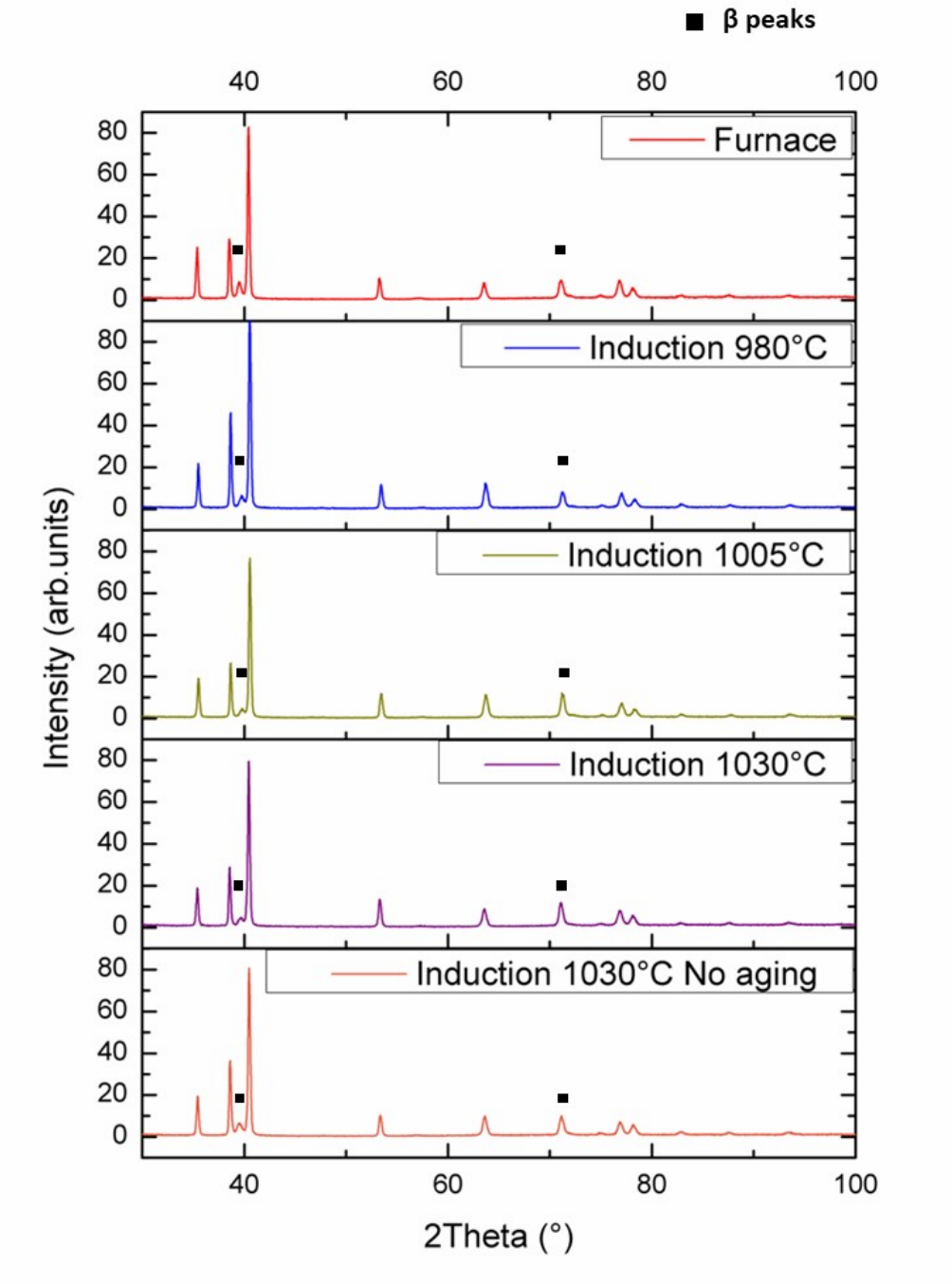


Figure 5.2. XRD spectrum obtained from SLM Ti-6Al-4V subjected to different heat treatments

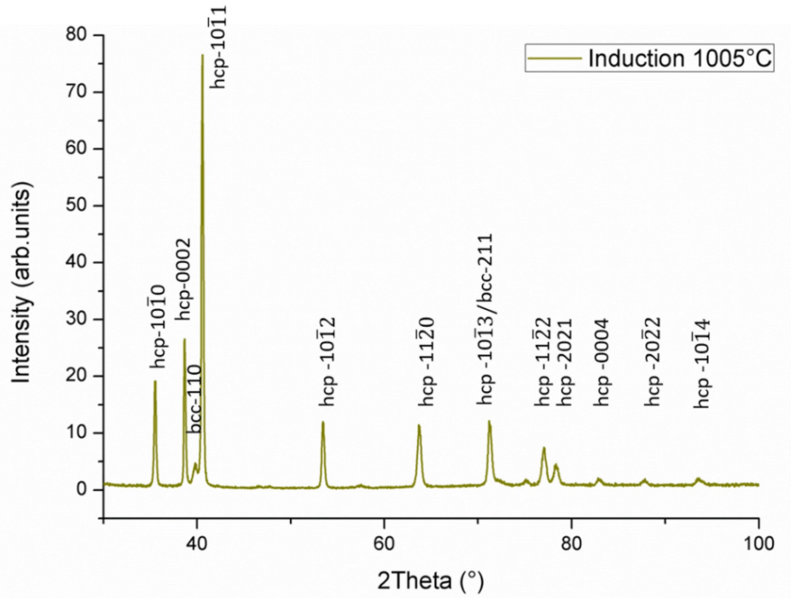


Figure 5.3. Interpretation of XRD spectrum with corresponding crystalline structure and orientation, sample was induction heat treated above 1005°C

The bcc pattern represents the β phase, which is clearly characterised by the (110) reflection. While the hcp pattern here should be interpreted as α phase, considering the cooling rate experienced in all conditions, which is 7°C/min for conventional heat treatment and 4°C/s for induction heat treatment. Thus, no matter what kind of heat treatment SLM Ti-6Al-4V samples experienced in the previous chapter, the final microstructure is always a mixture of α+β phases.

As conventional heat treatments were conducted at a slow heating rate of 10°C/min, they can be considered as near equilibrium conditions. When SLM Ti-6Al-4V anneal at a temperature, which is above the martensite start temperature M_s (~800°C) and below the β transus temperature (~1000°C), like 925°C in the present study, the starting structure, martensitic α', will transform into a mixture of hcp α and bcc β (Sallica-Leva et al., 2016, Qazi et al., 2003). On the air cooling after annealing, some high temperature β phase transform into α while others remain as residual β. The following ageing at a relatively lower temperature (700°C) does not alter the existing microstructure at the micron-scale (Carreon et al., 2017). However, research suggested the ageing can help to promote the precipitation of intermetallic

nanometre-sized α_2 (Ti_3Al) particles inside the α phase (Lee et al., 2004, Carreon et al., 2017). Therefore, the room temperature microstructural constituents of furnace treated SLM Ti-6Al-4V, as the XRD pattern reveals, are a combination of α phase and β phase.

Compared to conventional heat treatments, induction heat treatments were conducted at a much higher heating rate of 10°C/s. Ivasishin and Teliovich (1999) reported an alternative decomposition route for metastable α' in titanium alloys under rapid heating, during which the α' first transform into metastable β then decompose to α+β, instead of directly decomposing into α+β. However, for Ti-6Al-4V, such alternative route normally feasible at a heating rate above 50°C/s (Ivasishin and Teliovich, 1999), much higher than that which has been applied in this study. Therefore the decomposition of α' during the conducted induction heat treatment still follows α'→α+β route.

During the induction heating, α' starts to decompose when the temperature exceeds the martensite start temperature M_s (~800°C). As the temperature further rises, the material evolves towards the one phase field. Therefore the α phase, which is decomposed from the α', gradually transform to the high temperature phase, until reaching the point that the entire material consists of only the high temperature phase. The XRD spectrum of the induction heat treated samples suggest that, other than β phase, no additional high temperature phases are generated during this heating process. Since any potential additional high temperature phases are likely to introduce new reflection in the XRD spectrum, during the cooling process, the evolution of the β phase is similar to what happens in the furnace heat treatment. Therefore, the final microstructural constituents of induction heat treated SLM Ti-6Al-4V is also a mixture of α+β.

5.2 Typical microstructure of SLM Ti-6Al-4V that were subjected to different heat treatment

For metallic materials, like Ti-6Al-4V, different heat treatment routes usually result in a diversity of the final microstructure. In order to interpret the microstructure evolution during heat treatment, first of all, the initial microstructure should be characterised. Therefore, the typical microstructure of as-built SLM Ti-6Al-4V is described in section 5.2.1, followed by the microstructure of conventional heat treated and induction heat treated samples in section 5.2.2 and 5.2.3, respectively.

Without additional specification, all the microstructure images in this chapter are analysed on the frontal plane of the specimens, in which the building direction (Z direction) is parallel to the height of the image, as indicated in Figure 5.4.

5.2.1 Typical microstructure of SLM Ti-6Al-4V in as-built condition

Figure 5.4 shows the typical microstructure of the untreated as-built SLM Ti-6Al-4V. Columnar prior-β grains with an average width of 83.81 ± 8.25 μm are observed in Figure 5.4(a), prolonged along the building direction. The width of the prior-β grain is positively correlated with the applied hatch distance, while the columnar shape is caused by the direction cooling as well as the successive layer deposition during the printing (Wu et al., 2016c). During the solidification of the melt pool, heat dissipates through the underneath solidified layers, in a direction parallel to the building direction, which decides the growth direction of the columnar grain (Shunmugavel et al., 2017).

Figure 5.4(b) – (d) show fine, acicular α' needles filled within prior-β grains, with average width close to 1μm, which is the results of fast cooling as discussed in the previous section. Interweaved pattern of α' martensites

suggests a concurrent growth of different variants during cooling (Wu et al., 2016c).

As α' martensite is a metastable phase that contains a high density of dislocations and twins (Zhang et al., 2018), those metallurgy faults lead to a brittle appearance for as-built specimens in the tensile test, as shown in chapter 4. It is also known that the columnar shape is an anisotropy structure, its mechanical properties vary with test direction, which would potentially lead to premature failure under loading in an unfavourable direction (Zhang et al., 2018). In chapter 4, the tensile tests were conducted in a direction parallel to the growth direction of the columnar prior-β grain, which is the most favourable loading direction of the columnar grain. Therefore, the tensile properties exhibited in chapter 4 are likely to be the best results that as-built material can achieve in all test directions (Guzanová et al., 2017, Yang et al., 2017).

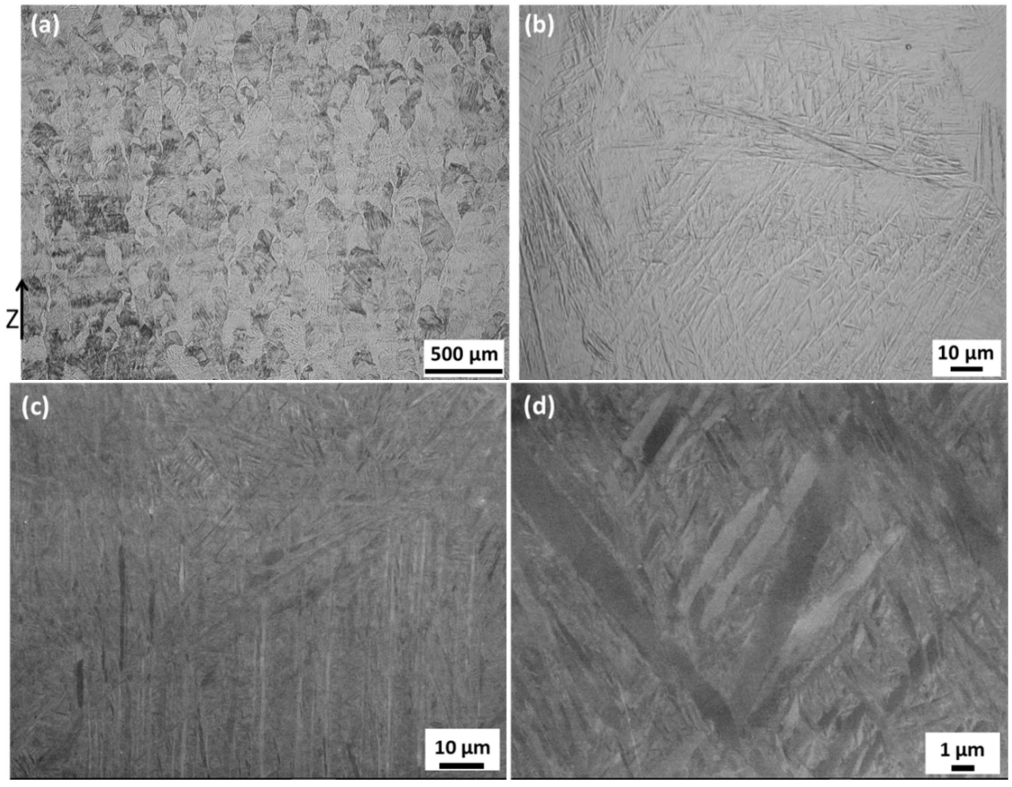


Figure 5.4. Typical microstructure of the as-built specimen: (a) optical microscope image showing columnar prior-β grains parallel to the building direction; (b) optical microscope image showing fine acicular α' martensite

within the prior-β grains; (c) (d) backscattered electron image showing the details of the fine acicular α' martensite.

5.2.2 Typical microstructure of SLM Ti-6Al-4V that were treated with conventional heating

In chapter 4, a group of SLM Ti-6Al-4V was conventional heat treated following published standards, soaking at 925°C for 2 hours then ageing at 700°C for 4 hours, which provides the reference tensile properties that can be achieved by the conventional heat treatment at its best. The microstructure after such heat treatment is exhibited in Figure 5.5.

Similarities are noticed when comparing the microstructures of the sub-transus heat treated SLM Ti-6Al-4V with the as-built ones. The same columnar prior-β grains are presented in Figure 5.5 (a), which grow along the building direction with an average width of 87.09 ± 10.94 μm, similar to what was observed in the as-built specimen. Multi-crossover α and β lamellas, as characterised in Figure 5.5 (b) and (c), forms basket wave morphology. Research suggests when martensite α' decompose during the heat treatment, α phase first nucleate within the acicular α' phase, pushes vanadium in the alloy to the boundary of the newly formed α phase (Zhang et al., 2018). The elements partitioning then leads to the formation of β phase in the vanadium-rich area between α lamellas (Zhang et al., 2018). The elements partitioning can be evidenced by the different contrast showing in the SEM images (Figure 5.5 (c) and (d)), where the vanadium enriched area has a lighter appearance. Consequently, the observed interlaced arrangement of α and β lamellas are expected to be inherited from the interweaved pattern of the as-built α' martensites.

Therefore, sub-transus heat treated microstructure is believed to be closely linked to the as-built one. Sub-transus heat treatment only decomposes original α' into α+β with the inheritance of interweaved pattern, but will not trigger any significant recrystallisation or grain growth that will lead to the change of the size and shape of the original prior-β grain.

α lamellas with an average width of 1.39 ± 0.12 µm can be clearly characterised in Figure 5.5 (c) and (d), which presents a significant coarsening when compared with the width of the initial α' martensite (smaller than 1µm). The observed coarsening is believed to be driven by the reduction of interfacial energy and the competitive growth between α and β phase at high temperature (Zhang et al., 2018). This mechanism can also be evidenced by the presence of equiaxed α grains, indicated by white arrows in Figure 5.5 (d). The change in morphology of the α phase during heat treatment has been the subject of ongoing investigations and might be related to the globularising phenomena described in related literature (Stefansson and Semiatin, 2003).

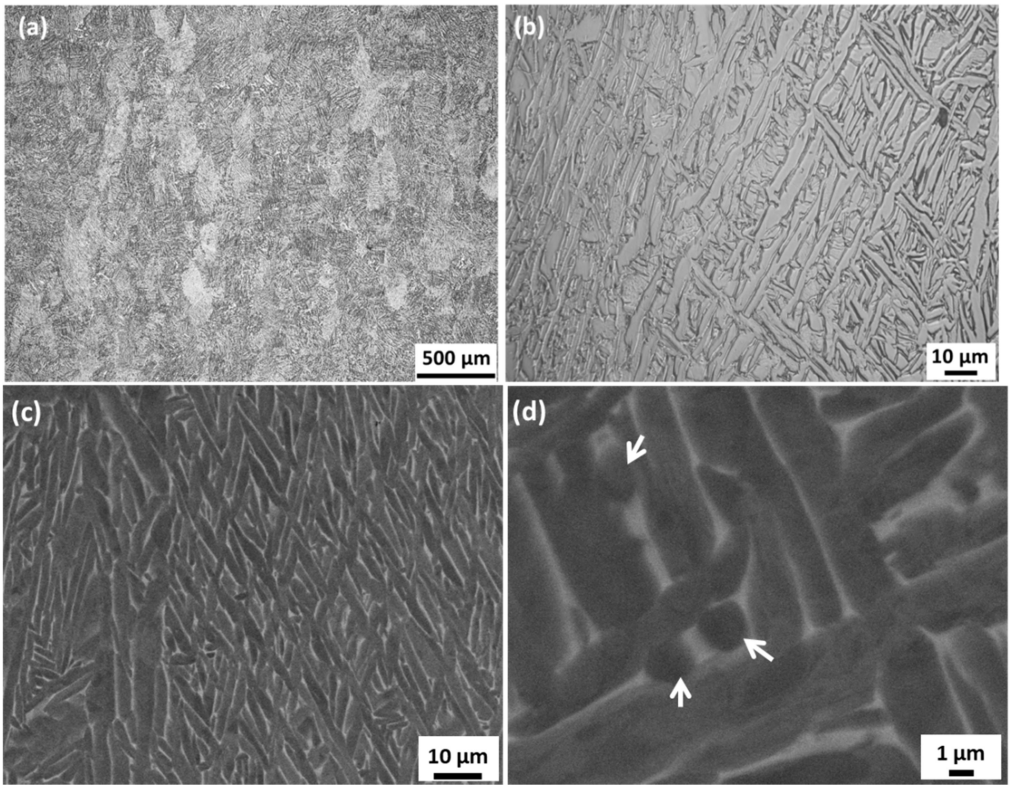


Figure 5.5. Typical microstructure of the SLM Ti-6Al-4V after furnace treated at 925°C for 2 hours then ageing treated at 700°C for 4 hours: (a) optical microscope image showing columnar prior-β grains parallel to the building direction, similar to what has been observed in as-built condition; (b) optical microscope image showing interweaved lamellar α+β within the prior-β grains (c) backscattered electron image showing the details of the interweaved lamellar α+β; (d) backscattered electron image showing the

coarsening of α lamella and the appearance of globularised α phase, as indicated by white arrows.

Nevertheless, it is believed that the decomposition of α' martensites eliminates most of the dislocations and twins stored in the metastable phase via annihilation and rearrangement (Sallica-Leva et al., 2016). The heat treatment also relieves most of the residual stresses stored in the as-built material. These factors and the concurrent action of the two phases (α+β) all lead to more balanced properties in ductility and strength. This explains why the conventional heat treated samples have a much better ductility (15.89%) compared to the as-built samples (5.19%), as well as the decline in strength. However, the columnar shape remains unchanged after sub-transus heat treatment, which means the sub-transus heat treated samples still present anisotropy behaviours. In this case, the tensile properties exhibited in chapter 4 are likely to be the best results conventional heat treated sample that can be achieved in all test directions.

Contrary to sub-transus heat treatment, conventional super-transus heat treatment of SLM Ti-6Al-4V often leads to unfavourable properties, as has been reported in many places (Vrancken et al., 2012, Luca et al., 2010, AmirMahyar et al., 2017). As a quick comparison, microstructure of SLM Ti-6Al-4V that were conventional heat treated above β transus is presented in Figure 5.6. It has been soaked at 1030°C for 2 hours to conduct uniform β annealing. It can be observed that the original columnar shape of the prior-β grains develops to equiaxed or quasi-equiaxed shape, with vast increases in grain size, some even have a diameter larger than 1mm, as shown in Figure 5.6 (a). Parallel lamellar α+β is dominated within prior-β grains, as characterised in Figure 5.6 (b). This parallel assembly, which is different from the interweaved structure in sub-transus heat treated specimen, suggests growth from the same variant (Wu et al., 2016c). Lack of resemblance in texture between super-transus heat treated specimen and sub-transus heat treated ones indicates that significant recrystallisation or grain growth happens in the single high temperature phase region. Continuous grain

boundary α is observed in Figure 5.6 (b), located by a series of white arrows. The grain boundary α, which cannot be seen in sub-transus heat treated specimens (Figure 5.5), is thicker than the α lath inside the prior-β grain. When cooling from the single β phase region, the α phase firstly forms at the boundary of the prior-β grain (Kumar et al., 2015). Therefore, the grain boundary α has a longer growth duration compare to the α lath inside the prior-β grain, which leads to a thicker morphology.

Generally, a certain amount of soaking time (over 1 hour) is required for conventional furnace heat treatment to achieve uniform heating within specimens. However, Ti-6Al-4V grains grow rapidly once they enter into the single phase region, which leads to the observed coarse grain structure after conventional super-transus heat treatment (Figure 5.6(a)). Based on the Hall-Petch Relationship detail explained in section 2.3.4, as well as the related experimental evidence (Ivasishin and Teliovich, 1999), is clear that the properties of titanium alloys strongly depend on the grain size of the high temperature phase, the smaller the grain size is, the better mechanical properties the material can achieve. Therefore, the observed coarse prior-β grain structure leads to a worse strength and ductility for conventional super-transus heat treated specimens, when compared with sub-transus heat treated ones, as reported in many researches (Vrancken et al., 2012, Luca et al., 2010, AmirMahyar et al., 2017).

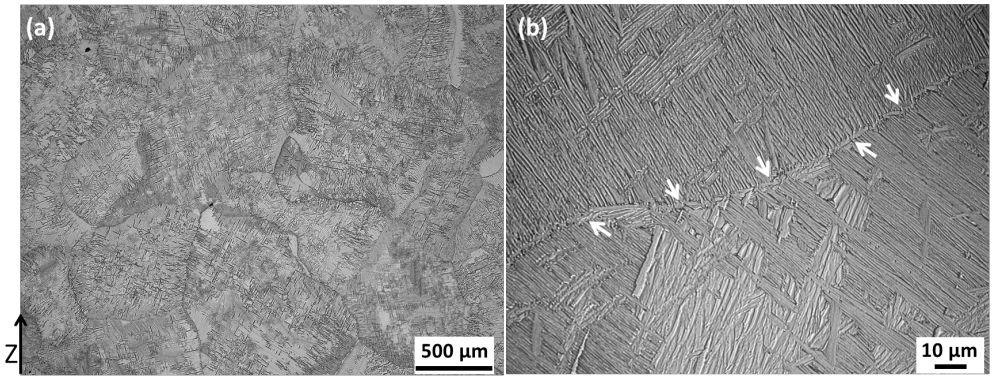


Figure 5.6. Typical microstructure of the SLM Ti-6Al-4V after furnace treated at 1030°C for 2hours: (a) optical microscope image showing coarse equiaxed prior-β grain in enormous size; (b) optical microscope image showing parallel

lamellar α+β fill inside the prior-β grain with continuous grain boundary α (as indicated by white arrows) at the prior-β grain boundaries.

5.2.3 Typical microstructure of SLM Ti-6Al-4V that were treated with induction heating

Four different types of induction heat treatments were conducted in chapter 4. All the specimens were heated up to a temperature around the β transus temperature. The main differences between them are the peak temperature and whether they are with or without a subsequent ageing process. The microstructures of these four group specimens are presented from Figure 5.7 to Figure 5.10.

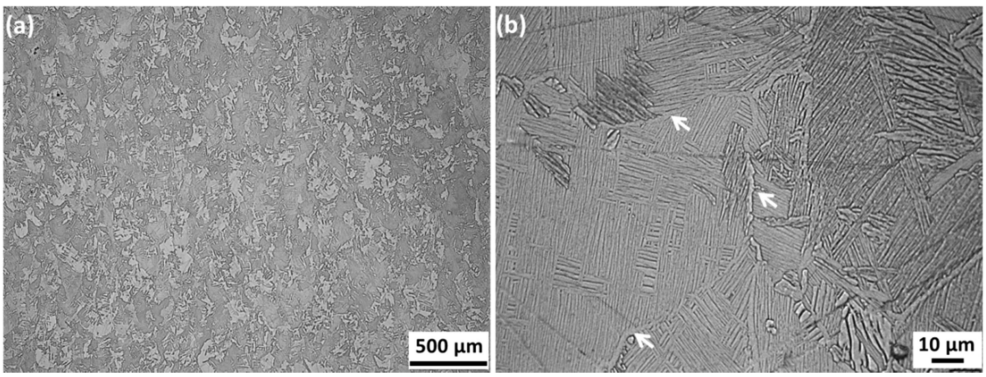
It can be observed from Figure 5.7 (a), Figure 5.8 (a), Figure 5.9 (a) and Figure 5.10 (a) that, in every induction heated specimens, the prior-β grains develop an equiaxed or quasi-equiaxed morphology. This transformation is similar to that which has been observed on the specimens that have been conventionally heated above β transus (Figure 5.6). The specimens that were subject to induction heat treatment however exhibit a much smaller average grain diameter, as reported in Table 5.1. The difference in grain diameter suggests that the recrystallisation or the grain growth of the prior-β grains were suppressed to a minimal level. This is mainly due to the limited duration these specimens were exposed in the high temperature phase region during the induction heat treatment, which helps to preserve the fine structure of the newly developed prior-β grains.

However, a certain level of elongated prior-β grain structure can still be observed in specimens heated just above 980°C (Figure 5.7 (a)). Since the temperature, 980°C, is slightly below the β transus temperature (~1000°C), it can be assumed that the material has not fully entered into single phase region during the heat treatment. The residual α phase may maintain some of the original prior-β grain structure, as seen in Figure 5.7 (a).

Table 5.1. The average width of the prior-β grain and the average thickness of the α lath in different tested condition

	Average width of the prior-β grain (μm)	Average thickness of the α lath (μm)
As-built	83.81 ± 8.25	/
Conventional heat treatment	87.09 ± 10.94	1.39 ± 0.12
Induction 980°C	40.56 ± 9.46	0.66 ± 0.06
Induction 1005°C	34.32 ± 5.13	0.56 ± 0.07
Induction 1030°C	36.14 ± 7.97	0.60 ± 0.02
Induction 1030°C No ageing	31.88 ± 3.89	0.59 ± 0.07

Parallel lamellar α+β is identified to be the predominant texture within prior-β grains, as shown in all four figures from Figure 5.7 to Figure 5.10. α lamellar with an average width of approximately 0.6μm can be clearly characterised in both Figure 5.7 (d), Figure 5.8 (d), Figure 5.9 (d) and Figure 5.10 (d), detail values are reported in Table 5.1. Continues grain boundary α with an average width of about 2-3 μm is also observed in all four figures, clearly plot the boundary of prior-β grains, as marked by white arrows. These features share certain resemblances to what is exhibited in the conventional β annealed specimen (Figure 5.6 (b)).



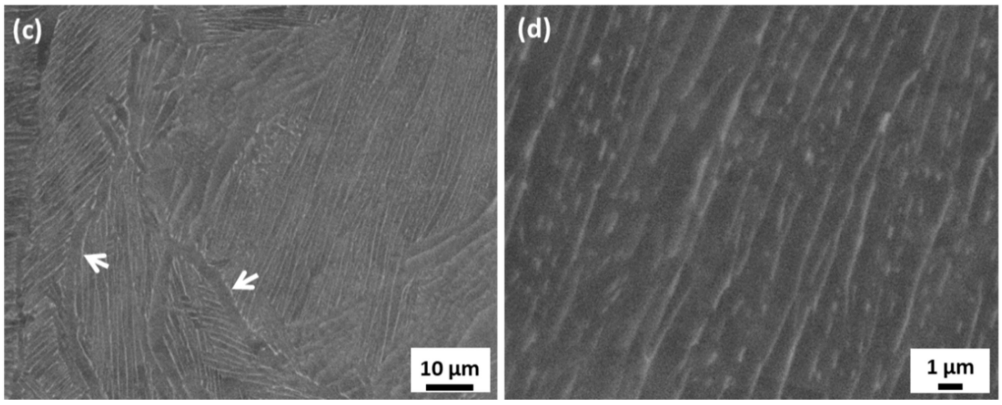


Figure 5.7. Typical microstructure of SLM Ti-6Al-4V after induction heated above 980°C, captured at different magnification: (a) optical microscope image, 5 x; (b) optical microscope image, 100 x, (c) backscattered electron image, 1000 x, (d) backscattered electron image, 5000 x. The locations of the continues grain boundary α are plotted by the white arrows.

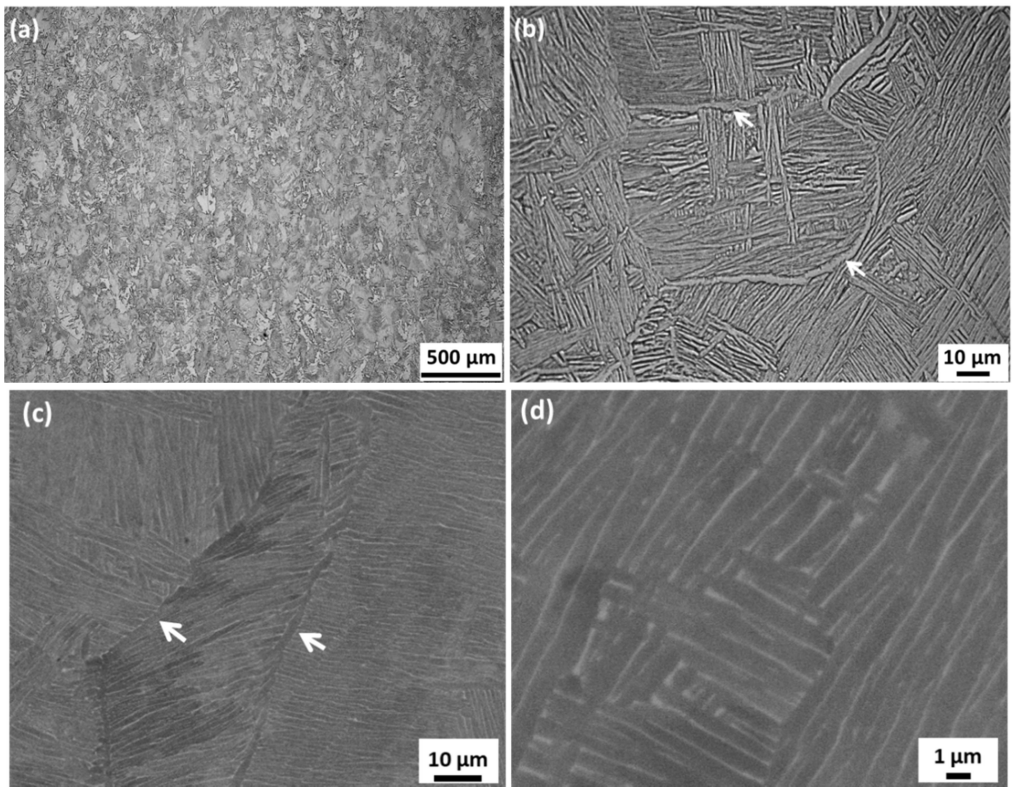


Figure 5.8. Typical microstructure of SLM Ti-6Al-4V after induction heated above 1005°C, captured at different magnification: (a) optical microscope image, 5 x, (b) optical microscope image, 100 x, (c) backscattered electron image, 1000 x, (d) backscattered electron image, 5000 x. The locations of the continues grain boundary α are plotted by the white arrows.

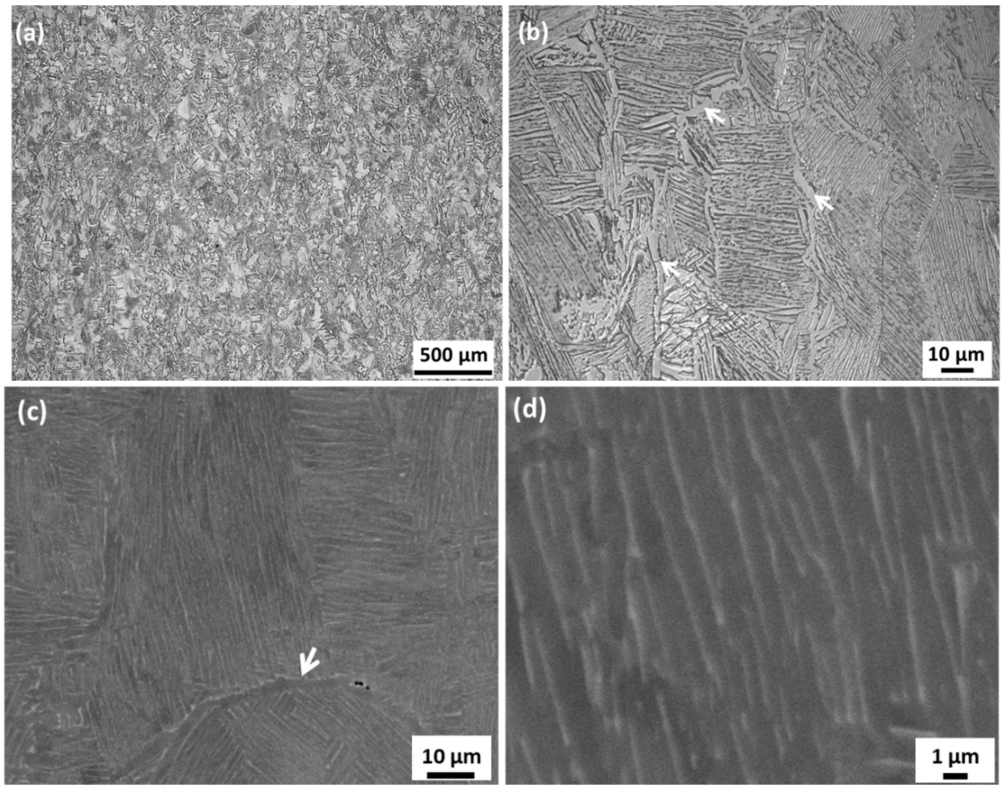


Figure 5.9. Typical microstructure of SLM Ti-6Al-4V after induction heated above 1030°C, captured at different magnification: (a) optical microscope image, 5 x, (b) optical microscope image, 100 x, (c) backscattered electron image, 1000 x, (d) electron microscope image, 5000 x. The locations of the continues grain boundary α are plotted by the white arrows.

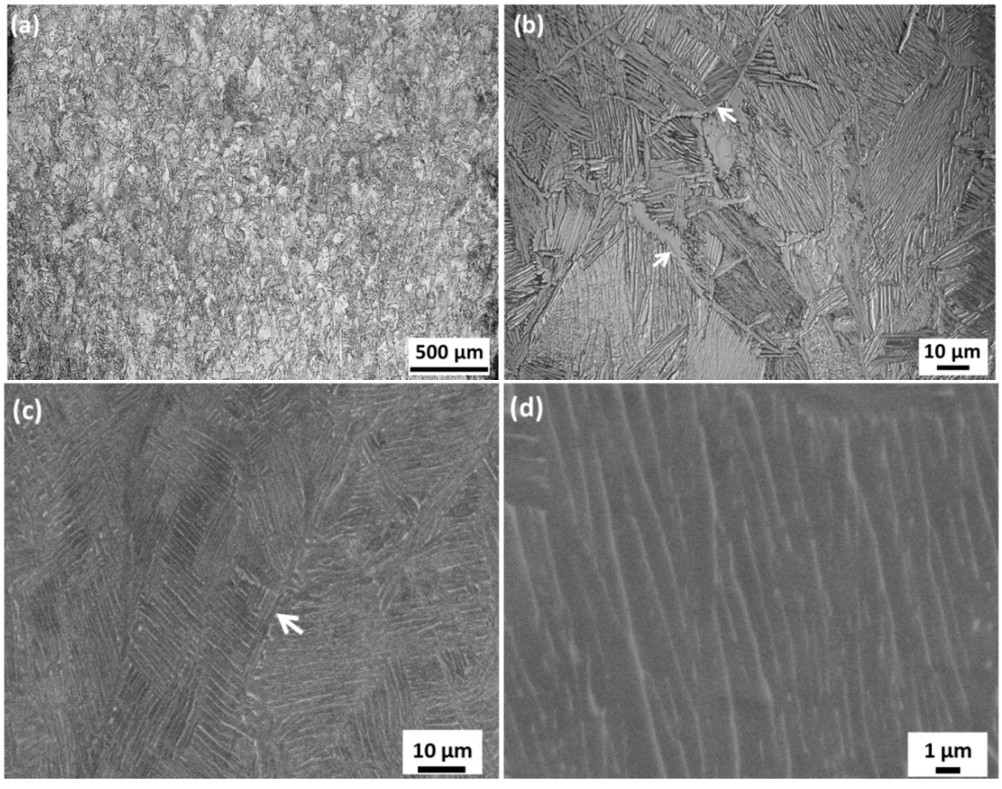


Figure 5.10. Typical microstructure of SLM Ti-6Al-4V after induction heated above 1030°C without subsequent ageing process, captured at different magnification: (a) optical microscope image, 5 x, (b) optical microscope image, 100 x, (c) backscattered electron image, 1000 x, (d) backscattered electron image, 5000 x. The locations of the continues grain boundary α are plotted by the white arrows.

Therefore, one of the most noticeable differences of the induction heat treated specimens is the size of their prior-β grains, which is not only significantly smaller than those that have been furnace β annealed, most importantly, but also smaller than those soaking at a temperature below the β transus. The observed refinement of the β grains has not been reported before in AM specimens after heat treatment. This refinement is also believed to be the reason that induction heated specimens exhibit tensile properties are comparable or even superior to the furnace treated samples, as reported in Chapter 4. It can also explain why specimens that been induction heated at the temperature just below β transus (980°C) present a tensile property slightly worse than short time β annealed specimens since it still retains some of the original coarse prior-β grain structure.

Compared to SLM Ti-6Al-4V that been furnace treated at a temperature below the β transus (Figure *5.5*), induction heated specimens have two other significate features: (a) the appearance of grain boundary α at prior-β grain boundaries, which has a similar width to α lamella in furnace heated specimens (2-3 μm); (b) the fine structure of α lamella within the prior-β grains (1 μm compare to 2-3 μm in conventional heat treated one).

The two features are considered to be favourable for fatigue resistance. Colony boundaries at the prior-β grain boundaries can act as microstructural barriers for cracks to grow, thus improve the resistance to fatigue (Jeong et al., 2017). A more packed parallel α lamella structure can further suppress the crack initiated by slip band cracking, since the crack needs to cross through more of the β ribs between α lamellas, again presenting more microstructural barriers for cracks to grow (Peng et al., 2012). Similar yield

strength for induction heated and conventional heated specimens suggest they share the same level of resistance to crack nucleation (Jeong et al., 2017). Therefore, it could be assumed that the induction heated-short time β annealed-specimens can achieve a better fatigue property than furnace heat treated specimens.

5.3 Crystallographic textures and phase orientation maps of SLM Ti-6Al-4V that were subjected to different heat treatment

Phase orientation maps and the following analysis can help to further understand the observed microstructure, as well as the mechanism associated with the development of the microstructure. Two types of phase orientation maps are included in this section. The α-orientation map was measured at room temperature (20°C) through Electron Back-Scattered Diffraction (EBSD), while the β- orientation map was reconstructed from the room temperature α-phase via the Burger Orientation Relationship (BOR).

Without additional specification, all the orientation maps in this section are analysed on the frontal plane of the specimens, in which the building direction (Z direction) is parallel to the height of the map, as indicated in Figure 5.11. The orientation data are all mapped in Z-IPF with the colour scheme presented in Figure 5.11 (d).

5.3.1 Crystallographic textures and phase orientation of SLM Ti-6Al-4V in as-built condition

Figure 5.11 demonstrates the typical phase orientation maps in as-built condition. It can be observed from the α-orientation map in Figure 5.11 (a) that fine α martensites with various orientations interweaved with each other inside the prior-β grain. Theoretically, there are 12 possible α/α' orientations (variants) corresponding to a given β orientation (Qiu et al.,

2016). However, only 5 to 7 variants can be counted within each prior-β grain in Figure 5.11 (a). The lack of existence for certain α' variants suggests a selection of variants happens during the solidification of the melt pool, which may be a result of multiple factors, like the cooling rate and localised stress (Sargent et al., 2012, Shi and Wang, 2013).

The reconstructed β-orientation map of as-built SLM Ti-6Al-4V in Figure 5.11(b) shows the elongated structure of prior-β grains with an average width of 100-150 µm, corresponding to what is observed in microscopy images (Figure 5.4). Within each prior-β grain the reconstructed β is similarly orientated across the length of the entire prior-β grain with an orientation spread within 10°. The distribution of calculated β grain boundary angles is presented via the histogram shown in Figure 5.11 (c) as well as the colourised boundaries in the orientation map of Figure 5.11 (b). The β grain boundary angles spread in a range between 15° to 65°, with moderate concentrate between 35° to 60°.

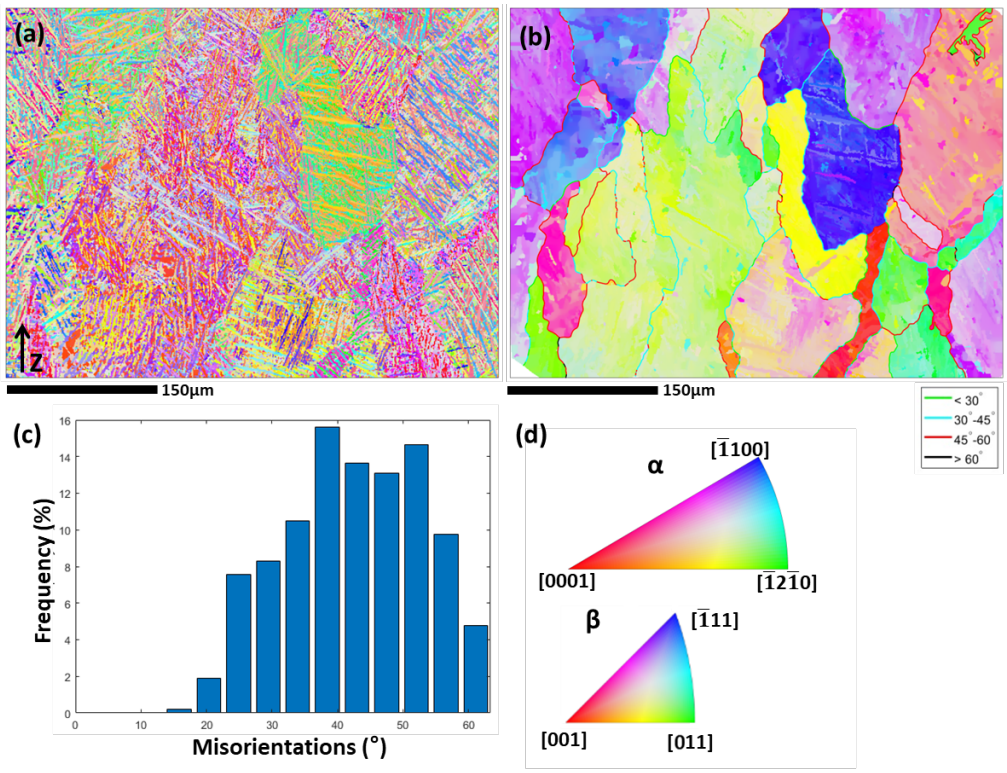


Figure 5.11. (a) Typical α-orientation map in Z-IPF of SLM Ti-6Al-4V in as-built condition; (b) Reconstructed β-orientation map in Z-IPF from the as-built

microstructure; (c) The misorientation distribution at the prior-β grain boundary in the as-built condition; (d) Standard colour scheme used to map the orientation data.

5.3.2 Crystallographic textures and phase orientation of SLM Ti-6Al-4V that were treated with conventional heating

Orientation maps of sub-transus conventional heat treated SLM Ti-6Al-4V are presented in Figure 5.12, which was soaked at 925°C for 2 hours. Coarsened α lamellas clearly characterised from the α-orientation map, as shown in Figure 5.12 (a), is distinct from the acicular feature of α' martensite in as-built condition (Figure 5.11(a)). The reconstructed β-orientation map in Figure 5.12 (b) demonstrates the inheritance of elongated columnar morphology for prior-β grains after conventional sub-transus heat treatment. This inheritance is further evidenced by the distribution of β grain boundary angles shown in Figure 5.12 (c) since it shares a similar misorientation distribution with the as-built condition. It also confirms the deduction from section 5.2.2 that such applied heat treatment cannot trigger significate recrystallisation of the β phase. The recrystallisation is driven by the movement of high angle boundary (HAB). With the migrating of the HAB, the original low angle boundary will be consumed, and new HAB will be introduced. Therefore, for any Ti-6Al-4V samples that experienced a recrystallised process, the distribution of the β grain boundary angle will be concentrated in the high angle region (Pilchak et al., 2017).

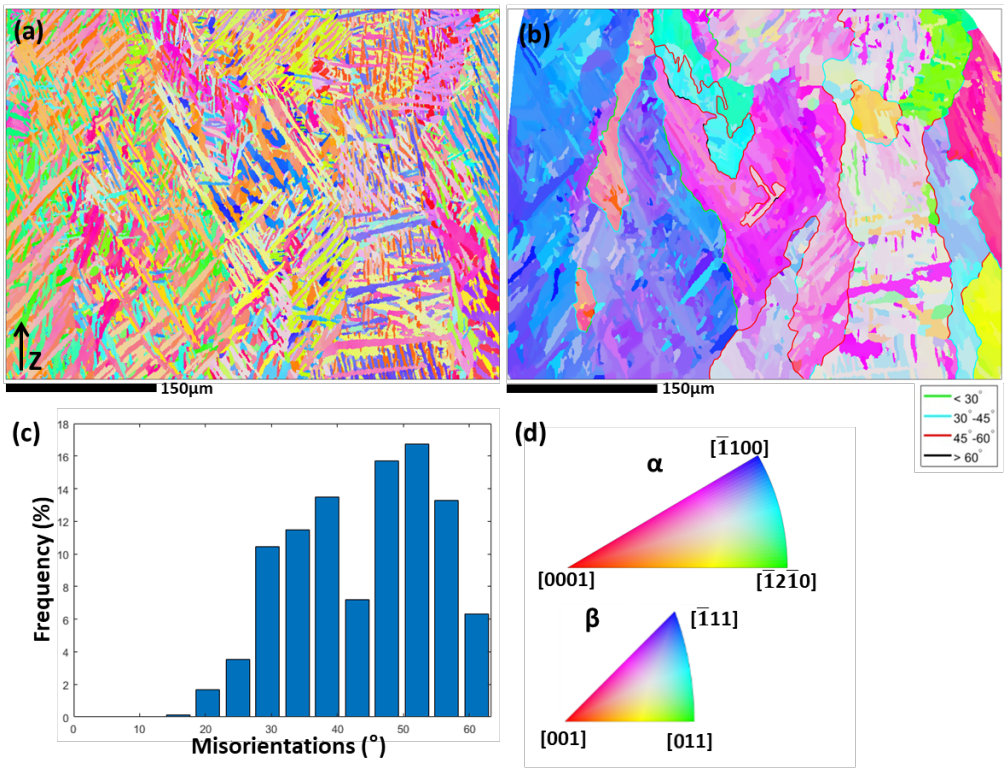


Figure 5.12. (a) α-orientation map in Z-IPF of SLM Ti-6Al-4V after furnace treated at 925°C for 2 hours then ageing treated at 700°C for 4 hours; (b) Corresponding reconstructed β-orientation map in Z-IPF; (c) The misorientation distribution at the prior-β grain boundary; (d) Standard colour scheme used to map the orientation data.

5.3.3 Crystallographic textures and phase orientation of SLM Ti-6Al-4V that were treated with induction heating

Phase orientation maps of induction heated SLM Ti-6Al-4V are presented from Figure 5.13 to Figure 5.16, respective to different conditions.

Instead of individual α/α' laths observed in α-orientation map from as-built and furnace heated conditions (Figure 5.12(a) and Figure 5.13(a) respectively), α colonies are characterised in all four α-orientation maps subjected to different induction heated conditions, as shown in Figure 5.13 (a), Figure 5.14 (a), Figure 5.15 (a) and Figure 5.16 (a). It confirms the deduction that the parallel aligned α lamellas, observed in the microscopy images from section 5.2.3, indeed grow from the same α variants.

The refinement and the morphology development of prior-β grain, which is described in section 5.2.3, can be confirmed by the orientation maps of the β phase, as shown in Figure 5.13 (d), Figure 5.14 (d), Figure 5.15 (d) and Figure 5.16 (d). Equiaxed or quasi-equiaxed prior-β grains with an average diameter of 20 -100 µm are noticeably characterised in these images.

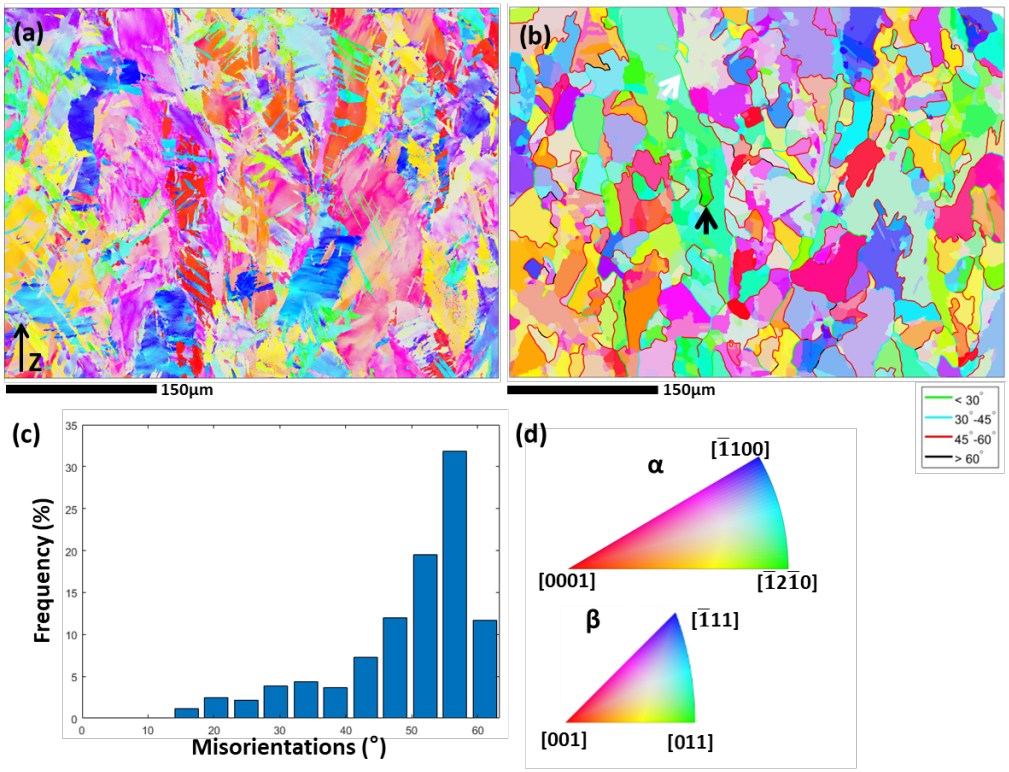


Figure 5.13. (a) α-orientation map in Z-IPF of SLM Ti-6Al-4V after induction heated above 980°C; (b) Corresponding reconstructed β-orientation map in Z-IPF, white arrow indicates the existence of long continuous moderately misorientated grain boundary, while black arrow indicates distinct small grain located in the centre of the columnar grain ; (c) The misorientation distribution at the prior-β grain boundary; (d) Standard colour scheme used to map the orientation data.

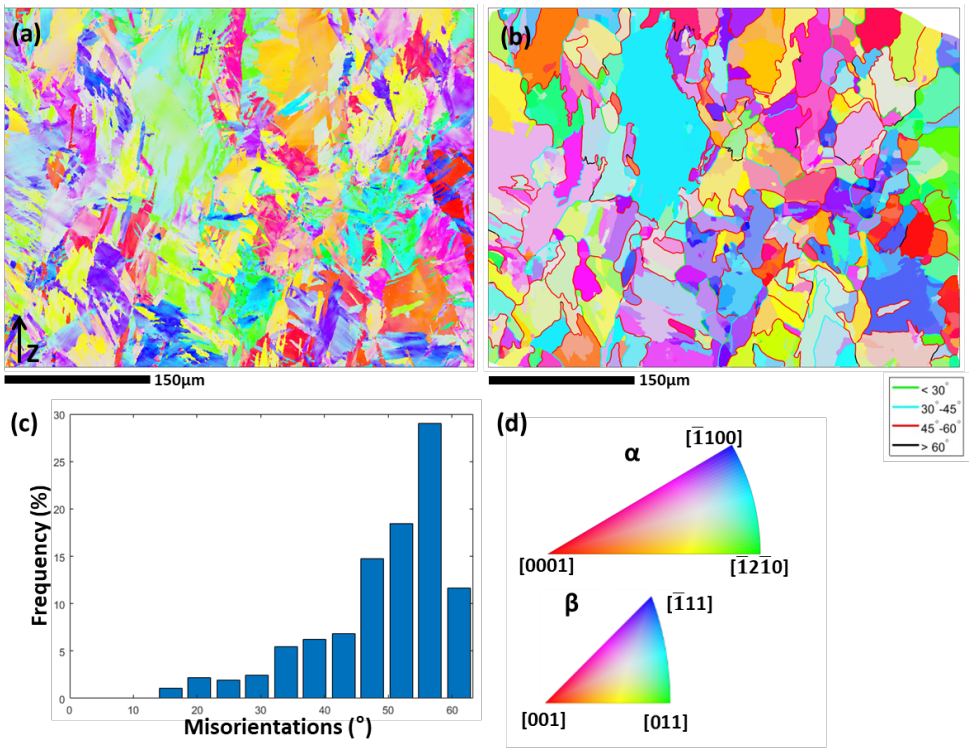


Figure 5.14. (a) α-orientation map in Z-IPF of SLM Ti-6Al-4V after induction heated above 1005°C; (b) Corresponding reconstructed β-orientation map in Z-IPF; (c) The misorientation distribution at the prior-β grain boundary; (d) Standard colour scheme used to map the orientation data.

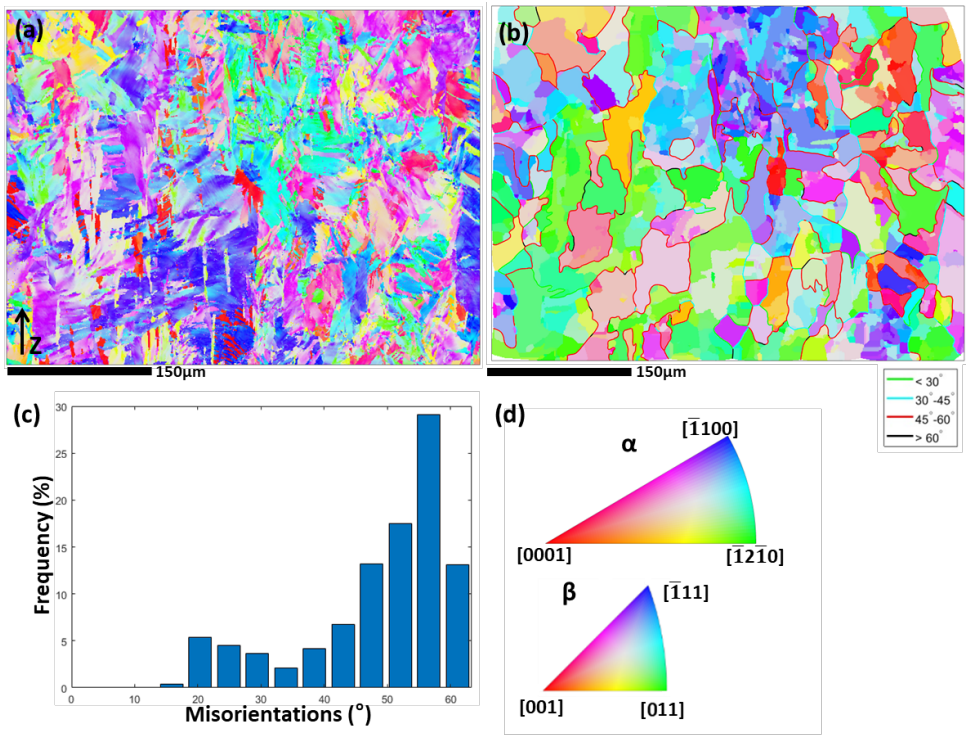


Figure 5.15. (a) α-orientation map in Z-IPF of SLM Ti-6Al-4V after induction heated above 1030°C; (b) Corresponding reconstructed β-orientation map in

Z-IPF; (c) The misorientation distribution at the prior-β grain boundary; (d) Standard colour scheme used to map the orientation data.

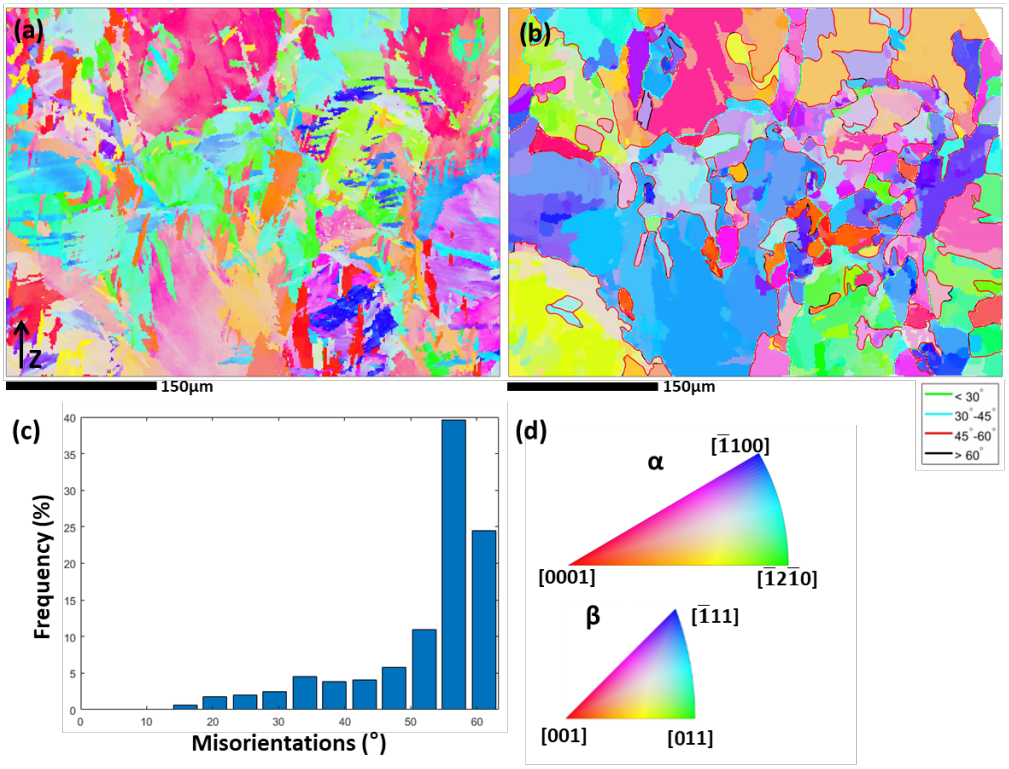


Figure 5.16. (a) α-orientation map in Z-IPF of SLM Ti-6Al-4V after induction heated above 1030°C without subsequent ageing process; (b) Corresponding reconstructed β-orientation map in Z-IPF; (c) The misorientation distribution at the prior-β grain boundary; (d) Standard colour scheme used to map the orientation data.

The distribution of β grain boundary angles are severely concentrated in the high angle region, as shown in both Figure 5.13 (c), Figure 5.14 (c), Figure 5.15 (c) and Figure 5.16 (c). Most of the β grain boundary angles are spread in a limited range from 50° to 60°, with a preference towards 60°. Such evident development in the boundary angle distribution suggests that a significant scale of recrystallisation took place during the applied heat treatment, which not only replace the original moderately misorientated β grain boundary with HAB but also introduces new HAB. Such evolution can be evidenced by the extensive increase in the total length of the β grain boundary.

Some elongated columnar β grain structures are still characterised in Figure 5.13 (b), which have been induction heated to a temperature just below the

β transus temperature (980°C). As discussed in section 5.2.3, some of the original prior-β grain structure can be maintained at such a temperature. Furthermore, the existence of long continuous moderately misorientated grain boundary, which is adjacent to these elongated structures, as pointed by the white arrow, confirm the nature of elongated grain as the residual original structure.

In Figure 5.13 (b), a distinct small grain can be observed, which is located in the centre of the columnar grain, as indicated by the black arrow. A high angle boundary (HAB) separates it from the surrounding β matrix, which suggests it is a newly recrystallised grain. The location of this recrystallised grain suggests it originated at the inside of the original columnar grain. Since the HAB has higher mobility compared to the surrounding β matrix (W. Kurz, 1991), therefore, if the observed microstructure develops further, the recrystallised grain will grow faster when competing with the surrounding β matrix for growth. In the end, it will lead to the breakdown of the original morphology.

The current understanding associated to the nucleation and growth of the β phase during conventional heat treatment of martensitic Ti-6Al-4V is that, after an initial recovery of the microstructure, the α+β→β transition occurs by movement of the α/β interface until only the parent β phase exists (Ivasishin and Teliovich, 1999, Idhil Ismail et al., 2016). It is also believed that nucleation of β grains of new orientations does not take place because the shear stress associated to the HCP → BCC lattice transformation is too low to induce recrystallisation of β grains with no BOR with existing α during the α+β→β transformation (Ivasishin and Teliovich, 1999, Idhil Ismail et al., 2016). However, this theory does not explain the observed recrystallisation and refinement of the β grains.

Additional data and information are required to understand the observed refinement mechanisms, which will be presented in chapter 7.

5.4 Summary

In this chapter, microstructures of SLM Ti-6Al-4V subjected to different investigated conditions are thoroughly analysed via XRD, microscopy images and EBSD. Features of each microstructure can be summarised as follow:

- In the as-built condition, the typical microstructure consists of fine acicular α' martensites interweaved with each other in columnar prior-β grains. The fine α' martensites possess a width of around 1µm, while the columnar prior-β grains possess an average width of 83.81 ± 8.25 µm. The misorientation angle at the prior-β grain boundary spread in a range between 15° to 65°, with moderate concentrate between 35° to 60°.
- After conventional sub-transus heat treatment, the typical microstructure consists of interweaved α+β lamellas in prior-β grains which maintained original columnar morphology, with an average width of 87.09 ± 10.94 µm. The α lamellas have an average width of 1.39 ± 0.12 µm. The interweaved arrangement of the α/β lamellas suggests an inheritance from the original microstructure. The distribution of the misorientation angle at the prior-β grain boundary is similar to the distribution in as-built conditions.
- After conventional super-transus heat treatment, the typical microstructure consists of parallel α+β lamellas in coarse equiaxed prior-β grains.
- After induction heating to a temperature around the β transus temperature, the typical microstructure consists of parallel α+β lamellas in refined equiaxed or quasi-equiaxed prior-β grains. The α lamellas have an average width of about 0.6 µm, while the average diameter of the refined prior-β grains varies between 30 - 40 µm, detail values for each tested condition are reported in Table 5.1. The distribution of the misorientation angle at the prior-β grain boundary is severely concentrated in the high angle region.

The observed refinement of the β grains has never been reported before in AM Ti-6Al-4V after heat treatment. It ensures the induction heat-treated SLM Ti-6Al-4V achieves tensile properties comparable or even superior to those

conventional heat treated ones, as demonstrated in chapter 4. The microstructure analysis also suggests that such heat treatment can achieve improved fatigue properties than furnace heat treatment (Peng et al., 2012, Jeong et al., 2017).

The refinement is believed to be the results of limited exposure duration in the high temperature phase region and the recrystallisation of β grains during heat treatment. The recrystallisation is evidenced by the analysis of the phase orientation map. However, at this point, the mechanism leading to the early stage recrystallisation is unclear and will be further elucidated in chapters 6 and 7.

CHAPTER 6

6. Early stages of microstructural evolution during beta annealing of SLM Ti-6Al-4V

In Chapter 5, it was reported that the prior-β grains of SLM Ti-6Al-4V transform from a columnar morphology to a refined equiaxed or quasi-equiaxed morphology during short time beta annealing. In order to characterise and understand the microstructure evolution, which leads to the observed morphological change, designed gradient heating of SLM Ti-6Al-4V were conducted. By creating a shielded cold end at one side of the SLM Ti-6Al-4V cylinder during the induction heating as described in section 3.2.3, a temperature gradient is created within the material. Since the original microstructure at different locations within the heated cylinder should be considered as the same, the final microstructure after heating is only subject to the peak temperature the material experienced at the specified location. Therefore, a continuous microstructure evolution corresponding to the heating temperature range can be plotted within the material.

The work of Chapter 5 also showed that the morphological change of prior-β grains can be clearly observed after heating at 985°C, but not at 925°C. Therefore, the starting temperature of the described evolution should be at a temperature between 925°C and 985°C. Test results suggest that gradient heating from 965°C to 985°C can be used to characterise the early stage of this microstructure evolution. Such gradient heating can also create a series of microstructure, which is continuously transformed, thereafter refer to as the “transformation zone”. The microstructural morphology of the transformation zone is reported and analysed in section 6.1. The orientation

maps of the interested areas within the transformation zone are presented and discussed in section 6.2.

Without additional specification, all the microstructure images and orientation maps in this chapter are analysed on the frontal plane of the specimens, in which the building direction (Z direction) is parallel to the height of the image, as indicated in Figure 6.1. The orientation data all mapped in Z-IPF with the colour scheme presented in Figure 6.4.

6.1 The evolution of microstructural morphology during the early stages of β annealing

The microstructure of SLM Ti-6Al-4V, which was gradient heated between 965°C to 985°C, is presented in Figure 6.1. The peak temperature, which was recorded at different heights of the specimen, is indicated at the corresponding height in Figure 6.1. During gradient heating, the heat generated by the rapid induction heating is conductively extracted by the shielded cold end. The cold end is set at the bottom of the heated SLM Ti-6Al-4V cylinder. The closer to the cold end, the lower peak temperature the material will experience. Therefore, within the recorded length shown in Figure 6.1, the top side experienced the highest peak temperature of 985°C, and the bottom side experienced the lowest peak temperature of 965°C, with the peak temperature distribution gradually increased from bottom to top. At the different height of the specimen, the microstructure evolved under a different peak temperature.

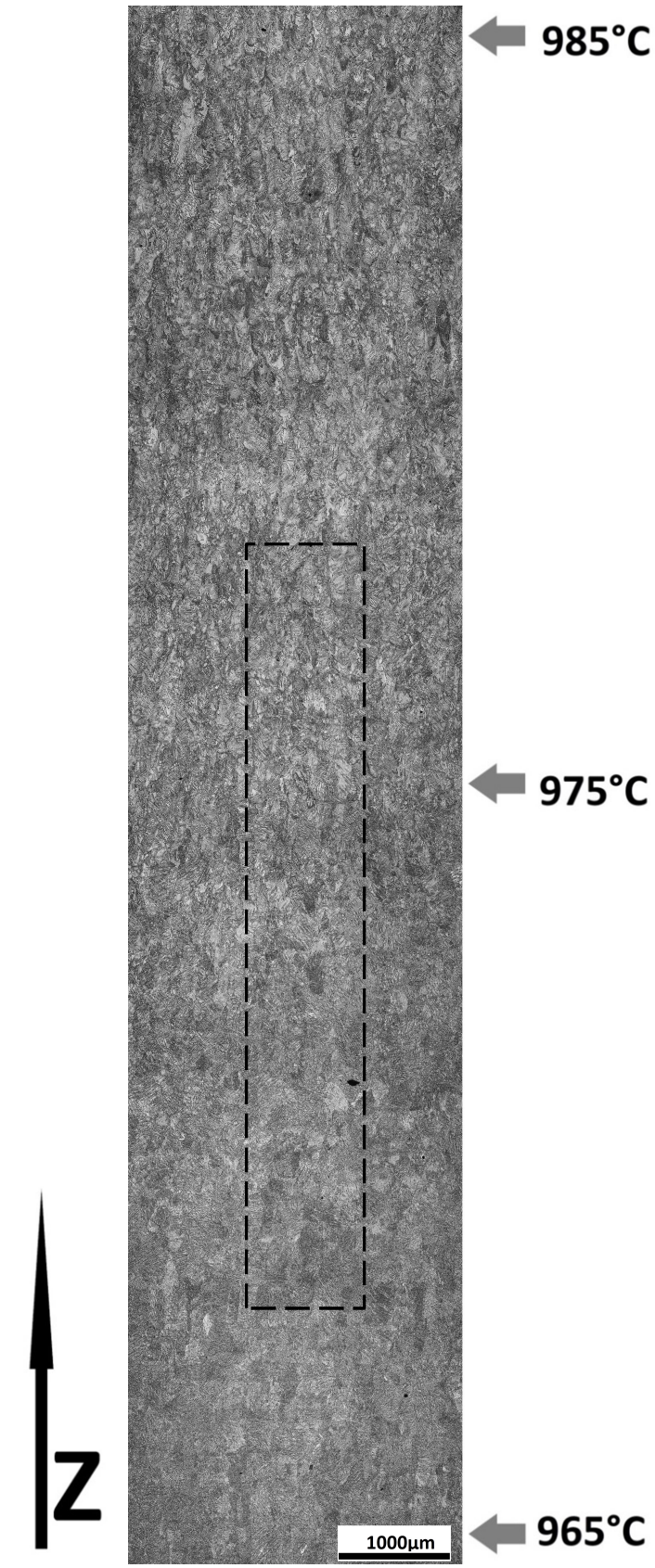


Figure 6.1. Optical microscope image showing a continuously transformed microstructure demonstrates the progressive evolution of microstructural morphology of the SLM Ti-6Al-4V during the early stages of β annealing.

In the bottom side of Figure 6.1, a typical sub-transus heat treated texture is observed after being heated to 965°C; the columnar morphology of the prior-β grain remains unchanged and no other morphology of the prior-β grain observed under this temperature. As the temperature rises, a weakening of the original columnar morphology is observed. Fine quasi-equiaxed prior-β grains first appear in the microstructure generated at a temperature between 965°C to 975°C. Microstructure that includes a mixed morphological make up of columnar grains and quasi-equiaxed grains starts to replace the original columnar morphology, which lasts thereafter and is shown in Figure 6.1. It can also be noticed that the ratio of quasi-equiaxed grain to columnar grain within the mixed morphology increases with the temperature experienced by the material. Only a limited amount of columnar prior-β grains can be observed in the microstructure generated at 985°C, which corresponds to the finding reported in Chapter 5. Detailed optical microscope images of the microstructure obtained at 985°C in the gradient heating will be presented in Figure 6.2 (e) and (f).

For a detailed observation, microstructure generated at different temperatures are presented in Figure 6.2.

The microstructure generated at 965°C, as shown in Figure 6.2 (a) and (b), is a typical sub-transus heat treated texture. In this microstructure, the columnar prior-β grains are filled with interweaved lamellar α+β plates where there does not appear to be any grain boundary α at the β grain boundary. All features are strictly inherited from the as-built texture.

The microstructure generated at 975°C, as shown in Figure 6.2 (c) and (d), already includes several refined quasi-equiaxed prior-β grains. Some of the refined quasi-equiaxed prior-β grains are indicated by black arrows in Figure 6.2 (d). Other than that, large amount of continuous grain boundary α appears in this microstructure at 975°C, as indicated by the white arrows in Figure 6.2 (d). The grain boundary α is not the original feature presented in the as-built texture. As a new feature introduced by the heating, it can only

be transformed from the high temperature β generated during heat treatment. The appearance of grain boundary α in the microstructure obtained at 975°C suggest that the microstructure existing at such temperature already has enough β phase in the matrix to support an α variants selection process, when the material is cooling from the said temperature to room temperature. Therefore, new features like the observed grain boundary α will be introduced into the microstructure.

The observed mixed morphology of columnar and quasi-equiaxed prior-β grains continues at 985°C, with an increase in the amount of quasi-equiaxed grains, as shown in Figure 6.2 (e) and (f).

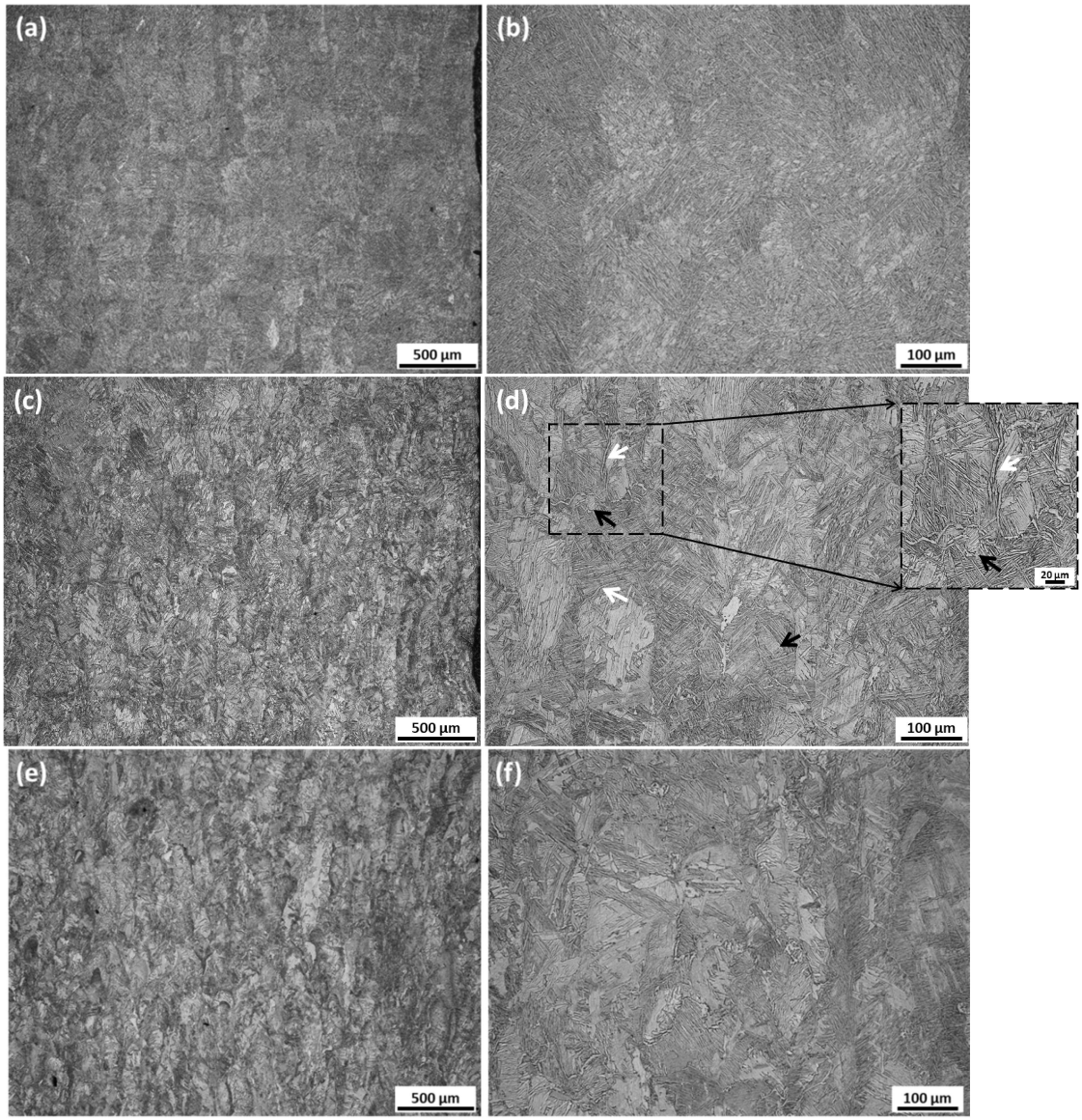


Figure 6.2. Optical microscope images showing the microstructure generated at different temperature: (a)(b) 965°C, (c)(d) 975°C, (e)(f) 985°C. Black arrows in (d) indicate the refined quasi-equiaxed prior-β grains that were newly transformed. White arrows in (d) indicate the continuous grain boundary α appeared at 975°C.

Further observation of the microstructure evolution and microstructure generated at a higher temperature (near β transus) is present in Figure 6.3. The columnar morphology of the prior-β grains can still be observed within the matrix of refined quasi-equiaxed grains in the microstructure generated at 1000°C, as shown in Figure 6.3 (a) and (b). The microstructure converts into full quasi-equiaxed morphology at 1010°C, where no presence of any columnar feature in the microstructure can be observed, as shown in Figure

6.3 (c) and (d). Therefore, it can be considered as the end of the observed microstructure evolution. The final temperature, 1010°C, is exactly the β transus temperature of test material ascertained by Simultaneous Differential Analysis (SDT), as reported in section 3.1.

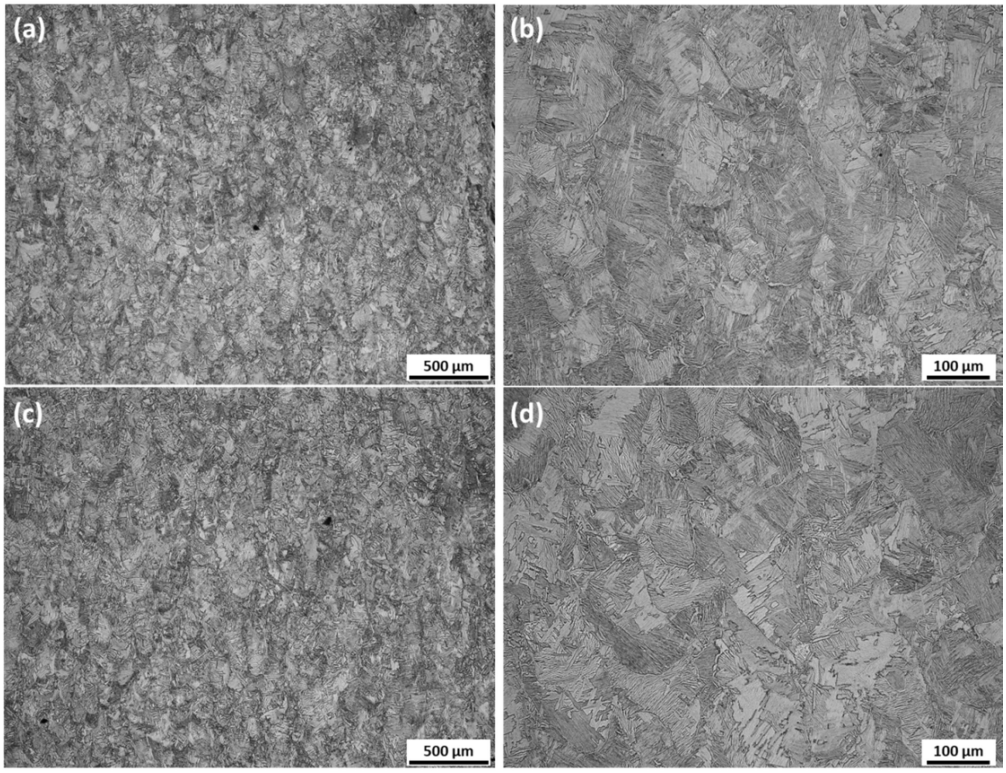


Figure 6.3. Optical microscope images showing the microstructure generated at temperature near β transus: (a)(b) 1000°C, (c)(d) 1010°C. The columnar morphology of the prior-β grains still can be observed at 1000°C, while the microstructure converts into full quasi-equiaxed morphology at 1010°C

Optical microscope images evidence that the microstructure evolution, which leads to the observed columnar morphology to refined quasi-equiaxed morphology transformation of the prior-β grains, is a progressive process. It occurs with the existence of a mixed morphology of columnar and quasi-equiaxed features at the early stage of the microstructure evolution, under the temperature range from 975°C to 1010°C. The appearance of mixed morphology suggests that the mechanism leads to the early stage evolution is unlikely to be the shearing force induced by α→β (hcp→bcc) transformation, as proposed by Vilaro et al. (2011). Since the proposed shearing will break the columnar grains into several smaller grains, this means a direct

replacement of the original columnar morphology with a quasi-equiaxed morphology, without any intermediate transition. This proposed hypothesis cannot entirely explain the observed mixed morphology.

The observed early-stage microstructure evolution completes synchronously with the transformation of the α phase to the β phase, both of which also occurs in a similar temperature range. It suggests that there is a relationship between these two progressive processes. Idhil Ismail et al. (2016) suggest that, at a heating rate approximately 10°C/s, the mass fraction of β phase in Ti-6Al-4V is around 58% at 950°C, and 68% at 975°C. Considering that new features like grain boundary α and quasi-equiaxed prior-β grains begin to appear when the temperature approaches 975°C, it can be assumed that the microstructure evolution accumulates sufficient β phase in the α+β matrix, at least at a localised scale. The columnar feature does not eliminate until the material reaches its β transus temperature, suggesting that the retention of original features positively correlates to the remaining α in the α+β matrix.

The interpretation of the optical morphologies also suggests that the microstructure of SLM Ti-6Al-4V responds sensitively to the high temperature in the range from 965°C to 1010°C, where the different microstructure corresponds to a different temperature. Therefore, in the conducted gradient heating, microstructural morphologies can be used to interpret or represent the peak temperature the material experiences. In Figure 6.1, the microstructure located at the same height has no has no apparent or notable difference difference. Therefore, it can be assumed that the material located at the same height experienced a similar peak temperature during gradient heating, which suggests a uniform temperature distribution in the material at the same height of the sample from edge to centre during the induction heating.

6.2 The evolution of crystallographic texture during the early stages of β annealing

The microstructural evolution is identified as a progressive process with the existence of mixed prior-β grain morphology, as shown in Figure 6.1. In order to further study the beginning of the microstructural evolution, an area of approximately 6mm*1mm was scanned with EBSD, which was exposed to a limited temperature range around 975°C. The approximate location of the scanned area is highlighted by the black dotted line in Figure 6.1. The measured α orientation map is presented in Figure 6.4, where material located at a lower height in the map experienced a relatively lower temperature during the gradient heating.

At the location where material experienced a relatively lower temperature (bottom of Figure 6.4), it can be observed that, after cooling to room temperature, most of the α phases are interweaved α plate (lamellar α) with various orientations. This texture is similar to the typical α texture obtained after the sub-transus heat treatment, as described in Chapter 4, which suggests certain inheritance from the as-built microstructure. However, a few α colonies with irregular shape can be observed in the α matrix. Such features are distinct from the lamellar α. The observed α colonies are not inherited from the original microstructure, indicating that they are most likely transformed from the high temperature β. Therefore, it suggests the existence of β colonies in the α+β matrix, when the material was heated to the corresponding temperature.

Moving from the bottom towards the top in Figure 6.4, as the temperature increases, an increase of α colonies can be seen. The area fraction of the α colonies, as well as the size of individual α colony, are both increased. Such increases correspond to the increase in the mass fraction of the β phase at elevated temperatures (Idhil Ismail et al., 2016). The accumulation of β phase eliminates the original α phase locally, leading to the formation of β

colonies with irregular morphology. Coarsening of the remaining α plate can also be observed as the temperature increases, which suggests a competitive growth of α and β phase at a temperature lower than the β transus (Vrancken et al., 2012).

In order to plot the texture of prior-β grains at the early stage of the microstructure evolution, reconstruction of the β texture were conducted at four specified locations highlighted by the black line in Figure 6.4. The locations are numbered in the order of increasing temperature, as shown in Figure 6.4. Therefore, the material in Area 1 experienced the lowest peak temperature while the material in Area 4 experienced the highest peak temperature.

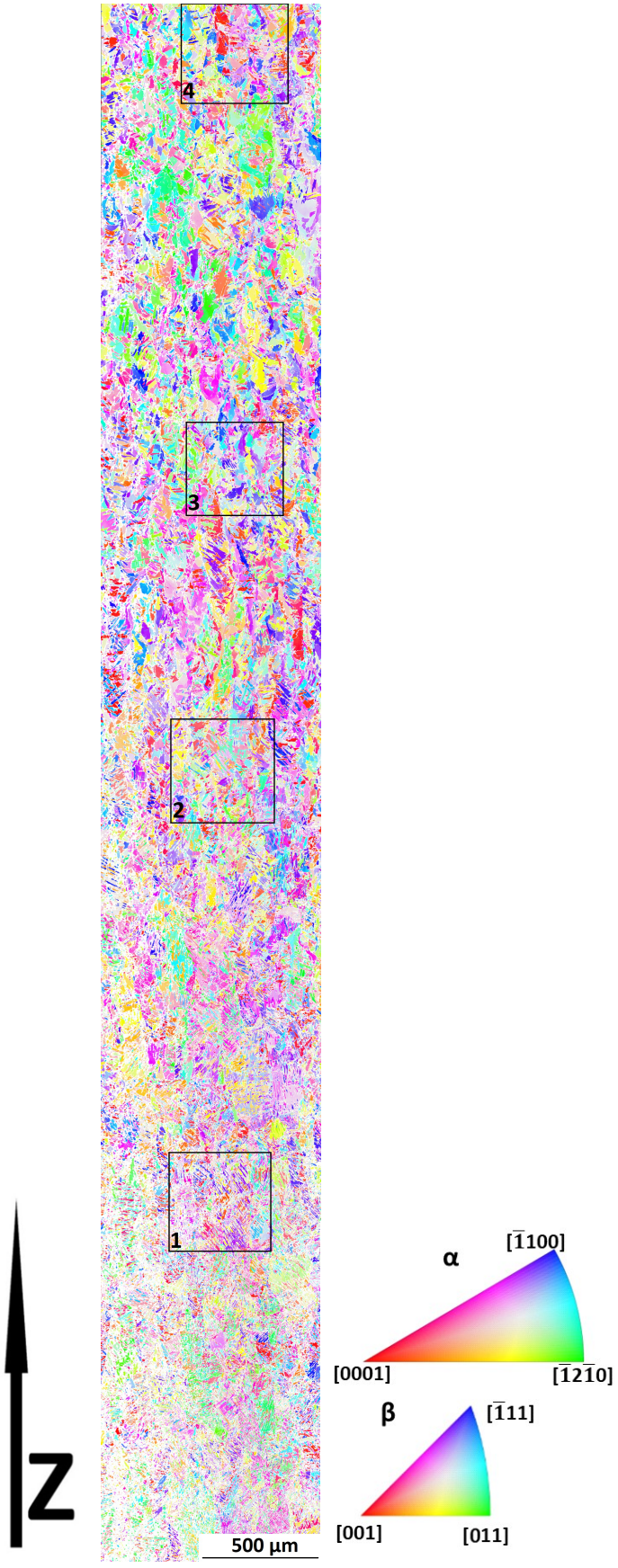


Figure 6.4. α orientation map in Z-IPF shows a continuously transformed texture of the α phase at the beginning of the microstructure evolution

Detailed α orientation map of Area 1 and the corresponding reconstructed β orientation map are presented in *Figure 6.5*. α orientation map in *Figure 6.5* (a) presents an α microstructure consisting of various interweaved α plates with a limited amount of α colonies, suggesting that Area 1 might capture the initial stages of the microstructural evolution. The primary morphology of the prior-β grains at this stage is still elongated and columnar, as shown in *Figure 6.5* (b). However, some fine equiaxed or quasi-equiaxed β grains with high angel boundaries (HABs) can be observed. Some of the fine β grains are indicated by white arrows in *Figure 6.5* (b).

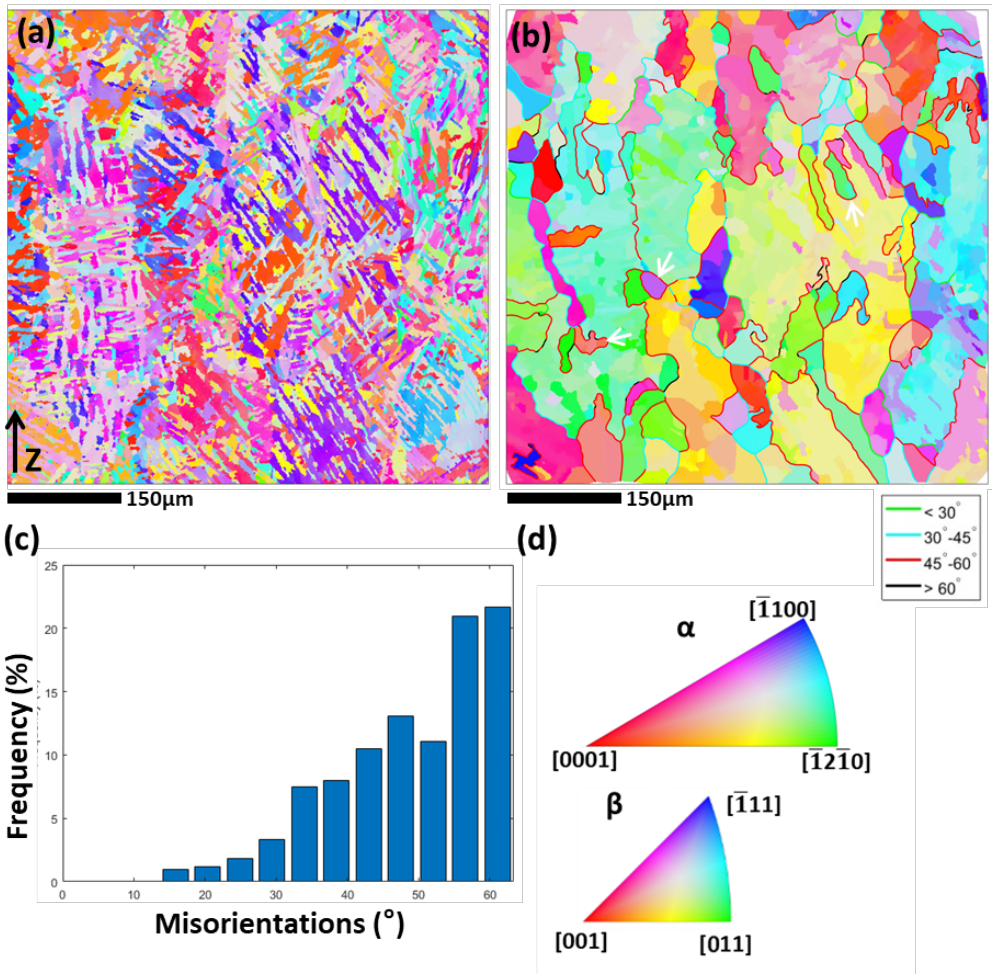


Figure 6.5.(a) α orientation map in Z-IPF of Area 1; (b) Corresponding reconstructed β-orientation map in Z-IPF, white arrows indicate some of the fine β grains; (c) The misorientation distribution at the prior-β grain boundary; (d) Standard colour scheme used to map the orientation data.

The misorientation distribution at the prior-β grain boundary in Area 1 is reported in Figure 6.5(c). In section 5.3.1, the misorientation distribution at the prior-β grain boundary in as-built condition was reported as spreading in a range between 15° to 65°, with moderate concentrate between 35° to 60°. A direct comparison between the misorientation distributions in these two conditions suggests an increase in HABs for the specimens that experienced heating up to a temperature just below 975°C. It indicates that the fine grains with HABs might form new structures, which is not strictly inherited from the original microstructure. This observation suggests that recrystallisation of β, which was identified in the induction heat treated SLM Ti-6Al-4V in chapter 4, might have already occurred at the initial stage of the microstructure evolution.

α orientation maps of Area 2 to 4 and the corresponding reconstructed β orientation maps are presented in Figure 6.6 to Figure 6.8, respectively. Compared to the initial stage α texture (Figure 6.5 (a)), an increase of the α colonies can be observed in α orientation maps, as shown in Figure 6.6 (a) to Figure 6.8 (a). Corresponding to that, an increase of HAB fine β grains can be observed from the β orientation maps, which leads to the weakening of the original coarse columnar morphology and the formation of a refined morphology, as shown in Figure 6.6 (b) to Figure 6.8 (b).

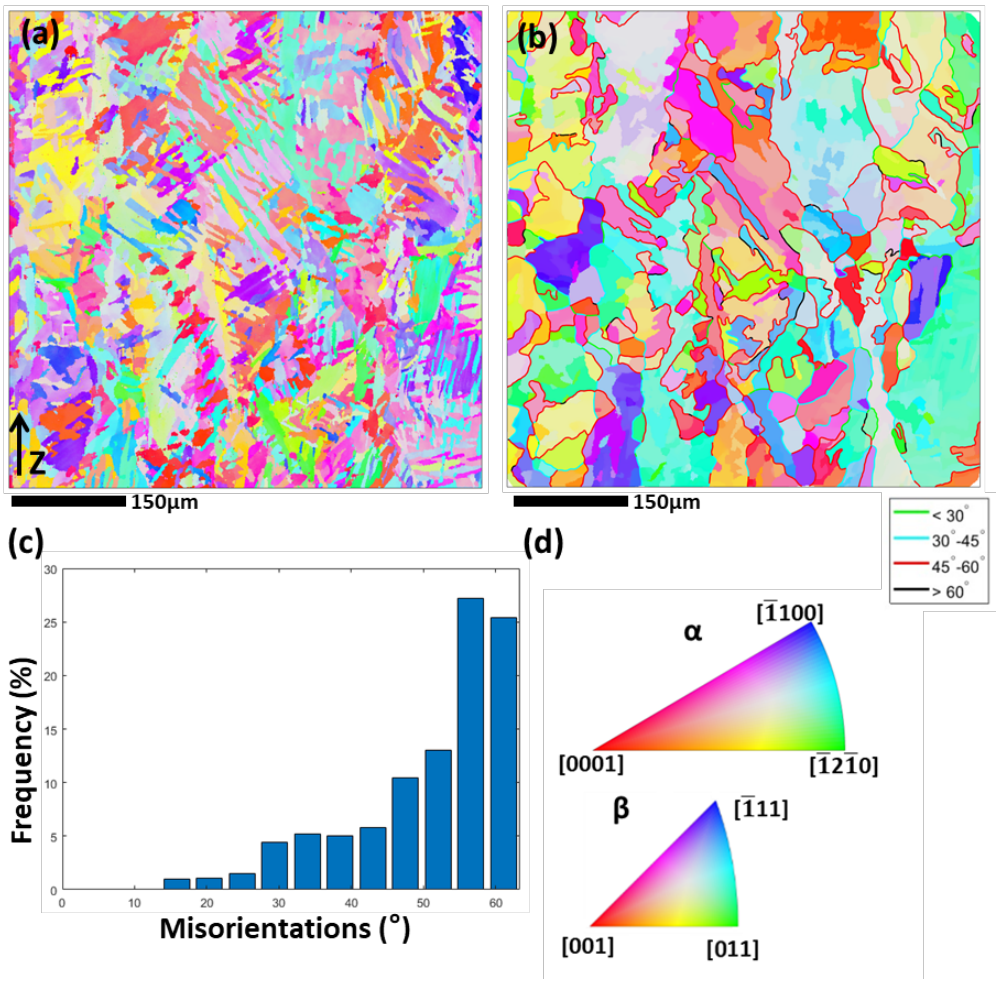


Figure 6.6. (a) α orientation map in Z-IPF of Area 2; (b) Corresponding reconstructed β-orientation map in Z-IPF; (c) The misorientation distribution at the prior-β grain boundary; (d) Standard colour scheme used to map the orientation data.

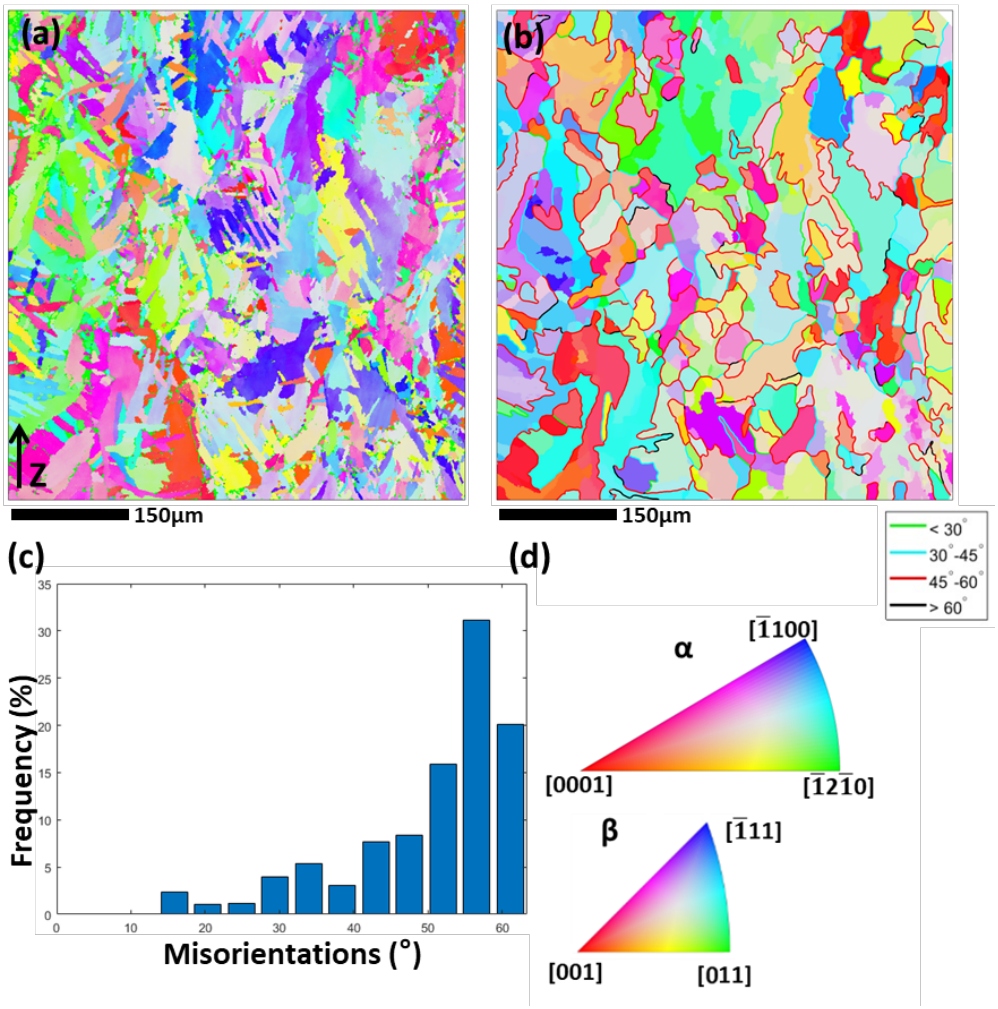


Figure 6.7. (a) α orientation map of Area 3 in Z-IPF; (b) Corresponding reconstructed β-orientation map in Z-IPF; (c) The misorientation distribution at the prior-β grain boundary; (d) Standard colour scheme used to map the orientation data.

In all 3 areas, the misorientation distribution at the prior-β grain boundary is highly concentrated in the high angles range around 60°, as demonstrated in histograms from Figure 6.6(c) to Figure 6.8(c), suggesting the further development of the recrystallisation. Therefore, one can assume that the nucleation and growth of the recrystallised HAB β at the elevated temperature near the β transus might result in the observed early stage microstructural evolution and the refinement of the prior-β grains.

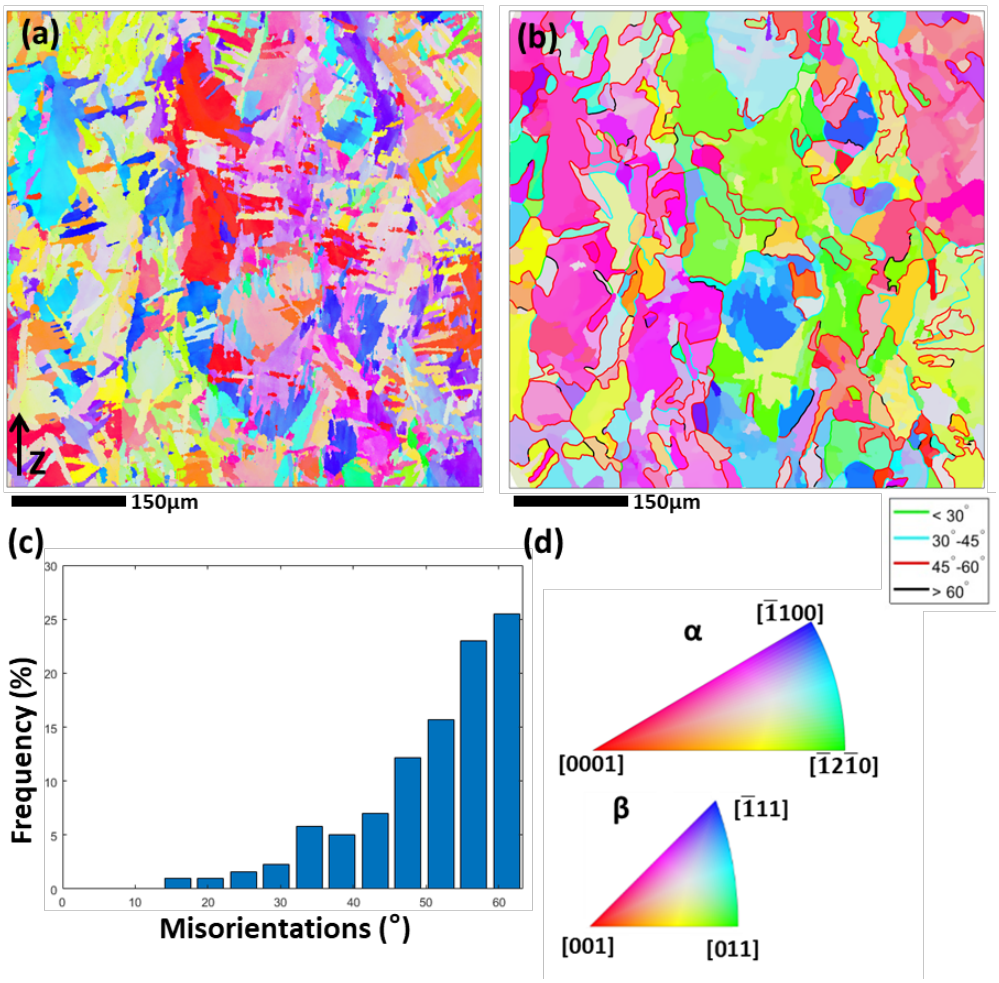


Figure 6.8. (a) α orientation map in Z-IPF of Area 4; (b) Corresponding reconstructed β-orientation map in Z-IPF; (c) The misorientation distribution at the prior-β grain boundary; (d) Standard colour scheme used to map the orientation data.

Due to the large computational requirements, the reconstruction of β texture was only conducted at limited areas in this chapter. Therefore, the orientation maps from Figure 6.5 to Figure 6.8 are from quite local regions of the sample, and might not reflect the entire story of the microstructural evolution. However, the evolution of the α texture can be well characterised by Figure 6.4, and the reconstruction of β texture was conducted at the sites where the α texture is quite representative. Therefore, it is believed that the conducted study can still provide useful insights related to the evolution of crystallographic texture during the early stages of β annealing

6.3 Summary

In this chapter, the early stage microstructural evolution during β annealing was characterised. The study of these stages is particularly important, as it could inform an effective strategy for controlling the original morphology of prior-β grains, an unwanted signature of the SLM manufacturing.

It is observed that the typical sub-transus heat treated texture develops to a mixed columnar and quasi-equiaxed morphology at a temperature between 965°C and 975°C. The microstructural morphology gradually develops with increasing of the quasi-equiaxed structure as the temperature rises. Eventually, it fully transforms to a refined quasi-equiaxed morphology when it temperature reaches β transus temperature.

Nucleation and growth of the recrystallised HAB β are identified at the initial stage of the microstructure evolution. This recrystallisation process weakens the original coarse columnar morphology and results in the refinement of the prior-β grains. The mechanism leads to observed recrystallisation, which will be further discussed in the next Chapter.

CHAPTER 7

7. Epitaxial recrystallisation of β grain in SLM Ti-6Al-4V during rapid heat treatment

In previous Chapters, recrystallisation of high angle boundary (HAB) β grain was characterised and identified in SLM Ti-6Al-4V annealed at a temperature near or above the β transus. The nucleation and growth of the recrystallised HAB β grains weaken the original coarse columnar morphology of prior-β grains and results in a gradual replacement of the columnar morphology with refined quasi-equiaxed morphology.

The current understanding, which associates with the nucleation and growth of the β phase during conventional heat treatment of martensitic Ti-6Al-4V, does not explain the observed recrystallisation and the refinement of the β grains during the rapid heating of specimens produced by SLM. In order to understand the mechanisms and the nature of this recrystallisation, high-temperature EBSD investigations of the SLM Ti-6Al-4V were conducted. A heating rate of 0.5°C/s was used for all the high-temperature EBSD investigations in this chapter.

In this chapter, the initial high-temperature EBSD investigation, which only scanned a relatively small area, is reported in section 7.1. The scanned area is about 24μm in width and 18μm in height. Through this investigation, the development of individual α/β grain during heating can be observed. In addition, the relationship between the newly formed β grain and the surrounding α grains can be studied. Therefore, the nature of these β grain can be identified and discussed.

The following high-temperature EBSD investigation, which scanned a larger area, is reported in section 7.2. The scanned area is about 350μm in width and 260μm in height. Through this investigation, the recrystallisation of β can be discussed from a more general view. The influence of the recrystallisation on the original β texture is also analysed in this section.

Without additional specification, all the microstructure images and orientation maps in this chapter are analysed on the frontal plane of the specimens, in which the building direction (Z direction) is parallel to the height of the image, as indicated in Figure 7.1 (a). The orientation data all mapped in Z-IPF with the colour scheme presented in Figure 7.1 (d).

7.1 Development of α and β phase in SLM Ti-6Al-4V during heating

7.1.1 Microstructural evolution from room temperature to 800°C

The room temperature microstructure of the observed area in the initial high-temperature EBSD scan of SLM Ti-6Al-4V is shown in Figure 7.1. A fully acicular α' martensitic microstructure is observed, as shown in Figure 7.1 (a) and (b), with no retained β in the structure, as shown in Figure 7.1 (c). Only vertical prior-β structure can be identified from forescatter electron micrographs. The boundary of the prior- β grain is indicated by white arrows shown in Figure 7.1 (a). Multiple α' grains of distinct orientations are visible in the prior-β microstructure, and reveal a weak crystallographic texture.

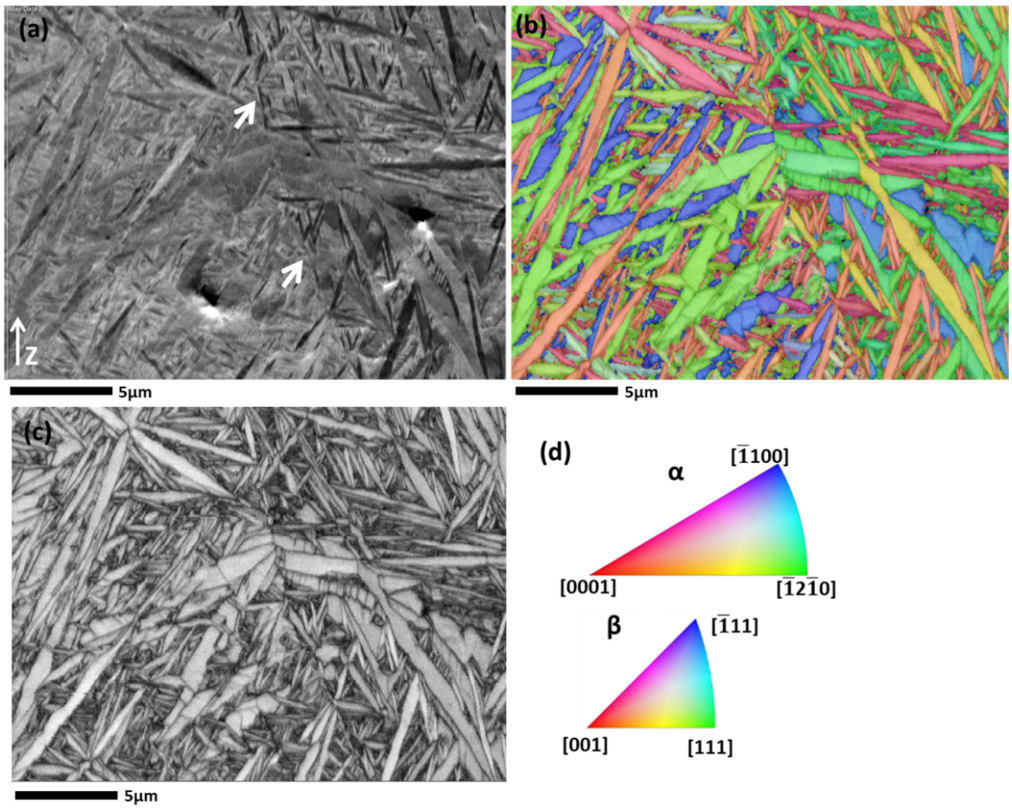


Figure 7.1. Room temperature microstructure of the observed area in the high-temperature EBSD scan of SLM Ti-6Al-4V: (a) Microstructure image captured by forescatter detectors; (b) Measured α orientation map in Z-IPF overlaid on band contrast image; (c) Measured β orientation map in Z-IPF overlaid on band contrast image; (d) Standard colour scheme used to map the orientation data.

As the temperature rises, no visible microstructural changes can be observed at 400°C and 500°C, as shown in Figure 7.2. At this relatively low temperature, only recovery of the sub-grain structure occurs, which includes relaxation of the residual stress, annihilation and rearrangement of the dislocations (Callister and Rethwisch, 2007). This recovery process occurs without the migration of any high-angle grain boundaries and will not trigger any evolution in the microstructural constituents (Callister and Rethwisch, 2007, Sallica-Leva et al., 2016). Therefore, no visible changes can be noticed in the forescatter electron micrographs.

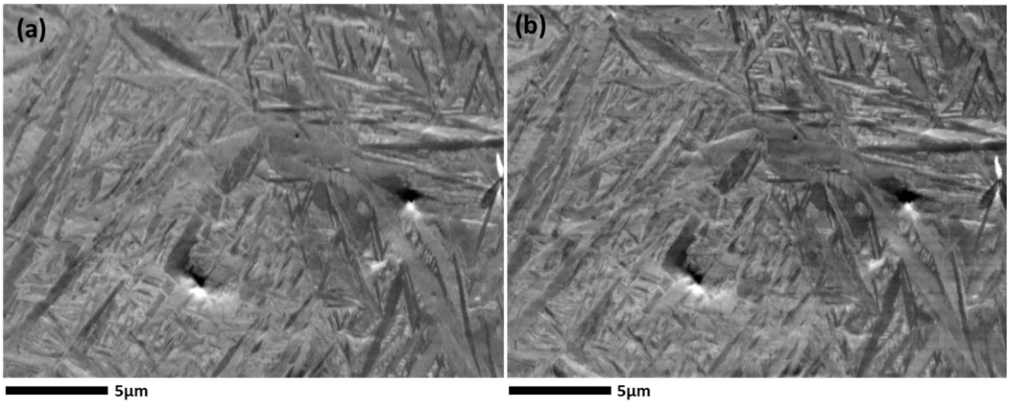


Figure 7.2. Forescatter electron micrographs showing the microstructure of the observed area: (a) at 400°C; (b) at 500°C.

Visible changes can be observed at a higher temperature. Coarsening of the microstructure can be noticed at 600°C, as shown in Figure 7.3 (a), which leads to emerging of the topographical feature in the image. At 700°C, the forescatter detectors are completely saturated. The microstructure image is captured by secondary electron detectors hereafter, as shown in Figure 7.3 (b). At this temperature, the grain structure appears more clearly and the boundary of each α/α' grain is well marked. Solute diffusion and elements partitioning become significant at an elevated temperature, which leads to the decomposition of α' into α+β (Sallica-Leva et al., 2016, Zhang et al., 2018). The visible changes of the topography of the grain boundary it is likely to be associated to the nucleation and growth of the β phase, which takes place at the boundary of the newly formed α phases (Zhang et al., 2018).

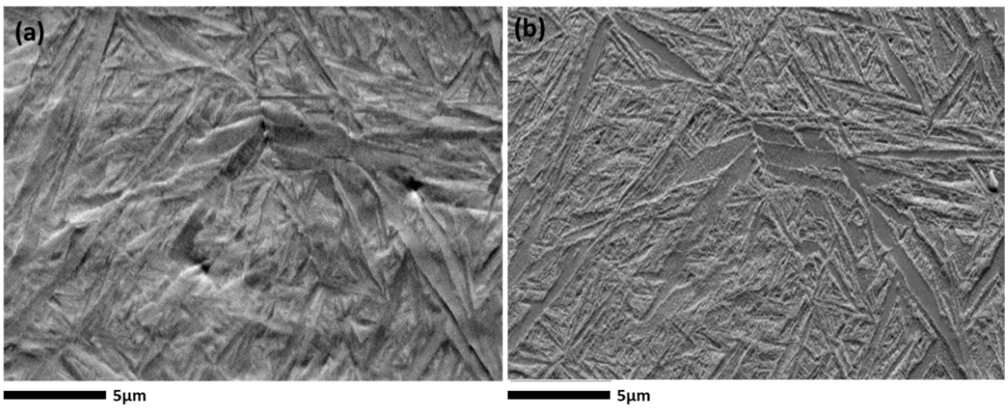


Figure 7.3. Microstructure image of the observed area, obtained at an elevated temperature: (a) at 600°C, captured by forescatter detectors; (b) at 700°C, captured by secondary electrons detectors.

Microstructure at 800°C is depicted in Figure 7.4. At this temperature, it is expected that the original α' is nearly fully decomposed (Wu et al., 2016c). A further coarsening of the α phase is observed in the image.

The inserts in Figure 7.4 show the orientation maps of α and β phase of the marked area, respectively. Both maps are overlaid with band contrast images in order to distinguish different grains. Notable growth of β phase can be observed not only at the α boundary but also in the interior of the α phase. A recent study suggests that for Ti-6Al-4V, other than nucleation at the vanadium enrich area located between α phases, the β phase can also nucleate at the lattice defects (dislocations, twins, sub-grain boundaries etc.) within α/α' phases during heating (Haubrich et al., 2019). The observed interior β could be one of those β, which have nucleated at the lattice defects located within the α/α' phase.

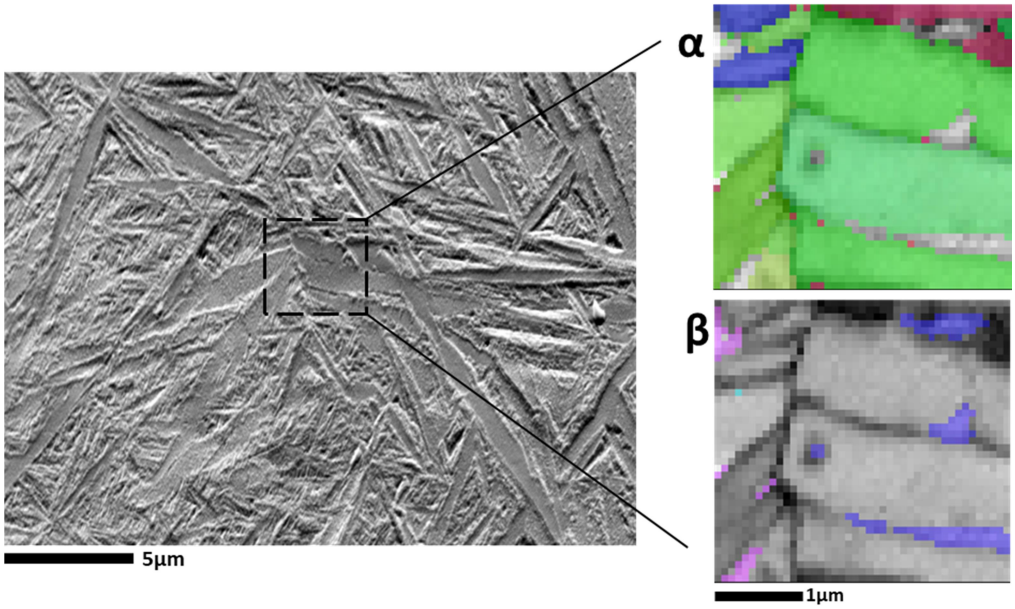


Figure 7.4. Secondary electrons micrographs showing the microstructure of the observed area at 800°C, with insets showing α and β orientation maps in Z-IPF (overlaid with band contrast image) of the marked area respectively.

7.1.2 Recrystallisation of β grain observed in the microstructure at 850°C

The α/β transformation continues at 850°C, as shown in Figure 7.5. At this temperature, regions that consist of β phases, which can be identified from the orientation map, are covered with a specific stepped topography in the electron image. This topography might be the result of the bcc structure of the β phase

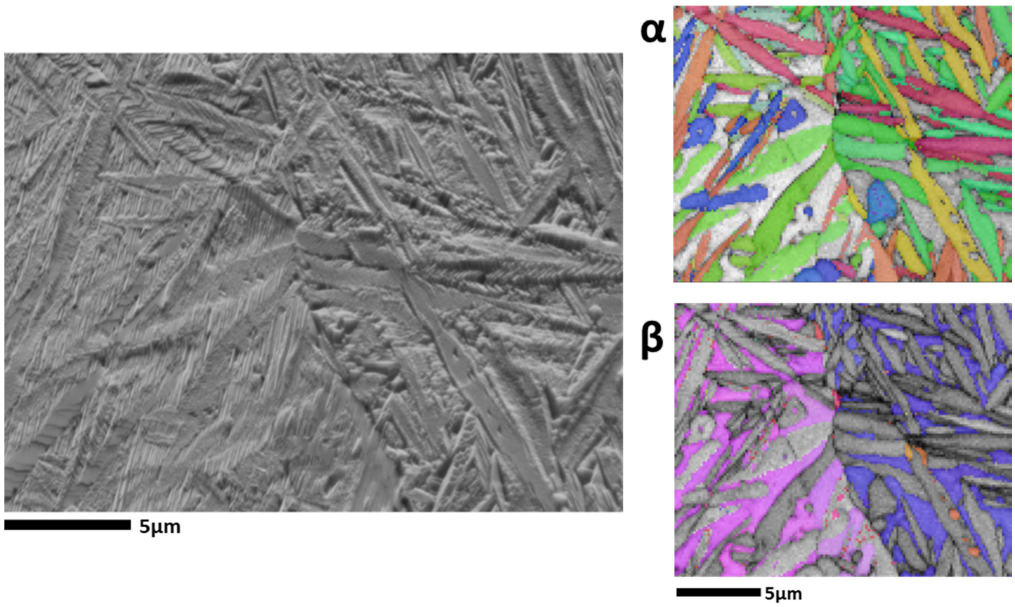


Figure 7.5. Secondary electrons micrograph showing the microstructure of the observed area at 850°C, orientation maps in Z-IPF overlaid with band contrast image showing the crystallographic texture.

Orientation maps of α and β phases at 850°C are enlarged in Figure 7.6. The orientation maps show two distinct prior-β grains, both of which contains multiple α variants. Within each prior-β grain, the dominant β is similarly orientated across the length of the entire prior-β grain (orientation spread <10°), as shown in Figure 7.6 (b). For the prior-β grain located at the left side of the image (hereafter called as G_L), the orientation of the dominant β (β_1) is colour coded in magenta. For the prior-β grain located at the right side of the image (hereafter called as G_R), the orientation of the dominant β (β_2) is colour coded in slate blue. Other than two dominant β, few foreign β with different orientation (HAB β) can be noticed in Figure 7.6 (b). Some of them are colour coded in orange (β_3) located at the boundary and interior of the α grain (α_8). Others are colour coded in purple-red (β_4) or red (β_5), located at the prior-β grain boundary. The average orientations of each marked grains in Figure 7.6 are listed in Table 7.1.

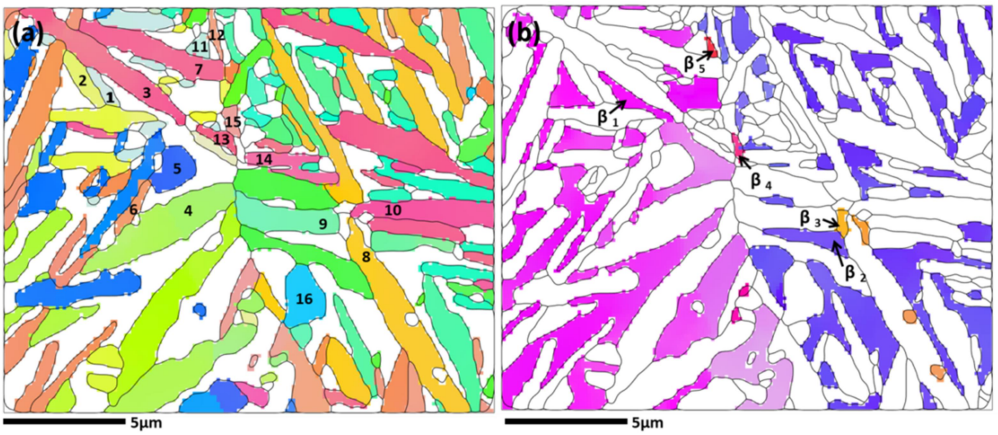


Figure 7.6. Detailed orientation map in Z-IPF showing the crystallographic texture at 850°C: (a) α phases; (b) β phases.

Table 7.1. Average orientation of marked grains in Figure 7.6

ID	Orientation in Euler angles
α_1	(150°, 112°, 194°)
α_2	(117°, 61°, 235°)
α_3	(38°, 31°, 198°)
α_4	(83°, 110°, 236°)
α_5	(25°, 88°, 205°)
α_6	(37°, 29°, 188°)
α_7	(16°, 149°, 200°)
α_8	(6°, 137°, 239°)
α_9	(153°, 97°, 183°)
α_{10}	(110°, 145°, 219°)
α_{11}	(84°, 109°, 227°)
α_{12}	(109°, 145°, 229°)
α_{13}	(31°, 26°, 201°)
α_{14}	(110°, 145°, 219°)
α_{15}	(107°, 145°, 226°)
α_{16}	(93°, 88°, 220°)
β_1	(118°, 150°, 226°)
β_2	(181°, 135°, 221°)

β_3	(94°, 165°, 194°)
β_4	(240°, 166°, 232°)
β_5	(215°, 173°, 238°)

The further understanding the information embedded in Figure 7.6, the orientation relationship between the individual β and adjacent α is expressed in the corresponding pole figure presented in Figure 7.7 and Figure 7.8. In the pole figures, the reflections of the orientations are plotted via the representing colour of each grain. Therefore, for example, the light green points in Figure 7.7(a) represent the orientation of α_4 in *Figure 7.6* (a), while royal blue points represent α5.

The orientation relationship between the dominant β and the multiple α variants across the prior-β grain is firstly expressed in Figure 7.7. The pole figures of the dominant β in G_L, β_1, are compared with pole figures of α_1 to α_7, which are also located in the G_L, as shown in Figure 7.7 (a). It can be noticed that the (0001) α plane of each α lath is parallel to one of the (110) β planes of β_1, while one to three <11$\bar{2}$0> α reflections are parallel to one of the <111> β. This parallelism indicates that the β_1 is the parent phase of α_1 to α_7, and that they are strictly related via Burger Orientation Relationship (BOR). A similar orientation relationship is found in Figure 7.7 (b), which suggests β_2 is the parent phase of α_8, α_9, α_{10} and α_{16}. To further support this conclusion, the theoretical value of the orientation of some parent β are calculated in Table 7.2. Each parent β corresponds to different α combinations, and calculation is conducted based on the BOR. The calculated misorientation between these theoretical values and measured β is also given in the table, which shows that the differences are marginal. This indicates that the observed dominant β in the β orientation map is the parent β, which is related to each α/α' within the prior-β grain via BOR.

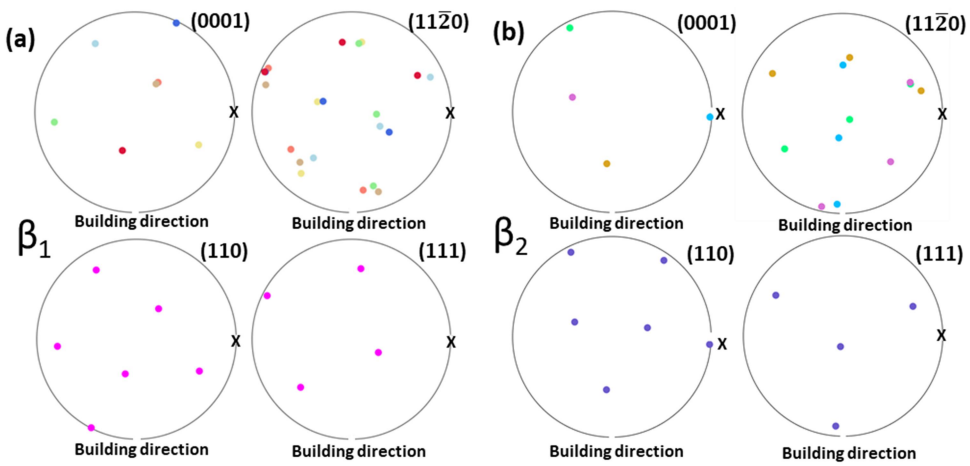


Figure 7.7. Pole figures representing the orientation of the investigated α/β grains. These demonstrate the orientation relationship between the dominant β and a cluster of nearby α laths in the prior-β grain: (a) α_1 to α_7 vs β_1; (b) $\alpha_8/\alpha_9/\alpha_{10}/\alpha_{16}$ vs β_2.

Table 7.2. Calculated parent β orientation for different α combination

Combination of α	Corresponding parent β	Misorientation with dominate β
$\alpha_1+\alpha_2+\alpha_3$	(248.293°, 109.645°, 338.438°)	1.1541°
$\alpha_4+\alpha_5+\alpha_6$	(165.621°, 70.5623°, 336.266°)	2.6683°
$\alpha_8+\alpha_9+\alpha_{10}$	(0.1845°, 47.1474°, 228.963°)	2.3447°

The orientation relationship between the foreign HAB β and the corresponding adjacent α is expressed in Figure 7.8. The analysis shows that β_3 and β_4 are crystallographically related to individual adjacent α/α' laths via BOR, as shown in Figure 7.8 (a) and (b) respectively. Black circles are used to mark the BOR relationship between the foreign HAB β and the corresponding adjacent α. Both β_3 and β_4 have a ~60° misorientation with the surrounding dominant β (β_2). Such misorientation is not random but related to β_2 by precise axis-angle rotation pairs, as shown in Table 7.3. Therefore β_3 and β_4 appear to be the nuclei of epitaxially recrystallised β, which is similar to that recently observed in hot-worked metastable β titanium alloy (Balachandran

et al., 2017). These sub-grains correspond effectively to one of the six equivalent BOR transformations that link α to β phases.

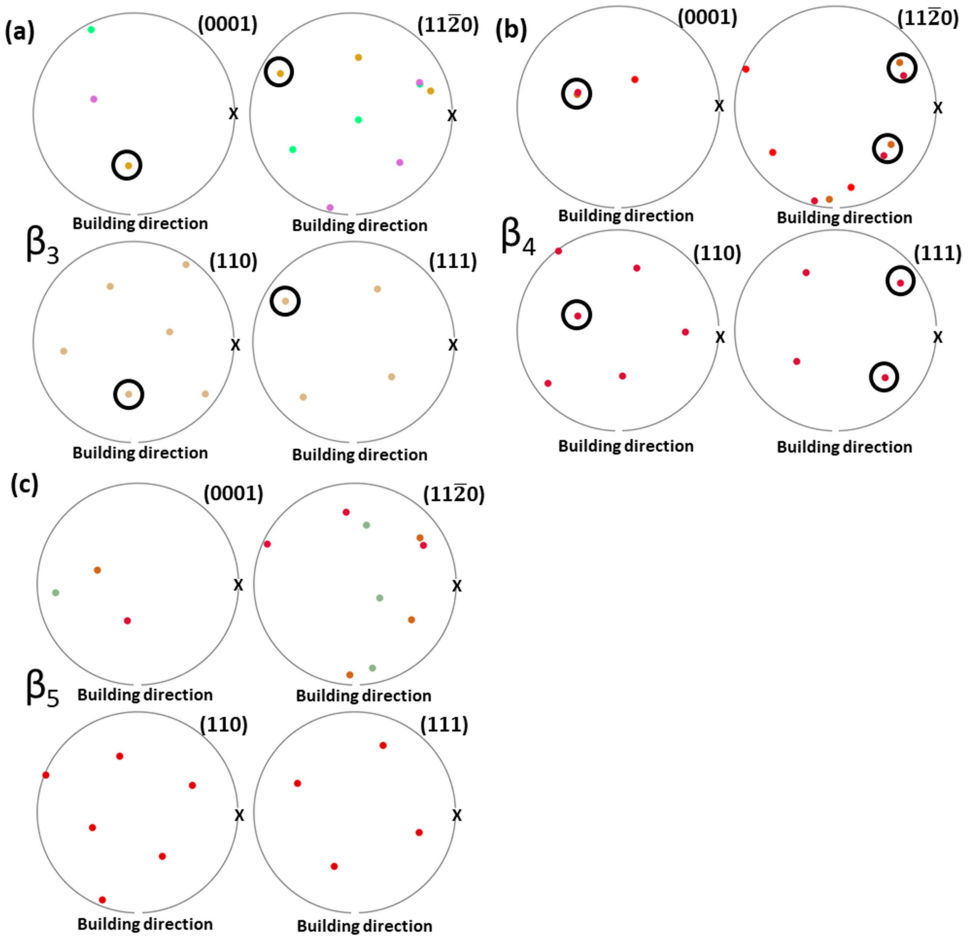


Figure 7.8. Pole figures representing the orientation of the investigated α/β grains. These demonstrate the orientation relationship between the foreign HAB β and corresponding adjacent α: (a) $\alpha_8/\alpha_9/\alpha_{10}$ vs β_3; (b) $\alpha_{13}/\alpha_{14}/\alpha_{15}$ vs β_4; (c) $\alpha_7/\alpha_{11}/\alpha_{12}$ vs β_5.

Table 7.3. Misorientations of β_3 and β_4 to the surrounding dominant β_2

	Grain	Misorientation (axis/angle)
Surrounding dominant β_2 (181°, 135°, 221°)	β_3	[-1, 1, 1]/60.00°
	β_4	[-1, 0, 1]/60.00°

In addition, it is observed in *Figure 7.8* (c) that there is another HAB β (β_5) that does not show any apparent orientation relationship with adjacent α/α' laths. The misorientation of β_5 relative to dominant β (both β_1 and β_2) cannot

be described by any meaningful axis-angle rotation pair. However, it cannot be excluded that β_5 originates from similar recrystallisation mechanisms originating under the plane of investigation, as it will be discussed later in section 7.2.

The analysis indicates that three types of β grains are identified in SLM Ti-6Al-4V at 850°C, a temperature that is below the β transus:

- Dominant β within the prior-β grain, which is related to the whole cluster of adjacent α/α' laths via BOR, located only between α/α' laths. This is the parent β, and hereafter will be referred to as β_A
- Recrystallised β, which is related to individual adjacent α/α' laths via BOR, located in the interior of individual α/α', between α/α' lath or at the prior-β grain boundary. It is the epitaxially recrystallised β, and hereafter will be referred to as β_B
- Recrystallised β, which does not show any apparent orientation relationship with adjacent α/α' laths, located only at the prior-β grain boundary. The nature of this recrystallised β needs further discussion. This type of β will be referred to as β_C hereafter.

The recrystallisation phenomena that lead to the formation of HAB β are significantly different from the recovery of the α+β microstructure and the grain growth of the parent β phase (β_A) (Zhang et al., 2018, Idhil Ismail et al., 2016) and, to the authors knowledge, have not been reported before in any Ti alloys produced by any AM process. Drawing an analogy with the recrystallisation of deformed Ti alloys, it is assumed that the driving force for the observed epitaxial recrystallisation derives from the stored energy of deformation that is typically expressed by the high densities of lattice defects found after SLM in the core and at the boundary of the martensitic as-built microstructure (Wang et al., 2017). Haubrich et al. (2019) recently reported the observation of β nucleated at lattice defects within individual α grain in SLM Ti-6Al-4V. The substructure of the martensitic α', like low angle boundary, dislocations and twins, could therefore act as a nucleation site for

epitaxial recrystallised β allowing the formation of new variants during the α+β→β transformation.

Previous research indicates that under similar heating rates of ~10°C/s, there is only a marginal increase in the temperature of the onset α→β transformation (Idhil Ismail et al., 2016) and therefore the high-temperature EBSD (near equilibrium conditions) experiments presented in this study can capture the range of temperatures at which the phase transformation occurs during the applied rapid induction heat treatment. It is also well understood, however, that rapid heating processes (like induction heating) can retain the substructure of the martensitic phase to higher temperatures and promote higher nucleation rates of HAB grains (Ivasishin and Teliovich, 1999), which would exacerbate epitaxial recrystallisation and result in observed significant refinement of the structure as reported in Chapter 5 and Chapter 6.

7.1.3 Microstructural evolution above 850°C

As the temperature increases from 850°C and approaches towards the β transus temperature, more and more α converts to the β phase. The microstructure at 900°C is shown in Figure 7.9, an increase of area covered by stepped topography can be observed when compared to Figure 7.5, which evidences the increase of β phase in the α+β matrix.

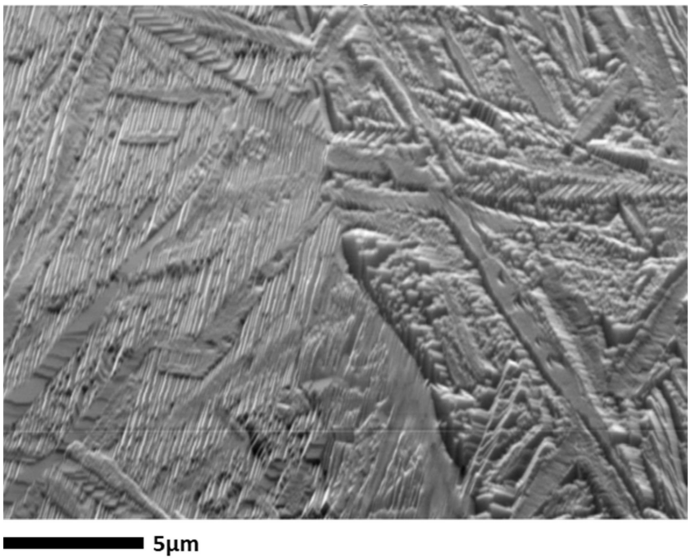


Figure 7.9. Secondary electron micrograph showing the microstructure of the observed area at 900°C.

At 950°C, only a limited amount of α is remained, as shown in Figure 7.10. The substructure within the α grain is so apparent at this temperature that can be directly identified in the electron image, as pointed by the white arrow. Recrystallised HAB β can be observed at the prior-β grain boundary, which colour coded in orange as pointed by the black arrow.

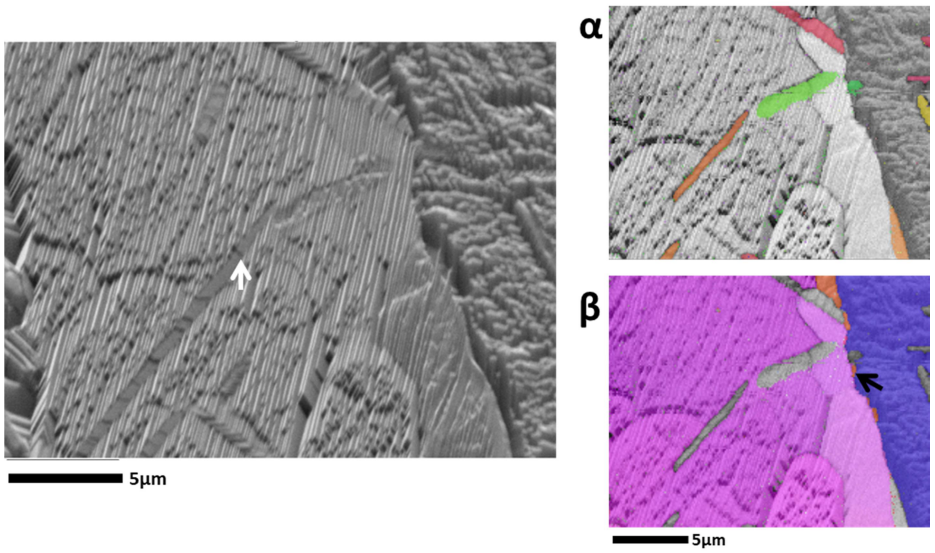


Figure 7.10. Secondary electrons micrograph showing the microstructure of the observed area at 950°C, orientation maps in Z-IPF overlaid with band contrast image showing the crystallographic texture.

The observed region at 950°C is slightly shifted compared to the starting position. It is because the focusing and adjusting are affected by the extremely high temperature, which reaches the limitation of the apparatus. However, by matching the orientation of the remaining α with the α orientation map obtained at 850°C, the relative position can still be determined, as shown in Figure 7.11. In Figure 7.11, the α grains with the same orientation at 850°C and 950°C are marked with the same number. By comparing the locations of the same orientated α grains, it can be noticed that the original prior-β grain boundary remains unchanged at 950°C, which corresponds to what was reported in Chapter 6.

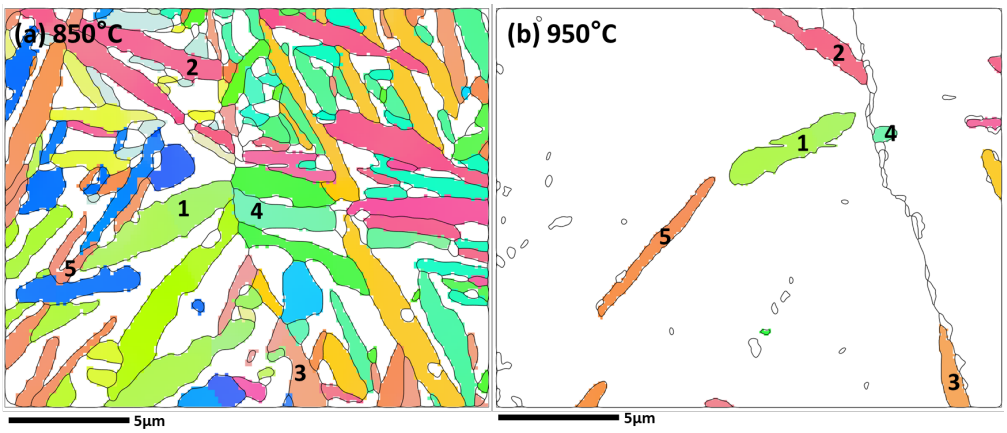


Figure 7.11. α orientation map in Z-IPF of obtained at different temperatures, the observed region is slightly shifted between the two observation: (a) 850°C; (b) 950°C. α grains with the same orientation at different temperature are marked with the same number. Therefore, the relative position can still be determined.

With the specimen approaching the β transus temperature, the amount of retained α decreases significantly (Idhil Ismail et al., 2016). Therefore, α phases could be locally eliminated in some areas. The microstructure of the observed region at 980°C is presented in Figure 7.12. No α phase is presented in the observed region at this temperature as suggested by the stepped topography evident in the micrograph. It can be seen that the original prior-β grain boundary is also eliminated from the observed region. Since the remaining α and original prior-β grain boundary are eliminated simultaneously, it can be assumed that during the heating process, the

original prior-β grain boundaries is pinned by the remaining α. Should be noted here that at this stage, the instrument has already reached its limit. Therefore, it is possible that the recorded temperature of 980°C is not an accurate measurement, the real temperature may be higher than that value, which could also be the reason why α phase is eliminated in the observed area.

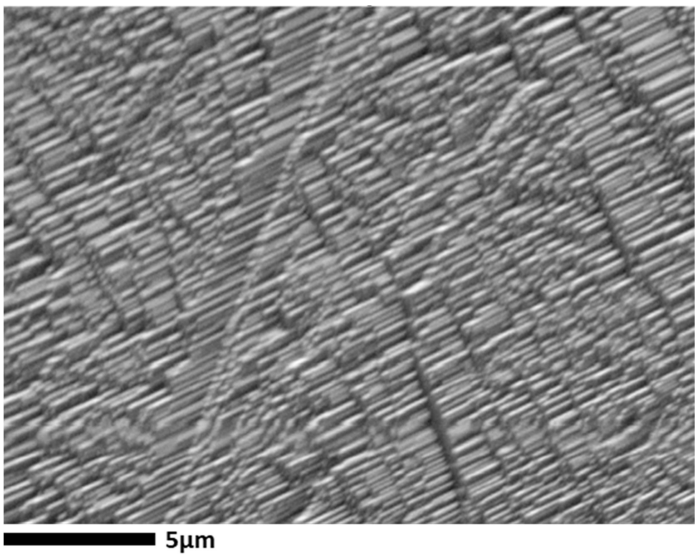


Figure 7.12. Secondary electrons micrograph showing the microstructure of the observed area at 980°C.

7.2 Development of the recrystallised β in SLM Ti-6Al-4V during heat treatment

In the initial high-temperature EBSD investigation of SLM Ti-6Al-4V, which is reported in section 7.1, the recrystallisation of HAB β at 850°C are detail identified and analysed locally. The mechanism that may induce the recrystallisation is also discussed. In order to investigate the recrystallisation phenomena of SLM Ti-6Al-4V from a more general view, and its influence on the original β texture, further high-temperature EBSD investigations ware carried out.

In the present high-temperature EBSD investigation of SLM Ti-6Al-4V, a relatively large area of approx. 350µm*260 µm was scanned. The measured

room temperature α orientation map and the reconstructed β orientation map of the observed area are revealed in Figure 7.13, which show the starting microstructure. A typical as-built microstructure is presented in the images.

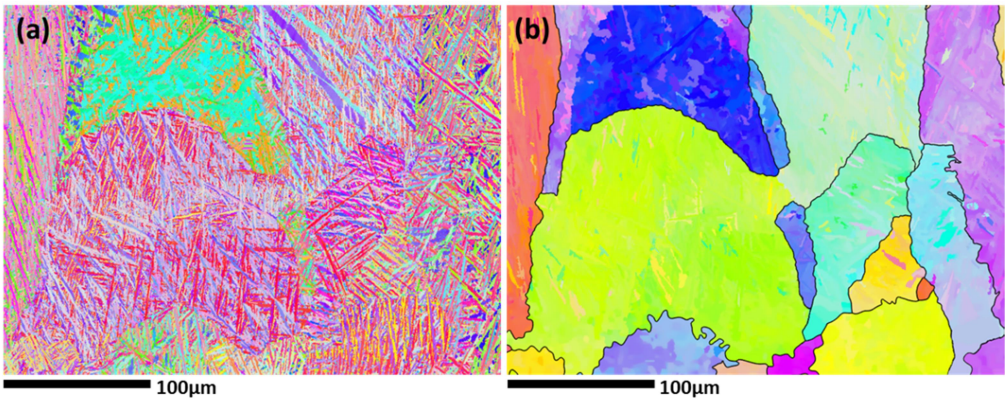


Figure 7.13. Room temperature microstructure of observed area in the present high-temperature EBSD scan of SLM Ti-6Al-4V: (a) Measured α orientation map in Z-IPF; (b) Reconstructed β orientation map in Z-IPF.

As the temperature rises, the microstructure at 850°C is shown in Figure 7.14. By comparing the β orientation map at 850°C (Figure 7.14 (b)) with the room temperature ones (Figure 7.13 (b)), parent β grains and recrystallised β grains can be easily identified. Four of the recrystallised β grains are marked and numbered with black arrows in Figure 7.14 (b), their relative positions in the α orientation map are also circled out with black dotted lines. Among these four grains, β_{21} is located in the interior of prior-β grain, while the remaining three are all located at the prior-β grain boundaries.

The orientation relationship between these four recrystallised β grains and their corresponding adjacent α grains are analysed in Figure 7.15. The pole figures show that both of the two types of the recrystallised β, which are summarised in section 7.1.2, can be identified in this dataset. Both β_{21}, β_{22} and β_{24} are related to individual adjacent α/α' laths via BOR, as shown in Figure 7.15 (a), (b) and (d) respectively. Therefore, they belong to the category of β_B. While β_{23} does not show any apparent orientation

relationship with adjacent α/α’ laths, as shown in Figure 7.15 (c), can be categorised as β_c.

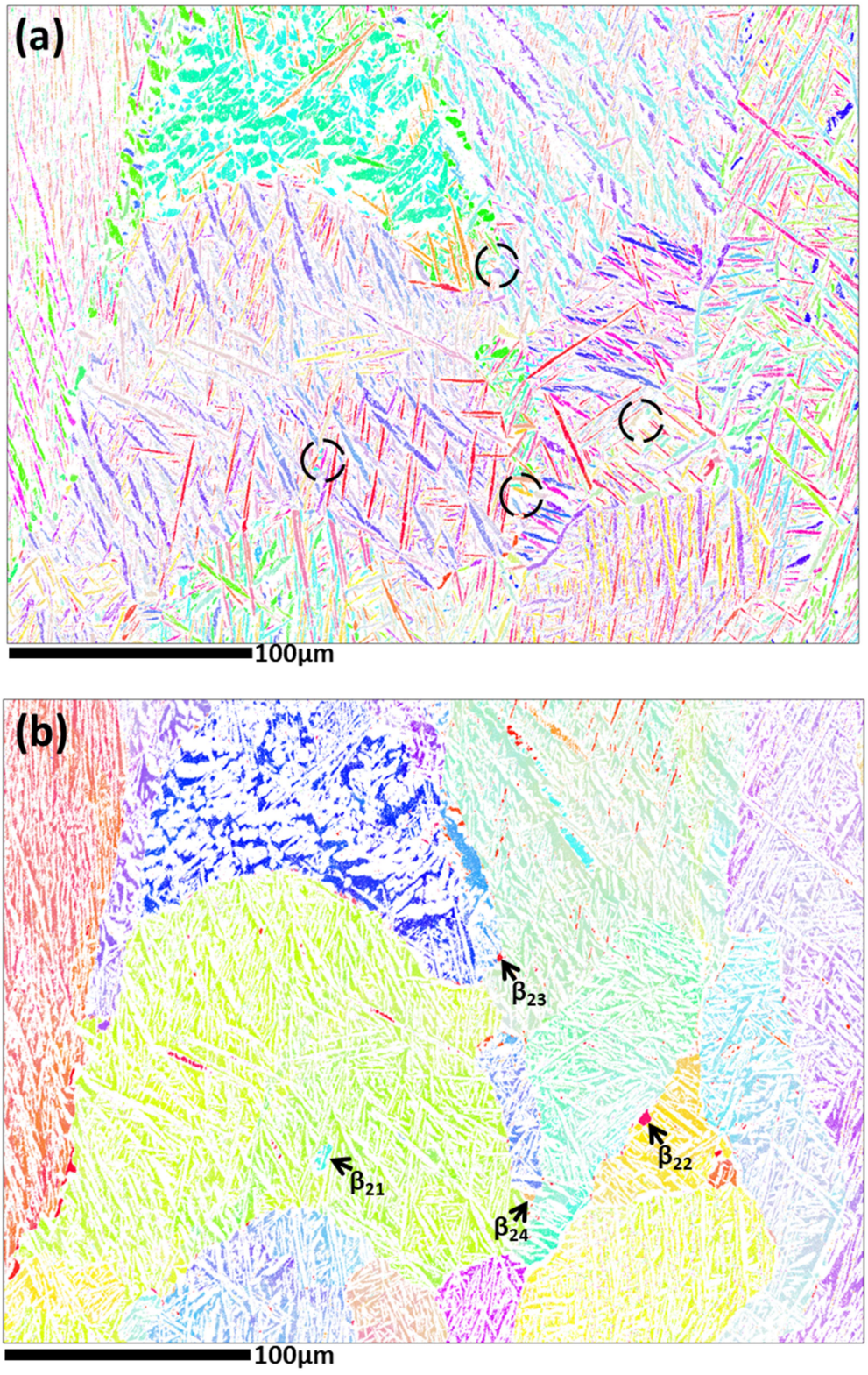


Figure 7.14. Microstructure of the observed area at 850°C: (a) Measured α orientation map in Z-IPF; (b) Measured β orientation map in Z-IPF. Four of the recrystallised β grains are marked and numbered with black arrows, their

relative positions in the α orientation map are also circled out with black dotted lines.

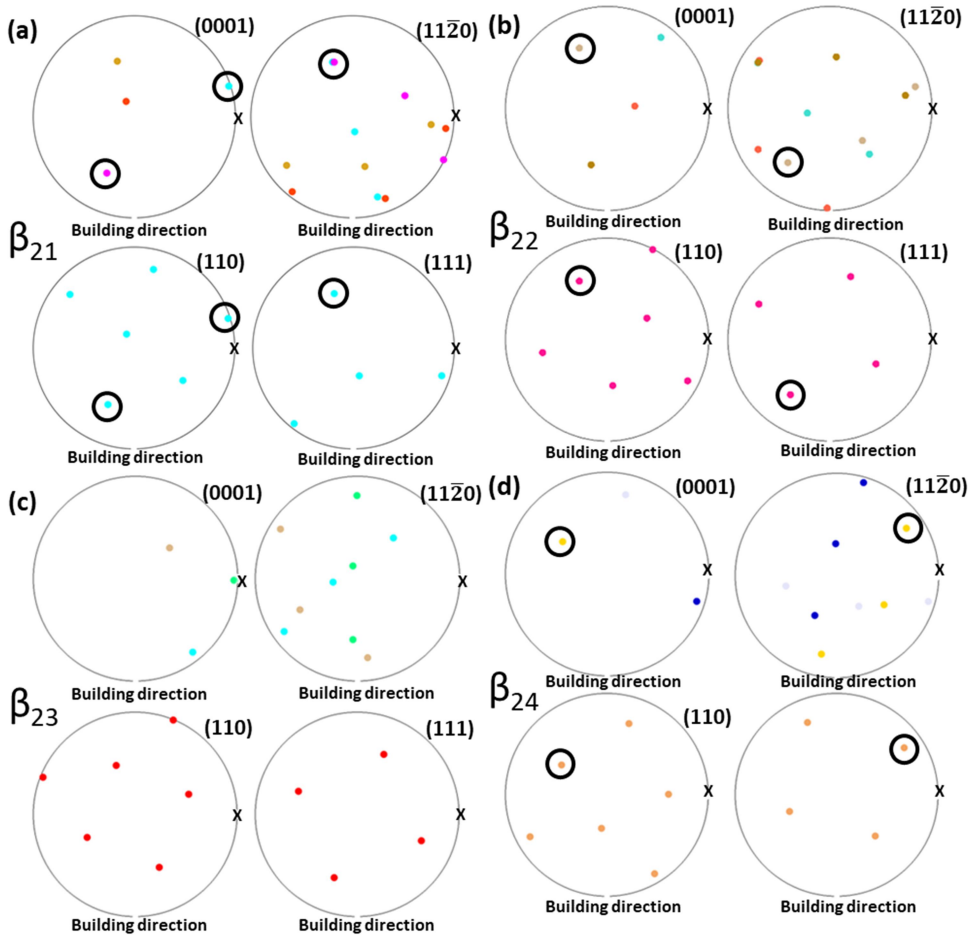


Figure 7.15. Pole figures representing the orientation of the investigated α/β grains. These demonstrate the orientation relationship between the marked recrystallised β and corresponding adjacent α: (a) β_{21}; (b) β_{22}; (c) β_{23}; (d) β_{24}.

When the temperature is further increased to 925°C, more β phase is transformed from the α phase, as evidenced in Figure 7.16. As the temperature is increased from 850° to 925°C, comparing Figure 7.16 (b) to Figure 7.14 (b), an increase in the amount of recrystallised HAB β can be observed. Other than that, it is observed that the recrystallised β grains grow competitively with the surrounding matrix (β_A) and that some of the newly formed grains grow faster than others. In addition, these grains grow with no preferred grain growth direction aligned to any of sample coordinate system (as the heating is uniform as opposed to the directional heating imposed by SLM). The retained α laths pin the original prior-β grain boundaries locally,

and therefore the overall β morphology remains unchanged during heat treatments below the β transus temperature. Subsequently, as the heating approaches towards the β transus temperature, no α-pinning could take place. It is plausible that the HAB, of higher mobility than the surrounding matrix β_A, could migrate at a higher rate (Pilchak et al., 2017) and thus change the original columnar morphology to an equiaxed or quasi-equiaxed morphology, as reported in Chapter 5 and 6.

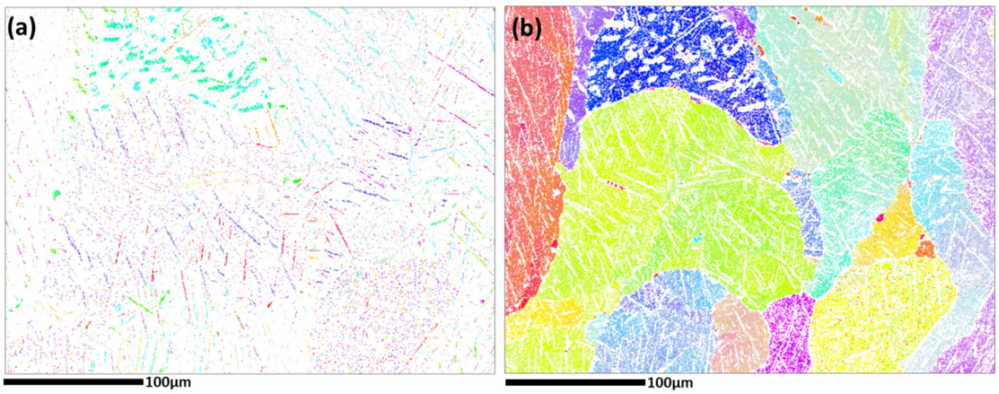


Figure 7.16. The evolved microstructure of the observed area at 925°C, showing an increase in the amount of recrystallised HAB β comparing to the microstructure at a relatively low temperature: (a) Measured α orientation map in Z-IPF; (b) Measured β orientation map in Z-IPF

In order to examine the possible evolution of the texture during heat treatment, the pole figures of the reconstructed as-built β texture are compared to the β texture measured at the elevated temperature, as shown in Figure 7.17. Above the β transus temperature, abnormal grain growth occurs, so it was not possible to directly observe changes in texture via EBSD. Below the β transus temperature, the dominant texture is that of the parent β phase (recrystallisation during slow EBSD heating below the β transus temperature is limited). Minor texture components derived from the epitaxial recrystallisation could only be identified through discrete pole figures.

In Figure 7.17 (a), the reflections of the calculated β phase (referred to as β_A, i.e. the parent phase of the martensitic α' observed at room temperature)

and those of the measured β at 925°C are overlaid. It is observed that all the parent β orientations that present in the pole figures measured at 925°C are within an orientation scatter of 10°. As β_A does not show a large spread in orientation along the vertical axis of the columnar grain, it is unlikely that this possesses boundaries with high mobility capable of causing the refinement observed after the rapid induction heat treatment. On the other hand, the HAB recrystallised grains can be clearly observed as extra reflections at 925°C and marked in the figure via black arrows.

By overlaying the reflections of the β phase measured at 850° and 925°C, as shown in Figure 7.17 (b), insights on the growth of the β phase can be evinced. It is noted that as the temperature increases from 850° to 925°C, there is an apparent decrease in the orientation scatter. This is due to the fact that several β sub-grains isolated at 850°C are merging as one at 925°C, which appears in the discrete pole figures as reduced in the number of reflections. No further new β orientations appear during the growth of the β phase from 850 ° to 925°C as no additional HAB reflections are observed in *Figure 7.17* (b). This implies that most likely the recrystallised β, which we categorised as β_c in the previous content, is not formed with random orientations to the surrounding phases but with BOR with α laths underneath the plane of observation. Because if β_c is formed with random orientations, the increase in the amount of β_c is likely to bring in new orientations, which would appear as extra reflections in the discrete pole figures. Therefore, all the recrystallised HAB β appeared in heat treatment can be recognised as a result of epitaxial recrystallisation, and are related to individual adjacent α/α' laths via BOR.

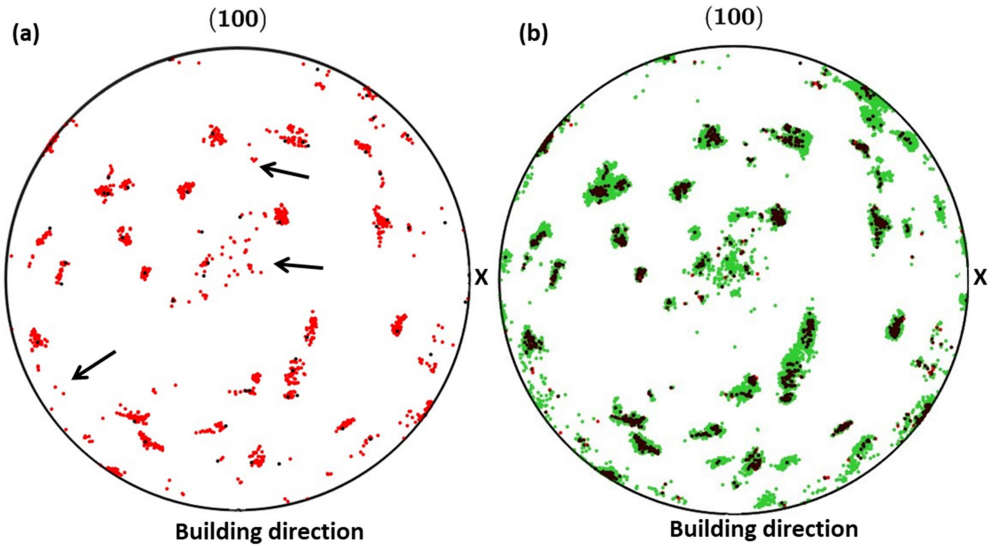


Figure 7.17. (a) Overlaid discrete pole figures of calculated parent β (black) and measured β at 925°C (red); (b) Overlaid discrete pole figures of measured β at 850°C (green) and 925°C (red/black). Black arrows indicate the HAB recrystallised grains existed at 925°C.

7.3 Summary

In this chapter, the recrystallisation of high angle boundary (HAB) β in SLM Ti-6Al-4V is studied via high-temperature EBSD and, for the first time, the mechanisms and the nature of this recrystallisation is discussed. The analysis shows that it can be considered as epitaxial recrystallisation, which is similar to that recently discovered in hot-worked metastable β titanium alloy (Balachandran et al., 2017). The recrystallised β is related to individual adjacent α/α' laths via BOR, and can be located in the interior of individual α/α', between α/α' lath or at the prior-β grain boundary.

It could be assumed that the driving force for the observed epitaxial recrystallisation derives from the stored energy of deformation that is typically expressed by the high densities of lattice defects found after SLM in the core and at the boundary of the martensitic as-built microstructure.

It was observed that the recrystallised β grains grow competitively with the surrounding matrix (β_A) below β transus temperature, while the retained α laths pin the original prior-β grain boundaries locally. When the heating

temperature approaches or is above the β transus temperature, no α-pinning could take place. As the HAB has higher mobility than the surrounding matrix β_A, it might migrate at a higher rate (Pilchak et al., 2017), which leads to a change of the original columnar morphology. Since under the uniform heating, grains would grow with no preferred grain growth direction aligned to any of sample coordinate system, an equiaxed or quasi-equiaxed grain morphology is encouraged during induction heat treatments.

The high-temperature EBSD (near equilibrium conditions) experiments presented in this chapter can capture the range of temperatures at which the phase transformation occurs during the rapid induction heat treatment applied in previous chapters. However, it is well understood that rapid heat treatment can retain the substructure of the martensitic phase to higher temperatures and promote higher nucleation rates of HAB grains (Ivasishin and Teliovich, 1999). Therefore, the applied induction heat treatment would exacerbate the observed epitaxial recrystallisation and result in significant refinement of the structure, as reported in Chapter 5 and Chapter 6.

CHAPTER 8

8. Conclusions and future work

Over the course of this study, new information and knowledge have been generated. Hence, a brief summary of these results will be presented with the corresponding conclusions in section 8.1. In addition to what has been studied, there are still further areas of research can be built based on this knowledge. A summary of these areas of future work will be presented in section 8.2.

8.1 Conclusions

In this research, SLM Ti-6Al-4V specimens were heat treated to a temperature around the β transus (~ 1010°C) using a bespoke induction heating system. The tensile properties and microstructure obtained after such heat treatments were compared with those in the as-built condition and those after conventional heat treatments. Based on these comparisons, the results of the conducted induction heating treatments and their potentialities was evaluated. A refined microstructure was observed in the specimens that were treated with induction heating. By using gradient heating, the microstructure evolution results in such refinement were characterised. The mechanisms behind the observed microstructure evolution were studied via high-temperature EBSD. The major findings obtained from this research are summarised as follow:

- The typical microstructure in as-built SLM Ti-6AL-4V consists of columnar prior-β grains filled with fine acicular α’ martensites in various orientations. Such microstructure results in a tensile property with high strength and low ductility. This microstructural arrangement also implies mechanical anisotropy as demonstrated in several related studies (Vilaro et al., 2011, Wauthle et al., 2015, Liu and Shin, 2019).

- After conventional sub-transus heat treatment, the typical microstructure consists of prior-β grains filled with interweaved α+β lamellas. The prior-β grains, however, maintained the original columnar morphology, which is consistent with the morphology of the prior-β grains in the as-built condition. This microstructure provides a balance between strength and ductility in terms of tensile property, but it also suggests an inheritance of the anisotropy behaviours.

- After conventional super-transus heat treatment (also known as β annealing), the typical microstructure consists of coarse equiaxed prior-β grains filled with parallel α+β lamellas. Extensive β grain growth occurs during the conventional β annealing, which would result in an unacceptable loss in strength and ductility.

- After heat treated to a temperature around β transus via induction heating (short time β annealing), the typical microstructure consists of equiaxed or quasi-equiaxed prior-β grains, which are also filled with parallel α+β lamellas. In comparison to the microstructure obtained after conventional sub-transus heat treatment, the morphology of the prior-β grains appears refined. The width of the α lamellae is also smaller than what was observed in specimens subjected to conventional heat treatment. This microstructure provides tensile properties equivalent to or better than what was obtained after conventional heat treatment, and also might provide a potential to achieve isotropic behaviour and improve fatigue resistance.

- The observed refinement of the prior-β grains after induction heat treatment is the first time reported for additively manufactured Ti alloys. The refinement is believed to be the result of the recrystallisation of the β phase. Due to the recrystallisation process, high angle boundary (HAB) β are nucleated during the induction heat treatment. The nuclei can grow with no preferred grain growth direction aligned to any of the sample coordinate systems, as the

heating imparted by the induction system is uniform. This results in the appearance of a mixed morphology of prior-β grains when the temperature approaches β transus. Such mixed morphology consists of both newly formed equiaxed prior-β grains and original columnar prior-β grains. Since the HAB has higher mobility, the equiaxed HAB β grain grows faster compared to the original β grains. Therefore, the original columnar morphology is gradually replaced. In that way, the microstructure evolves toward the observed refined quasi-equiaxed morphology.

- The nature of the recrystallisation process is identified as epitaxial recrystallisation since the recrystallised β is related to individual adjacent α/α' laths via Burger Orientation Relationship (BOR). The recrystallised β can be nucleated either in the interior of the individual α phase, at the α/β boundary or at the prior-β grain boundary. To date, these have never been demonstrated in additively manufactured Ti alloys. It can be assumed that the driving force for the observed epitaxial recrystallisation origins from the stored energy of deformation that is typically expressed by the high densities of lattice defects found after SLM in the core and at the boundary of the martensitic as-built microstructure.

- Rapid heating processes, like the applied induction heat treatment, can retain the substructure of the martensitic phase to high temperatures and promote the higher nucleation rates of HAB grains (Ivasishin and Teliovich, 1999). Therefore, the applied short time β annealing and induction heat treatment would exacerbate the observed epitaxial recrystallisation and result in significant refinement of the structure.

8.2 Future work

As this research provides lots of new information for the additively manufactured Ti alloys, there is great potential for future research and exploitation. Some of the work in this research can be continued further, as described below:

- **Testing for anisotropy/isotropic behaviour**

  Microstructure analysis reported in chapter 4 suggests that, after the applied induction heat treatment, there is a potential that the mechanical properties of SLM Ti-6Al-4V can exhibit isotropic behaviour, while the mechanical properties of those treated with conventional heating still exhibit anisotropy behaviour.

  In order to verify such analysis, Ti-6Al-4V specimens should be built at various orientations (different build angle to the build platform), and then post-process treated with different heat treatments, like sub-tansus heat treatment or induction heat treatments. In the end, the resulting microstructure and tensile property should be compared to examine if there is any preferred testing direction.

- **Fatigue test**

  Microstructure analysis also suggests that, after the applied induction heat treatment, the SLM Ti-6Al-V can obtain improved fatigue resistance.

  To verify such analysis, a fatigue test should be conducted. Ti-6Al-4V specimens manufactured at same build angle should be grouped for different heat treatments. The fatigue property after different heat treatment then will be compared. Different fatigue resistance will lead to a different crack growth rate.

- **Further refinement of the morphology of the prior-β grains**

  From what is established in this research, it is safe to assume that by exacerbating the epitaxial recrystallisation process, the morphology of the prior-β grains can be further refined.

  Based on the classic recrystallisation theory, such a process can be exacerbated by increasing the nucleation rate of the recrystallised nuclei. One possible method to increase the nucleation rate is to provide more nucleation sites. Therefore, more lattice defects need to be retained at a high temperature. There are 3 possible approaches to achieve this goal: a) a higher heating rate for the induction heat treatment; b) optimise the process parameters for SLM Ti-6Al-4V, so that a higher density of the lattice defects could be obtained in as-built status; c) adding alloy elements in the Ti-6Al-4V material system.

Appendix A

The 3D orientation of a crystal cell could be described by defining the rotation of the crystal coordinate system relative to the sample coordinate system, and then applied with the symmetry of the crystal. Such rotation is usually expressed via a triplet of angles, (φ 1, Φ, φ 2), which also known as Euler angles. It means the rotation about the axis that is needed to make the crystal coordinate system overlapped with the sample coordinate system. In this study, the crystal coordinate system used to describe the measured orientation was defined by the MATLAB Toolbox MTex. Through Bunge's convention, the Euler angles therefore can be further described in the form of a matrix. Such convention is defined as follow:

$$R(\varphi 1,\Phi,\varphi 2)=\begin{bmatrix} \cos\varphi 1\cos\varphi 2-\sin\varphi 1\sin\varphi 2\cos\Phi & \sin\varphi 1\cos\varphi 2+\cos\varphi 1\sin\varphi 2\cos\Phi & \sin\varphi 2\sin\Phi \\ -\cos\varphi 1\sin\varphi 2-\sin\varphi 1\cos\varphi 2\cos\Phi & -\sin\varphi 1\sin\varphi 2+\cos\varphi 1\cos\varphi 2\cos\Phi & \cos\varphi 2\sin\Phi \\ \sin\varphi 1\sin\Phi & -\cos\varphi 1\sin\Phi & \cos\Phi \end{bmatrix}$$

Due to the symmetry of the crystal system, multiple rotations can lead to an equivalent 3D orientation of a certain crystal. Therefore, the rotational symmetry elements need to be applied, so that the independent orientations can be distinguished. The rotational symmetry elements of the α and β phases used in this research are listed in Table 1 and Table 2.

The orientation of the α phase and the orientation of the corresponding parent β phase are related via Burgers orientation relationship (BOR). Such relationship can also be expressed by a rotation matrix D (135°, 90°, 354.74°). Previous researches have shown that, by applying the rotation matrix, it is possible to determine the orientation of the parent β phase from the orientations of a cluster of α phases (at least 3).

Table 1. Rotational elements of the cubic symmetry (β phase)

Rotational elements of the cubic symmetry	
E (0, 0, 0)	$C_{4x+}(0, \pi/2, 0)$
$C_{2x}(0, \pi, 0)$	$C_{4y+}(\pi/2, \pi/2, 3\pi/2)$
$C_{2y}(\pi, \pi, 0)$	$C_{4z+}(\pi/2, 0, 0)$
$C_{2z}(\pi, 0, 0)$	$C_{4x-}(\pi, \pi/2, \pi)$
$C_{31+}(\pi/2, \pi/2, 0)$	$C_{4y-}(3\pi/2, \pi/2, \pi/2)$
$C_{32+}(3 \pi/2, \pi/2, \pi)$	$C_{4z-}(3\pi/2,0 ,0)$
$C_{33+}(3 \pi/2, \pi/2, 0)$	$C_{2a}(\pi/2, \pi, 0)$
$C_{34+}(\pi/2, \pi/2, \pi)$	$C_{2b}(3\pi/2, \pi, 0)$
$C_{31-}(\pi, \pi/2, \pi/2)$	$C_{2c}(\pi/2, \pi/2, \pi/2)$
$C_{32-}(0, \pi/2, 3\pi/2)$	$C_{2d}(\pi, \pi/2, 0)$
$C_{33-}(\pi, \pi/2,3 \pi/2)$	$C_{2e}(3\pi/2, \pi/2, 3\pi/2)$
$C_{34-}(0, \pi/2, \pi/2)$	$C_{2f}(0, \pi/2, \pi)$

Table 2. Rotational elements of the hexagonal symmetry (α phase)

Rotational elements of the hexagonal symmetry	
E (0, 0, 0)	${}^{H}C'_{21}(\pi, \pi, 0)$
${}^{H}C_{6z+}(\pi/3, 0, 0)$	${}^{H}C''_{22}(\pi, \pi, \pi/3)$
${}^{H}C_{3z+}(2\pi/3, 0, 0)$	${}^{H}C''_{23}(\pi, \pi, 2\pi/3)$
${}^{H}C_{2x}(0, 0, \pi)$	${}^{H}C''_{21}(\pi, \pi, \pi)$
${}^{H}C_{3z-}(4\pi/3, 0, 0)$	${}^{H}C'_{22}(\pi, \pi, 4\pi/3)$
${}^{H}C_{6z-}(-\pi/3, 0, 0)$	${}^{H}C''_{23}(\pi, \pi, 5\pi/3)$

The orientation of the parent β phase is computed from the angular information of α texture measured at room temperature during EBSD analysis. A Matlab code is created to conduct the back calculation. In order to provide the information needed to conduct the reconstruction, 3 input files are exported from the OIM data analysis software. The name and the content of these three exported files is specified as follow:

- **neighbors.txt**

  Each row contains ID_grain_n (identification of the α grain_n), number of adjacent grains to the grain_n, identification of adjacent grains.
- **average.txt**

  Each row contains an identification of grain_n, three Euler angles that define the average orientation of ID (Bunge convention).
- **pixels.txt**

  Each row contains the spatial information ("x" and "y" coordinates) of each α grain_n and the corresponding identification.

The Matlab script used to conduct the β reconstruction is presented as follow, the reliability of this script will be validated in Appdienx B:

```
function [ebsd] = auto (threashold)
%startup
m=dlmread('neighbors.txt'); % ID grain, number of neighbours,
ID neighbours
angoli=dlmread('average.txt'); % ID grain , three average euler
degree
m(isnan(m))=0;
read1=m;
[totgrani, ncolonne]=size(read1);
% initizializza
dovesono=1;
storer=1;
cs=crystalSymmetry('cubic');
ss=crystalSymmetry('triclinic');
beta=orientation('Euler',0,0,0,cs,ss);
% fine inizializza
for rigan=1:totgrani

    grano1=read1(rigan,1);% numero intero
    nneigh=read1(rigan,2);
    contatore=0;
```

```
    if (nneigh>=3)% devono esistere almeno 3 grani comunicanti
per ric beta
        numerocolonne=nneigh+2;
        numerocicli=numerocolonne-4;% numero tripplette
esaminate
                    for add=1:numerocicli

                                grano2=read1(rigan,2+add);
                                grano3=read1(rigan,3+add);
                                grano4=read1(rigan,4+add);
                                [solutionbeta,minimo] =
arturo(grano1, grano2, grano3, grano4,angoli,threashold);

                                if(minimo<threashold)
                                    contatore=contatore+1;
                                    storer(rigan,1)=grano1;%
sempre lui
                                    if (contatore==1) % ti serve l
info di 3 grani
                                        storer(rigan,2)=grano2;
                                        storer(rigan,3)=grano3;
                                        storer(rigan,4)=grano4;
                                    else

storer(rigan,contatore+2)=grano3;
                                    end


                                    %beta(rigan)=solutionbeta;

[phib,thetab,psib]=Euler(solutionbeta,'Bunge');
                                   phibeta=rad2deg(phib);
                                   thetaneta=rad2deg(thetab);
                                   psibeta=rad2deg(psib);

angles=[phibeta,thetaneta,psibeta,storer(rigan,:)];

dlmwrite('info_beta.txt',angles,'-append','delimiter','\t');
                                   solutionbeta=0;
                                   phibeta=0;
                                   thetaneta=0;
                                   psibeta=0;
                                else
                                    bananas=999999;
                                end




                    end




    else
```

```
        % nn fai nulla
    end



end


m=dlmread('info_beta.txt');
pixels=dlmread('pixels.txt'); % x and y and ID
m(isnan(m))=0;
fileEBSD=m;

[totgrani, larghezza]=size(fileEBSD);
IDdistinti=fileEBSD(:,4);
IDpixels=pixels(:,3);
matrice=zeros(totgrani, 5);
for rigan=1: totgrani
    ID=IDdistinti(rigan);

                [righeconID, colonneconID]=find(fileEBSD==ID);

                molt=size(righeconID);
                molteplicita=molt(1,1);
                for ind=1: molteplicita
                    phi(ind)=fileEBSD(righeconID(ind,1),1);
                    theta(ind)=fileEBSD(righeconID(ind,1),2);
                    psi(ind)=fileEBSD(righeconID(ind,1),3);
                end

              phi_medio=phi(ind);
              theta_medio=theta(ind);
              psi_medio=psi(ind);



              phi=0;
              theta=0;
              psi=0;
              [indicex y]=find(IDpixels==ID);
              molt2=size(indicex);
              molteplicita2=molt2(1,1);
              for scorri=1:molteplicita2
                  posx(scorri)=pixels(indicex(scorri,1),1);
                  posy(scorri)=pixels(indicex(scorri,1),2);
                  phi_(scorri)= phi_medio;
                  theta_(scorri)= theta_medio;
                  psi_(scorri)=psi_medio;


              end
                 matrice=[phi_;theta_;psi_;posx;posy]';
                 dlmwrite('ebsd_file.txt', matrice,'-
append','delimiter','\t');
                 matrice=0;
                 posx=0;
                 posy=0;
                 phi_=0;
                 theta_=0;
```

```
                psi_=0;

end


fileebsd=dlmread('ebsd_file.txt');
[col_size,raw_size]=size(fileebsd);
ones_row=ones(col_size,1);
m=size(ones_row);
ebsd_raw=[fileebsd,ones_row];
ebsd_file=unique(ebsd_raw,'rows','stable');
dlmwrite('ebsd_organised.txt', ebsd_file,'-
append','delimiter','\t');



cs=crystalSymmetry('cubic');
ss=crystalSymmetry('triclinic');
ebsd=loadEBSD_generic('ebsd_organised.txt', 'CS', cs, 'SS', ss,
'ColumnNames', {'Euler1', 'Euler2', 'Euler3', 'y','x','phase'},
'Bunge');

% compute grains
[grains,ebsd.grainId]=calcGrains(ebsd,'Euler1', 'Euler2',
'Euler3', 'y','x','phase','angle',5*degree);

% remove small grains

 ebsd(grains(grains.grainSize < 25)) = [];

% and repeat the grain computation
 [grains,ebsd.grainId] = calcGrains(ebsd,'angle',15*degree);

%smooth grain
 grains = smooth(grains,10);

%fill voids inside the grains
F = halfQuadraticFilter;
F.alpha = 0.01;
F.eps = 0.001;
ebsd_smoothed = smooth(ebsd,F,'fill',grains);

figure
plot(ebsd_smoothed('1'),ebsd_smoothed('1').orientations)
hold on

% plot the boundary of all grains
plot(grains.boundary,'linewidth',0.75)

% stop overide mode
hold off
```

```
function [soluzione,minimo] = arturo (grano1, grano2, grano3,
grano4, angoli,threashold)


read2=angoli;
ind1=find(read2(:,1)==grano1);
phi1=read2(ind1,2);
theta1=read2(ind1,3);
psi1=read2(ind1,4);

ind2=find(read2(:,1)==grano2);
phi2=read2(ind2,2);
theta2=read2(ind2,3);
psi2=read2(ind2,4);

ind3=find(read2(:,1)==grano3);
phi3=read2(ind3,2);
theta3=read2(ind3,3);
psi3=read2(ind3,4);

ind4=find(read2(:,1)==grano4);
phi4=read2(ind4,2);
theta4=read2(ind4,3);
psi4=read2(ind4,4);


var=rotation('Euler',phi1*degree, theta1*degree, psi1*degree,
'Bunge');
var2=rotation('Euler',phi2*degree, theta2*degree, psi2*degree,
'Bunge');
var3=rotation('Euler',phi3*degree, theta3*degree, psi3*degree,
'Bunge');
var4=rotation('Euler',phi4*degree, theta4*degree, psi4*degree,
'Bunge');


cs=crystalSymmetry('hexagonal');
ss=crystalSymmetry('triclinic');
ori_1=orientation(var, cs,ss);
ori_2=orientation(var2, cs,ss);
ori_3=orientation(var3, cs,ss);
ori_4=orientation(var4, cs,ss);

s=symmetrise(ori_1);
s2=symmetrise(ori_2);
s3=symmetrise(ori_3);
s4=symmetrise(ori_4);

d=rotation('Euler', 135*degree, 90*degree,
354.74*degree,'Bunge');


    beta=s*inv(d);
    beta2=s2*inv(d);
    beta3=s3*inv(d);
    beta4=s4*inv(d);

cs=crystalSymmetry('cubic');
```

```
ss=crystalSymmetry('triclinic');
for j=1:3
    ori(j)=orientation(beta(j), cs,ss);
    ori2(j)=orientation(beta2(j), cs,ss);
    ori3(j)=orientation(beta3(j), cs,ss);
    ori4(j)=orientation(beta4(j), cs,ss);

end

for j=4:6
    ori(j)=orientation(beta(j+3), cs,ss);
    ori2(j)=orientation(beta2(j+3), cs,ss);
    ori3(j)=orientation(beta3(j+3), cs,ss);
    ori4(j)=orientation(beta4(j+3), cs,ss);

end
beta_1=ori;
beta_2=ori2;
beta_3=ori3;
beta_4=ori4;


for i=1:6
    for j=1:6
    mis12(i,j)=angle(beta_1(i),beta_2(j))/degree;
    mis13(i,j)=angle(beta_1(i),beta_3(j))/degree;
    mis32(i,j)=angle(beta_3(i),beta_2(j))/degree;
    mis14(i,j)=angle(beta_1(i),beta_4(j))/degree;
    end
end
mis12;
[x,y]=find(mis12==min(min(mis12)));
value=mis12(x(1),y(1));
if (value < threashold)
    beta1=beta_1(x(1));
    beta2=beta_2(y(1));
    [xx,yy]=find(mis13==min(mis13(x(1),:)));
    value2 =mis13(xx(1),yy(1));
        if (value2 < threashold)
            beta3=beta_3(yy(1));
            value3=mis32(yy(1),y(1));

            if (value3 < threashold)
                value4 =min(mis14(x(1),:));

                if (value4 < threashold)
                    soluzione=beta1;
                    minimo=threashold-1;

               else
                  annulla=0; %non fa nulla
                  minimo=threashold+1;
                  soluzione=0;
                end
           else
            annulla=0; %non fa nulla
            minimo=threashold+1;
            soluzione=0;
            end
```

```
        else
          annulla=0;
          minimo=threashold+1;%non fa nulla
          soluzione=0;
          end
else
                    annulla=0; %non fa nulla
                    minimo=threashold+1;
                    soluzione=0;
end
```

Appendix B

The high temperature EBSD dataset presented in section 7.1 will be used to validate the reliability of the Matlab script presented in Appendix A. This script is aimed to reconstruct the crystallographic texture of the parent β phase. The reconstruction will be conducted based on the crystallographic texture of the α' phase measured at the room temperature. The reconstructed results then will be compared with the β orientation map measured at 850°C, to examine the consistency and accuracy between the computed results and experimental results.

The crystallographic texture of the α' phase measured at the room temperature is presented in Figure 1. The orientation data is mapped in Z-IPF with the colour scheme presented in Figure 1 (c). As discussed in section 7.1, a total of two prior-β grains locates in the observed area, with the prior-β grain boundary across the middle of the image.

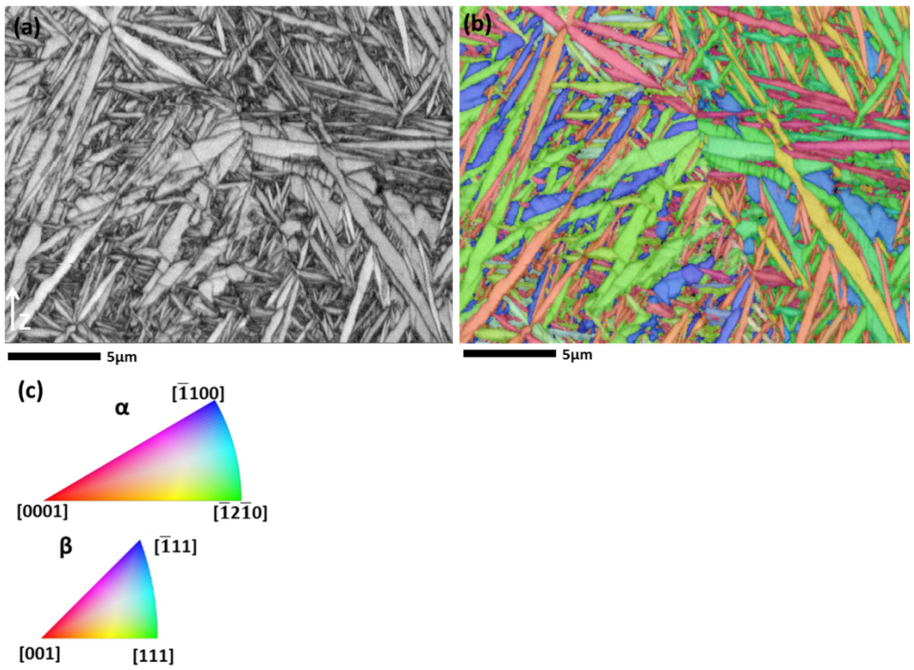


Figure 1. The crystallographic texture of the α' phase measured at the room temperature: (a) band contrast image; (b) measured α orientation map; (c) Standard colour scheme used to map the orientation data.

The reconstructed parent β orientation map is presented in Figure 2, and the β orientation map of the same location measured at 850°C is presented in Figure 3. By comparing both of the orientation of the parent β and the location of prior-β grain boundary in two images, consistency can be observed. Therefore, the reliability of the Matlab script has been validated.

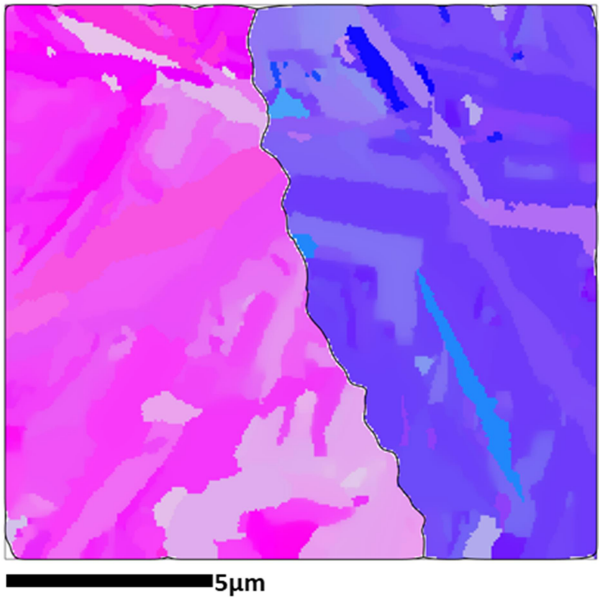


Figure 2. Parent β orientation map reconstructed from the crystallographic texture of the room temperature α' phase

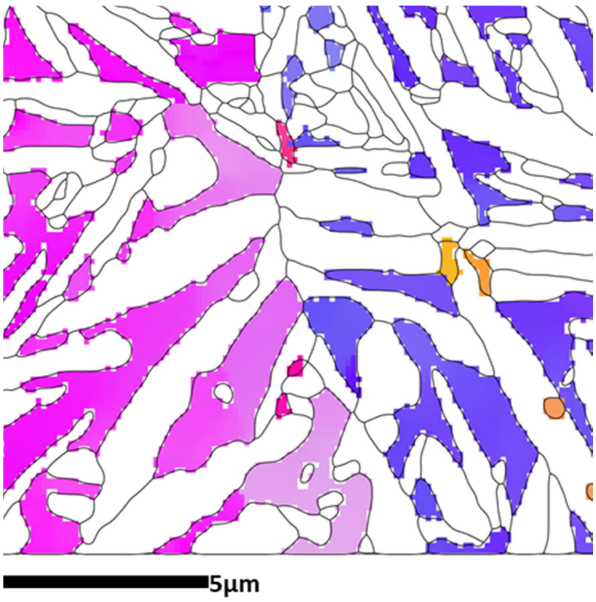


Figure 3. β orientation map of the same location measured at 850°C

References

ACERO, J., ALONSO, R., BURDIO, J. M., BARRAGAN, L. A. & PUYAL, D. 2006. Analytical equivalent impedance for a planar circular induction heating system. *IEEE Transactions on Magnetics,* 42**,** 84-86.

ADAMS, B. L., KALIDINDI, S. R. & FULLWOOD, D. T. 2013. Chapter 16 - Electron Backscatter Diffraction Microscopy and Basic Stereology. *In:* ADAMS, B. L., KALIDINDI, S. R. & FULLWOOD, D. T. (eds.) *Microstructure Sensitive Design for Performance Optimization.* Boston: Butterworth-Heinemann.

AHMED, T. & RACK, H. J. 1998. Phase transformations during cooling in α+β titanium alloys. *Materials Science and Engineering: A,* 243**,** 206-211.

ALI, H., GHADBEIGI, H. & MUMTAZ, K. 2018. Effect of scanning strategies on residual stress and mechanical properties of Selective Laser Melted Ti6Al4V. *Materials Science and Engineering: A,* 712**,** 175-187.

ALI, H., MA, L., GHADBEIGI, H. & MUMTAZ, K. 2017. In-situ residual stress reduction, martensitic decomposition and mechanical properties enhancement through high temperature powder bed pre-heating of Selective Laser Melted Ti6Al4V. *Materials Science and Engineering: A,* 695**,** 211-220.

AMIRMAHYAR, K., IAN, G., MOSHE, G. & GUY, L. 2017. On the role of different annealing heat treatments on mechanical properties and microstructure of selective laser melted and conventional wrought Ti-6Al-4V. *Rapid Prototyping Journal,* 23**,** 295-304.

ASTM 2013. Standard Specification for Titanium and Titanium Alloy Bars and Billets. ASTM Internationa.

ASTM 2014a. Standard Specification for Additive Manufacturing Titanium-6 Aluminum-4 Vanadium ELI (Extra Low Interstitial); with Powder Bed Fusion. ASTM International.

ASTM 2014b. Standard Specification for Additive Manufacturing Titanium-6 Aluminum-4 Vanadium with Powder Bed Fusion. ASTM International.

ASTM, I. 2016. ASTM E8/E8M-16a: Standard Test Methods for Tension Testing of Metallic Materials. *West Conshohocken, PA, USA: ASTM International*.

BAKER, A. H., COLLINS, P. C. & WILLIAMS, J. C. 2017. New Nomenclatures for Heat Treatments of Additively Manufactured Titanium Alloys. *JOM,* 69**,** 1221-1227.

BAKER, R. M. 1957. Design and calculation of induction-heating coils. *Transactions of the American Institute of Electrical Engineers, Part II: Applications and Industry,* 76**,** 31-40.

BALACHANDRAN, S., KUMAR, S. & BANERJEE, D. 2017. On recrystallization of the α and β phases in titanium alloys. *Acta Materialia,* 131**,** 423-434.

BARRIOBERO-VILA, P., GUSSONE, J., HAUBRICH, J., SANDL BES, S., DA SILVA, C. J., CLOETENS, P., SCHELL, N. & REQUENA, G. 2017. Inducing Stable α + β Microstructures during Selective Laser Melting of Ti-6Al-4V Using Intensified Intrinsic Heat Treatments. *Materials,* 10.

BECKER, T. H., BECK, M. & SCHEFFER, C. 2015. Microstructure and mechanical properties of direct metal laser sintered Ti-6Al-4V. *South African Journal of Industrial Engineering,* 26**,** 1-10.

BEESE, A. M. & CARROLL, B. E. 2016. Review of Mechanical Properties of Ti-6Al-4V Made by Laser-Based Additive Manufacturing Using Powder Feedstock. *JOM,* 68**,** 724-734.

BIDARE, P., BITHARAS, I., WARD, R. M., ATTALLAH, M. M. & MOORE, A. J. 2018. Fluid and particle dynamics in laser powder bed fusion. *Acta Materialia,* 142**,** 107-120.

BOADI, A., TSUCHIDA, Y., TODAKA, T. & ENOKIZONO, M. 2005. Designing of suitable construction of high-frequency induction heating coil by using finite-element method. *IEEE Transactions on Magnetics,* 41**,** 4048-4050.

BOIVINEAU, M., CAGRAN, C., DOYTIER, D., EYRAUD, V., NADAL, M.-H., WILTHAN, B. & POTTLACHER, G. 2006. Thermophysical Properties of Solid and Liquid Ti-6Al-4V (TA6V) Alloy. *International Journal of Thermophysics,* 27**,** 507-529.

BURGERS, W. G. 1934. On the process of transition of the cubic-body-centered modification into the hexagonal-close-packed modification of zirconium. *Physica,* 1**,** 561-586.

CALLISTER, W. D. & RETHWISCH, D. G. 2007. *Materials science and engineering: an introduction*, John wiley & sons New York.

CANDEO, A., DUCASSY, C., BOCHER, P. & DUGHIERO, F. 2011. Multiphysics Modeling of Induction Hardening of Ring Gears for the Aerospace Industry. *IEEE Transactions on Magnetics,* 47**,** 918-921.

CARREON, H., SAN MARTIN, D., CABALLERO, F. G. & PANIN, V. E. 2017. The effect of thermal aging on the strength and the thermoelectric power of the Ti-6Al-4V alloy. *Physical Mesomechanics,* 20**,** 447-456.

CARTER, L. N., MARTIN, C., WITHERS, P. J. & ATTALLAH, M. M. 2014. The influence of the laser scan strategy on grain structure and cracking behaviour in SLM powder-bed fabricated nickel superalloy. *Journal of Alloys and Compounds,* 615**,** 338-347.

CAYRON, C. 2008. Importance of the $\alpha \rightarrow \beta$ transformation in the variant selection mechanisms of thermomechanically processed titanium alloys. *Scripta Materialia,* 59**,** 570-573.

CHANDRAMOHAN, P., BHERO, S., VARACHIA, F., OBADELE, B. A. & OLUBAMBI, P. A. 2018. Laser Additive Manufactured Ti–6Al–4V Alloy: Heat Treatment Studies. *Transactions of the Indian Institute of Metals,* 71**,** 579-587.

CHATTERJEE, A. K. 2001. 8 - X-Ray Diffraction. *In:* RAMACHANDRAN, V. S. & BEAUDOIN, J. J. (eds.) *Handbook of Analytical Techniques in Concrete Science and Technology.* Norwich, NY: William Andrew Publishing.

CHEN, L. Y., HUANG, J. C., LIN, C. H., PAN, C. T., CHEN, S. Y., YANG, T. L., LIN, D. Y., LIN, H. K. & JANG, J. S. C. 2017. Anisotropic response of Ti-6Al-4V alloy fabricated by 3D printing selective laser melting. *Materials Science and Engineering: A,* 682**,** 389-395.

CHEN, S.-C., JONG, W.-R. & CHANG, J.-A. 2006. Dynamic mold surface temperature control using induction heating and its effects on the surface appearance of weld line. *Journal of Applied Polymer Science,* 101**,** 1174-1180.

CHUDJUARJEEN, S., SANGSWANG, A. & KOOMPAI, C. 2011. An Improved LLC Resonant Inverter for Induction-Heating Applications With Asymmetrical Control. *IEEE Transactions on Industrial Electronics,* 58**,** 2915-2925.

CRIALES, L. E., ARıSOY, Y. M., LANE, B., MOYLAN, S., DONMEZ, A. & ÖZEL, T. 2017. Laser powder bed fusion of nickel alloy 625: Experimental investigations of effects of process parameters on melt pool size and shape with spatter analysis. *International Journal of Machine Tools and Manufacture,* 121**,** 22-36.

DA SILVA, S. L. R., KERBER, L. O., AMARAL, L. & DOS SANTOS, C. A. 1999. X-ray diffraction measurements of plasma-nitrided Ti–6Al–4V. *Surface and Coatings Technology,* 116-119**,** 342-346.

DAS, S. 2003. Physical Aspects of Process Control in Selective Laser Sintering of Metals. *Advanced Engineering Materials,* 5**,** 701-711.

DAVIES, E. J. 2007. *Conduction and Induction Heating*, IET.

DE FORMANOIR, C., MICHOTTE, S., RIGO, O., GERMAIN, L. & GODET, S. 2016. Electron beam melted Ti–6Al–4V: Microstructure, texture and mechanical behavior of the as-built and heat-treated material. *Materials Science and Engineering: A,* 652**,** 105-119.

DEBROY, T., WEI, H. L., ZUBACK, J. S., MUKHERJEE, T., ELMER, J. W., MILEWSKI, J. O., BEESE, A. M., WILSON-HEID, A., DE, A. & ZHANG, W. 2018. Additive manufacturing of metallic components – Process, structure and properties. *Progress in Materials Science,* 92**,** 112-224.

DECKERS, J., MEYERS, S., KRUTH, J. P. & VLEUGELS, J. 2014. Direct Selective Laser Sintering/Melting of High Density Alumina Powder Layers at Elevated Temperatures. *Physics Procedia,* 56**,** 117-124.

DING, H. Y., QIU, P. K., HAN, Y. F., SUN, Z. G., HUANG, J., CHU, M. Q. & LU, W. J. 2017a. Influence of post heat treatment on microstructure and mechanical property of Ti6Al4V parts produced by selective laser melting.

DING, H. Y., QIU, P. K., HAN, Y. F., SUN, Z. G., HUANG, J., CHU, M. Q. & LU, W. J. 2017b. Influence of post heat treatment on microstructure and mechanical property of Ti6Al4V parts produced by selective laser melting.

DODD, C. V. & DEEDS, W. E. 1968. Analytical Solutions to Eddy‐Current Probe‐Coil Problems. *Journal of Applied Physics,* 39**,** 2829-2838.

DONACHIE, M. J. 2000. *Titanium: a technical guide,* Materials Park, United States, ASM International.

DUTTA, B. & FROES, F. H. 2016. *Additive manufacturing of Titanium alloys: state of the art, challenges and opportunities*, Butterworth-Heinemann.

DUTTA, B. & FROES, F. H. 2017. The Additive Manufacturing (AM) of titanium alloys. *Metal Powder Report,* 72**,** 96-106.

ETTER, T., ENGELL, R. & KUENZLER, A. 2015a. *Method for post-built heat treatment of additively manufactured components made of gamma-prime strengthened superalloys*.

ETTER, T., KUNZE, K., GEIGER, F. & MEIDANI, H. 2015b. Reduction in mechanical anisotropy through high temperature heat treatment of Hastelloy X processed by Selective Laser Melting (SLM). *IOP Conference Series: Materials Science and Engineering,* 82**,** 012097.

EVERTON, S. K., HIRSCH, M., STRAVROULAKIS, P., LEACH, R. K. & CLARE, A. T. 2016. Review of in-situ process monitoring and in-situ metrology for metal additive manufacturing. *Materials & Design,* 95**,** 431-445.

FACCHINI, L. & MAGALINI, E. 2012. *Heat treatment method for martensitic stainless steel parts made with rapid prototyping techniques and the like and hardened by precipitation*.

FAN, X. G., MENG, M., GAO, P. F. & ZHAN, M. 2018. Coupled effects of deformation and cooling on the evolution of primary and secondary alpha of two-phase Ti-alloys. *Materials Science and Engineering: A,* 710**,** 271-279.

FAN, Z. & FENG, H. 2018. Study on selective laser melting and heat treatment of Ti-6Al-4V alloy. *Results in Physics,* 10**,** 660-664.

FLESCH, T. & MOTTIN, J. B. 2013. *Sintering and laser fusion device, comprising a means for heating powder by induction*.

FOX, J. C., MOYLAN, S. P. & LANE, B. M. 2016. Effect of Process Parameters on the Surface Roughness of Overhanging Structures in Laser Powder Bed Fusion Additive Manufacturing. *Procedia CIRP,* 45**,** 131-134.

FRANK, W. & DER, C. Solid state RF generators for induction heating applications. Conf. Rec. IEEE-IAS Annu. Meeting, 1982. 939-944.

FROES, F. H. E. 2015. *Titanium : physical metallurgy processing and applications / F. H. Froes, editor*, Materials Park, Ohio : ASM International.

GIL MUR, F. X., RODR GUEZ, D. & PLANELL, J. A. 1996. Influence of tempering temperature and time on the α′ -Ti-6Al-4V martensite. *Journal of Alloys and Compounds,* 234**,** 287-289.

GLAVICIC, M. G., KOBRYN, P. A., BIELER, T. R. & SEMIATIN, S. L. 2003. A method to determine the orientation of the high-temperature beta phase from measured EBSD data for the low-temperature alpha phase in Ti-6Al-4V. *Materials Science and Engineering: A,* 346**,** 50-59.

GLAVICIC, M. G., KOBRYN, P. A. & SEMIATIN, S. L. 2004. Validation of an automated EBSD method to deduce the β-phase texture in Ti–6Al–4V with a colony-α microstructure. *Materials Science and Engineering: A,* 385**,** 372-376.

GONG, H., RAFI, K., STARR, T. & STUCKER, B. The effects of processing parameters on defect regularity in Ti-6Al-4V parts fabricated by selective laser melting and electron beam melting. 24th Annual International Solid Freeform Fabrication Symposium, 2013 2013 Austin, TX. 12-14.

GRAICHEN, A. 2013. *METHOD FOR MANUFACTURING A COMPONENT BY SELECTIVE LASER MELTING*.

GREITEMEIER, D., PALM, F., SYASSEN, F. & MELZ, T. 2017. Fatigue performance of additive manufactured TiAl6V4 using electron and laser beam melting. *International Journal of Fatigue,* 94**,** 211-217.

GUZANOV , A., IŽAR KOV , G., BREZINOV , J., ŽIVČ K, J., DRAGANOVSK , D. & HUD K, R. 2017. Influence of Build Orientation, Heat Treatment, and Laser Power on the Hardness of Ti6Al4V Manufactured Using the DMLS Process. *Metals,* 7.

HAIKO POHL, A. S., MUNTHER ISSA AND HUGO CALEFI DIAS 2001. Thermal Stresses in Direct Metal Laser Sintering. *Solid Freeform Fabrication Symposium.* Austin, Texas.

HAIMBAUGH, R. E. 2001. *Practical Induction Heat Treating,* Materials Park, OH, USA, ASM International.

HAUBRICH, J., GUSSONE, J., BARRIOBERO-VILA, P., K RNSTEINER, P., J GLE, E. A., RAABE, D., SCHELL, N. & REQUENA, G. 2019. The role of lattice defects, element partitioning and intrinsic heat effects on the microstructure in selective laser melted Ti-6Al-4V. *Acta Materialia,* 167**,** 136-148.

HELDWEIN, M. L., NUSSBAUMER, T. & KOLAR, J. W. Differential mode EMC input filter design for three-phase AC-DC-AC sparse matrix PWM converters. Power Electronics Specialists Conference, 2004. PESC 04. 2004 IEEE 35th Annual, 20-25 June 2004 2004. 284-291 Vol.1.

HOSSAIN, M. S., GONZALEZ, J. A., HERNANDEZ, R. M., SHUVO, M. A. I., MIRELES, J., CHOUDHURI, A., LIN, Y. & WICKER, R. B. 2016. Fabrication of smart parts using powder bed fusion additive manufacturing technology. *Additive Manufacturing,* 10**,** 58-66.

HUANG, Q., LIU, X., YANG, X., ZHANG, R., SHEN, Z. & FENG, Q. 2015. Specific heat treatment of selective laser melted Ti–6Al–4V for biomedical applications. *Frontiers of Materials Science,* 9**,** 373-381.

HUMBERT, M., MOUSTAHFID, H., WAGNER, F. & PHILIPPE, M. J. 1994. Evaluation of the high temperature texture of the β phase of a TA6V sample from the individual orientations of grains of the low temperature α phase. *Scripta Metallurgica et Materialia,* 30**,** 377-382.

HUMBERT, M., WAGNER, F., MOUSTAHFID, H. & ESLING, C. 1995. Determination of the Orientation of a Parent β Grain from the Orientations of the Inherited α Plates in the Phase Transformation from Body-Centred Cubic to Hexagonal Close Packed. *Journal of Applied Crystallography,* 28**,** 571-576.

IAN GIBSON, D. R., BRENT STUCKER 2015. *Additive Manufacturing Technologies_ 3D Printing, Rapid Prototyping, and Direct Digital Manufacturing,* New York, Springer.

IDA, N. 2015. *Engineering Electromagnetics*, Springer.

IDHIL ISMAIL, A., DEHMAS, M., AEBY-GAUTIER, E. & APPOLAIRE, B. 2016. In-Situ Investigation of Phase Transformation Kinetics in Ti-6Al-4V Under Rapid Heating Condition Using High-Energy Synchrotron Diffraction. *Proceedings of the 13th World Conference on Titanium***,** 591-598.

IVASISHIN, O. M. & TELIOVICH, R. V. 1999. Potential of rapid heat treatment of titanium alloys and steels. *Materials Science and Engineering: A,* 263**,** 142-154.

JAN, W., YVES‐CHRISTIAN, H., WILHELM, M. & KONRAD, W. 2013. Additive manufacturing of ZrO2‐Al2O3 ceramic components by selective laser melting. *Rapid Prototyping Journal,* 19**,** 51-57.

JEONG, D., KWON, Y., GOTO, M. & KIM, S. 2017. High cycle fatigue and fatigue crack propagation behaviors of β-annealed Ti-6Al-4V alloy. *International Journal of Mechanical and Materials Engineering,* 12**,** 1.

KARBASIAN, H. & TEKKAYA, A. E. 2010. A review on hot stamping. *Journal of Materials Processing Technology,* 210**,** 2103-2118.

KASCHNITZ, E., REITER, P. & MCCLURE, J. L. 2002. Thermophysical Properties of Solid and Liquid 90Ti–6Al–4V in the Temperature Range from 1400 to 2300 K Measured by Millisecond and Microsecond Pulse-Heating Techniques. *International Journal of Thermophysics,* 23**,** 267-275.

KHAIRALLAH, S. A., ANDERSON, A. T., RUBENCHIK, A. & KING, W. E. 2016. Laser powder-bed fusion additive manufacturing: Physics of complex melt flow and formation mechanisms of pores, spatter, and denudation zones. *Acta Materialia,* 108**,** 36-45.

KING, W., ANDERSON, A. T., FERENCZ, R. M., HODGE, N. E., KAMATH, C. & KHAIRALLAH, S. A. 2015. Overview of modelling and simulation of metal powder bed fusion process at Lawrence Livermore National Laboratory. *Materials Science and Technology,* 31**,** 957-968.

KOHLI, R. 2012. Chapter 3 - Methods for Monitoring and Measuring Cleanliness of Surfaces. *In:* KOHLI, R. & MITTAL, K. L. (eds.) *Developments in Surface Contamination and Cleaning.* Oxford: William Andrew Publishing.

KONAS, W. W. 1970. New Power Supply - Solid State Converters. *IEEE Transactions on Industrial Electronics and Control Instrumentation,* IECI-17**,** 327-331.

KRUTH, J. P., FROYEN, L., VAN VAERENBERGH, J., MERCELIS, P., ROMBOUTS, M. & LAUWERS, B. 2004. Selective laser melting of iron-based powder. *Journal of Materials Processing Technology,* 149**,** 616-622.

KRUTH, J. P., WANG, X., LAOUI, T. & FROYEN, L. 2003. Lasers and materials in selective laser sintering. *Assembly Automation,* 23**,** 357-371.

KUMAR, K. N., MUNESHWAR, P., SINGH, S. K., JHA, A. K., PANT, B. & GEORGE, K. M. 2015. Effect of Grain Boundary Alpha on Mechanical Properties of Ti5.4Al3Mo1V Alloy. *JOM,* 67**,** 1265-1272.

KUROSE, H., MIYAGI, D., TAKAHASHI, N., UCHIDA, N. & KAWANAKA, K. 2009. 3-D Eddy Current Analysis of Induction Heating Apparatus Considering Heat

Emission, Heat Conduction, and Temperature Dependence of Magnetic Characteristics. *IEEE Transactions on Magnetics,* 45**,** 1847-1850.
L TJERING, G. & WILLIAMS, J. C. 2007. *Titanium*, Springer Science & Business Media.
LANE, B. & MOYLAN, S. 2016. Thermographic measurements of the commercial laser powder bed fusion process at NIST. *Rapid Prototyping Journal,* 22**,** 778-787.
LEBRUN, T., NAKAMOTO, T., HORIKAWA, K. & KOBAYASHI, H. 2015. Effect of retained austenite on subsequent thermal processing and resultant mechanical properties of selective laser melted 17–4 PH stainless steel. *Materials & Design,* 81**,** 44-53.
LEE, D.-G., LEE, S. & LEE, C. S. 2004. Quasi-static and dynamic deformation behavior of Ti–6Al–4V alloy containing fine α2-Ti3Al precipitates. *Materials Science and Engineering: A,* 366**,** 25-37.
LEUDERS, S., LIENEKE, T., LAMMERS, S., TR STER, T. & NIENDORF, T. 2014. On the fatigue properties of metals manufactured by selective laser melting – The role of ductility. *Journal of Materials Research,* 29**,** 1911-1919.
LEUDERS, S., TH NE, M., RIEMER, A., NIENDORF, T., TR STER, T., RICHARD, H. A. & MAIER, H. J. 2013. On the mechanical behaviour of titanium alloy TiAl6V4 manufactured by selective laser melting: Fatigue resistance and crack growth performance. *International Journal of Fatigue,* 48**,** 300-307.
LI, W., LIU, J., ZHOU, Y., WEN, S., WEI, Q., YAN, C. & SHI, Y. 2016. Effect of substrate preheating on the texture, phase and nanohardness of a Ti–45Al–2Cr–5Nb alloy processed by selective laser melting. *Scripta Materialia,* 118**,** 13-18.
LIANG, W., LIU, Y., ZHU, B., ZHOU, M. & ZHANG, Y. 2015. Conduction heating of boron alloyed steel in application for hot stamping. *International Journal of Precision Engineering and Manufacturing,* 16**,** 1983-1992.
LIN, J. J., LV, Y. H., LIU, Y. X., XU, B. S., SUN, Z., LI, Z. G. & WU, Y. X. 2016. Microstructural evolution and mechanical properties of Ti-6Al-4V wall deposited by pulsed plasma arc additive manufacturing. *Materials & Design,* 102**,** 30-40.
LIU, Q., DANLOS, Y., SONG, B., ZHANG, B., YIN, S. & LIAO, H. 2015. Effect of high-temperature preheating on the selective laser melting of yttria-stabilized zirconia ceramic. *Journal of Materials Processing Technology,* 222**,** 61-74.
LIU, S. & SHIN, Y. C. 2019. Additive manufacturing of Ti6Al4V alloy: A review. *Materials & Design,* 164**,** 107552.
LMAZ, ERMIS, M. & CADIRCI, I. 2012. Medium-Frequency Induction Melting Furnace as a Load on the Power System. *IEEE Transactions on Industry Applications,* 48**,** 1203-1214.
LOSERTOV , M. & KUBEŠ, V. 2017. Microstructure and mechanical properties of selective laser melted Ti6Al4V alloy. *IOP Conference Series: Materials Science and Engineering,* 266**,** 012009.
LUC, O., BURD, J. M., MILL, I., ACERO, J. & BARRAG, L. A. 2010. Efficiency-Oriented Design of ZVS Half-Bridge Series Resonant Inverter With Variable Frequency Duty Cycle Control. *IEEE Transactions on Power Electronics,* 25**,** 1671-1674.
LUC, O., MAUSSION, P., DEDE, E. J. & BURD, J. M. 2014. Induction Heating Technology and Its Applications: Past Developments, Current Technology, and Future Challenges. *IEEE Transactions on Industrial Electronics,* 61**,** 2509-2520.
LUCA, F., EMANUELE, M., PIERFRANCESCO, R., ALBERTO, M., SIMON, H. & KONRAD, W. 2010. Ductility of a Ti‐6Al‐4V alloy produced by selective laser melting of prealloyed powder. *Rapid Prototyping Journal,* 16**,** 450-459.

LY, S., RUBENCHIK, A. M., KHAIRALLAH, S. A., GUSS, G. & MATTHEWS, M. J. 2017. Metal vapor micro-jet controls material redistribution in laser powder bed fusion additive manufacturing. *Scientific Reports,* 7**,** 4085.

MEINERS, W., WISSENBACH, K. & OVER, C. 2004. *Method and device for the selective laser sintering of metallic substances*.

MENG, M., FAN, X. G., YANG, H., GUO, L. G., ZHAN, M. & GAO, P. F. 2017a. Precipitation of secondary alpha in competition with epitaxial growth of primary alpha in two-phase titanium alloys. *Journal of Alloys and Compounds,* 714**,** 294-302.

MENG, M., YANG, H., FAN, X. G., YAN, S. L., ZHAO, A. M. & ZHU, S. 2017b. On the modeling of diffusion-controlled growth of primary alpha in heat treatment of two-phase Ti-alloys. *Journal of Alloys and Compounds,* 691**,** 67-80.

MERTENS, A., REGINSTER, S., PAYDAS, H., CONTREPOIS, Q., DORMAL, T., LEMAIRE, O. & LECOMTE-BECKERS, J. 2014. Mechanical properties of alloy Ti–6Al–4V and of stainless steel 316L processed by selective laser melting: influence of out-of-equilibrium microstructures. *Powder Metallurgy,* 57**,** 184-189.

MISTURE, S. T. & SNYDER, R. L. 2001. X-ray Diffraction. *In:* BUSCHOW, K. H. J., CAHN, R. W., FLEMINGS, M. C., ILSCHNER, B., KRAMER, E. J., MAHAJAN, S. & VEYSSI RE, P. (eds.) *Encyclopedia of Materials: Science and Technology*. Oxford: Elsevier.

MOLETSANE, M., KRAKHMALEV, P., KAZANTSEVA, N., DU PLESSIS, A., YADROITSAVA, I. & YADROITSEV, I. 2016. Tensile properties and microstructure of direct metal laser-sintered TI6AL4V (ELI) Alloy. *South African Journal of Industrial Engineering,* 27**,** 110-121.

MUCHA, G. M., NOVORSKY, D. E. & PFAFFMANN, G. D. 1987. Method for hardening gears by induction heating. U.S. Patent No. 4,675,488.

MURR, L. E., GAYTAN, S. M., RAMIREZ, D. A., MARTINEZ, E., HERNANDEZ, J., AMATO, K. N., SHINDO, P. W., MEDINA, F. R. & WICKER, R. B. 2012. Metal Fabrication by Additive Manufacturing Using Laser and Electron Beam Melting Technologies. *Journal of Materials Science & Technology,* 28**,** 1-14.

NANDWANA, P., LEE, Y., RANGER, C., ROLLETT, A. D., DEHOFF, R. R. & BABU, S. S. 2019. Post-processing to Modify the α Phase Micro-Texture and β Phase Grain Morphology in Ti-6Al-4V Fabricated by Powder Bed Electron Beam Melting. *Metallurgical and Materials Transactions A,* 50**,** 3429-3439.

NAZAROVA, T. I., IMAYEV, V. M., IMAYEV, R. M. & PAVLINICH, S. P. 2015. Microstructure and Mechanical Tensile Properties of a VT6 Alloy Manufactured by Selective Laser Melting. *Russian Physics Journal*.

PARRY, L., ASHCROFT, I. A. & WILDMAN, R. D. 2016. Understanding the effect of laser scan strategy on residual stress in selective laser melting through thermo-mechanical simulation. *Additive Manufacturing,* 12**,** 1-15.

PENG, X., GUO, H., WANG, T. & YAO, Z. 2012. Effects of β treatments on microstructures and mechanical properties of TC4-DT titanium alloy. *Materials Science and Engineering: A,* 533**,** 55-63.

PHILIPPI, J. & MATTES, T. 2009. *Method of manufacturing three-dimensional objects by laser sintering*.

PILCHAK, A. L., SARGENT, G. A. & SEMIATIN, S. L. 2017. Early Stages of Microstructure and Texture Evolution during Beta Annealing of Ti-6Al-4V. *Metallurgical and Materials Transactions A*.

POLMEAR, I., STJOHN, D., NIE, J.-F. & QIAN, M. 2017. *Light Alloys: metallurgy of the light metals,* Oxford, Butterworth-Heinemann.

POPOVICH, A., SUFIIAROV, V., BORISOV, E. & POLOZOV, I. 2015. Microstructure and Mechanical Properties of Ti-6Al-4V Manufactured by SLM. *Key Engineering Materials,* 651-653**,** 677-682.

PORCH, A. & MCFARLAND, G. 2016. *Additive manufacturing apparatus and method*.

QAZI, J. I., SENKOV, O. N., RAHIM, J. & FROES, F. H. 2003. Kinetics of martensite decomposition in Ti–6Al–4V–xH alloys. *Materials Science and Engineering: A,* 359**,** 137-149.

QIAN, M., XU, W., BRANDT, M. & TANG, H. P. 2016. Additive manufacturing and postprocessing of Ti-6Al-4V for superior mechanical properties. *MRS Bulletin,* 41**,** 775-784.

QIU, C., ADKINS, N. J. E. & ATTALLAH, M. M. 2013. Microstructure and tensile properties of selectively laser-melted and of HIPed laser-melted Ti–6Al–4V. *Materials Science and Engineering: A,* 578**,** 230-239.

QIU, D., ZHAO, P., SHI, R., WANG, Y. & LU, W. 2016. Effect of autocatalysis on variant selection of α precipitates during phase transformation in Ti-6Al-4V alloy. *Computational Materials Science,* 124**,** 282-289.

ROBERTS, I. A. 2012. *Investigation of residual stresses in the laser melting of metal powders in additive layer manufacturing.* PhD, University of Wolverhampton.

ROBINSON, J., ASHTON, I., FOX, P., JONES, E. & SUTCLIFFE, C. 2018. Determination of the effect of scan strategy on residual stress in laser powder bed fusion additive manufacturing. *Additive Manufacturing,* 23**,** 13-24.

ROLLETT, A. D. & BARMAK, K. 2014. 11 - Orientation Mapping. *In:* LAUGHLIN, D. E. & HONO, K. (eds.) *Physical Metallurgy (Fifth Edition).* Oxford: Elsevier.

ROMBOUTS, M., KRUTH, J. P., FROYEN, L. & MERCELIS, P. 2006. Fundamentals of Selective Laser Melting of alloyed steel powders. *CIRP Annals - Manufacturing Technology,* 55**,** 187-192.

RUDNEV, V., LOVELESS, D., COOK, R. L. & BLACK, M. 2002. *Handbook of induction heating*, CRC Press.

RUDOLF, R., MITSCHANG, P. & NEITZEL, M. 2000. Induction heating of continuous carbon-fibre-reinforced thermoplastics. *Composites Part A: Applied Science and Manufacturing,* 31**,** 1191-1202.

SAE 2014. Heat Treatment of Titanium Alloy Parts. SAE International.

SAE 2016. Titanium Alloy Direct Deposited Products 6Al - 4V Annealed. SAE International.

SALEM, A. A., GLAVICIC, M. G. & SEMIATIN, S. L. 2008. A coupled EBSD/EDS method to determine the primary- and secondary-alpha textures in titanium alloys with duplex microstructures. *Materials Science and Engineering: A,* 494**,** 350-359.

SALLICA-LEVA, E., CARAM, R., JARDINI, A. L. & FOGAGNOLO, J. B. 2016. Ductility improvement due to martensite α' decomposition in porous Ti − 6Al − 4V parts produced by selective laser melting for orthopedic implants. *Journal of the Mechanical Behavior of Biomedical Materials,* 54**,** 149-158.

SARGENT, G. A., KINSEL, K. T., PILCHAK, A. L., SALEM, A. A. & SEMIATIN, S. L. 2012. Variant Selection During Cooling after Beta Annealing of Ti-6Al-4V Ingot Material. *Metallurgical and Materials Transactions A,* 43**,** 3570-3585.

SCHWARZE, D. & SCHOENEBORN, H. 2015. *METHOD AND DEVICE FOR CONTROLLING AN IRRADIATION SYSTEM*.

SCOTT, J. A. & SPRUIELL, J. E. 1974. Grain refinement of wrought austenitic stainless steels by rapid heating. *Metallurgical Transactions,* 5**,** 255.

SEMIATIN, S. L., KNISLEY, S. L., FAGIN, P. N., BARKER, D. R. & ZHANG, F. 2003. Microstructure evolution during alpha-beta heat treatment of Ti-6Al-4V. *Metallurgical and Materials Transactions A,* 34**,** 2377-2386.

SHI, R., DIXIT, V., FRASER, H. L. & WANG, Y. 2014. Variant selection of grain boundary α by special prior β grain boundaries in titanium alloys. *Acta Materialia,* 75**,** 156-166.

SHI, R., DIXIT, V., VISWANATHAN, G. B., FRASER, H. L. & WANG, Y. 2016. Experimental assessment of variant selection rules for grain boundary α in titanium alloys. *Acta Materialia,* 102**,** 197-211.

SHI, R. & WANG, Y. 2013. Variant selection during α precipitation in Ti–6Al–4V under the influence of local stress – A simulation study. *Acta Materialia,* 61**,** 6006-6024.

SHIM, D.-S., BAEK, G.-Y. & LEE, E.-M. 2017. Effect of substrate preheating by induction heater on direct energy deposition of AISI M4 powder. *Materials Science and Engineering: A,* 682**,** 550-562.

SHIPLEY, H., MCDONNELL, D., CULLETON, M., COULL, R., LUPOI, R., O'DONNELL, G. & TRIMBLE, D. 2018. Optimisation of process parameters to address fundamental challenges during selective laser melting of Ti-6Al-4V: A review. *International Journal of Machine Tools and Manufacture,* 128**,** 1-20.

SHUNMUGAVEL, M., POLISHETTY, A., SINGH, R. & LITTLEFAIR, G. 2017. A comparative study of mechanical properties and machinability of wrought and additive manufactured (selective laser melting) titanium alloy – Ti-6Al-4V. *Rapid Prototyping Journal,* 23**,** 1051-1056.

SIMONELLI, M. 2014. *Microstructure Evolution and Mechanical Properties of Selective Laser Melted Ti-6Al-4V.* PhD, Loughborough University.

SIMONELLI, M., TSE, Y. Y. & TUCK, C. 2014. Effect of the build orientation on the mechanical properties and fracture modes of SLM Ti–6Al–4V. *Materials Science and Engineering: A,* 616**,** 1-11.

STARR, T. L., RAFI, K., STUCKER, B. & SCHERZER, C. M. Controlling phase composition in selective laser melted stainless steels. Solid Freeform Fabrication Symposium, 2012 Austin, TX. 439-446.

STEFANSSON, N. & SEMIATIN, S. L. 2003. Mechanisms of globularization of Ti-6Al-4V during static heat treatment. *Metallurgical and Materials Transactions A,* 34**,** 691-698.

STEIGERWALD, R. L. 1988. A comparison of half-bridge resonant converter topologies. *IEEE Transactions on Power Electronics,* 3**,** 174-182.

SUTTON, A. T., KRIEWALL, C. S., LEU, M. C. & NEWKIRK, J. W. 2017. Powder characterisation techniques and effects of powder characteristics on part properties in powder-bed fusion processes. *Virtual and Physical Prototyping,* 12**,** 3-29.

TER HAAR, G. M., BECKER, T. H. & BLAINE, D. C. 2016. Influence of heat treatments on the microstructure and tensile behaviour of selective laser melting-produced TI-6AL-4V parts. *South African Journal of Industrial Engineering,* 27**,** 174-183.

TER HAAR, M. G. & BECKER, H. T. 2018. Selective Laser Melting Produced Ti-6Al-4V: Post-Process Heat Treatments to Achieve Superior Tensile Properties. *Materials,* 11.

TH NE, M., LEUDERS, S., RIEMER, A., TR STER, T. & RICHARD, H. A. Influence of heat-treatment on selective laser melting products - E.g. Ti6al4v. 23rd Annual International Solid Freeform Fabrication Symposium, 2012. 492-498.

THIJS, L., VERHAEGHE, F., CRAEGHS, T., HUMBEECK, J. V. & KRUTH, J.-P. 2010. A study of the microstructural evolution during selective laser melting of Ti–6Al–4V. *Acta Materialia,* 58**,** 3303-3312.

TOTTEN, G. E. 2006. *Steel heat treatment: equipment and process design*, CRC Press.

TRAPP, J., RUBENCHIK, A. M., GUSS, G. & MATTHEWS, M. J. 2017. In situ absorptivity measurements of metallic powders during laser powder-bed fusion additive manufacturing. *Applied Materials Today,* 9**,** 341-349.

ULABY, F. T. 2014. *Fundamentals of applied electromagnetics(seventh edition)*, Upper Saddle River, NJ: Prentice-Hall, Inc,.

URIONDO, A., ESPERON-MIGUEZ, M. & PERINPANAYAGAM, S. 2015. The present and future of additive manufacturing in the aerospace sector: A review of important aspects. *Proceedings of the Institution of Mechanical Engineers, Part G: Journal of Aerospace Engineering,* 229**,** 2132-2147.

VAYRE, B., VIGNAT, F. & VILLENEUVE, F. 2012. Metallic additive manufacturing: State-of-the-art review and prospects. *Mechanics and Industry,* 13**,** 89-96.

VILARO, T., COLIN, C. & BARTOUT, J. D. 2011. As-Fabricated and Heat-Treated Microstructures of the Ti-6Al-4V Alloy Processed by Selective Laser Melting. *Metallurgical and Materials Transactions A,* 42**,** 3190-3199.

VORA, P., MUMTAZ, K., TODD, I. & HOPKINSON, N. 2015. AlSi12 in-situ alloy formation and residual stress reduction using anchorless selective laser melting. *Additive Manufacturing,* 7**,** 12-19.

VRANCKEN, B., BULS, S., KRUTH, J.-P. & HUMBEECK, J. V. 2016. Preheating of Selective Laser Melted Ti6Al4V: Microstructure and Mechanical Properties. *Proceedings of the 13th World Conference on Titanium.* John Wiley & Sons, Inc.

VRANCKEN, B., THIJS, L., KRUTH, J.-P. & VAN HUMBEECK, J. 2012. Heat treatment of Ti6Al4V produced by Selective Laser Melting: Microstructure and mechanical properties. *Journal of Alloys and Compounds,* 541**,** 177-185.

W. KURZ, D. J. F. 1991. *Fundamentals of solidification,* Aedermannsdorf, Aedermannsdorf : Trans Tech Publications.

WANG, S. C., AINDOW, M. & STARINK, M. J. 2003. Effect of self-accommodation on α/α boundary populations in pure titanium. *Acta Materialia,* 51**,** 2485-2503.

WANG, Y. M., VOISIN, T., MCKEOWN, J. T., YE, J., CALTA, N. P., LI, Z., ZENG, Z., ZHANG, Y., CHEN, W., ROEHLING, T. T., OTT, R. T., SANTALA, M. K., DEPOND, PHILIP J., MATTHEWS, M. J., HAMZA, A. V. & ZHU, T. 2017. Additively manufactured hierarchical stainless steels with high strength and ductility. *Nature Materials***,** nmat5021.

WAUTHLE, R., VRANCKEN, B., BEYNAERTS, B., JORISSEN, K., SCHROOTEN, J., KRUTH, J.-P. & VAN HUMBEECK, J. 2015. Effects of build orientation and heat treatment on the microstructure and mechanical properties of selective laser melted Ti6Al4V lattice structures. *Additive Manufacturing,* 5**,** 77-84.

WELSCH, G., BOYER, R. & COLLINGS, E. 1993. *Materials properties handbook: titanium alloys*, ASM international.

WEN, S. F., YAN, C. Z., WEI, Q. S., ZHANG, L. C., ZHAO, X., ZHU, W. & SHI, Y. S. 2014. Investigation and development of large-scale equipment and high performance materials for powder bed laser fusion additive manufacturing. *Virtual and Physical Prototyping,* 9**,** 213-223.

WOJDA, R. P. & KAZIMIERCZUK, M. K. 2013. Analytical Optimization of Solid-Round-Wire Windings. *IEEE Transactions on Industrial Electronics,* 60**,** 1033-1041.

WU, M.-W., LAI, P.-H. & CHEN, J.-K. 2016a. Anisotropy in the impact toughness of selective laser melted Ti–6Al–4V alloy. *Materials Science and Engineering: A,* 650**,** 295-299.

WU, S. Q., LU, Y. J., GAN, Y. L., HUANG, T. T., ZHAO, C. Q., LIN, J. J., GUO, S. & LIN, J. X. 2016b. Microstructural evolution and microhardness of a selective-laser-melted Ti–6Al–4V alloy after post heat treatments. *Journal of Alloys and Compounds,* 672**,** 643-652.

WU, S. Q., LU, Y. J., GAN, Y. L., HUANG, T. T., ZHAO, C. Q., LIN, J. J., GUO, S. & LIN, J. X. 2016c. Microstructural evolution and microhardness of a selective-laser-melted Ti–6Al–4V alloy after post heat treatments. *Journal of Alloys and Compounds,* 672**,** 643-652.

XU, W., BRANDT, M., SUN, S., ELAMBASSERIL, J., LIU, Q., LATHAM, K., XIA, K. & QIAN, M. 2015. Additive manufacturing of strong and ductile Ti–6Al–4V by selective laser melting via in situ martensite decomposition. *Acta Materialia,* 85**,** 74-84.

XU, W., LI, S., WHITELY, N. & PAN, W.-P. 2005. Fundamentals of TGA and SDT.

XU, W., LUI, E. W., PATERAS, A., QIAN, M. & BRANDT, M. 2017a. In situ tailoring microstructure in additively manufactured Ti-6Al-4V for superior mechanical performance. *Acta Materialia,* 125**,** 390-400.

XU, Y., LU, Y., SUNDBERG, K. L., LIANG, J. & SISSON, R. D. 2017b. Effect of Annealing Treatments on the Microstructure, Mechanical Properties and Corrosion Behavior of Direct Metal Laser Sintered Ti-6Al-4V. *Journal of Materials Engineering and Performance,* 26**,** 2572-2582.

YADROITSEV, I., GUSAROV, A., YADROITSAVA, I. & SMUROV, I. 2010. Single track formation in selective laser melting of metal powders. *Journal of Materials Processing Technology,* 210**,** 1624-1631.

YANG, J., YU, H., WANG, Z. & ZENG, X. 2017. Effect of crystallographic orientation on mechanical anisotropy of selective laser melted Ti-6Al-4V alloy. *Materials Characterization,* 127**,** 137-145.

YANG, J., YU, H., YIN, J., GAO, M., WANG, Z. & ZENG, X. 2016. Formation and control of martensite in Ti-6Al-4V alloy produced by selective laser melting. *Materials & Design,* 108**,** 308-318.

YAP, C. Y., CHUA, C. K., DONG, Z. L., LIU, Z. H., ZHANG, D. Q., LOH, L. E. & SING, S. L. 2015. Review of selective laser melting: Materials and applications. *Applied Physics Reviews,* 2**,** 041101.

ZAEH, M. & BRANNER, G. 2010. Investigations on residual stresses and deformations in selective laser melting. *Production Engineering,* 4**,** 35-45.

ZANMING, W., XIAOGUANG, Y., YOUHUA, W. & WEILI, Y. 2001. Eddy current and temperature field computation in transverse flux induction heating equipment for galvanizing line. *IEEE Transactions on Magnetics,* 37**,** 3437-3439.

ZENG, L. & BIELER, T. R. 2005. Effects of working, heat treatment, and aging on microstructural evolution and crystallographic texture of α, α′, α″ and β phases in Ti–6Al–4V wire. *Materials Science and Engineering: A,* 392**,** 403-414.

ZHANG, X.-Y., FANG, G., LEEFLANG, S., B TTGER, A. J., ZADPOOR, A. & ZHOU, J. 2018. Effect of subtransus heat treatment on the microstructure and mechanical properties of additively manufactured Ti-6Al-4V alloy. *Journal of Alloys and Compounds,* 735**,** 1562-1575.

ZINN, S. & SEMIATIN, S. L. 1988. *Elements of Induction Heating : Design, Control, and Applications,* Materials Park, OH, USA, ASM International.